Scrutinizing the Top Quark at Lepton Colliders with Higher Orders

From Fixed Order to Resummation and Matching

vorgelegt von
Bijan Chokoufe Nejad

Hamburg
2017

Dissertation zur Erlangung des Doktorgrades an der Fakultät
für Mathematik, Informatik und Naturwissenschaften
Fachbereich Physik der Universität Hamburg

DESY-THESIS-2017-029

Gutachter der Dissertation:	Dr. Jürgen Reuter Prof. Dr. Sven-Olaf Moch
Zusammensetzung der Prüfungskommission:	Dr. Jürgen Reuter Prof. Dr. Sven-Olaf Moch Prof. Dr. Gudrid Moortgat-Pick Prof. Dr. Dieter Horns PD Dr. Andreas Meyer
Vorsitzender der Prüfungskommission:	Prof. Dr. Dieter Horns
Datum der Disputation:	12.07.2017
Vorsitzender Fach-Promotionsschuss PHYSIK:	Prof. Dr. Wolfgang Hansen
Leiter des Fachbereichs PHYSIK:	Prof. Dr. Michael Potthoff
Dekan der Fakultät MIN:	Prof. Dr. Heinrich Graener

Zusammenfassung

Wir präsentieren in dieser Arbeit detaillierte Studien von Topquarkpaarproduktion mit ($t\bar{t}H$) und ohne assoziiertem Higgsboson ($t\bar{t}$) in e^+e^--Kollisionen. Diese Prozesse sind von besonderem Interesse für das Topphysikprogramm künftiger Elektron-Positron-Beschleuniger. Insbesondere erlauben sie Präzisionsmessungen der Topquarkmasse und der Yukawa-Kopplung. Wir zeigen hierzu Vorhersagen für off-shell $t\bar{t}$- und $t\bar{t}H$ Produktion, wobei nichtresonante und Interferenzeffekte bis zur nächstführenden Ordnung (NLO) in perturbativer Quantenchromodynamik (QCD) berücksichtigt werden. Dies erlaubt eine Topquarkphänomenologie im Kontinuum auf bislang unerreichtem Niveau. Wir zeigen, dass off-shell Effekte und NLO QCD-Korrekturen für diese Prozesse im Allgemeinen nicht faktorisieren. Insbesondere präsentieren wir die Abhängigkeit des Wirkungsquerschnitts von der Yukawa-Kopplung, welche negative Korrekturen durch beträchtliche Interferenzterme erhält. Ferner fügen wir eine Diskussion von p_T-Resummation und der assoziierten Unsicherheit hinzu, in Form der Kombination von NLO Vorhersagen mit dem Partonshower mittels POWHEG-Matching.

Zur Behandlung großer Coulombsingularitäten an der Schwelle arbeiten wir die nächstführende logarithmische (NLL) Schwellenresummation, abgeleitet in nichtrelativistischer QCD (NRQCD), für $t\bar{t}$ Produktion ein. Dies resultiert in einem Formfaktor, welchen wir in einen vollrelativistischen Wirkungsquerschnitt einbetten, faktorisiert in einer erweiterten Doppelpolapproximation. Hierbei sind QCD-Korrekturen zum Topzerfall inbegriffen. Wir kombinieren diese Rechnung mit den vollen QCD NLO Korrekturen für $W^+W^-b\bar{b}$ Produktion, um eine Rechnung zu erhalten, welche nicht nur an der Schwelle gültig ist, sondern nahtlos ins Kontinuum übergeht. Dies ermöglicht uns die erste Vorhersage für exklusive $W^+W^-b\bar{b}$ Produktion an einem Elektron-Positron-Beschleuniger zu machen, welche ein konsistentes Matching zwischen der Top-Antitop-Schwelle und den Kontinuumsregionen vorweisen kann. Diese Rechnung ist nicht nur notwendig, um die intermediären Energieregionen zu beschreiben, sondern erlaubt zudem auch erstmals Schwelleneffekte in volldifferentiellen Verteilungen zu betrachten und enthält wichtige elektroschwache und relativistische Korrekturen.

Alle Rechnungen sind im automatisierten NLO Monte Carlo Eventgenerator WHIZARD implementiert. Daher geben wir ferner einen Überblick über die wesentlichen Aspekte des Programms und die verschiedenen zusätzlichen Features, die wir implementiert haben.

Abstract

In this thesis, we present detailed studies of top-pair production with ($\mathrm{t\bar{t}H}$) and without association of a Higgs boson ($\mathrm{t\bar{t}}$) in $\mathrm{e^+e^-}$ collisions. These processes are of utmost interest for the top physics program of future lepton colliders. They allow in particular a precise measurement of the top quark mass and the Yukawa coupling. For this purpose, we present predictions for off-shell $\mathrm{t\bar{t}}$ and $\mathrm{t\bar{t}H}$ production including non-resonant and interference contributions up to next-to-leading order (NLO) in perturbative quantum chromodynamics (QCD). This allows for top-quark phenomenology in the continuum at an unprecedented level of accuracy. We show that off-shell effects and NLO QCD corrections for these processes do not factorize in general. In particular, we present the Yukawa coupling dependence of the cross section, which receives negative corrections due to sizable interference terms. We also add a discussion of p_T resummation in the form of combining the NLO prediction via Powheg matching with the parton shower and the associated uncertainties.

To handle large Coulomb singularities at threshold, we include the next-to-leading log (NLL) threshold resummation derived in nonrelativistic QCD (NRQCD) for $\mathrm{t\bar{t}}$ production. This results in a form factor that we incorporate in a fully relativistic cross section, which is factorized within an extended double-pole approximation. Fixed-order QCD corrections are included, hereby, for the top decay. We combine this calculation with the full fixed-order QCD results at NLO for $\mathrm{W^+W^-b\bar{b}}$ production to obtain a computation that is not only valid at threshold but smoothly interpolates to the continuum. This allows us to present the first prediction for exclusive $\mathrm{W^+W^-b\bar{b}}$ production at a lepton collider with a consistent matching between the top-antitop threshold and continuum regions. This computation is not only required to describe the intermediate energy region but also allows to study threshold resummation effects in fully differential distributions and incorporates important electroweak and relativistic corrections.

All computations are implemented within the automated NLO Monte Carlo event generator Whizard. Thus, we review the important aspects of the program and various new features that we have implemented.

Contents

Chapter 1

Introduction

The first runs of the Large Hadron Collider (LHC) have been an incredible success story for the Standard Model (SM) of particle physics. With the discovery of the Higgs boson [1, 2], all particles that are required for a consistent theory of electroweak (EW) symmetry breaking have been observed. Countless distributions of numerous processes have been studied and so far everything agrees very well with the SM, at least as long as sophisticated theory predictions are used. This success comes with a major conundrum though: While there is observational evidence of beyond the SM (BSM) physics in the form of dark matter and energy from e.g. the measurement of the cosmic microwave background or galaxy rotation curves, none of the numerous searches at the LHC and other high-energy experiments have discovered any new particles. Furthermore, it was theoretically expected that new particles have to be found at energies close to the Higgs mass, as a scalar field otherwise receives large quantum corrections, which can only be removed with a severe fine-tuning. This mechanism, also known as naturalness or hierarchy problem, has been a guiding principle for decades. Confronted with the lack of new discoveries, nowadays new ideas like relaxion models [3] aim to solve this problem with a time-dependent ansatz, whereby the unnaturally low observed Higgs mass is just the result of the time evolution. Independently of the potential interpretation of the results, first and foremost the main task (aside from ongoing direct searches of new particles) is to measure and predict observables to ever higher accuracy in order to look for deviations and inconsistencies of the SM. This is the indirect path for discoveries, which was often a successful one in history, and also results in more precise measurements of masses and couplings.

One of the key particles of interest, hereby, is the top quark. It is the heaviest particle of the SM, and its detailed study offers great potential to probe the electroweak, flavor and Higgs sector. The close connection between the Higgs boson and the top quark is most apparent in the stability of the EW vacuum. It is mainly determined from the running of the Higgs quartic coupling, which can become negative at high scales and is very sensitive to the top mass as studied in detail in Ref. [4–9]. The upshot of these computations is that the current world averages for the Higgs, top, W and Z masses place the EW vacuum right at the border between stability and meta-stability. Meta-stability implies a finite lifetime of the EW vacuum, which is, however, longer than the age of the universe.

The near-criticality of the Higgs mass stimulated new ideas, where this point might be an attractor point of a dynamical evolution [8]. While such concepts may provide new insights, one firstly has to work out the exact situation within the SM. Especially, as the current uncertainties still allow for a strictly stable solution within 1.3σ of the top mass [9]. Decreasing the uncertainty on the top mass measurement is thus the single most important parameter to conclusively compute the fate of the EW vacuum. As it has been pointed out e.g. in Ref. [6], a future high-energy electron-positron collider would reduce this uncertainty possibly by an order of magnitude. Furthermore, the precise measurement of the top mass is an important input to global fits of the SM, which can reveal tensions within the model when uncertainties are sufficiently decreased [10].

To understand why the top mass cannot be easily measured more precisely at the LHC, we have to take a closer look: While the combination of Tevatron and LHC measurements of the top-quark mass gives a promisingly precise result of $m_\mathrm{t} = (173.34 \pm 0.76)\,\mathrm{GeV}$ [11], care has to be taken on how to interpret this number. In Ref. [8], the authors assume that this is in fact a measurement of the pole mass but due to inherent uncertainties associated to it, an additional error of $\pm 0.3\,\mathrm{GeV}$ is heuristically added. These uncertainties arise in QCD because the pole mass resolves scales of order Λ_QCD, which probe the non-perturbative nature of QCD close to the Landau pole. Going back to the measurements, we have to realize that all of the most precise top mass measurements determine the top mass by using template fits sensitive to hadronic distributions and thus merely obtain the parameter of the used Monte Carlo (MC) program, often called MC mass. This is problematic, as effects like color reconnection [12] of the top decay products affect the interpretation of the mass that is used in the fixed-order computation. That cannot only lead to underestimated uncertainties but to a systematic shift of the central value. First attempts to relate a MC and the pole mass using differential results have been presented in Ref. [13], leading to a difference between the MC mass in PYTHIA8 [14] and the pole mass of 900 MeV to 600 MeV using $\mathrm{e}^+\mathrm{e}^-$ 2-Jettiness for top-pair production at next-to- and next-to-next-to-leading-logarithmic order. Prior to this, a calibration of a MC mass to the pole mass using inclusive $\mathrm{t}\bar{\mathrm{t}}$ production has been performed [15]. Overall, we can expect these issues to be far better understood at a lepton collider, where the initial state needs no QCD modeling, neither in the form of the underlying event nor QCD initial-state radiation. Also the color state is simpler, as top-pair production is at leading order a pure EW production at lepton colliders, while it is a QCD process at hadron colliders.

The problems in the interpretation of direct top mass measurements call for more indirect measurements of the top mass. Ideally, one never uses the pole mass in the first place, which is by definition plagued by renormalon uncertainties [16]. Instead, a theoretically well defined short-distance mass, like the $\overline{\mathrm{MS}}$ mass, can be used as input parameter to inclusive observables like the top-pair production cross section [17]. However, this yields measurements with significantly larger errors of about 2.6 GeV [18]. Similarly, one can use inclusive single-top production [19] to obtain the $\overline{\mathrm{MS}}$ mass. While this is not quite as sensitive as $\mathrm{t}\bar{\mathrm{t}}$, it can help to find inconsistencies in parton distribution functions (PDFs) and in fact the differences of results obtained with different PDFs are by far larger than all other uncertainties. In summary, a measurement of a short-distance mass at a hadron collider at the $\mathcal{O}\,(100\,\mathrm{MeV})$ level seems unrealistic.

To truly reach this level of precision, a future linear lepton collider, such as the proposed International Linear Collider (ILC) [20, 21] or Compact Linear Collider (CLIC) [22] is needed. With respect to top physics, the two most interesting processes to be studied in lepton collisions are top-pair production with and without an associated Higgs boson. Top-pair production allows to measure the top-quark mass at threshold in a short-distance scheme, like the 1S [23] or PS scheme [24], with uncertainties at or below 100 MeV [25–29]. Associated $\mathrm{t\bar{t}H}$ production, on the other hand, is our best handle to measure the top Yukawa coupling with per cent level precision, see e.g. Ref. [30, 31]. Note that while it has been suggested that the top Yukawa coupling can be measured at the $\mathrm{t\bar{t}}$ threshold to the per cent level as well [26], the computation [27] shows that the measurement using $\mathrm{t\bar{t}}$ at threshold would more likely be of $\mathcal{O}\,(20\,\%)$.

Aside from top physics, high-energy lepton colliders also give unique possibilities to measure all Yukawa couplings with unprecedented precision, the Higgs self-couplings and the total Higgs width with per cent accuracy [32]. Especially, polarized beams allow to disentangle possible new physics contributions in EW form factors and to study asymmetries in detail. Most of these measurements are at this level of precision not possible at the LHC and thus both colliders complement each other nicely. Obviously, most of the physical parameters can only be extracted with the quoted levels of precision when the theoretical uncertainties are under control and match their experimental counterparts.

As we already remarked in the beginning of this chapter, the extent of the success story of the LHC was only possible due to numerous higher-order computations for various processes. In recent years, the theory community has progressed considerably in automating precision computations. Advances reach from the automated and fast generation of one-loop matrix elements [33–36] and the full computation of processes at NLO in generic MC event generators [37–40], to NNLO computations for diboson production [41–45] up to NNNLO computations for Higgs boson production [46], to name a few. It is crucial to understand the effects of higher orders both on signal strengths as well as on distributions, before some mild deviation in some distribution can be attributed to BSM physics. For example, the top-quark forward-backward asymmetry measured by DØ [47] and CDF [48] at the Tevatron was a longstanding mystery as the NLO QCD+EW prediction was systematically lower than the measurements. This has spurred various explanations in new physics models. It is, however, brought nicely into accordance with the SM by calculating the NNLO corrections [49].

Returning to top quark physics at lepton colliders, we have to remark that most theoretical efforts have concentrated on on-shell computations. For relativistic computations of $\mathrm{t\bar{t}}$, which are valid in the continuum energy region, the main ingredients have been obtained to NNNLO in QCD inclusively [50] and the differential cross section can be computed to NNLO [51, 52]. The NLO QCD effects on the irreducible final state $\mathrm{W^+W^-b\bar{b}}$ have been considered at NLO [53, 54] but a study of the full physical final state $\mathrm{b\bar{b}}4f$ is missing. For $\mathrm{t\bar{t}H}$, only QCD [55] and EW [56] NLO corrections have been computed and $\mathrm{W^+W^-b\bar{b}H}$ or even $\mathrm{b\bar{b}}4f\mathrm{H}$ have not been considered. However, for the precision measurement of the top Yukawa coupling and studies of the forward-backward asymmetry, it is mandatory to understand off-shell effects and their interplay with QCD corrections in detail. Furthermore, it can be used to determine experimental efficiencies in measurements when higher-order computations are used that do not account for off-shell effects. This can only be achieved by computing the full final states, which we show in this thesis.

At the $\mathrm{t\bar{t}}$ threshold, we have to stress that the naive counting of orders in terms of the strong and electroweak couplings is not appropriate. Instead, bound state effects due to soft Coulomb singularities are so important that gluon ladder diagrams have to be resummed, usually in NRQCD, even at "LO". Furthermore, an expansion in terms of α_s, v and α_{em} is performed, with the assumption that $\alpha_s \sim v \sim \sqrt{\alpha_{\mathrm{em}}}$. As the strong corrections can be considered under control by virtue of the NNNLO [57] and NNLL [58] results, the relativistic and electroweak corrections have to be taken under closer investigation. Given the threshold order counting, already taking one tree-level decay in the nonrelativistic approximation into account is considered an NLO effect [59, 60] and the fixed-order QCD correction to $\mathrm{W^+W^-b\bar{b}}$ an NNLO contribution [61, 62]. While there has been considerable progress in obtaining those NNLO contributions [61, 63] within unstable-particle effective field theory [64], one can obtain especially the background contributions also from the full $\mathrm{W^+W^-b\bar{b}}$ at fixed NLO. This is possible if one is able to remove the double counting of Coulomb singularities, as we present in this thesis. Finally, we emphasize that all of the nonrelativistic computations are only valid close to threshold and are either given for specific observables as the three-momentum distribution [23] or only known fully inclusively. Both of these issues are solved in this thesis by matching the resummed with the fixed-order computation consistently and implementing the result in an event generator. Specifically, we incorporate the $\mathrm{t\bar{t}}$ form factor with NLL threshold resummation, derived in NRQCD, into a relativistic cross section that is factorized within an extended double-pole approximation. Fixed-order QCD corrections are included, hereby, for the top decay.

This work is divided in three parts. In Part I, we review relevant aspects of NLO and Powheg event generation. Furthermore, we present the automated implementation in the MC event generator Whizard. We show in Part II predictions for $\mathrm{t\bar{t}}$ and $\mathrm{t\bar{t}H}$ production and decay at future lepton colliders including all non-resonant and interference contributions for leptonic decays up to NLO in QCD. In Part III, we present the first prediction for exclusive $\mathrm{W^+\,b\,W^-\,\bar{b}}$ production at a lepton collider with a consistent matching between the top-antitop threshold and continuum regions. Finally, we summarize our findings and conclude with a short outlook on possible extensions of the presented results in Chapter 9.

Part I

Fixed order and matched event generation

Chapter 2

NLO event generation

In this chapter, we will discuss various aspects of NLO calculations, at first in general and then in the context of the WHIZARD event generator. We will concentrate in this work solely on QCD corrections and thus often use NLO as a synonym to NLO QCD. We note, though, that basically all ideas and approaches are applicable to electroweak corrections in the same way. Also our implementations within WHIZARD are for the most part generic enough to allow for a straightforward generalization to EW corrections (potentially even in BSM models), which is ongoing work in the WHIZARD project.

We start with the underpinnings of NLO predictions in Section 2.1. This is followed by a more detailed description of the Frixione, Kunszt, Signer (FKS) subtraction scheme in Section 2.2. In Section 2.3, we give a brief description of the WHIZARD event generator and the infrastructure changes we have implemented to use it for NLO computations. Then, we discuss the possibility to separate the real contributions into singular and finite pieces in Section 2.4 and show the simplicity of the matrix-element method at NLO when FKS subtraction is used in Section 2.5. In Section 2.6, we address the issue of resonance-aware subtraction and its implementation in WHIZARD.

2.1 NLO computations

It can be shown [65] that the transition amplitude of an incoming state to an outgoing state is given at leading order by applying the Feynman rules of the given Lagrangian to construct the sum of all possible tree-level amplitudes, $\mathcal{M}_n^{(0)}$. With this, the differential, leading order (LO) cross section is given by

$$\mathrm{d}\sigma^{\mathrm{LO}} = \mathrm{d}\Phi_n \left|\mathcal{M}_n^{(0)}\right|^2 \tag{2.1}$$

We absorb, hereby, the flux factor for the incoming state, four-momentum conservation as well as the integration over final-state momenta in the phase-space measure $\mathrm{d}\Phi_n$. It becomes more interesting when we try to compute the one-loop correction for a given process. The integration over the loop momenta can yield divergences, both for small, i.e. infrared (IR), as well as large, i.e. ultraviolet (UV), momenta. The UV singularities can be removed by renormalization, whereby the divergence is canceled by appropriate counter terms to the bare Lagrangian [65]. This leaves us with IR singularities in the one-loop expression for n particles. It turns out that these are canceled by the corresponding $n+1$ particle contributions, which also diverge when a *massless* particles becomes soft or two massless particles become collinear. It has been shown by Kinoshita [66] as well as Lee and Nauenberg [67] that these *mass singularities* cancel out in general as long as one sums over degenerate states. This is commonly referred to as the KLN theorem and has been realized in QED already by Bloch and Nordsieck [68]. Physically, it corresponds to the fact that one cannot distinguish a final state from another one that is accompanied with an infinitely soft gluon or photon. Diagrammatically, one can see that both *virtual*

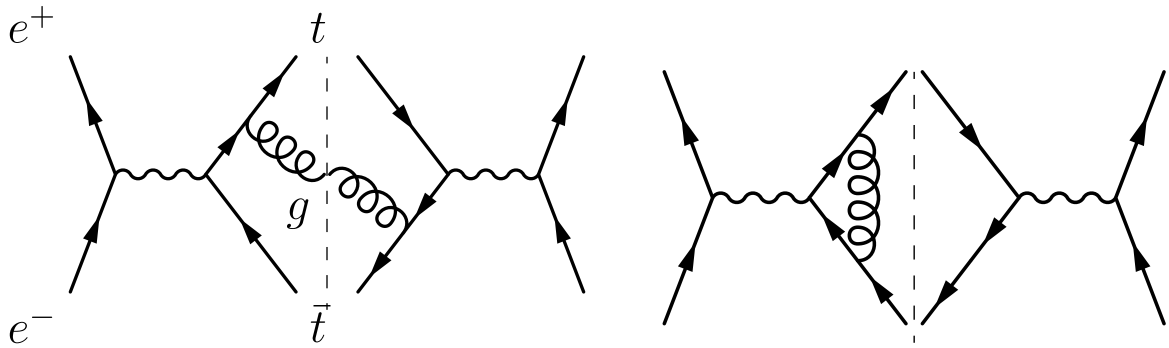

Figure 2.1 Exemplary Feynman diagrams for real and virtual corrections to on-shell top-pair production at a lepton collider

corrections, $V = 2\,\mathrm{Re}\big[\mathcal{M}_n^{(0)}\mathcal{M}_n^{(1)*}\big]$, as well as *real* corrections, $R = \Big|\mathcal{M}_{n+1}^{(0)}\Big|^2$, belong to the same set of Feynman graphs that is cut by an arbitrarily drawn line [67] as depicted in Fig. 2.1. Note that the guarantee of finite results of the KLN theorem only holds for *IR safe observables*. IR safety means that the observable should not be sensitive to extremely soft or collinear momenta. To ensure this for collinear momenta, usually a clustering algorithm is employed, which recombines momenta that are close.

We can write down the differential NLO cross section, which also includes the leading-order (Born) contribution $B = \Big|\mathcal{M}_n^{(0)}\Big|^2$, as

$$\mathrm{d}\sigma^{\mathrm{NLO}} = \mathrm{d}\Phi_n B + \mathrm{d}\Phi_{n+1} R + \mathrm{d}\Phi_n V \ . \tag{2.2}$$

Note that this also requires a fixed order counting in B such that

$$B = \mathcal{O}\big(\alpha^n, \alpha_s^m\big) \quad \text{and} \quad \{R, V\} = \mathcal{O}\big(\alpha^n, \alpha_s^{m+1}\big) \ . \tag{2.3}$$

for QCD corrections and analogously for QED corrections n is increased.

Eq. (2.2) works perfectly fine in analytic computations, where IR singularities show up in dimensional regularization as explicit $1/\epsilon$, $1/\epsilon^2$, ... poles (after phase-space integration of R), whereby ϵ is related to the space-time dimensions as $D = 4 - 2\epsilon$. But a numerical

MC integration over physical momenta, which is necessary for complicated processes, can only be done in four dimensions. Thus, we have to find a way to have finite results in $D = 4$ dimensions, canceling the IR divergences for n and $n+1$ kinematics separately. The most commonly used solution is the subtraction method, whereby we add and subtract a subtraction term $C\left[\Phi_{n+1}\right]$:

$$\mathrm{d}\sigma^{\mathrm{NLO}} = \mathrm{d}\Phi_n B + \mathrm{d}\Phi_{n+1}\left(R\big|_{\epsilon=0} - \mathbb{P}\left[\Phi_{n+1} \to \Phi_n\right] C\big|_{\epsilon=0}\right) + \mathrm{d}\Phi_n \left(V + \int \mathrm{d}\Phi_{\mathrm{rad}}\, C\right)\Bigg|_{\epsilon=0} . \tag{2.4}$$

Hereby, both R and C are finite in $D = 4$ for finite momenta, whereby in the soft/collinear limit the arising divergence is canceled by the local counterterm $\mathbb{P}C$. Note the subtlety that is introduced by the projector $\mathbb{P}\left[\Phi_{n+1} \to \Phi_n\right]$: While C can still be evaluated as a function of the real phase-space Φ_{n+1}, the projector ensures that all counterterms are fixed to n-body kinematics in the differential phase-space. Thus, the addition and subtraction of C nicely cancels in all IR safe distributions. The explicit ϵ poles of V are canceled by the term $\int \mathrm{d}\Phi_{\mathrm{rad}} C$. The integration of C over the radiation phase-space can be performed analytically such that we have an object that is finite in $D = 4$ and only depends on the n-body phase-space:

$$\tilde{V}\left[\Phi_n\right] = V\left[\Phi_n\right] + \int \mathrm{d}\Phi_{\mathrm{rad}}\, C\left[\Phi_{n+1}\right] \equiv V\left[\Phi_n\right] + \tilde{C}\left[\Phi_n\right] \tag{2.5}$$

$\tilde{C}$ are commonly called integrated subtraction terms.

2.1.1 Subtraction schemes

The definition of C is not unique and in fact different subtraction schemes are preferred by different groups. The most frequently used subtraction schemes are Catani-Seymour (CS) [69–71] and FKS [72–74] subtraction. In CS subtraction, a real phase-space point is related to multiple Born phase-space points according to the different possible splittings. Thus, it is an $n + 1 \to n$ mapping. On the other hand, in FKS subtraction, we start with an underlying Born configuration and construct all possible real emissions: an $n \to n + 1$ mapping. As we show in this part, this yields some technical benefits for event generation. The drawback of the FKS subtraction is that the phase-space generation has to be coordinated with the subtraction. Specifically, it has to be expressed in the same coordinates that are used in the subtraction such that not any generic phase-space parametrization for $\mathrm{d}\Phi_{n+1}$ can be used, which is possible in CS.

Furthermore, the kind of splittings that are used are different. In CS, the dipole factorization formula plays a central role, i.e.

$$C = \sum_{\mathrm{dipoles}} B \otimes V_{\mathrm{dipole}} . \tag{2.6}$$

It is in fact a generic feature of QCD (and QED) factorization that the real emission pattern can be written as B times a universal factor that encodes the soft and collinear divergences. The convolution, indicated by $\otimes$, has to respect the spin and color correlations of R, which originate from interference terms between diagrams with emissions from different legs. In case of CS subtraction, these universal functions use dipoles, which consist of an *emitter* and a *spectator*. Thus, it is a $3 \to 2$ mapping. In the FKS subtraction, the phase-space is known exactly and thus R can be separated into disjoint regions $R = \sum R_{ij}$, where by construction in each region only one pair of particles, (i,j), can become collinear, w.r.t. each other, or either of them soft. This simplifies the construction of the collinear limits in C and allows to use $1 \to 2$ kinematics in combination with a boost of the recoiling momenta.

Notable further subtraction schemes are Nagy-Soper [75] and antenna [76] subtraction, which have, however, not yet been used in a general purpose NLO MC.

2.2 FKS subtraction

The automation of FKS subtraction within Whizard has been mentioned for the first time in Ref. [77] and was discussed in Refs. [40, 78]. A far more detailed description of all formulae required for the implementation can be found in Ref. [79]. We review in this section the core ideas and set the necessary notation for the following.

As we noted in the previous section, the FKS subtraction relies on the separation into disjoint singular regions, enumerated in the following by α. These regions are characterized by the FKS tuples (i,j), indicating the final state particles that can induce divergences. They form a set

$$\mathcal{P}_{\text{FKS}} = \left\{(i,j) : i \neq j \ , \ R \to \infty \text{ if } E_i \to 0 \text{ or } E_j \to 0 \text{ or } \boldsymbol{k}_i \parallel \boldsymbol{k}_j \right\} \ . \tag{2.7}$$

With this set, one can construct the separation of R by applying appropriate phase-space partitions $\mathcal{S}_\alpha$ such that

$$R_\alpha = \mathcal{S}_\alpha R \quad \text{and} \quad \sum_{\alpha \in \mathcal{P}_{\text{FKS}}} \mathcal{S}_\alpha = 1 \ . \tag{2.8}$$

The important point is that R_α diverges only when i and/or j become collinear/soft and not in any other phase-space region. Thus, the other divergences, which are certainly present, have to be suppressed in R_α. The concrete implementation is arbitrary but it has been observed that smooth functions lead to improved numerical behavior compared to Heaviside distributions, which leads to a reduced variance of the generated function and easier integration grid adaption. Omitting symmetrization factors and special treatments for $g \to gg$ splittings, we can use the simple form

$$\mathcal{S}_\alpha \equiv \mathcal{S}_{ij} = \frac{d_{ij}^{-1}}{\sum_{kl \in \mathcal{P}_{\rm FKS}} d_{kl}^{-1}} \,, \tag{2.9}$$

which obviously fulfills the unitary condition of Eq. (2.8). The standard expression for the distance measure d_{ij} is

$$d_{ij} = 2(k_i \cdot k_j) \frac{E_i E_j}{(E_i + E_j)^2} \,, \tag{2.10}$$

which guarantees the conditions demanded in Eq. (2.7) and at the same time suppresses other divergences in combination with Eq. (2.9). To construct the subtracted real correction term with these ingredients, we first have to discuss the phase-space construction.

2.2.1 Radiation phase-space

As noted earlier, the $\mathrm{d}\Phi_{n+1}$ phase-space factorizes into the radiation phase-space and the underlying Born configuration:

$$\mathrm{d}\Phi_{n+1} = \mathrm{d}\Phi_n \, \mathrm{d}\Phi_{\rm rad} = \mathrm{d}\Phi_n \, \mathcal{J}(\xi, y, \phi) \, \mathrm{d}\xi \, \mathrm{d}y \, \mathrm{d}\phi \,. \tag{2.11}$$

The Jacobian $\mathcal{J}$ enters due to the change of the radiation integration variables to the three dimensionless, independent variables ξ, y and ϕ. ξ parametrizes the energy of the radiated parton in the range of $[0, \xi_{\rm max}]$ with $\xi_{\rm max} \leq 1$ and

$$E_{\rm rad} = \frac{\sqrt{s}}{2} \xi \,. \tag{2.12}$$

Equation (2.12) is modified for the treatment of resonances, which is discussed in Section 2.6, or in the case of decays, cf. Eq. (2.23). $\xi_{\rm max}$ ensures, hereby, that the radiation uses at most the available energy that leaves the emitter with enough energy to stay on-shell (which is zero for massless emitters). With $y \in [-1, 1]$, we denote the angular separation of emitter and emitted parton. In case of massless emitters, it is simply $\cos\theta$ but the definition is more involved for massive emitters. Finally, $\phi \in [0, 2\pi]$ is the azimuthal angle that rotates emitter and emitted parton of the real phase-space around the original flight direction of the emitter in the Born phase-space. As there are of course multiple emitters, we have to combine this construction with the FKS tuples.

2.2.2 Subtraction terms

The non-subtracted real correction term can be written as

$$\mathrm{d}\Phi_{n+1}\, R = \mathrm{d}\Phi_n \sum_{\alpha\in\mathcal{P}_{\mathrm{FKS}}} \mathrm{d}\Phi^{\alpha}_{\mathrm{rad}}\, R_\alpha\,. \tag{2.13}$$

Now, one can handle the singular behavior for each α separately. For massless final-state emissions, this is simply given by $1/\xi^2$ and $1/(1-y)$ due to the possibly divergent propagator of the combination of emitter and emitted parton. This allows to define an *IR-finite* $\tilde{R}_\alpha$:

$$R_\alpha = \frac{1}{\xi^2}\frac{1}{1-y}\left(\xi^2(1-y)R_\alpha\right) \equiv \frac{1}{\xi^2}\frac{1}{1-y}\tilde{R}_\alpha\,. \tag{2.14}$$

Dimensional regularization allows to extract the explicit poles in ϵ. It yields, using Eq. (2.14),

$$\mathrm{d}\Phi_{\mathrm{rad}} R_\alpha = \mathrm{d}\Omega^{2-2\epsilon}\; \mathrm{d}y\; (1-y)^{-1-\epsilon}\; \mathrm{d}\xi\; \xi^{-1-2\epsilon}\; \mathcal{J}(\epsilon)\; \tilde{R}_\alpha(\xi, y)\,, \tag{2.15}$$

where we have absorbed some ϵ dependent constants in $\mathcal{J}(\epsilon)$ and $\mathrm{d}\Omega^{2-2\epsilon}$ is the analog to $\mathrm{d}\phi$ in $4-2\epsilon$ dimensions. The divergent behavior occurs, hereby, at $y=1$ and $\xi=0$ for collinear and soft singularities, respectively. This motivates the use of *plus-distributions*, defined as

$$\int \mathrm{d}x\; \left(g(x)\right)_+ f(x) = \int \mathrm{d}x\; g(x)\left(f(x) - f(s)\right)\,, \tag{2.16}$$

for a function g that diverges at s, which can be 0 for ξ and 1 for y. Note that Eq. (2.16) is finite for all x. With the plus-distributions, we can regulate the divergences and expand the terms of Eq. (2.15) as

$$\frac{1}{(1-y)^{1+\epsilon}} = -\frac{2^{-\epsilon}}{\epsilon}\delta(1-y) + \left(\frac{1}{1-y}\right)_+ - \epsilon\left(\frac{\log(1-y)}{1-y}\right)_+ + \mathcal{O}\left(\epsilon^2\right) \tag{2.17}$$

and

$$\frac{1}{\xi^{1+2\epsilon}} = -\frac{1}{2\epsilon}\delta(\xi) + \left(\frac{1}{\xi}\right)_+ - 2\epsilon\left(\frac{\log\xi}{\xi}\right)_+ + \mathcal{O}\left(\epsilon^2\right)\,. \tag{2.18}$$

These expressions allow to write the differential real contribution as a sum of a finite part in four dimensions and three divergent parts:

$$\begin{aligned}\mathrm{d}\Phi_{\mathrm{rad}} R_\alpha = {} & \mathrm{d}\phi\; \mathrm{d}y\; \mathrm{d}\xi\; \mathcal{J}(\xi, y, \phi)\left(\frac{1}{\xi}\right)_+\left(\frac{1}{1-y}\right)_+ \tilde{R}_\alpha(\xi, y) \\ & + I_{\mathrm{coll}} + I_{\mathrm{soft}} + I_{\mathrm{soft-coll}} + \mathcal{O}\left(\epsilon\right)\end{aligned} \tag{2.19a}$$

$$I_{\text{coll}} = -2^{-\epsilon}\mathrm{d}\Omega^{2-2\epsilon}\,\mathrm{d}\xi \left[\frac{1}{\epsilon}\left(\frac{1}{\xi}\right)_+ - 2\left(\frac{\log\xi}{\xi}\right)_+\right]\tilde{R}_\alpha(\xi,1) \tag{2.19b}$$

$$I_{\text{soft}} = -\frac{1}{2}\mathrm{d}\Omega^{2-2\epsilon}\,\mathrm{d}y \left[\frac{1}{\epsilon}\left(\frac{1}{1-y}\right)_+ - \left(\frac{\log(1-y)}{1-y}\right)_+\right]\tilde{R}_\alpha(0,y) \tag{2.19c}$$

$$I_{\text{soft}-\text{coll}} = \mathrm{d}\Omega^{2-2\epsilon}\left(\frac{2^{-\epsilon}}{2\epsilon^2}\right)\tilde{R}_\alpha(0,y) \tag{2.19d}$$

In Eqs. (2.19b) to (2.19d), the delta distributions of Eqs. (2.17) and (2.18) have been evaluated. In the language of Section 2.1, I_{coll}, I_{soft} and $I_{\text{soft}-\text{coll}}$ are the integrated subtraction terms that will be added to the virtual component after analytic integration over the remaining radiation phase-space. On the other hand, the differential subtraction terms are already subtracted in the finite part of Eq. (2.19a). Explicitly, the finite part reads

$$\mathrm{d}\phi\,\mathrm{d}y\,\mathrm{d}\xi\,\mathcal{J}(\xi,y,\phi)\,\frac{1}{1-y}\frac{1}{\xi}\Big(\tilde{R}_\alpha(\xi,y) - \tilde{R}_\alpha(0,y) - \tilde{R}_\alpha(\xi,1) + \tilde{R}_\alpha(0,1)\Big)\ . \tag{2.20}$$

The soft limit, $\tilde{R}(0,y)$, can be straightforwardly derived and results in a simple expression of a convolution of the Born with eikonal factors:

$$\tilde{R}_\alpha(0,y) = 4\pi\alpha_s \sum_{ij} \frac{k_i\cdot k_j}{(k_i\cdot k)(k\cdot k_j)} B_{ij}\ , \tag{2.21}$$

where B_{ij} is the color-correlated Born matrix-element and k the momentum of the emitted parton. Note that the sum over ij in Eq. (2.21) goes over all particles of the process, thus accounting for any possible interference terms. For Part III, we will have to restrict this summation to smaller subsets as we will neglect some of these interferences. Similarly, one can obtain the collinear and soft-collinear terms for $q \to q$g, g $\to qq$ and g $\to$ gg splittings, which include spin-correlated instead of color-correlated Born matrix-elements. These spin-correlated matrix-elements stem from gluon polarization vectors (of g $\to qq$ and g $\to$ gg) that mix amplitudes with different Lorentz polarizations of the gluon in the underlying matrix-element. Thus, they are only relevant if a gluon is present in the LO process definition, which applies for none of the processes presented in this thesis.

To obtain the virtual subtraction terms, one has to integrate the eikonal factors of Eq. (2.21), leading to the eikonal integrals $\mathcal{E}_{ij,\rho}(m_i,m_j)$. Hereby, the finite contribution is given for $\rho = 0$ as it corresponds to the coefficient of power of ϵ in the Laurent expansion. Analogously, the collinear limits have to be integrated, leading to terms of the form $\mathcal{Q}_i B$ and m_i, m_j are the masses of the involved particles. Note that the spatial integration simplifies the spin-correlated matrix-elements to the simple Born matrix-element B in $\mathcal{Q}_i B$. Finally, there are of course also finite contributions of the one-loop amplitude, $V_{\text{fin}}^{\text{loop}}$, that we will obtain from a One-Loop Provider (OLP) program. Thus, the virtual subtracted component can be written as

$$\tilde{V} = \sum_{kl} \mathcal{E}_{kl,0}(m_i, m_j) B_{kl} + \sum_i \mathcal{Q}_i B + V_{\text{fin}}^{\text{loop}} \, . \tag{2.22}$$

This completes our top-level review of the FKS subtraction and how we obtain events at NLO.

2.3 The WHIZARD event generator at NLO

For numerous linear collider studies, the multi-purpose event generator Whizard [77, 80, 81] is the standard simulation tool, as it supports beamstrahlung, QED initial-state radiation (ISR) and beam polarization out of the box and gives fast and reliable tree-level predictions even for full ten particle final states. In general, it supports any combination of lepton and hadron beams. While most event generators have focused their efforts during the last decades on improving the QCD precision for SM processes at the LHC, Whizard has traditionally targeted BSM physics and spearheaded many phenomenological studies [82–87]. For an easier implementation of new models, automated FeynRules [88] and Sarah [89] interfaces have been developed, cf. Ref. [90] and [91], respectively. With these, already a multitude of BSM models is supported but this will be extended to basically any Lagrangian-based BSM theory with the full support of the universal FeynRules output (UFO) format [92], which is currently completed.

First attempts of implementing NLO QED effects in Whizard have concentrated on fixed order as well as resummed soft photons for chargino production at the ILC [93, 94]. We note, though, that these results have never been merged in the official Whizard release, among other reasons as they were based on Whizard 1, which was not as modular and extensible as Whizard 2.2. The real emission contributions of the NLO QCD corrections to the $pp \to b\bar{b}b\bar{b}$ [95, 96] process have been computed with Whizard. However, the (CS) subtraction was custom-tailored for this process and not easily extensible to generic processes. But with the advances in NLO automation and the emphasis on precision computations, generic corrections are becoming feasible and mandatory. Especially, the tremendous advances in the automation of the computation of one-loop amplitudes is a key component in this endeavor. Publicly available OLPs such as Helac-1Loop [97, 98], OpenLoops [34], GoSam [33], Recola [35, 36] or MadLoop [99] can compute arbitrary virtual matrix-elements in the SM. In practice though, these programs are limited by computing power and have strongly varying performance due to the different employed algorithms and strategies concerning the numerical stability. Some additional details on the idea behind OpenLoops, Recola and Helac-1Loop will be given in Section 4.3. With these OLPs, complete NLO QCD support has so far been achieved within the frameworks of Helac-NLO [98], Madgraph5_aMC@NLO [38], Sherpa [37] and Herwig7 [39], while generic EW support is actively pursued by multiple groups [100–104]. Whizard presently supports a very broad class of processes at NLO QCD. However, before full QCD support is claimed, the full and thorough validation against numerous existing results still has to be finished. As noted in the beginning of this chapter, at the same time EW support is currently being developed.

The WHIZARD program has three well separated sub-packages: O'MEGA [80], VAMP [105] and CIRCE [106]. O'MEGA computes multi-leg tree-level matrix-elements as helicity amplitudes in a recursive way that avoids Feynman diagrams. VAMP is used for Monte-Carlo integration and grid sampling. Color information is treated in O'MEGA using the color-flow formalism [107]. It combines the multi-channel approach [108] with the classic VEGAS algorithm [109] to automatically integrate cross sections with non-factorizable singularities. The CIRCE package can be used to create and evaluate lepton beam spectra and is also interfaced to GUINEAPIG [110, 111], which can closely model the beam spectrum from the machine setup of a linear collider design. We have devised an alternative mode for O'MEGA, which is discussed in Section 2.3.3 together with WHIZARD's parallelization options.

The generic NLO framework in WHIZARD builds upon the FKS subtraction scheme, as discussed in Section 2.2. FKS subtraction allows for the application of WHIZARD's optimized multi-channel phase-space generation for the underlying Born kinematics, from which real kinematics are generated. It is also very well suited to the employed matching procedure, as described below. WHIZARD can use OPENLOOPS, GOSAM as well as RECOLA as one-loop matrix-element providers as well as for the computation of color- and spin-correlated Born matrix-elements. At tree-level, they can also be used as alternatives to O'MEGA. For the $\mathrm{t\bar{t}}$ threshold specific matrix elements of Part III, we use a similar plugin mechanism as for the OLPs to allow the use of squared amplitudes and interference terms instead of complex matrix-elements in WHIZARD.

To obtain automated NLO corrections, we firstly use WHIZARD's abilities to find automatically all possible decay processes. Combined with the information which splittings are allowed ($q \to q\mathrm{g}$, $\mathrm{g} \to qq$ and $\mathrm{g} \to \mathrm{gg}$), we can thus construct all contributing real processes. From this, the FKS tuples are constructed to compute subtracted real and virtual corrections.

2.3.1 Event generation

WHIZARD can be used for event generation on parton level as well as for the subsequent shower and hadronization. For this purpose, it has its own analytical [112], a k_T-ordered parton shower, and a built-in interface to PYTHIA6. Hereby, the results of PYTHIA6 are reinterpreted by WHIZARD, which allows to use WHIZARD's event analysis or write events out to any of the numerous supported file formats like HEPMC [113], LCIO [114, 115] (the event data model for linear collider detector studies that is particularly suited for particle-flow algorithms), STDHEP or various ASCII file formats. We have modernized the interfaces to the parton showers and the interplay with matching and merging algorithms, taking advantage of the object-oriented structure of WHIZARD 2.2. The effect of matching procedures has been abstracted, apart from technicalities, to two hooks: `before_shower` and `after_shower`. In both calls the matching algorithm receives the particle set and can modify it or return a veto. The new infrastructure allows to add new shower interfaces and/or matching and merging algorithms more easily.

At NLO, WHIZARD can produce weighted fixed-order events. Especially the output to HEPMC allows for flexible phenomenological fixed order studies in combination with RIVET's [116] generic event analysis capabilities. By virtue of Linux `FIFO`s, which are special files that act as a pipe, one can even setup WHIZARD and RIVET such that histograms are directly created without having to write events to (slow) disks. This is necessary for very high multiplicities at high precision, as the disk space and time to read those events becomes prohibitive. In the NLO event samples, we associate Born kinematics with a weight of $B + \tilde{V} - \sum_\alpha C_\alpha$. Together with this Born event, we generate for each singular region α, a real-emission event with weight R_α. Note, though, that R requires a lot more statistics due to the more complex final state and $\tilde{V}$ is more expensive to evaluate per phase-space point due to the loop integrals. Thus, it is possible to split up weighted NLO simulations into separate integrations and event generations. Hereby, the real events will contain also Born kinematics to accommodate the subtraction terms. We discuss another possibility to generate n-particle events with NLO information in Section 2.5. The matching of NLO predictions to parton showers is described in Section 3.3.

2.3.2 NLO widths

Apart from scattering processes, WHIZARD is also able to integrate decay widths for $1 \to N$ processes at LO and NLO. Due to the flexible SINDARIN syntax, the computed decay width can be directly used to set the model parameters. In the other NLO MC event generators such a rich feature is not straightforwardly accessible but has to be realized with external scripts. As we show in Part II, a consistent computation of the width of unstable particles according to all parameters, even the renormalization scale, and corresponding to the same level of off-shellness as the scattering process is necessary for a precision description.

The final-state phase space of the decays is built in the usual fashion, whereas the initial-state phase space is adapted for decays. This phase-space is somewhat special, as the momentum of the decaying particle R has to be fixed to $p_\mathrm{R} = (m_\mathrm{R}, \mathbf{0})$. Thus, the standard algorithm to generate initial-state radiation [79], which we omitted in Section 2.2 as this thesis is focused on lepton colliders, cannot be directly applied. Instead, we first generate the gluon as in the standard approach with the identification $\sqrt{s} = m_\mathrm{R}$

$$p_{n+1} = m_\mathrm{R}\, \xi \left(1, \sqrt{1-y^2}\sin\phi, \sqrt{1-y^2}\cos\phi, y\right) . \tag{2.23}$$

Hereby, ξ is sampled within $0 < \xi < \xi_\mathrm{max}$ such that the remainder momentum, $p_\mathrm{rem} =$

$p_\mathrm{R} - p_{\mathrm{n}+1}$, which represents the remaining momenta of the decay and recoils in the rest frame decay of the resonance back-to-back against the gluon, still has enough energy to generate all final-state particles of the decay on-shell. We then recursively use $1 \to 2$ kinematics and the associated rest- to lab-frame boosts [117] to generate the final-state momenta of the decay products. Thus, after the first iteration the momentum of the first decay product is fixed and we are left with a new remainder momentum (in case, it is a $1 \to N$ decay with $N > 2$). The recursion finalizes when there are only two decay products left, which then form the final $1 \to 2$ decay to fix their momenta.

2.3.3 OVM and parallelization

O'Mega, the automated tree-level matrix element generator, normally writes out Fortran90 source code that is compiled and linked to Whizard at runtime. For very complex processes with $\mathcal{O}$ (GBs) of source code, this compilation can fail and/or take several hours. Thus, we have implemented a virtual machine, the Omega virtual machine (OVM), which does not require recompilation and has a runtime that is very competitive with compiled code, as described in Ref. [118, 119]. Runtimes for the OVM compared to compiled code from O'Mega is shown exemplary for n gluon amplitudes in the left plot of Fig. 2.2.

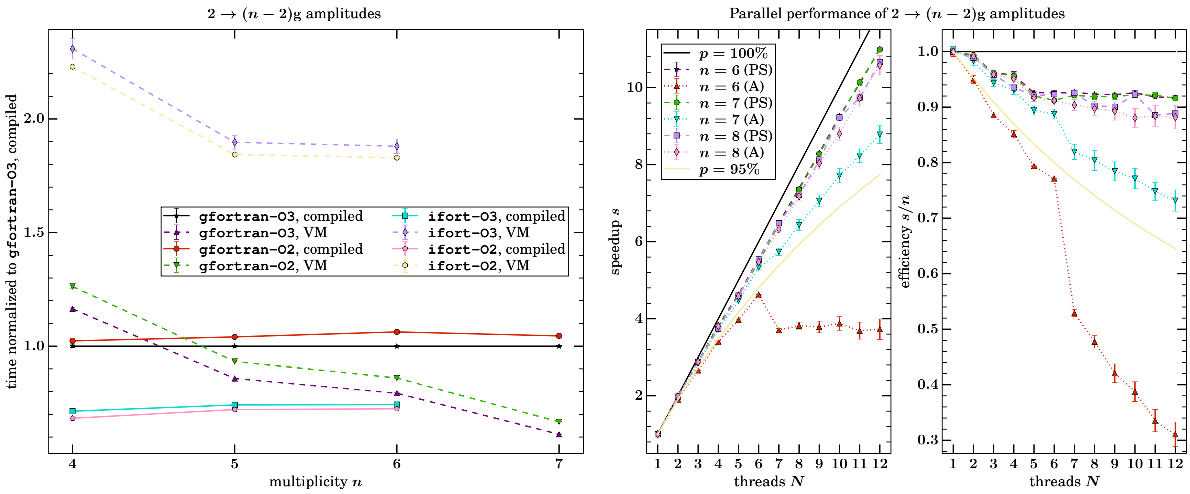

Figure 2.2 CPU times normalized for each process to the compiled source code using `gfortran -O3`. Dashed (solid) lines represent the OVM (compiled source code). The right plot shows speedup and efficiency for a fixed number of phase-space points: dashed and dotted lines indicate a parallel evaluation of multiple phase-space points (PS) and the parallel evaluation of the amplitude itself (A). The solid lines represent Amdahl's law for a fixed value of the parallelizable part p. See Ref. [118, 119] for details.

For parallelization, there are multiple options, whereby it depends on the process, which one is the most efficient: The sum over helicities in O'Mega and some aspects of phase-space generation can be parallelized with OpenMP, which is fairly efficient for large numbers of helicities and given there is enough memory to compute the matrix element of the process multiple times in parallel. For very complicated processes, the computation of a single helicity can instead be parallelized within the OVM with OpenMP instead [118, 119]. In the right plot of Fig. 2.2, we show the speedup and efficiency to compute a fixed number of phase-space points for n gluon processes, either computing each helicity in parallel (A) or computing each phase-space point in parallel (PS). Finally, the message passing interface (MPI) parallelization of the Vamp integration has been recently reimplemented with modern MPI features, which allows to access far larger speed-ups with multiple nodes that do not have to share memory. For event generation and scans over parameters like $\sqrt{s}$, we have implemented such an MPI parallelization externally with the Python code Whizard-Wizard. This scales perfectly as no communication is required but cannot speed up the integration of a single parameter point.

2.4 Separation of finite and singular real contributions

Real contributions should not all be treated equally. While we have centered our discussion in this part so far on the singular aspects of R, there are also finite contributions, which are not described by the soft/collinear factorization. This is e.g. the case for diagrams that involve the splitting of gluons into massive top quarks, because the invariant mass of the gluon propagator is then bound from below by $2m_{\mathrm{t}}$. In this case, no mass singularity occurs and the contribution is finite. Applying the subtraction to such terms, which might dominate in certain phase-space regions, can actually hamper the convergence of the integration. Also, in anticipation of the Powheg matching in Section 3.3, we note that a resummation of such terms can lead to unwanted, artificial effects. Thus, it is well motivated to introduce a general separation of R into a finite, R_{fin}, and a singular piece, R_{sing},

$$R = R_{\mathrm{fin}} + R_{\mathrm{sing}} \,. \tag{2.24}$$

Hereby, subtraction terms are only added to R_{sing}, while the finite part is integrated separately like an ordinary $n+1$ LO calculation. In fact, Whizard automatically adds a separate integration component for the finite part alongside the usual components for the NLO computation. Such a separation has been first introduced in the FKS and Powheg framework in Refs. [120, 121]. It can be easily achieved with a multiplicative approach and has some similarity with slicing methods[1],

$$R^{\alpha}_{\mathrm{sing}} = R^{\alpha} F(\Phi^{\alpha}_{n+1}) \quad \text{and} \quad R_{\mathrm{fin}} = R(1 - F(\Phi_{n+1})) \tag{2.25}$$

[1] Phase-space slicing methods can also be used to obtain NLO or NNLO cross sections. They can, however, not be automated as easily and have artificial dependencies on the slicing parameters, rendering them not the preferred solutions.

We have devised a fairly generic ansatz for this suppression factor

$$F(\Phi_{n+1}) = \begin{cases} 1 & \text{if } \exists\,(i,j) \in \mathcal{P}_{\text{FKS}} \quad \text{with} \quad \sqrt{(p_i + p_j)^2} < h + m_i + m_j \\ 0 & \text{else} \end{cases} . \tag{2.26}$$

Thus, a phase-space point is singular ($F = 1$), if any of the potentially divergent FKS tuples form an invariant mass that is smaller than the hardness scale h, which parametrizes the separation, and the sum of the individual masses. Note that this catches both soft and collinear divergences. This becomes obvious in the massless case, where Eq. (2.26) simplifies to

$$F(\Phi_{n+1}) = \begin{cases} 1 & \text{if } \exists\,(i,j) \in \mathcal{P}_{\text{FKS}} \quad \text{with} \quad 2E_iE_j(1-\cos\theta_{ij}) < h^2 \\ 0 & \text{else} \end{cases} . \tag{2.27}$$

The step function in Eq. (2.26) could of course be generalized to a smooth function for potentially better convergence. However, the sharp separation of the real phase-space has the benefit of making the unambiguous separation of resolved and unresolved emissions, which we can use in the next section.

In Whizard, we have verified that this splitting reproduces the full cross section, i.e. that $\int R = \int R_{\text{sing}} + \int R_{\text{fin}}$. This is not fully trivial as for R_{sing} the FKS phase-space is used while R_{fin} is handled with a standard LO phase-space, as we already indicated in Eq. (2.25) by omitting α in the finite part. Different definitions of $F(\Phi_{n+1})$ can easily be implemented as we have based it on an abstract class with clearly defined interfaces, similar to the shower and matching algorithms, mentioned in Section 2.3.1.

2.5 Matrix-element method at NLO

The matrix-element method (MEM) [122, 123] is a powerful experimental technique to extract the maximal amount of information out of measured events. It is thus a tool especially suited for processes where only a handful of events can be measured due to low cross sections. It allowed, e.g., to perform top mass measurements with a precision of $\sim 5\,\text{GeV}$ at the Tevatron [124, 125] using less than 100 events. The basic idea is to use an experimentally measured event and compute the likelihood of this event with a matrix element. Of course, for this to be useful, the effects of the detector, parton shower and hadronization have to be unfolded, which are encoded in *transfer functions*, $W(\{p\}^{\text{jets}}_{\text{measured}}, \{p\}^{\text{jets}}_{\text{partonic}})$. The transfer functions are usually obtained from MC data send through a detector simulation or at least smeared with a Gaussian. In theoretical studies, these are often ignored by replacing them with a delta distribution. With this simplification, the likelihood of a model parameter Ω for a set of n-parton events $\{p_n\}_i$ is given at LO by

$$\mathcal{L}^{\mathrm{LO}}(\Omega) = \prod_i \frac{1}{\sigma^{\mathrm{LO}}(\Omega)} \frac{\mathrm{d}\sigma^{\mathrm{LO}}(\Omega)}{\mathrm{d}\left\{p_n\right\}_i} . \tag{2.28}$$

The theory parameter can then be extracted by maximizing this likelihood or the corresponding log-likelihood. Note that this requires an integration over all invisible particles that participate in σ^{LO}, which quickly increases the computational cost of the method. At the energies of the LHC, one further has to deal with large amounts of QCD ISR, which leads to additional correction factors [126].

Going to NLO, several subtleties occur. Firstly, the observed n jet event might contain unresolved additional radiation from the $n+1$ contributions, which is of course important to guarantee the cancellation of IR divergences. Thus, an appropriate mapping has to be in place and one has to integrate over all unresolved real contributions that lead to the same n jet event. Secondly, at NLO it cannot be guaranteed that the differential cross section is positive in all phase-space regions and for all renormalization scale choices. Assuming a sensible scale choice, the remaining negative differential distributions have to be considered as areas where fixed-order perturbation theory is not applicable and the method cannot be used.

There has been quite some activity around the topic of how one can construct the MEM with NLO accuracy based on CS subtraction [127–131]. In CS subtraction, it is not straightforward to construct one n-particle event, as we alluded in Section 2.1.1, because it is a $\Phi_{n+1} \to N\Phi_n$ mapping with $N > 1$. The considered solutions range from the construction of a special forward branching phase space generator [132] to $3 \to 2$ clusterings [130]. The impact of using the MEM@NLO compared to LO is undeniably relevant, as shown for example in Ref. [130], where the use of a NLO likelihood indeed reproduces the input top mass in $\mathrm{e}^+\mathrm{e}^- \to \mathrm{t}\bar{\mathrm{t}}$ while the LO likelihood yields an offset of $\sim 4\,\mathrm{GeV}$. In the FKS subtraction and its application to Powheg matching, cf. Section 3.3, however, the main ingredients for the MEM@NLO are already present, as also noted in Ref. [127]. Here, we write the NLO cross section starting from the underlying Born configuration $\mathrm{d}\Phi_n$,

$$\mathrm{d}\sigma^{\mathrm{NLO}} = \mathrm{d}\Phi_n \bar{B} \quad \text{with} \quad \bar{B} = B + \tilde{V} + \sum_\alpha \mathrm{d}\Phi^{\mathrm{rad}} \left(\frac{1}{\xi}\right)_+ \left(\frac{1}{1-y}\right)_+ \tilde{R}_\alpha , \tag{2.29}$$

using the definitions of Eqs. (2.19a) and (2.22). With Section 2.4 in mind, we should actually use R_{sing} in Eq. (2.29). The exact separation is related to the definition of unresolved radiation in the experiment. In fact, we could use at the same time R_{fin} for resolved $n+1$ particle events. However, for these areas we would basically only have LO accuracy, as it is purely described by the real LO matrix-elements but might help with statistics. For unresolved emissions, we can write down the MEM@NLO trivially as

$$\mathcal{L}^{\mathrm{NLO}}(\Omega) = \prod_i \frac{1}{\sigma^{\mathrm{NLO}}(\Omega)} \frac{\mathrm{d}\sigma^{\mathrm{NLO}}(\Omega)}{\mathrm{d}\,\{p_n\}_i} \,. \tag{2.30}$$

where it is understood that in Eq. (2.29) the integration over the emission phase-space is performed. For resolved emissions, we would simply replace $\bar{B}$ in Eq. (2.30) with R_{fin} and take the product over all $n+1$ particle events. Finally, we note that if one is able to define an n-particle probability at NLO, one can also generate unweighted NLO events, which is a welcome byproduct. In WHIZARD, we have implemented the possibility to generate unweighted NLO events according to Eq. (2.29), whereby we perform the integration over the radiation phase-space with a MC sampling. To use it in an experimental analysis, a new interface has to be devised, where unfolded n (and possibly $n+1$) particle events are given to WHIZARD and the probabilities are returned.

2.6 Resonance-aware FKS subtraction

The standard approach to compute automated NLO corrections can be very inefficient if partons originate from the decay of a narrow resonance. For example, in Part II we study processes like $\mathrm{W^+W^-b\bar{b}}$ production, where this issue arises from $\mathrm{H \to b\bar{b}}$ and $\mathrm{t \to Wb}$. As discussed for the first time in Ref. [133], the problem is due to the fact that the momentum of the resonant particle can be different in the Born phase-space and the corresponding real phase-spaces[2]. This is problematic for the subtraction, as it can invalidate the soft/collinear factorization, cf. e.g. Eq. (2.21), due to the wildly different values of the resonant propagators.

To understand this in more depth, consider the $H \to b\bar{b}$ splitting with the very narrow Higgs resonance $\Gamma_H = \mathcal{O}(1\,\mathrm{MeV})$. This occurs as a Higgsstrahlung background process to $\mathrm{e^+e^- \to W^+W^-b\bar{b}}$ and its decays. Thus, the squared matrix-element of the total process contains a term with the contribution of the squared Higgs propagator,

$$D_H^{\mathrm{B}} = \left[(p_{bb}^2 - m_H^2)^2 + m_H^2\Gamma_H^2\right]^{-1} \,, \tag{2.31}$$

where p_{bb}^2 denotes the invariant mass of the $b\bar{b}$-pair in the Born phase space. The Higgs propagator in the corresponding real squared matrix-element has the form

$$D_H^{\mathrm{R}} = \left[(p_{bbg}^2 - m_H^2)^2 + m_H^2\Gamma_H^2\right]^{-1} \,. \tag{2.32}$$

Hereby, the Higgs virtuality is made up by the invariant mass of the $b\bar{b}$-system and the additional gluon, p_{bbg}^2. We can parametrize the change of the Higgs virtuality from the

[2] This mismatch also occurs in CS subtraction, where the real phase-space is mapped to multiple Born phase-spaces.

Born to the real value by Δ

$$p_{bbg}^2 = p_{bb}^2 + \Delta^2 \,. \tag{2.33}$$

Furthermore, we can define the Born off-shellness $\delta = p_{bb}^2 - m_H^2$ and check the ratio of the propagators

$$\mathcal{D} := \frac{D^{\mathrm{B}}}{D^{\mathrm{R}}} = 1 + \frac{\Delta^4 + 2\Delta^2\delta}{\delta^2 + m_H^2\Gamma_H^2} \stackrel{\delta\to 0}{=} 1 + \frac{\Delta^4}{m_H^2\Gamma_H^2} \,. \tag{2.34}$$

For the real amplitude and its soft and collinear approximation in the subtraction terms to match, it is required that $\mathcal{D} \approx 1$ in the soft as well as the collinear limit. At the resonance, $\delta \to 0$, we see that this condition is fulfilled if $\Delta^4 \ll m_H^2\Gamma_H^2$. We immediately see that this poses a problem in the collinear limit, as Δ^4 can become large if a hard-collinear gluon is emitted. However, also in the soft limit a significant mismatch can occur if the denominator $m_H^2\Gamma_H^2$ is sufficiently small. This is definitely the case for the Higgs, with $m_H^2\Gamma_H^2 = (0.720\,\mathrm{GeV})^4$, while for the top quark the problem is less severe with $m_t^2\Gamma_t^2 = (15.4\,\mathrm{GeV})^4$. Note that, as mentioned in Chapter 1, at lepton colliders, top-pair production is a pure electroweak process while it is a strong production at hadron colliders. This also implies that $H \to b\bar{b}$ is not included in the off-shell description at hadron colliders. In general, we can expect that the handling of electroweak resonances has to be more precise at lepton colliders due to the initial state. In Ref. [133], a modification of the FKS subtraction procedure was presented, which addresses the problem of narrow resonances, and implemented for single-top production in the POWHEG-BOX. We implement this approach for generic processes in WHIZARD. This makes WHIZARD the first fully automated, publicly available NLO MC with a dedicated resonance treatment.

In the *resonance-aware* FKS approach, one does not only partition the phase-space in distinct singular regions but also in distinct regions with a well-defined resonance structure. In each of these regions, the real phase-space is constructed such that the invariant mass of the particles, which originate from the same resonance, is kept fixed. This is in contrast to the default approach, where the momentum of the emitted parton is shared across all Born momenta. Here, the radiation only affects the decay products of the resonance and the remaining final states maintain their Born momenta. Thus, the deviation Δ in Eq. (2.34) is exactly zero for this resonance by construction, and hence $\mathcal{D} = 1$. Hereby, we make use of modified FKS mappings, which are evaluated in the rest frame of the corresponding resonance. This leads to the problem that the sum over all singular regions does not reproduce the full real matrix-element anymore. As shown in Ref. [133], this can be solved by introducing an additional component, the *soft mismatch*, which we discuss in Section 2.6.1.

In the resonance-aware FKS approach, the standard FKS projectors $\mathcal{S}_\alpha$, cf. Eq. (2.9), are extended by resonance projectors $\mathcal{P}_{f_r}$. These have a similar purpose as $\mathcal{S}_\alpha$ in the sense that $\mathcal{P}_{f_r} \to 1$ if $\delta \to 0$, whereby δ belongs to a resonance of the resonance history f_r. On the other hand, $\mathcal{P}_{f_r} \to 0$ when another resonance goes on-shell that is not contained in the resonance history. Resonance histories can contain multiple, potentially nested, resonances, which form the set $\mathrm{Nd}(f_r)$. Motivated by the narrow-width limit of a resonant process, $\mathcal{P}_{f_r}$ can be computed with a product of Breit-Wigner factors of a given resonance structure[3]

$$\mathcal{P}_{f_r} = \prod_{i \in \mathrm{Nd(f_r)}} \frac{m_i^2}{(p_i^2 - m_i^2)^2 + m_i^2 \Gamma_i^2} \,. \tag{2.35}$$

Hereby, p_i is the momentum of the resonance in the underlying Born phase-space. The normalization that takes care of other regions is then analogous to Eq. (2.9):

$$\mathcal{S}_\alpha = \frac{\mathcal{P}_{f_r(\alpha)} d^{-1}(\alpha)}{\sum_{f_r' \in T(\alpha)} \mathcal{P}_{f_r'} \left(\sum_{\alpha' \mathcal{P}_{\mathrm{FKS}}(f_r')} d^{-1}(\alpha') \right)} \,, \tag{2.36}$$

where we used that we can always identify a resonance history for each singular region $f_r(\alpha)$. $T(\alpha)$ is the set of resonance histories compatible with the flavor structure of α. The d terms have to be evaluated in the resonance rest-frame. Note the order of the summation: we sum for each resonance history over all compatible FKS tuples and then sum over all resonance histories. Thus, a singular region in the traditional sense can be evaluated multiple times and even have distinct d values due to different frames. Overall, the number of resonance-aware singular regions increases and can be at most the number of resonance histories times the number of standard singular regions. Usually, it is less than this as not all singular regions are compatible with all resonance histories as they might refer to a pair of particles not contained in the resonance history.

In Whizard, resonance information is computed for every process, already at leading order, by using information about the vertices and masses of a physics model. This information is used by the multi-channel integrator Vamp, where all relevant resonance structures are sampled for an efficient MC integration. We use exactly these resonance structures to set up the resonance-aware FKS subtraction. Thus, in principle, each of Whizard's integration channels could be identified with the resonance histories, also using the internal mappings used in the construction of the Born phase-space. However, we decided to introduce resonance histories using the projectors of Ref. [133] independently of the Monte Carlo integration channels. This ensures that the result does not depend on unphysical weights, which only have to improve integration performance. In the event output, we only construct an entry for a real emission for each distinct phase-space structure, which is given by emitter and the decaying particles. For each of these, we sum over all singular regions, which are compatible with the phase-space structure. This ensures that we only create the minimal number of events necessary, keeping event generation efficient. Moreover, the soft mismatch is not a separate entry but included in

[3] Another possibility are factorized matrix elements, which have the benefits of correctly accounting for the relative weights of the resonance histories due to coupling constants and other effects. However, in this case, one has to take care to only evaluate them on-shell as they are otherwise gauge-dependent, c.f. the discussion of gauge dependency in Section 6.3. Thus, either a generic on-shell projection has to be in place or one fulfills it approximately with a cutoff on the off-shellness.

the subtraction weight.

Employing the resonance-aware FKS subtraction scheme for off-shell top-pair production and decay in leptonic collisions, which we study in Part II, is not straightforward. This is due to at least two issues. Firstly, there are production-like configurations, which cannot be associated to any of the standard FKS regions. In these, the gluon is emitted from the production process, i.e. from one of the top quarks before their decay. Thus, we would like to produce the gluon momentum such that both top resonances remain on their Born value. For this, we could introduce additional resonance histories, similar to the ones used at hadron colliders, where such configurations are produced naturally by the QCD ISR. As weight for the projectors, one could use the double resonance configuration with the associated Breit-Wigner factor. It remains unclear, though, how to construct the gluon momentum without changing the initial state as one can do at hadron-colliders. Another potential issue is the soft limit when multiple resonances are present. While we can construct $\mathcal{D} = 1$ for one resonance, we cannot ensure this for multiple resonances. Thus, there are $\Delta^4/m^2\Gamma^2$ terms in the soft limit remaining. As we said earlier, in the SM this is mainly problematic for Higgs contributions as all other resonances are regulated by $\mathcal{O}\,(\mathrm{GeV})$ widths. However, at lepton colliders Higgs contributions as electroweak resonances are due to the higher electroweak couplings more likely to be present than at hadron colliders. Thus, a solution for the soft problem of multiple resonances should be constructed. We emphasize that in the collinear limit, no such problem exists as the collinear configuration has to, by construction, belong to the same resonance and cannot belong to a different resonance.

Finally, we want to note that the resonance-aware FKS subtraction scheme allows to include a definite resonance history assignment in the event output. This enables the parton shower to maintain the invariant mass of the resonance decay products fixed to the generated value. Without this information, one cannot perform a consistent matching of fixed-order NLO predictions with parton-shower generators for processes with intermediate resonances [133, 134]. This information is already important at LO and significantly changes the number of particles created by the parton shower and hadronization. In fact, the assignment of resonances at LO is currently being implemented in WHIZARD and uses basically the same infrastructure that we created for the resonance-aware FKS subtraction.

2.6.1 Soft mismatch

The use of the resonance-aware FKS mappings generates a global soft mismatch compared to the traditional FKS subtraction. It has its origin in the different, local meaning of the soft limit for different resonances. To repair this, one can introduce the *soft mismatch* component, given by [133]

$$R_\alpha^{\mathrm{mism}} = \int d\Phi_B \int_0^\infty d\xi \int_{-1}^1 dy \int_0^{2\pi} d\phi \frac{s\xi}{(4\pi)^3} \left\{ R_\alpha^{\mathrm{soft}} \left(\exp\left[-\frac{2k \cdot k_{\mathrm{res}}}{k_{\mathrm{res}}^2}\right] - \exp\left[-\xi\right] \right) \right.$$

$$- \frac{32\pi\alpha_s C_F}{s\xi^2} B \left(\exp\left[-\frac{\bar{k}_{\mathrm{em}} \cdot k_{\mathrm{res}}}{k_{\mathrm{res}}^2} \frac{k^0}{\bar{k}_{\mathrm{em}}^0} \right] - \exp\left[-\xi\right] \right) (1 - \cos\theta)^{-1} \Bigg\} , \quad (2.37)$$

which is evaluated for each individual singular region α. Correspondingly, R_α^{soft} is the soft limit of the real matrix-element in this region. k and k_{res} are the momenta of the radiated gluon and the intermediate resonance, respectively, and $\bar{k}_{\mathrm{em}}$ is the momentum of the emitter in the Born phase space. Note that, in contrast to the traditional FKS subtraction, where $\xi = 2k^0/\sqrt{s} \leq 1$, a generalized $\xi \in [0, \infty)$ is used, which originates from using integral identities. Therefore, the soft mismatch has to be evaluated with its own phase space and must be treated as a separate integration component in Whizard. This integration is automatically performed and included as an additional contribution next to Born, real and virtual components when the resonance-aware FKS subtraction is activated.

2.6.2 Validation and efficiency

We have checked our implementation of resonance-aware FKS subtraction using the production of two massive quarks in association with two muons as a benchmark process, i.e. $\mathrm{e}^+\mathrm{e}^- \to \mathrm{b}\bar{\mathrm{b}}\,\mu^+\mu^-$. This process has only one radiative resonance topology with two different resonance histories, $\mathrm{Z} \to \mathrm{b}\bar{\mathrm{b}}$ and $\mathrm{H} \to \mathrm{b}\bar{\mathrm{b}}$. Thus, it is a combination of Z pair production and the Higgsstrahlung process ZH. We have set $m_{\mathrm{b}} = 4.2\,\mathrm{GeV}$ to focus on soft divergences. To avoid cuts, we set for the purpose of this validation the muon mass (artificially) to $m_\mu = 20\,\mathrm{GeV}$, which regulates small photon virtualities.

This process, as many others with intermediate narrow resonances, does not converge well with the standard FKS subtraction. Thus, we fix the Higgs width to the fictitious value $\Gamma_{\mathrm{H}} = 1000\,\mathrm{GeV}$. This allows a converging integration with both approaches and a reliable validation. In Tab. 2.1, we show results for σ_{real}, denoting the full real-subtracted

Table 2.1 Real-subtracted integration component, σ_{real}, and, in the case of resonance-aware subtraction, soft mismatch, σ_{mism}, as well as the number of calls n_{calls} used in the integration for $\Gamma_{\mathrm{H}} = 1000\,\mathrm{GeV}$ and $m_\mu = 20\,\mathrm{GeV}$. For the resonance-aware subtraction, we show n_{calls} for the integration of the real and the soft mismatch component.

	σ_{real}[fb]	σ_{mism}[fb]	n_{calls}
standard	$-1.9049 \pm 0.99\%$	n/a	$5 \times 100\,000$
resonances	$-0.9151 \pm 0.52\%$	$-0.9793 \pm 0.94\%$	$5 \times 20\,000 + 5 \times 20\,000$

matrix-element, and σ_{mism}, the result of the integration of the soft mismatch component. Adding the real and soft-mismatch components for the resonance-aware FKS subtraction, the difference between both approaches is five per mil, which is well within the integration error. We note the significantly higher number of integration calls required in the standard approach to reach roughly the same accuracy as in the resonance-aware subtraction scheme. Obviously, we can make this efficiency difference orders of magnitude larger by testing with a smaller width.

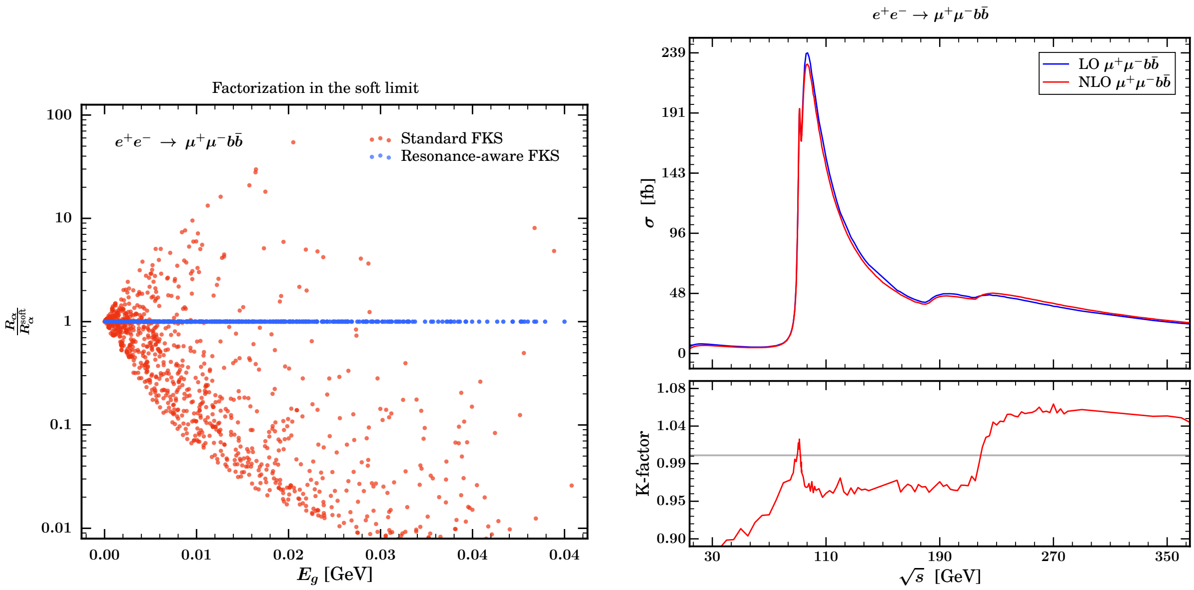

Figure 2.3 Left, scatter plot of the ratio of the real matrix-element over the soft approximation of the process $e^+e^- \to \mu^-\mu^+ b\bar{b}$ for the standard and the resonance-aware FKS subtraction. Each approach has been sampled with 1000 points at 500 GeV. In contrast to the validation described in the text, here the physical Higgs width have been used. Right, total cross section at LO and NLO using resonance-aware FKS subtraction.

For Fig. 2.3, we use the physical Higgs width. On the left, we show a scatter plot of the real matrix-element over the soft approximation for both the standard and the resonance-aware FKS subtraction. The effect of constructing $\mathcal{D} = 1$ can be clearly seen in the perfect agreement of the real matrix-element and its soft approximation in the resonance-aware approach. Note that although we are sampling fairly soft momenta, $E_g < 0.05$ GeV, the convergence to one is very slow in the standard FKS subtraction. A further effect that can be seen is that the ratio is systematically more often below one. This is because the Born events are generated preferably on the resonance. Thus, the radiation and the associated mismatch will put the Real events slightly off the maximal value of the Breit-Wigner, leading to $R_\alpha < R_\alpha^{\text{soft}}$ on average. For illustration, we also show a scan of the total cross section on the right of Fig. 2.3. There are two distinct peaks at m_Z and $m_Z + 2m_b$, as well as two less pronounced enhancements at $m_Z + m_H$ and $2m_Z$. NLO QCD corrections are in the range of +5% for $\sqrt{s} > 2m_Z$ and approximately −4% for $m_Z + 2m_b < \sqrt{s} < 2m_Z$. Below $\sqrt{s} = m_Z$, the K-factor (NLO/LO) is significantly smaller than 1.

Chapter 3

Parton showers, matching and merging

Fixed-order computations can give very reliable predictions in many phase-space regions with full control over the perturbative order. Despite this, they have some shortcomings. First of all, starting from the fully differential NLO result, fixed-order results are *always* IR divergent in soft and/or collinear regions of phase space. This is also reflected in the fact that they cannot be treated as physical events as they only contain a handful of partons instead of tens or hundreds of hadrons. This is foremost a practical problem as experimental analyses and detector simulations need realistic events as input to compare with data in fiducial phase-space regions. On the other hand, these divergences, although they cancel in sufficiently inclusive observables, should be resummed in a well-defined scheme to yield finite results in all regions of phase-space. While the latter problem can also be solved with analytic resummation [135], specifically crafted for the process, the only practical solution to the former are general-purpose MC event generators [136].

The generation of realistic events is divided into two steps: Firstly, during the *parton shower*, the resummation in soft and collinear regions is performed in a MC fashion, thus producing exclusive multi-parton events. We emphasize that this step can be handled completely perturbatively and improved with higher-order computations. Secondly, during the *hadronization*, a phenomenological model of hadron formation from partons at low scales is applied, which cannot be derived from first principles. This stage usually also includes hadron decays like $\pi \to \gamma\gamma$, which can be modeled classically by using the measured branching ratios. We will focus on the first step throughout this part and assume that the second step is performed externally. We note though that both stages contain parameters, which are not mutually independent and have to be determined with a *tune* to measured data. Thus any improvement of the parton shower has to be accompanied by a new tune of the full machinery. MC event generators have a long history of successfully describing data at hadron and lepton colliders [135]. The most commonly used implementations are Pythia [14], Herwig [39] and Sherpa [37].

We start this chapter by reviewing the parton-shower algorithm in Section 3.1. The traditional method of using LO matrix elements to generate events that are fed into a parton shower (PS) program is nowadays often called LO+PS. We will discuss in Section 3.2 several ideas to improve this approach. The matching of PS and NLO is accordingly called NLO+PS, one of the methods being Powheg, which we discuss in Section 3.3.

3.1 Parton showers

We review the parton shower mechanism in this section. This can be also found in the literature, e.g. in Section 41 in Ref. [137] as well as Refs. [136, 138]. A more formal proof of Sudakov exponentiation can be found e.g. in Ref. [139].

3.1.1 Sudakov form factors

As we have already established in Chapter 2, matrix-elements factorize in the soft and collinear regions of phase-space due to divergent propagators. From this behavior, the differential splitting probability $\mathcal{P}(t)$ at each scale t can be derived. We indicate with $\mathcal{P}$ a generic, unregularized splitting probability that can have different explicit forms. The only important property is the divergence for small scales, i.e. $\mathcal{P}(t) \to \infty$ for $t \to 0$. Accordingly, there can be different scale definitions but they have to be chosen such that it makes sense to define an ordering in them. A possible choice is $t = \log Q^2/\Lambda^2_{\mathrm{QCD}}$, where Q^2 is the virtuality. There are, though, multiple definitions of the scale variable t possible, whereby relative p_{T}, angles or virtuality are the most commonly used ones. The differential splitting functions are closely related to the Sudakov form factors [140], $\Delta\big(t\big)$, which form a central part of the parton shower formulation. They can be defined as the probability that no emission occurs between a high scale $t_{\max}$ and a low scale t. From this, we can infer that the probability for at least one branching P_{branch} at a scale t is given by the differential splitting probability times the probability that the parton did not branch already earlier. Thus,

$$\frac{\mathrm{d}P_{\mathrm{branch}}}{\mathrm{d}t} = \mathcal{P}(t)\Delta(t) \; . \tag{3.1}$$

On the other hand, we have $P_{\mathrm{branch}} = 1 - \Delta$ (either there is at least one branching or not), which results in the basic equation

$$\frac{\mathrm{d}\Delta}{\mathrm{d}t} = -\mathcal{P}(t)\Delta \tag{3.2}$$

Note the similarity of Eq. (3.2) with the differential equation that governs the radiative decay. Integrating Eq. (3.2) between a high scale t_1 and a low scale t_2 gives the Sudakov form factor

$$\Delta(t_1, t_2) = \exp\left\{ - \int_{t_2}^{t_1} \mathrm{d}t \, \mathcal{P}(t) \right\} \; . \tag{3.3}$$

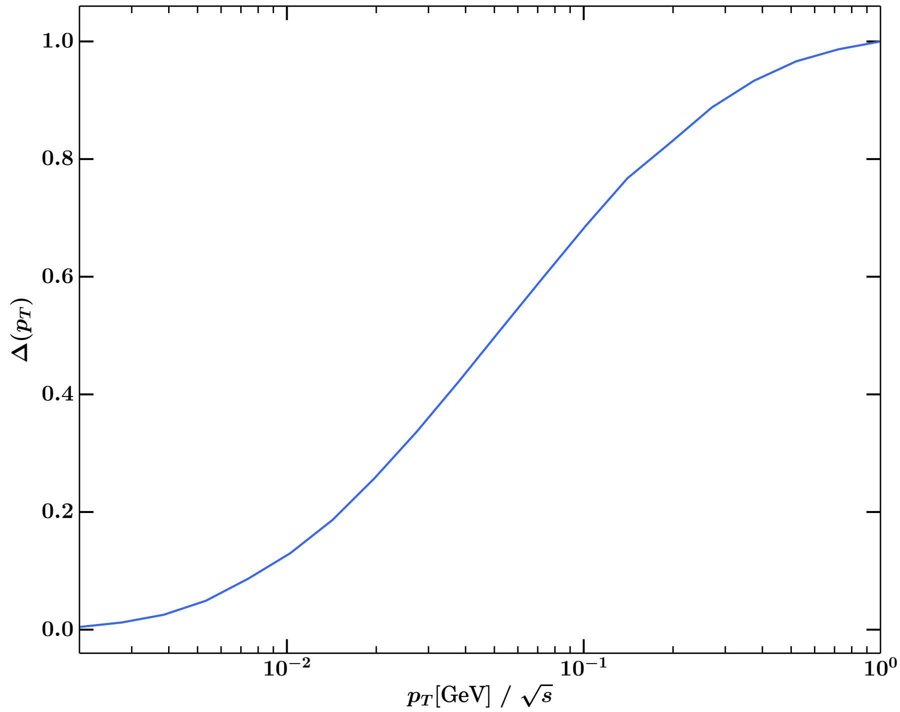

Figure 3.1 Sudakov form factor in $t\bar{t}$ production as a function of p_T as implemented in WHIZARD.

As we indicated earlier, we also use the shorthand notation $\Delta(t) = \Delta(t_{\max}, t)$. In Fig. 3.1, we show an exemplary representation of a Sudakov form factor as function of p_T, as it is implemented in WHIZARD, evaluated for $t\bar{t}$ production. As $\mathcal{P}$ diverges for small p_T, the probability that no emission occurs goes to zero. In the obtained distributions, this leads to a suppression of very low p_T emissions and yields finite results for all p_T.

3.1.2 Parton shower mechanism

Let us now assume that we can actually integrate $\mathcal{P}$ analytically, $\tilde{\mathcal{P}}$, and invert this function, $\tilde{\mathcal{P}}^{-1}$. Then, we can generate a random number x and solve $\Delta(t) = x$ for t to obtain the scale of the first splitting:

$$t = \tilde{\mathcal{P}}^{-1}\left(\tilde{\mathcal{P}}(t_{\max}) + \log x\right) \ . \tag{3.4}$$

Note that in case that we do not have a closed analytic form for the inverse primitive function $\tilde{\mathcal{P}}^{-1}$, we can also numerically search for the solution of

$$\tilde{\mathcal{P}}(t) = \tilde{\mathcal{P}}(t_{\max}) + \log x \ , \tag{3.5}$$

by varying t. In case t is lower than the set cut-off parameter t_{cut}, the emission will be ignored as those emissions are defined as unresolvable. Otherwise ($t > t_{\text{cut}}$), we need an additional random number to sample the energy splitting z between the two new partons according to $\mathcal{P}(t,z)$, which we have ignored so far[1]. A common choice to describe the z splittings are the well-known Altarelli-Parisi or DGLAP [141–143] splitting functions. We continue the evolution by resetting $t_{\max} = t$ and search for the next splitting scale as before. Given that we start this algorithm with a LO distribution, as defined in Eq. (2.1), we obtain with Eq. (3.1)

$$\mathrm{d}\sigma^{\text{shower}} = \mathrm{d}\sigma^{\text{LO}} \Bigg(\Delta(t_{\text{cut}}) + \mathrm{d}t\, \mathcal{P}(t)\, \Delta(t) \Bigg(\Delta(t, t_{\text{cut}}) + \mathrm{d}t'\, \mathcal{P}(t')\, \Delta(t,t') \Big(\Delta(t', t_{\max}) + \dots \Big) \Bigg) \Bigg) \,. \tag{3.6}$$

Hereby, the first term still has the Born kinematics as no emission did occur above the resolution threshold. In the second term, exactly one branching occurred at t but nothing further down to t_{cut}. This term approximates the real emission as it occurs in a NLO computation but at the same time includes the leading logarithm (LL) resummation by virtue of the Sudakov form factor. For clarification, we expand the second branching in the third term using $\Delta(t_{\max}, t_{\text{cut}}) = \Delta(t_{\max}, t)\Delta(t,t')\Delta(t', t_{\text{cut}})$ to obtain

$$\mathrm{d}\sigma^{\text{LO}}\, \mathrm{d}t\, \mathcal{P}(t)\, \mathrm{d}t'\, \mathcal{P}(t')\, \Delta(t_{\text{cut}}) \,. \tag{3.7}$$

Again, this is the exclusive probability for exactly two branchings. Further branchings are indicated by the ellipsis. It should be clear that the recursive parton-shower evolution yields a nested product of (nothing + something(nothing + ...)) that integrates to one by construction. This property holds no matter at which step one stops the recursion.

3.1.3 Sudakov veto algorithm

Realistic Sudakov form factors can be computed most easily numerically with the Sudakov veto algorithm [138, 144]. The problem is that primitive functions $\tilde{\mathcal{P}}$ or their inverse $\tilde{\mathcal{P}}^{-1}$ are often not available. To circumvent this problem, we can find a simple overestimator for $\mathcal{P}$, which we call $\hat{\mathcal{P}}$, that is larger than $\mathcal{P}$ for all t. Thus, the splitting probability for emissions is increased. We use this nicer function to construct the corresponding Sudakov form factor $\hat{\Delta}(t)$, which is for all t an underestimate of the true Sudakov form factor $\Delta(t)$. The scale t that we generate with the algorithm of the last subsection is then only accepted with the probability $\mathcal{P}/\hat{\mathcal{P}}$. In case it is rejected, we restart the evolution with $t_{\max} = t$. As we have underestimated the probability that there is no emission above t, we do not have to consider this region again. Visually, we can see from Fig. 3.1 that a sampling of

[1] In the POWHEG implementation, which we discuss in Section 3.3, we actually generate at first p_{T}, which is the scale, and then the energy of the emitted parton ξ. This fixes the angular separation y due to the definition of $p_{\mathrm{T}}(\xi, y)$.

an underestimation of Δ will suggest systematically larger scale values for an emission, which are however partly vetoed in the second step. It can be shown with an inductive proof [138, 144] that this indeed not only modifies the differential splitting probability but also the Sudakov exponent. The Sudakov veto method is incredibly useful as it allows to include any additional detail in the splitting function as well as the Sudakov exponent.

3.1.4 Multiple emission probabilities

So far, we have assumed that there is exactly one splitting probability for each event. This is of course not true as a gluon can e.g. split either in gluons or in quarks, there can be different partons that compete for the highest emission scale or one can combine EW and QCD showers. However, this fully factorizes, because

$$\Delta(t_1, t_2) = \exp\left\{ - \int_{t_2}^{t_1} \mathrm{d}t \sum_i \mathcal{P}_i(t) \right\} = \prod_i \Delta_i(t_1, t_2)\ . \tag{3.8}$$

Thus, one can generate the first emission according to the sum of splitting probabilities

$$\mathrm{d}P_{\text{branch}}(t) = \sum_i \mathcal{P}_i(t) \Delta(t)\, \mathrm{d}t \tag{3.9}$$

and randomly select one of the splittings according to $\mathcal{P}_i / \sum_j \mathcal{P}_j$. Then, the emission is of type i with the probability

$$\mathrm{d}P^i_{\text{branch}}(t) = \mathcal{P}_i(t) \Delta(t)\, \mathrm{d}t\ . \tag{3.10}$$

A bit more convenient is the so-called *highest bid* method, cf. also Appendix B in Ref. [145]. Hereby, we generate a t_i for each possible splitting separately, i.e. according to

$$\mathrm{d}P^i_{\text{branch}}{}'(t_i) = \mathcal{P}_i(t_i) \Delta_i(t_i)\, \mathrm{d}t_i\ . \tag{3.11}$$

Of these scales, we pick the largest one, t_i. The probability that a certain t_i is indeed the largest one is given by the product of probabilities, which describe all other splittings giving a t_j that is smaller. These probabilities in turn are given by the Sudakov form factors such that we have

$$\mathrm{d}P^i_{\text{branch}}{}'(t_i) \prod_{j \neq i} \Delta_j(t_i) = \mathrm{d}P^i_{\text{branch}}(t_i)\ , \tag{3.12}$$

which is of course Eq. (3.10) for $t_i = t$.

3.2 Improving the parton shower

Equation (3.6) presents different possibilities for improvements. As we have seen in Section 3.1.3, it is possible to maintain this *unitary* construction, i.e. the cross section is not changed by the parton shower, while correcting the parton shower with further details. Thus, we can replace the universal splitting function $\mathcal{P}$ with process-dependent matrix-elements accounting for various interference effects as well as finite contributions. This is especially important in *hard* regions of phase-space, where the soft approximation breaks down. By construction, the form of Eq. (3.6) will not be changed by this and the ratio of matrix-elements are resummed in a well-defined way. This approach has been coined by Giele, Kosower, Skands (GKS) as the unitary matching method [146]. It was used already in Ref. [147] to correct the first emission of the PYTHIA parton shower (actually this part was still called JETSET at the time [148]) with a LO matrix-element. Specifically, in the unitary approach, we introduce an additional veto step with the acceptance probability

$$\frac{|\mathcal{M}_{n+1}|^2}{\sum_i \left|\mathcal{M}_n^{(i)}\right|^2 \mathcal{P}_i} , \tag{3.13}$$

whereby i runs over all possible ways the final state could have been produced by the shower. However, the generalization to multiple emissions was not feasible at the time as fast automated matrix-element generators were not yet available. Furthermore, it requires on-shell partons at each shower step, which is not necessarily fulfilled by all parton-showers. Systematic combining of multiple LO matrix-elements with the parton shower was achieved by the schemes of M. L. Mangano (MLM) [149] and Catani, Krauss, Kuhn, Webber (CKKW) [150]. This is nowadays usually referred to as *merging* to separate it from the problem of *matching* a higher order computation of a fixed multiplicity with a parton shower. In the latter case, the focus is on the removal of the double-counting of radiation in both the parton shower and the fixed-order computation while in the former it is on increasing the parton-shower precision. As an aside, we note that there has been also progress in describing the splitting itself at NLO in the DIRE showers in PYTHIA and SHERPA though the numerical impact was found to be marginal [151].

3.2.1 Merging

Both the MLM and the CKKW merging belong to the class of *slicing* merging schemes: The radiation phase-space is sliced up into a matrix element and a parton shower domain according to some jet resolution parameter. The matrix-element region is then decorated with Sudakov factors, either by trial showers or by applying analytic Sudakov factors according to clustered scales. The MLM scheme has been implemented in WHIZARD and involves various veto steps, as illustrated in Appendix B.1, to ensure that the parton shower does not produce jets above the merging scale. The main benefit of the MLM scheme is that it does not require any modification of the shower program. The drawback is that the MLM merging misses intermediate Sudakov factors, e.g. from one to two additional jets described by matrix elements, as no reclustering is performed [152]. Furthermore, it does not converge when the merging scale is set too low, necessitating a tuning of the merging scale just to obtain smooth results [152]. Despite this, it is still in active use, especially in MADGRAPH, and can successfully describe data, where this effect is not important, as seen e.g. in Ref. [153]. But also for CKKW it requires a careful choice of all ingredients to show that the dependency on the arbitrary merging scale, separating both domains, can be removed through NLL precision [150]. Especially, the clustering has to be an exact inverse of the shower, employing the same scale definition. This realization led to the formulation of the CKKW-L class of merging, where the shower itself is used to generate the Sudakov form factors [152, 154]. Note that it is, compared to the unitary approach, not at all obvious that this merging machinery does not change the inclusive cross section. In fact, the original proposals have been shown to break unitary but can be corrected by subtracting the unitarity violating terms, as shown for PYTHIA8 (dubbed UMEPS) [155] and HERWIG [156, 157]. Such a subtraction can produce events with negative weights. This lowers the statistical quality of the events, as positive and negative weight events first cancel each other and only after this one can get finite contributions in histograms. As these events have to be passed through extremely time consuming detector simulations, this is in general undesirable. Thus, we consider the current so-called state of the art of merging schemes inferior to the unitary GKS merging method, which guarantees unitarity while maintaining unit event weights and resumming the matrix-elements to all orders in a well-defined way. First infrastructure for the GKS merging in WHIZARD has been created but the full implementation was not accomplished as we have focused on the completion of the other topics presented in this thesis. We note though that the POWHEG matching that we present in Section 3.3 can be considered as the NLO correction of the first emission within GKS merging. NLO merging, i.e. combining different jet multiplicities each described to NLO accuracy, is also possible in the unitary approach [158]. Due to the simple construction, it actually allows to reason about the correctness of the scheme far more easily compared to the NLO merging schemes that are currently in practice [157, 159, 160]. Next, we discuss the two popular matching solutions.

3.2.2 Matching

Opposed to merging, matching schemes have been invented not to increase the accuracy of the shower but to allow combining differential NLO cross sections with parton showers in the first place. The rigorous matching of NLO computations with parton showers has been pioneered with MC@NLO [161]. It relies on subtracting the expansion of the parton shower from the cross section to remove the double counting. As such this expansion has to be computed for each parton shower and adapted to each change to the parton shower. Furthermore, the event generation proceeds in two classes of events, resulting in negative weight events in all regions of phase space. P. Nason proposed a similar method that avoids the inherent problem of MC@NLO of producing negative weight events, in the sense that negative weighted events can only occur in regions where perturbation theory fails [162]. Following the first implementation [163], the algorithm has been worked out in detail [145] and dubbed the POWHEG method (Positive Weight Hardest Emission Generator). Contrary to the subtractive approach of MC@NLO, POWHEG is a unitary method that uses the Sudakov veto method that we introduced in Section 3.1.3. The hardest, i.e. highest relative p_{T}, emission is hereby not generated by the attached parton shower but by the algorithm itself. Thus, the NLO accuracy of the sample can be maintained, irrespective of the used shower. This requires, though, that the shower respects the hardest emission, which is easily satisfied with a veto of higher p_{T} on subsequent emissions. In case the ordering variable of the shower is not p_{T}, soft radiation before the hardest emission has to be added as well in terms of a *truncated* shower.

Following the detailed description of POWHEG in Ref. [145], the semi-automated NLO+PS event generator called POWHEG-BOX [164] has been developed. In this framework, a multitude of LHC processes has been made publicly available, which pushed the use of NLO predictions in experimental studies significantly. The drawback of the POWHEG-BOX is that it only automates parts of the algorithm meaning that adding a new process requires considerable theoretical effort (about half a PhD thesis per process) from the construction of the phase space to the implementation of the matrix elements. Thus, only a handful of processes also account for new physics contributions. Compared to this, an automatic event generation with flexible control over all aspects is preferable. In both SHERPA [165] as well as HERWIG [166], variants of the POWHEG method have been implemented. In the next section, we sketch the implementation of the POWHEG matching in WHIZARD. We will keep this description brief as the corresponding proofs and more detailed information can be found in Ref. [145, 162].

3.3 POWHEG matching

3.3.1 POWHEG algorithm

To generate events according to the POWHEG method, we at first have to define the total cross section. As we noted in Section 3.2, the idea is to not change the fixed-order cross section but to only modify differential distributions. Thus, we can start with the expression that we already used in Eq. (2.29) for the MEM@NLO:

$$\bar{B}\left[\Phi_n\right] = B\left[\Phi_n\right] + \tilde{V}\left[\Phi_n\right] + \int \mathrm{d}\Phi_{\mathrm{rad}}\, \tilde{R}\left[\Phi_n, \Phi_{\mathrm{rad}}\right] \tag{3.14}$$

We use this function for the initial integration in VAMP and to generate n-particle events correct to NLO, just as in Section 2.5. As before, the integral over the radiation phase-space $\mathrm{d}\Phi_{\mathrm{rad}}$ is evaluated numerically with a MC sampling. With this seed kinematic, we generate the hardest emission by using the real emission matrix elements. Hereby, we resum this emission to LL in p_{T} with a simple Sudakov exponentiation, cf. Section 3.1.1,

$$\Delta(p_{\mathrm{T}}) = \exp\left\{-\int \mathrm{d}\Phi_{\mathrm{rad}}\, \mathcal{P}(\Phi_{\mathrm{rad}})\, \theta\left(k_{\mathrm{T}}^2(\Phi_{\mathrm{rad}}) - p_{\mathrm{T}}^2\right)\right\}, \tag{3.15}$$

whereby the splitting probability is given by the process-dependent splitting function $\mathcal{P} = R(\Phi_{\mathrm{rad}})/B$. Note that in Eq. (3.15), we have implied that the integration over $\mathrm{d}\Phi_{\mathrm{rad}}$ goes over the full phase-space such that $\Delta(p_{\mathrm{T}})$ is the probability that no emission occurs between $p_{\mathrm{T}}^{\max}$ and p_{T}. $k_{\mathrm{T}}(\Phi_{\mathrm{rad}})$ is the relative k_{T} of a given configuration Φ_{rad}. We can expect that the shower evolution of the hardest emission is improved by using the process-dependent $\mathcal{P}$, as opposed to universal splitting functions, which are only valid in the very soft/collinear regions and do not include interference effects. A classic example for such interference effects are color dipoles, whereby the emission in between the colored legs is enhanced while it is suppressed outside as it forms a color singlet. Although, it is possible to construct $2 \to 3$ antenna showers, cf. VINCIA [146, 167, 168], the full color information of the n-particle process can only be obtained from matrix elements. We are resumming with Eq. (3.15) the full real corrections to all orders, which can lead to undesired effects, as we discuss in Section 3.3.2. This can easily be refined, though.

By using the shower algorithm, outlined in Section 3.1.2, and stopping after the first emission, we obtain the following distribution:

$$\mathrm{d}\sigma = \bar{B}\, \mathrm{d}\Phi_n \left(\Delta\big(p_{\mathrm{T}}^{\min}\big) + \mathrm{d}\Phi_{\mathrm{rad}}\Delta\big(k_{\mathrm{T}}(\Phi_{\mathrm{rad}})\big)\frac{R(\Phi_{\mathrm{rad}})}{B}\right). \tag{3.16}$$

So there is a finite, albeit small, probability $\Delta\big(p_{\mathrm{T}}^{\min}\big)$ for no radiation down to $p_{\mathrm{T}}^{\min}$, which is usually chosen at $\mathcal{O}(1\,\mathrm{GeV})$. In most cases though, there will be an emission at the scale $k_{\mathrm{T}}(\Phi_{\mathrm{rad}})$ and the generated event is given by the phase-space point $\Phi_n\Phi_{\mathrm{rad}}$. Again, we stress that the expression in parentheses in Eq. (3.16) integrates to one due to the unitary construction. This ensures that the inclusive NLO cross section $\bar{B}$ is conserved, implying that the POWHEG matching only changes the spectrum. Especially, it damps the divergent emission of soft and collinear radiation of the pure NLO prediction (induced by $\mathrm{d}\Phi_{\mathrm{rad}}R/B$) as it is multiplied with the no-emission Sudakov form factor $\Delta\big(k_{\mathrm{T}}(\mathrm{d}\Phi_{\mathrm{rad}})\big)$. This, in turn, goes to zero in these regions of phase-space, $\lim \Delta(k_{\mathrm{T}} \to 0) = 0$, yielding finite, resummed predictions for the full $n+1$ phase-space.

At this point, we want to emphasize the excellent interplay between FKS subtraction and POWHEG event generation. While we have written Eq. (3.15) in a general way, it is not straightforward to use it with CS subtraction, as there is no unique Born phase-space point, as we noted in Sections 2.1 and 2.5. Thus, one has to introduce e.g. an additional projection, similar to FKS itself [169]. On the other hand, there are multiple possible (real) singular regions α when one starts off with one Born configuration in FKS. Each of them has a different emission probability R_α/B with $R = \sum_\alpha R_\alpha$. Thus, the overall Sudakov form factor will be a product of the Δ_α of the different regions. These different real contributions, however, can be easily combined: The region with the largest p_T is kept, as described in Section 3.1.4, to distribute events according to Eq. (3.16).

While it is in principle possible to use the real matrix elements directly for the sampling of the Sudakov exponent, it is computationally very expensive. There are two ways to circumvent this problem: Firstly, one can use the universal properties of the splitting function, i.e. the known soft and collinear divergence structure, to construct an overestimator U weighted with a constant factor N. This computationally efficient splitting function NU can be used to generate possible emissions as an overestimator. These are accepted in an additional veto step according to the probability $(R/B)/(NU)$, which removes NU from the final result. A problem arises, hereby, similar to ordinary LO event generation, when N is chosen too low and excess events occur, i.e. when $(R/B) > NU$. As long as this occurs only in a very small number of events (below 1 %), this can be usually neglected but otherwise a new generation with a larger N is necessary. A different approach is the fully automated, numerical evaluation of the exponent in Eq. (3.15) as it is done in ExSample [170], whereby the Sudakov algorithm itself is modified. In our implementation, we decided to use a hybrid version, where N is a grid that depends on the radiation variables multiplied with the general U functions, similar to the approach in the Powheg-Box. Before the first Powheg event generation, this grid is filled with the maximal values of $(R/B)/U$ by sampling the radiation phase-space randomly. The exact binning and number of points for sampling can be adjusted to the process complexity. To further reduce the probability of the aforementioned excess events, one can multiply these maxima with a safety factor. More details on all veto steps that we perform can be found in Appendix B.2. A dedicated performance and validation comparison with ExSample featuring multiple processes would be an interesting future project.

3.3.2 POWHEG damping

While the preservation of the inclusive NLO cross section is very pleasing, there are also negative aspects in combination with the Sudakov form factor. As we noted earlier, we trust the parton-shower description in the soft and collinear phase-space regions, while the matrix elements are accurate in the hard areas. Comparing the differential NLO description with the Powheg matched one, as e.g. in the gluon energy in the left plot of Fig. 3.2, we see the expected suppression in the soft regions. Due to unitary, however, this relates to an enhancement for large gluon energies. Although this is arguably only a higher-order effect, it is preferable to recover the fixed-order predictions in the hard regions of phase-space. Thus, we aim to restrict the effect of the Sudakov suppression to the area where p_T is small.

To solve this, we can use the division of real radiation into a hard and a soft part as introduced in Section 2.4. Hereby, we use only the singular part, R_sing, for the cross section

$\bar{B}$ and the Sudakov Δ. The finite part, R_{fin}, is treated separately with an ordinary LO phase-space integration. Thus, Eq. (3.16) is replaced by

$$\mathrm{d}\sigma = \bar{B}_{\text{sing}}\,\mathrm{d}\Phi_n\left(\Delta_{\text{sing}}\big(p_{\mathrm{T}}^{\min}\big) + \mathrm{d}\Phi_{\text{rad}}\Delta_{\text{sing}}\big(k_{\mathrm{T}}(\Phi_{\text{rad}})\big)\frac{R_{\text{sing}}(\Phi_{\text{rad}})}{B}\right) + R_{\text{fin}}\,\mathrm{d}\Phi_{n+1}\,. \quad (3.17)$$

We emphasize that this separation into finite and singular pieces does not affect the unitary construction, i.e. the inclusive NLO cross section is reproduced as in standard POWHEG

$$\begin{aligned}\sigma \equiv \int \mathrm{d}\sigma &= \int \big(\bar{B}_{\text{sing}}\,\mathrm{d}\Phi_n + R_{\text{fin}}\,\mathrm{d}\Phi_{n+1}\big)\\ &= \int \bar{B}\,\mathrm{d}\Phi_n \equiv \sigma^{\text{NLO}}\,,\end{aligned} \quad (3.18)$$

where we have used that the bracket in Eq. (3.17) integrates to unity. By only using the singular part of the real radiation in the POWHEG part, we are effectively introducing a Heaviside theta distribution that restricts real radiation to the area where p_{T} is small, just as desired.

The associated freedom in the division between hard and soft part has to be regarded as a theoretical uncertainty. This is actually a feature as we have seen that multiple matching schemes can be devised that fulfill NLO+LL accuracy and thus we should not treat one scheme as the definite answer. However, similar to scale variations, one should only consider a sensible range of variations. If one goes to extreme variations, one encounters the following problems: When we remove the singular parts, nothing is left to resum and the finite part diverges. Vice versa, when we remove all of the finite parts, we are back to the problem of affecting the hard spectrum with the POWHEG matching, which we intend to solve with the separation of soft and hard part.

Finally, we note that the separation of R solves also the problem of *Born zeroes*. These are regions of phase-space that get finite contributions from R_{fin} but are zero in B. This leads to an artificially divergent R/B and was in fact the original motivation behind the so-called POWHEG *damping* of R in the POWHEG-BOX [120, 121]. However, as the idea is more general and can also be applied at fixed order, we preferred to introduce it already in Section 2.4.

3.3.3 Application for $\mathrm{t\bar{t}}$ and $\mathrm{t\bar{t}H}$ production at a future lepton collider

The impact of POWHEG matching on event shapes at a lepton collider like $e^+e^- \to$ hadrons has first been discussed in Ref. [171], where a significant improvement in the description of the measured data from LEP has been found in almost all observables, compared to LO with a matrix element correction. In Ref. [172], this work has been extended to consider on-shell top-pair production with semi-leptonic decays at the ILC. We will revisit in this section both $\mathrm{t\bar{t}}$ as well as $\mathrm{t\bar{t}h}$ production at a lepton collider. The results of this section have been partly presented in Refs. [173, 174].

In the following, jets are possible combinations of all occurring quarks, including the top quark, and gluons, clustered with FastJet [175]. We use the generalized anti-k_T algorithm (`ee_genkt` with $p = -1$), which employs energies and spherical coordinates instead of transverse momentum and rapidities as distance measure. The jet parameters are $R = 1.0$ and $E_{j,\text{min}} = 1\,\text{GeV}$. The shown events in this section have been simulated only up to the first emission, leaving out the normally following simulation chain, in order to focus only on the Powheg implementation. We have, however, verified that NLO+PS in combination with Pythia8 gives reasonable results, with $\mathcal{O}(10\,\%)$ differences compared to LO+PS. The top mass is set to $m_t = 172\,\text{GeV}$. We chose $\mu_r = m_t$ as renormalization scale. The coupling constants are $\alpha^{-1} = 132.160$ with no running and $\alpha_S(M_Z) = 0.118$ with a NLL running with 5 active flavors. LO and Powheg events are unweighted during generation, i.e. they are accepted according to their current weight compared to the maximal weight. The histograms are generated with Rivet [116], using 500 k LO and Powheg each, as well as 1500 k NLO events.

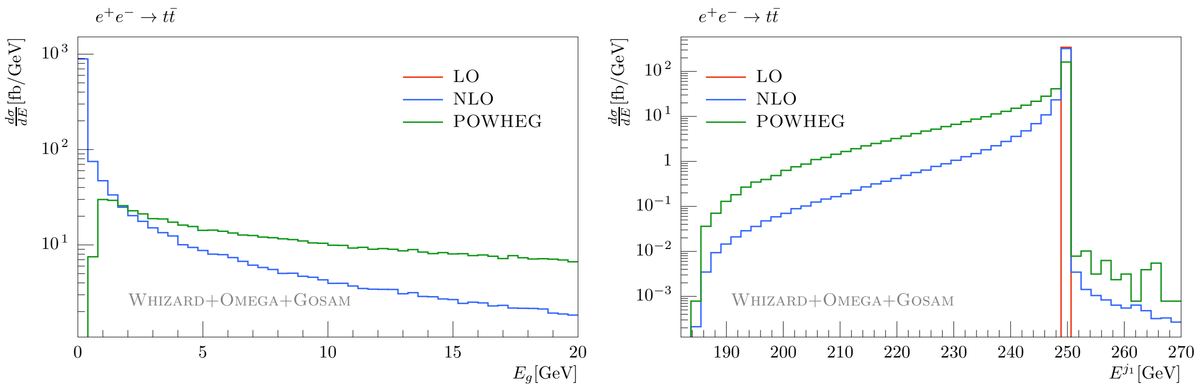

Figure 3.2 Energy distributions of the emitted gluon and of the hardest jet for $\mathrm{e}^+\mathrm{e}^- \to \mathrm{t}\bar{\mathrm{t}}$ at $\sqrt{s} = 500\,\text{GeV}$.

In Fig. 3.2, we show on-shell $t\bar{t}$ production at a lepton collider with $\sqrt{s} = 500\,\text{GeV}$. Polarization and beamstrahlung effects are neglected. The soft gluon divergence can be seen in the NLO event samples either directly in the (unphysical) energy distribution of the gluon or indirectly in the distribution of the hardest jet, which peaks around the Born value due to mostly soft gluons. By applying the Sudakov form factor, the Powheg events have the expected suppression of this divergence. Due to the unitary construction, this leads to an increase of the differential cross section in the remaining part of the spectrum, as we discussed earlier.

Next, we examine the impact of the separation of real contributions into finite and singular parts that we introduced in Section 3.3.2. For this, we show in Fig. 3.3 not only the NLO and Powheg description but also results for varying the real separation scale h from 1 GeV to 100 GeV. As expected, $h = 100\,\text{GeV}$ corresponds in this process to almost no R_{fin} contributions and thus basically the same prediction as standard Powheg. Only

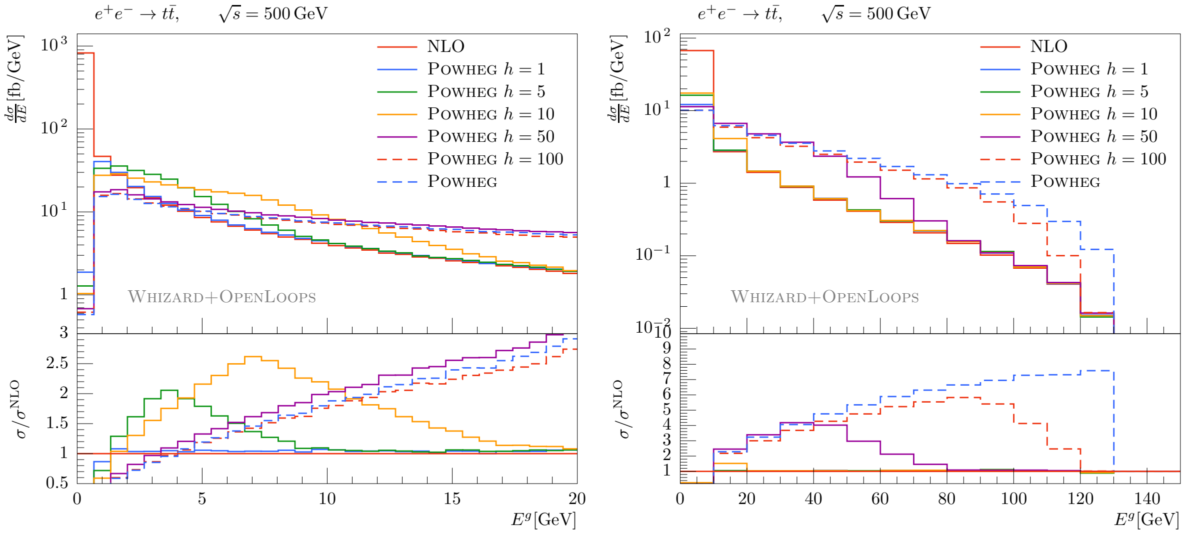

Figure 3.3 Gluon energy distribution up to 20 and 140 GeV for $\mathrm{e}^+\mathrm{e}^- \to \mathrm{t\bar{t}}$ at $\sqrt{s} = 500\,\mathrm{GeV}$.

for very high energies above $E^{\mathrm{g}} \sim 100\,\mathrm{GeV}$, we see significant deviations. On the other hand, $h = 1\,\mathrm{GeV}$ behaves very similar as NLO. In this case, R_{sing} is reduced to the bare minimum while most of R is treated as a finite contribution without resummation. Only for very small gluon energies, we see the suppression of the IR divergence. Note that in a region where R_{sing} vanishes, the Sudakov form factor is unity (no POWHEG emission occurs), and Eq. (3.17) corresponds to the differential NLO cross section. The other h values then smoothly interpolate between these extremes. For this process, we can see that h and E^{g} are very simply correlated, i.e. $R_{\mathrm{sing}} = R$ and $R_{\mathrm{fin}} = 0$ when $E^{\mathrm{g}} \lesssim h$ and vice versa. In Fig. 3.4, we depict the energy and transverse momentum distribution of the

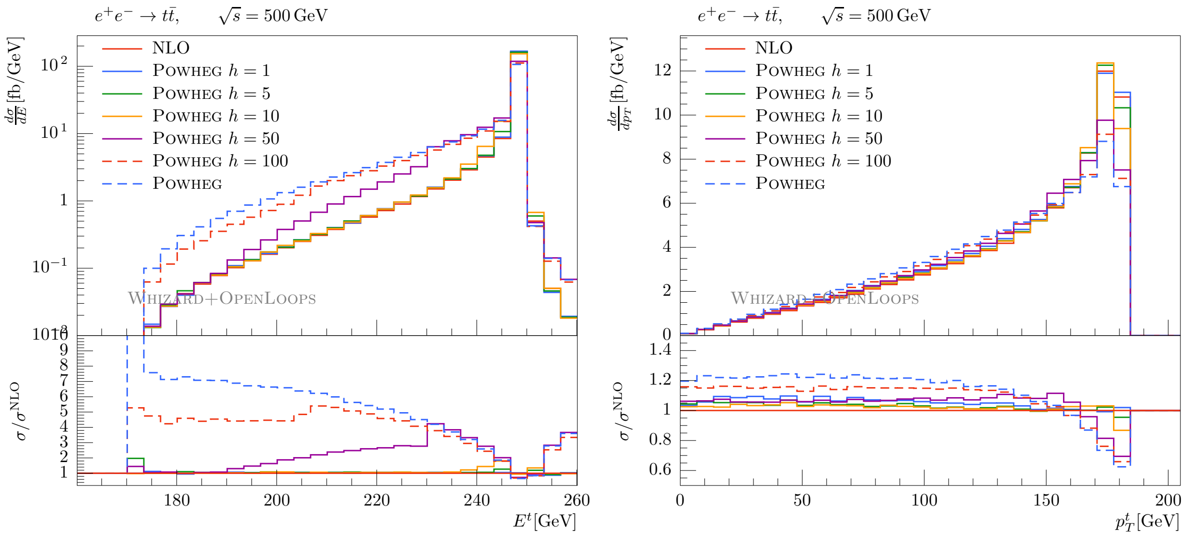

Figure 3.4 Energy and transverse momentum distribution for jets containing the top quark for $\mathrm{e}^+\mathrm{e}^- \to \mathrm{t\bar{t}}$ at $\sqrt{s} = 500\,\mathrm{GeV}$.

jet that contains the top quark. The top energy is very sensitive to the radiation pattern as the Born prediction is simply peaked at $E^{t} = 250\,\text{GeV}$. Thus, we see similar results as in Fig. 3.3. On the other hand, the transverse momentum is already smeared down to zero at Born level, thus the difference between NLO and Powheg are only ranging from $-40\,\%$ to $+20\,\%$. Again, the damping results interpolate between these limits. For the physics prediction, we think that a reasonable description would be obtained with $h \sim 20\,\text{GeV}$ as it is decently placed between the extremes of $1\,\text{GeV}$ and $100\,\text{GeV}$. Again, as we discussed in Section 3.3.2, the reason for chosing an intermediate value is that neither of the extremes have the desirable properties of a NLO+LL prediction. For the theory uncertainty, this scale should be at least varied by a factor of two although a more conservative choice would be a factor of four, as all of these choices are formally valid at NLO+LL. A general rule of thumb for choosing h would be $p_{\mathrm{T}}^{\mathrm{min}} \ll h \ll p_{\mathrm{T}}^{\mathrm{max}}$.

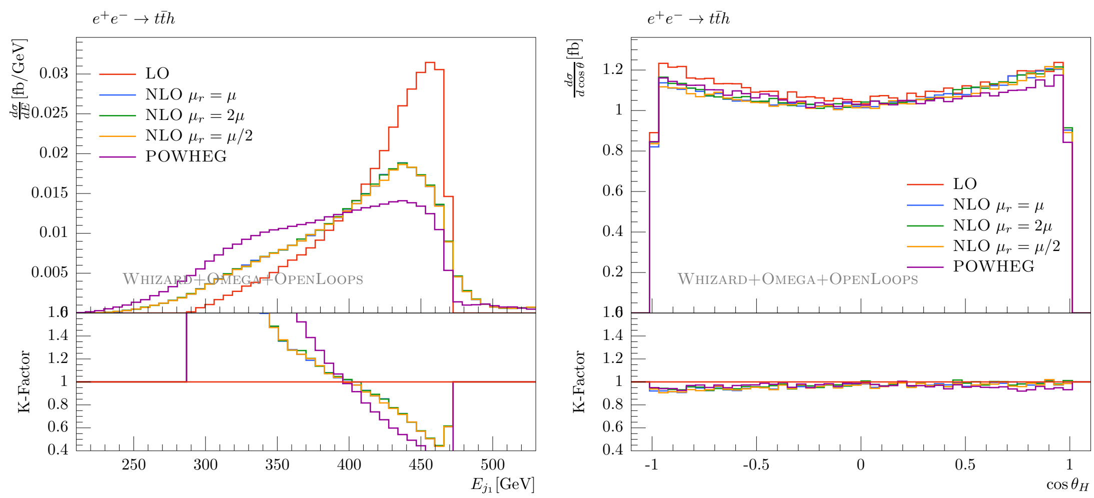

Figure 3.5 The energy distribution of the hardest jet and the angular distribution of the Higgs boson for $\mathrm{e}^+\mathrm{e}^- \to \mathrm{t}\bar{\mathrm{t}}\mathrm{H}$ at $\sqrt{s} = 1000\,\text{GeV}$.

Finally, we treat $e^+e^- \to t\bar{t}H$ with the same setup as above but at $\sqrt{s} = 1000\,\text{GeV}$. Fig. 3.5 shows distributions of two observables: In the energy distribution of the hardest jet, we can see again the effect of Sudakov suppression at the high energy peak. For comparison, we also show the effect of scale variation, which, as expected, does not cover the difference between NLO and Powheg. On the other hand, we observe that in inclusive quantities like the angular distribution of the Higgs boson, the Powheg matching has no significant effect. This is, of course, only a cross check that inclusive quantities remain correct to NLO. We find that although the total K-factor at this value of $\sqrt{s}$ is close to 1, distributions of observables that are sensitive to QCD radiation can change drastically.

Part II

NLO QCD Predictions for off-shell $t\bar{t}$ and $t\bar{t}H$ production

Chapter 4

Motivation and phenomenology

4.1 Introduction

As we motivated in Chapter 1, top-pair production with and without an associated Higgs boson is of utmost interest to measure physical quantities like the top mass in a short distance scheme or the top Yukawa coupling. To achieve high theoretical precision, the top quark needs, however, a careful treatment. Due to the relatively large top width, resulting from the decay into a bottom quark and a W boson, top quarks decay before they can form bound states. The produced W boson decays further via hadronic or leptonic channels, whereas the bottom quark hadronizes and can be identified as a tagged jet. Especially in the clean lepton collider environment, the charge of the b-jet can be reconstructed with reasonably high efficiency [176]. A consistent treatment of the associated finite width effects is both a conceptionally as well as a computationally nontrivial problem. Within the so-called narrow-width approximation (NWA), top quarks are produced on-shell and decay subsequently according to their (potentially spin correlated) branching ratios. Higher-order QCD predictions for on-shell top-pair production are well-known, the current best predictions being NNNLO [50] at the inclusive and NNLO at the fully differential level, using either a phase-space slicing [51] or antenna subtraction [52]. First NLO electroweak corrections have been obtained in Ref. [177]. For top-pair production in association with a Higgs boson, there are comprehensive studies of NLO QCD corrections available in Ref. [55]. First inclusive combined electroweak and QCD corrections have been computed in Ref. [56], followed by an in-depth study in Ref. [178].

While computationally simple, the NWA has the obvious drawback that various non-resonant background processes are not included. For off-shell $\mathrm{t\bar{t}}$ or $\mathrm{t\bar{t}H}$ production, however, especially single-top resonances contribute significantly and can hardly be distinguished experimentally from double-resonant contributions [179]. Furthermore, off-shell effects can only be treated approximatively via a Breit-Wigner parametrization, as in Ref. [180]. Non-resonant contributions and finite width effects can be consistently taken into account employing the complex-mass scheme [181], which guarantees gauge invariance at NLO. The trade-off for this is the increased computational complexity. Such a calculation for the process $\mathrm{e^+e^-} \to \mathrm{W^+W^-b\bar{b}}$ at NLO QCD has first been presented in Ref. [53]. It has recently been reevaluated in Ref. [54], with the aim of extracting the top-quark width via ratios of single- to double-resonant signal regions.

In this part, we study top-pair and Higgs associated top-pair production and decay including non-resonant contributions, off-shell effects and interferences at NLO. The simulation is done with WHIZARD, as introduced in Section 2.3. In this framework, we compare the on-shell processes $\mathrm{e}^+\mathrm{e}^- \to \mathrm{t\bar{t}}$ and $\mathrm{e}^+\mathrm{e}^- \to \mathrm{t\bar{t}H}$ with the off-shell processes $\mathrm{e}^+\mathrm{e}^- \to \mathrm{W}^+\mathrm{W}^-\mathrm{b\bar{b}}$ and $\mathrm{e}^+\mathrm{e}^- \to \mathrm{W}^+\mathrm{W}^-\mathrm{b\bar{b}H}$. At the differential level, the full processes including leptonic decays are considered, i.e. $\mathrm{e}^+\mathrm{e}^- \to \mu^+\nu_\mu\mathrm{e}^-\bar{\nu}_\mathrm{e}\mathrm{b\bar{b}}$ and $\mathrm{e}^+\mathrm{e}^- \to \mu^+\nu_\mu\mathrm{e}^-\bar{\nu}_\mathrm{e}\mathrm{b\bar{b}H}$. To our knowledge, NLO studies of $\mathrm{e}^+\mathrm{e}^- \to \mathrm{W}^+\mathrm{W}^-\mathrm{b\bar{b}H}$ or the complete off-shell processes $\mathrm{e}^+\mathrm{e}^- \to \mathrm{b\bar{b}}4f$ or $\mathrm{e}^+\mathrm{e}^- \to \mathrm{b\bar{b}}4f\mathrm{H}$ have not been performed prior to our work. In contrast, at hadron colliders off-shell top-pair production at NLO QCD has been studied in Refs. [182–187], and first NLO electroweak results have been presented in Ref. [188]. Furthermore, employing the resonance-aware method of Ref. [133], the process $\mathrm{pp} \to \mathrm{b\bar{b}}4f$ has been matched consistently to parton showers, as presented recently in Ref. [134]. For hadron colliders, corresponding NLO QCD corrections to top-quark pair production in association with a Higgs boson [189] or a jet [190, 191] including leptonic decays have also been studied.

While at hadron colliders top-pairs originate from QCD production, at lepton colliders they are produced via electroweak interactions. This implies that a fixed-order computation of the off-shell processes at a lepton collider comprises a considerably larger set of irreducible electroweak background processes. Such processes involve narrow resonances, like e.g. $\mathrm{H} \to \mathrm{b\bar{b}}$. In NLO computations, resonances with very small widths can severely hamper the quality of the infrared (IR) subtraction and consequently influence the convergence and quality of the integration. In order to have these resonance effects under control, we have implemented in WHIZARD an automated version of the resonance-aware scheme of Ref. [133], as described in Section 2.6. This is also a prerequisite for a future consistent matching of off-shell processes with parton showers.

The further organization of this part is as follows. In Section 4.2, the phenomenology of $\mathrm{t\bar{t}}$ and $\mathrm{t\bar{t}H}$ is briefly reviewed. In Section 4.3, we describe how we obtain the matrix elements for the processes of interest. The employed input parameters, scale choices and phase-space cuts as well as an overview of the performed validations can be found in Section 4.4. The main phenomenological results are in Sections 5.1 and 5.2. Hereby, we focus in Section 5.1 on results at the inclusive level, while we present in Section 5.2 the corresponding differential predictions. We discuss scale variations for the NLO QCD corrections, show results for polarized lepton beams and discuss the influence of the NLO QCD corrections on the extraction of the top Yukawa coupling. At the end, we present our conclusions in Section 5.3. We note that these results have been published in the research article [192].

4.2 Phenomenology of off-shell $\mathrm{t\bar{t}}$ and $\mathrm{t\bar{t}H}$ production

4.2.1 Phenomenology of off-shell $\mathrm{t\bar{t}}$ production

We want to investigate NLO QCD perturbative corrections in top-quark pair production at lepton colliders modeling off-shell and interference effects at increasing levels of precision. To this end, we will consider the following $2 \to 2, 2 \to 4$ and $2 \to 6$ processes,

$$\mathrm{e^+e^-} \to \mathrm{t\bar{t}} \; , \tag{4.1}$$

$$\mathrm{e^+e^-} \to \mathrm{W^+W^-b\bar{b}} \; , \tag{4.2}$$

$$\mathrm{e^+e^-} \to \mu^+\nu_\mu \mathrm{e^-}\bar{\nu}_\mathrm{e}\mathrm{b\bar{b}} \; , \tag{4.3}$$

whereby we treat the bottom quarks as massive. Top quarks almost exclusively decay via $\mathrm{t} \to \mathrm{bW}$, such that the process in Eq. (4.2) can be understood as the top-quark pair production process of Eq. (4.1) including top-quark decays. Beyond the NWA, the process in Eq. (4.2), however, receives not only double-resonant (signal) top-quark contributions. Also single-resonant and non-resonant (background) diagrams enter, including their interference. Example diagrams for all three production mechanisms are shown in Fig. 4.1. The sub-dominant single-top diagrams always occur via a fermion line between the two

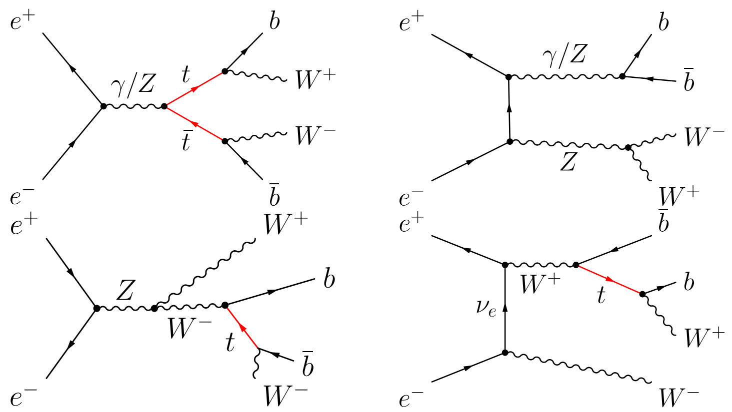

Figure 4.1 The double-resonant signal diagram (top left) besides example non-resonant (top right) and s- and t-channel single-top diagrams (bottom left and right, respectively) of the process $\mathrm{e^+e^-} \to \mathrm{W^+W^-b\bar{b}}$.

external bottom quarks. Thanks to the finite bottom mass even non-resonant contributions from diagrams with a $\gamma \to \mathrm{b\bar{b}}$ splitting, like the one in the top right of Fig. 4.1, can be integrated over the whole phase space without the necessity of cuts.

At the NLO QCD level, the calculation of the process in Eq. (4.2) includes corrections to top-quark pair production and decays together with non-factorizable corrections, which are formally of the order of $\mathcal{O}\left(\alpha_S \Gamma_\mathrm{t}/m_\mathrm{t}\right)$. Diagrammatically such non-factorizable contributions can interconnect production and decay stage. Furthermore, different decays can be

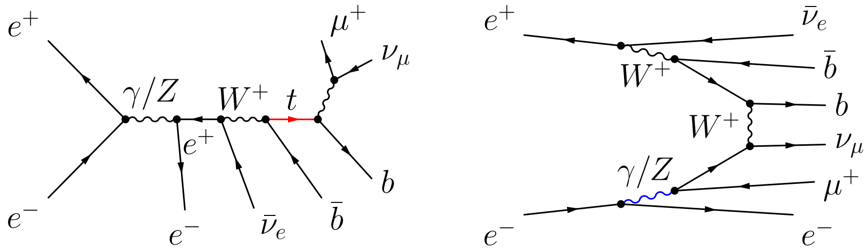

Figure 4.2 Possible topologies of the full process. The blue line indicates a potentially soft photon that gives rise to a leading-order singularity.

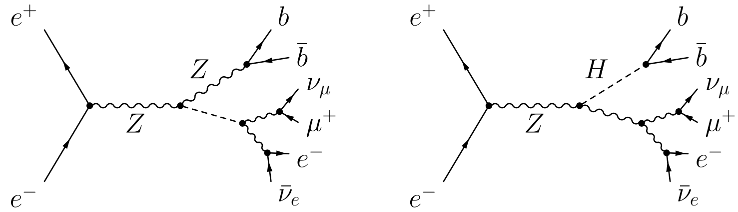

Figure 4.3 Contributions to the process $\mathrm{e}^+\mathrm{e}^- \to \mu^+\nu_\mu \mathrm{e}^-\bar{\nu}_\mathrm{e}\mathrm{b}\bar{\mathrm{b}}$ involving a Z or H resonance, treated with the resonance-aware FKS subtraction.

connected, as for example depicted in Fig. 4.6 (left). At the same time, NLO interference effects with single-resonant and non-resonant contributions and also spin correlations in the top decay are consistently taken into account.

In order to make contact with experimental signatures and to further increase theoretical precision, the process in Eq. (4.3) introduces also leptonic decays of the W-bosons including respective off-shell effects. Due to the purely EW nature of the leptonic W-boson decays, from a perturbative QCD point of view these additional decays do not increase the computational complexity compared to the process with on-shell W-bosons, i.e. the one of Eq. (4.2). However, besides the more involved phase-space integration, the number of contributing diagrams increases substantially due to additional single- and non-resonant contributions, as illustrated in Fig. 4.2. Note that the decays with initial-state lepton flavor introduce diagrams like the one on the right of Fig. 4.2. These show a singularity and cannot be integrated over the whole phase space without cuts. Here, we focus on the different lepton flavor case but an analysis for the very similar same flavor case can easily be performed with Whizard. An interesting further research topic are semi-leptonic and hadronic decays, where the non-factorizable backgrounds at NLO QCD are even more important.

Finally, we want to remark that the off-shell processes of Eqs. (4.2) and (4.3) contain diagrams with $\mathrm{Z/H} \to \mathrm{b}\bar{\mathrm{b}}$ splittings, as for example depicted in Fig. 4.3. Due to the small intermediate widths, the integration of such contributions benefits strongly from the extended resonance-aware FKS subtraction, described in Section 2.6. For the technical reasons discussed there in detail, we only apply the resonance-aware FKS subtraction for the intermediate Z/H resonances, but not for the top resonances. Employing the implementation of the resonance-aware subtraction scheme with these resonance histories,

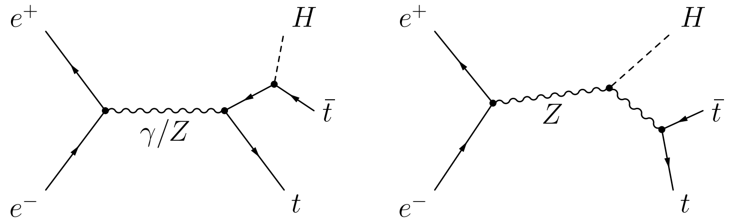

Figure 4.4 Contributing diagrams to $\mathrm{t\bar{t}H}$ production: associated production of a Higgs boson and a top quark pair and Higgsstrahlung with an off-shell $\mathrm{Z}^* \to \mathrm{t\bar{t}}$ line.

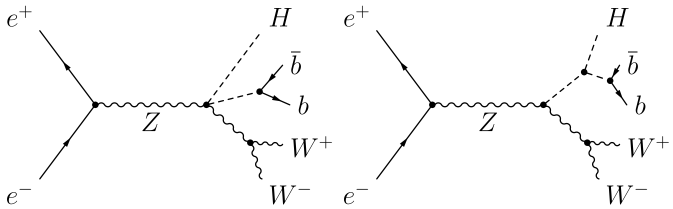

Figure 4.5 Two representative non-resonant diagrams contributing to $\mathrm{W^+W^-b\bar{b}H}$ production via a quartic ZZHH-coupling as well as a ZZH- and a triple H-coupling.

we observe a decent convergence of the numerical integration at the inclusive and differential level. Numerically, at LO the contribution from $\mathrm{H} \to \mathrm{b\bar{b}}$ splittings is at the level of 1-2% of the total off-shell $\mathrm{t\bar{t}}$ cross section and is clearly visible in finely binned $m_{\mathrm{b\bar{b}}}$ distributions. Obviously, neglecting the bottom mass would remove these contributions.

4.2.2 Phenomenology of off-shell $\mathbf{t\bar{t}H}$ production

Similar to top-quark pair production, we consider the following related $2 \to 3, 2 \to 5$ and $2 \to 7$ processes for the associated production of a Higgs boson together with a top-quark pair with increasing level of precision with respect to off-shell, non-resonant and interference effects,

$$\mathrm{e^+e^-} \to \mathrm{t\bar{t}H}\ , \tag{4.4}$$

$$\mathrm{e^+e^-} \to \mathrm{W^+W^-b\bar{b}H}\ , \tag{4.5}$$

$$\mathrm{e^+e^-} \to \mu^+\nu_\mu \mathrm{e}^-\bar{\nu}_\mathrm{e}\mathrm{b\bar{b}H}\ , \tag{4.6}$$

where again all b-quarks are treated as massive.

The diagrams involved in these processes are very similar to those of the corresponding $\mathrm{t\bar{t}}$ production processes, apart from the additional Higgs boson that couples to all massive internal or external particles $(\mathrm{t}, \mathrm{b}, \mathrm{W}, \mathrm{Z}, \mathrm{H})$. Already at the level of the on-shell processes of Eq. (4.4) this results into two competing contributions, as depicted in Fig. 4.4. The diagram on the left of Fig. 4.4 is proportional to the top Yukawa coupling y_t and will be denoted as $\mathrm{t\bar{t}H}$ signal contribution. The diagram on the right can be considered as irreducible Higgsstrahlung background in the ZH channel with an off-shell $\mathrm{Z}^* \to \mathrm{t\bar{t}}$ line.

Furthermore, at the level of the off-shell processes of Eqs. (4.5) and (4.6) new contributions arise from quartic EW as well as triple H couplings as illustrated in Fig. 4.5. In such contributions, as before, the tiny width of the Higgs boson requires a resonance-aware subtraction scheme to yield a converging integration at NLO over the whole phase space. We note that in our calculation on the one hand, we treat the Higgs boson as on-shell external particle, while at the same time, we introduce a finite physical Higgs width in order to regulate intermediate propagators. We accept this slight inconsistency in order to be able to provide results independent of a specific Higgs decay channel. In fact, the dominant Higgs decay mode would require in a fully unfactorized approach the calculation of $e^+e^- \to \mathrm{W^+W^-b\bar{b}b\bar{b}}$, which is in reach employing the developed automated tools but beyond the scope of this work. The numerical effect of the resulting inconsistency is very small with contributions from $\mathrm{H} \to \mathrm{b\bar{b}}$ for off-shell $\mathrm{t\bar{t}}$ as well as $\mathrm{t\bar{t}H}$ production being at the per cent level.

4.3 Matrix elements from OpenLoops

All necessary Born and one-loop amplitudes together with the color and helicity correlators required within the FKS subtraction are provided by the publicly available OpenLoops program [34, 193]. It generates tree-level and one-loop scattering amplitudes by means of a hybrid tree-loop recursion that generates cut-open loops as functions of the circulating loop momentum [34]. Similar to Recola [35, 36] and Helac-1Loop [97, 98], also OpenLoops is based on the idea [194] that one-loop diagrams can be related to tree-level diagrams with an auxiliary gluon. These can in turn be computed very efficiently using recursive algorithms [80, 195–197]. It has been shown [194] that this approach scales only exponentially, which is much better than the factorial growth of Feynman diagrams, and is completely process-independent. Combined with the CutTools [198] OPP reduction [199] library and the OneLOop library [200] or with the Collier [201] tensor integral reduction library based on Refs. [202–204], the employed recursion permits to achieve very high CPU performance and a high degree of numerical stability. In this study, we exclusively relied on Collier. OpenLoops uses a stability system to rescue the small number of potentially unstable phase space points with a re-evaluation at quadruple precision.

Within OpenLoops, ultraviolet (UV) and infrared (IR) divergences are dimensionally regularized and take the form of poles in $(4-D)$. However, all ingredients of the numerical recursion are handled in four space-time dimensions. The missing $(4-D)$-dimensional contributions (known as R_2 rational terms) are universal and can be restored from process-independent effective counterterms [205–212]. The idea, hereby, is that the R_2 part can be computed by relating one-particle irreducible amplitudes with up to four external legs with tree-level like Feynman Rules. In OpenLoops as well as Whizard, the strong coupling constant is renormalized in the $\overline{\mathrm{MS}}$ scheme. Unstable particles with a finite width are by default treated with an automated implementation of the complex-mass scheme [181].

The OpenLoops amplitude library includes all relevant matrix elements, including

Table 4.1 Overview of loop matrix elements at NLO QCD for the studied processes. Shown are the number of one-loop diagrams, the maximal number of loop propagators and the number of helicity structures (assuming charged leptons to be massless).

$\mathrm{e^+e^-} \to$	$n_{\text{loop diags}}$	Max. prop.	n_{hel}
$\mathrm{t\bar{t}}$	2	3	16
$\mathrm{W^+W^-b\bar{b}}$	157	5	144
$\mathrm{b\bar{b}}\bar{\nu}_e e^- \nu_\mu \mu^+$	830	5	16
$\mathrm{t\bar{t}H}$	17	4	16
$\mathrm{bW^+\bar{b}W^-H}$	1548	6	144
$\mathrm{b\bar{b}}\bar{\nu}_\mathrm{e}\mathrm{e}^-\nu_\mu\mu^+\mathrm{H}$	7436	6	16

color- and helicity-correlations and real radiation as well as loop-squared amplitudes, for more than a hundred LHC processes. Many libraries for lepton collisions can easily be taken from this LHC library, as any crossing of external particles is automatically done when a library is loaded. For example, we can use the one-loop library `ppll` (originally intended for the Drell-Yan process) to compute the process $\mathrm{e^+e^-} \to \mathrm{jj}$. For many other processes, especially those without massless quarks in the final state, dedicated lepton collider libraries have been added to the public OpenLoops amplitude repository.

The Whizard+OpenLoops interface is based on the Binoth Les Houches Accord (BLHA) standard [213] as an extension of Ref. [214]. Moreover, we extended this standard to allow the MC to request polarized amplitudes. To this end, the process registry can contain dedicated entries for each polarization configuration of initial state particles. This implements an automated NLO setup to study effects of beam polarization, which is an important feature at future linear colliders like the ILC. We note, however, that currently the full spin density matrix cannot be obtained from OpenLoops as polarizations for final state particles are not supported.

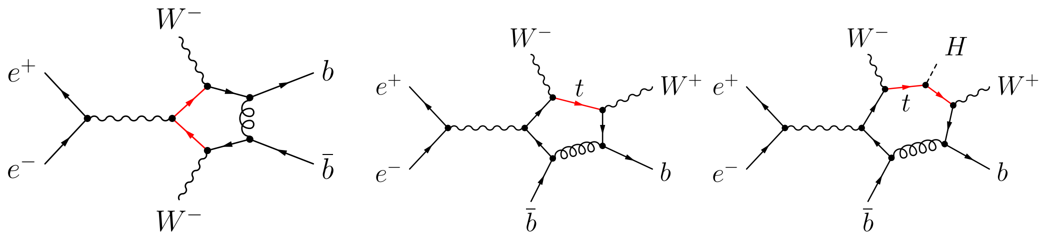

Figure 4.6 Example pentagon diagrams contributing to the $\mathrm{W^+W^-b\bar{b}}$ final-state process containing one or two (leftmost diagram) top resonances and an hexagon diagram contributing for $\mathrm{W^+W^-b\bar{b}H}$ production.

Tab. 4.1 lists information about the computational complexity with respect to the one-loop amplitudes of the processes studied in this part. Note that the total number of diagrams is not decisive for the computational effort in the OpenLoops recursion formalism. Instead, the crucial point is the maximal number of n-point functions involved. For the $\mathrm{bb}(\mathrm{W} \to \ell\nu)(\mathrm{W} \to \ell\nu)$ processes, the most complex integrals stem from pentagon diagrams, for which examples are depicted in Fig. 4.6. We also show a hexagon diagram contributing to the associated Higgs production process. The calculation of the off-shell processes including leptonic decays are less involved in terms of computational complexity compared to the corresponding processes with on-shell W-bosons. This is mainly due to the reduced number of contributing helicity structures and despite the increased number of diagrams. This decrease is due to the unique helicity combination of the final state containing massless (anti-) neutrinos.

4.4 Setup and validation

4.4.1 Input parameters, scale choice and phase-space cuts

The following masses enter the calculation as input parameters [215],

$$m_\mathrm{Z} = 91.1876\,\mathrm{GeV}\,, \qquad m_\mathrm{W} = 80.385\,\mathrm{GeV}\,, \tag{4.7}$$

$$m_\mathrm{b} = 4.2\,\mathrm{GeV}\,, \qquad m_\mathrm{t} = 173.2\,\mathrm{GeV}\,, \tag{4.8}$$

$$m_\mathrm{H} = 125\,\mathrm{GeV}\,. \tag{4.9}$$

The electron, the muon as well as the first two quark generations are considered massless. The electroweak couplings are derived from the gauge-boson masses and the Fermi constant, $G_\mu = 1.166\,378\,7 \times 10^{-5}\,/\mathrm{GeV}^2$, in the G_μ-scheme. The CKM matrix is assumed to be trivial, which is for the most relevant element of our computation (V_tb) consistent with the measured value (1.021 ± 0.032 [215]). Using the precisely measured value of G_μ absorbs the most important electroweak corrections to the top decay. As we are only at the LO electroweak level, it is advisable to use a scheme where the corrections to the top decay are small, which is the case for the G_μ-scheme [216]. Of course, this choice is not fully capturing the production dynamics, where a running $\alpha_\mathrm{em}\left[\sqrt{s}\right]$ might be more appropriate [177, 217]. Note, however, that the numerical difference between $\alpha_\mathrm{em}\left[G_\mu\right] = 1/132.233$ and $\alpha_\mathrm{em}\left[2M_t^{1S}\right] = 1/125.924$ (5 %) is not as large as to the Thomson limit $\alpha_\mathrm{em}\left[0\right] = 1/137.036$ (9 %). Either way, one can simply reweight our predictions with $(\alpha_\mathrm{em}\left[2M_t^{1S}\right]/\alpha_\mathrm{em}\left[G_\mu\right])^2$, which increases them by about 10 %, to obtain mixed scales. For the strong coupling constant, we use $\alpha_s(m_\mathrm{Z}) = 0.1185$ and a two-loop running including $n_f = 5$ active flavors.

With this setup, the gauge boson and top widths are computed directly with Whizard at LO and NLO, using massive b-quarks. In the NLO decay, we use either the mass of the decaying particle as renormalization scale or the same scale as in the scattering process, as discussed below. The obtained LO and NLO gauge boson widths, using $\mu_\mathrm{R} = m_{\mathrm{Z}/\mathrm{W}}$, are

$$\Gamma_\mathrm{Z}^\mathrm{LO} = 2.4409\,\mathrm{GeV}, \qquad \Gamma_\mathrm{Z}^\mathrm{NLO} = 2.5060\,\mathrm{GeV}, \tag{4.10}$$

$$\Gamma_{\mathrm{W}}^{\mathrm{LO}} = 2.0454\,\mathrm{GeV}, \qquad\qquad \Gamma_{\mathrm{W}}^{\mathrm{NLO}} = 2.0978\,\mathrm{GeV}. \tag{4.11}$$

In our calculation, we use Γ_{Z} and Γ_{W} at NLO throughout, i.e. also for off-shell cross sections at LO. This ensures that the effective W and Z leptonic branching ratios that result from $e^+e^- \to \mathrm{b\bar{b}}4f(\mathrm{H})$ matrix elements are always NLO accurate. In contrast, in order to guarantee that $\mathrm{t} \to Wb$ branching ratios remain consistently equal to one at LO and NLO, off-shell matrix elements and the top-decay width need to be evaluated at the same perturbative order. For the top width, we employ two distinct sets of values: one for the on-shell decay $\mathrm{t} \to \mathrm{W^+b}$ and one for the off-shell decay $\mathrm{t} \to f\bar{f}\mathrm{b}$, as also detailed in Ref. [184]. The value used for the off-shell top decay includes decays into three lepton generations and two quark generations, again with the trivial CKM matrix. It also involves the W width, for which we use the previously computed NLO value. The numerical values are

$$\Gamma_{\mathrm{t}\to\mathrm{W}b}^{\mathrm{LO}} = 1.4986\,\mathrm{GeV}, \qquad\qquad \Gamma_{\mathrm{t}\to\mathrm{W}b}^{\mathrm{NLO}} = 1.3681\,\mathrm{GeV}, \tag{4.12}$$
$$\Gamma_{\mathrm{t}\to f\bar{f}b}^{\mathrm{LO}} = 1.4757\,\mathrm{GeV}, \qquad\qquad \Gamma_{\mathrm{t}\to f\bar{f}b}^{\mathrm{NLO}} = 1.3475\,\mathrm{GeV}. \tag{4.13}$$

The Higgs width is set to $\Gamma_{\mathrm{H}} = 4.143\,\mathrm{MeV}$.

In the determination of the off-shell top width and in all calculations presented in this part, intermediate massive particles are treated in the complex-mass scheme [181]. This leads to a gauge-invariant treatment of finite width effects as well as perturbative unitarity [218]. The complex-mass scheme can be considered a complex extension of on-shell renormalization. Thus, the input mass parameters of Eq. (4.9) are pole masses and not short-distance masses as in Section 6.3.3. On the technical side, it necessitates complex-valued renormalized masses

$$\mu_i^2 = M_i^2 - \mathrm{i}\Gamma_i M_i \qquad \text{for } i = \mathrm{W}, \mathrm{Z}, \mathrm{t}, \mathrm{H}\ , \tag{4.14}$$

that imply for consistency a complex-valued weak mixing angle

$$\mathrm{s}_W^2 = 1 - \mathrm{c}_W^2 = 1 - \frac{\mu_{\mathrm{W}}^2}{\mu_{\mathrm{Z}}^2}\ . \tag{4.15}$$

For the electromagnetic coupling in the G_μ scheme, we set

$$\alpha_e = \frac{\sqrt{2}}{\pi} G_\mu \left|\mu_{\mathrm{W}}^2 s_w^2\right|, \tag{4.16}$$

which gives $\alpha_e^{-1} = 132.16916$.

For the on- and off-shell $\mathrm{t\bar{t}}$ and $\mathrm{t\bar{t}H}$ processes that we consider in this part, the renormalization scale μ_R is set to

$$\mu_\mathrm{R} = \xi_\mathrm{R}\mu_0, \quad \text{with} \quad \mu_0 = \begin{cases} m_\mathrm{t} & \text{for } \mathrm{t\bar{t}} \text{ processes} \\ m_\mathrm{t} + m_\mathrm{H} & \text{for } \mathrm{t\bar{t}H} \text{ processes} \end{cases} \tag{4.17}$$

$$\text{and} \quad \frac{1}{2} \leq \xi_\mathrm{R} \leq 2\,. \tag{4.18}$$

At lepton colliders pure QCD corrections do not involve radiation off the initial-state, and thus the hard scattering process happens at fixed energy, at least after unfolding EW ISR and beamstrahlung effects. Therefore, as the results presented in the following sections indicate, a very good perturbative description is possible with an appropriate fixed scale. Still, different dynamical scale choices, as commonly used at hadron colliders, might be appropriate for the description of specific differential observables. Our default scale choice corresponds to $\xi_\mathrm{R} = 1$ and theoretical uncertainties are probed by scale variations. However, scale uncertainties are obviously no complete assessment of the theoretical errors, but they are our best handle on perturbative QCD uncertainties. Particularly at LO the considered processes are independent of α_s, rendering corresponding uncertainty estimates meaningless.

Thanks to the finite bottom quark mass all on- and off-shell $\mathrm{t\bar{t}}$ and $\mathrm{t\bar{t}H}$ processes considered in this part can in principle be integrated over the whole phase space. However, for processes with final state electrons or positrons, a singularity emerges for small photon energy transfers, as depicted on the right-hand side of Fig. 4.2. To avoid this, we apply a mild phase-space cut for these processes

$$\sqrt{\left(k^\mathrm{in}_{e^\pm} - k^\mathrm{out}_{e^\pm}\right)^2} > 20\,\mathrm{GeV}. \tag{4.19}$$

For the definition of jets, we employ the generalized k_T algorithm (`ee_genkt` in FastJet) [175, 219] with $R = 0.4$ and $p = -1$. This jet definition is particularily suited for lepton collisions as it uses energies and angles instead of transverse momentum and ΔR. The negative power, $p = -1$, makes this an *anti-*k_T-type algorithm with the associated benefits [219]. A minimal jet energy of 1 GeV is required. We tag $\mathrm{b}/\mathrm{\bar{b}}$-jets according to their partonic content and denote them as $\mathrm{j_b}$ and $\mathrm{j_{\bar{b}}}$. Similarly, in the on-shell processes $\mathrm{e^+e^-} \to \mathrm{t\bar{t}}$ and $\mathrm{e^+e^-} \to \mathrm{t\bar{t}H}$, we identify the top quark with the jet containing a top quark. In the discussion of differential cross sections in Section 5.2, we always require at least two b-tagged jets during the analysis.[1]

[1] Since we do not impose any kinematic restriction on b-jets, requiring two b-jets amounts to a lower bound for their $\cos\theta_{ij}$ separation.

4.4.2 Validation

To validate the new automated subtraction within Whizard, we have performed various cross checks. All of the following checks have been performed at the per mil level, i.e. differences are all at the few per mil level and within two standard deviations of the MC integration. The NLO top-quark width computed by Whizard has been cross-checked both with the value used in Ref. [184] and the analytical formulae [220–222]. Total cross sections for simple $2 \to 2$ processes, like $e^+e^- \to \mathrm{q\bar{q}}$ and $e^+e^- \to \mathrm{t\bar{t}}$, have been validated against analytical calculations. For $\mathrm{e^+e^-} \to \mathrm{W^+W^-b\bar{b}}$, we have performed an in-depth cross check with various other results and generators. The total cross section of Ref. [54], therein computed with Madgraph5_aMC@NLO [38], has been reproduced. Moreover, we find excellent agreement between Whizard, Sherpa [37] and Munich [2] for the parameter set given in Section 4.4.1. This is especially encouraging as both Sherpa and Munich use CS subtraction [69, 70], while Madgraph5_aMC@NLO and Whizard use FKS subtraction [72]. The resonance-aware NLO calculation was validated internally, comparing the result with a computation based on the traditional FKS subtraction (see also Section 2.6.2). To this end, we used large widths in order to avoid problems in the traditional FKS approach.

[2] Munich is the abbreviation of "MUlti-chaNnel Integrator at Swiss (CH) precision", an automated parton level NLO generator by S. Kallweit. In preparation.

Chapter 5

Numerical predictions

5.1 Numerical predictions for inclusive cross sections

5.1.1 Integrated cross sections and scale variation

We start our discussion of the numerical results with an investigation of the NLO QCD corrections to inclusive top-quark pair production. Hereby, we show the cross sections, σ, depending on the center-of-mass energy, $\sqrt{s}$, of the leptonic collisions. In the left plot of Fig. 5.1, we show inclusive LO and NLO cross sections for the on-shell process $\mathrm{e}^+\mathrm{e}^- \to \mathrm{t}\bar{\mathrm{t}}$ and the off-shell process $\mathrm{e}^+\mathrm{e}^- \to \mathrm{W}^+\mathrm{W}^-\mathrm{b}\bar{\mathrm{b}}$ together with the corresponding K-factor ratios, defined as

$$K = \sigma^{\mathrm{NLO}}/\sigma^{\mathrm{LO}}\,. \tag{5.1}$$

Right above the production threshold $\sqrt{s} = 2m_{\mathrm{t}}$, both LO and NLO cross sections are strongly enhanced, and in the limit $\sqrt{s} \to 2m_{\mathrm{t}}$ the NLO corrections to the on-shell process $\mathrm{e}^+\mathrm{e}^- \to \mathrm{t}\bar{\mathrm{t}}$ diverge due to nonrelativistic threshold corrections. These manifest themselves as large logarithmic contributions to the virtual one-loop matrix element. On the other hand, in the off-shell process $\mathrm{e}^+\mathrm{e}^- \to \mathrm{W}^+\mathrm{W}^-\mathrm{b}\bar{\mathrm{b}}$ the Coulomb singularity is regularized by the finite top-quark width, and the NLO corrections remain finite. However, threshold corrections introduce a distinct peak in the NLO corrections at $\sqrt{s} = 2m_{\mathrm{t}}$ with a maximum K-factor of about 2.5. Below threshold the cross section drops sharply, but QCD corrections remain significant. Far above threshold, the NLO corrections are rather small for both the on-shell and the off-shell processes. For $\mathrm{e}^+\mathrm{e}^- \to \mathrm{t}\bar{\mathrm{t}}$, the corrections remain positive for all $\sqrt{s}$. In fact, for large center-of-mass energies, the effect of the top-quark mass becomes negligible and the corrections approach the universal massless quark-pair production correction factor at lepton colliders: α_s/π. In contrast, the NLO corrections to $\mathrm{e}^+\mathrm{e}^- \to \mathrm{W}^+\mathrm{W}^-\mathrm{b}\bar{\mathrm{b}}$ decrease significantly faster for large center-of-mass energies, are at the per cent level for $\sqrt{s} = 1500\,\mathrm{GeV}$, and come close to zero at $\sqrt{s} = 3000\,\mathrm{GeV}$. This is due to the non-resonant irreducible background and interference contributions that grow with energy relative to the $\mathrm{t}\bar{\mathrm{t}}$ signal contribution, which receives purely positive corrections. Our results suggest that at $\sqrt{s} = 800\,\mathrm{GeV}$, positive corrections to the signal process and

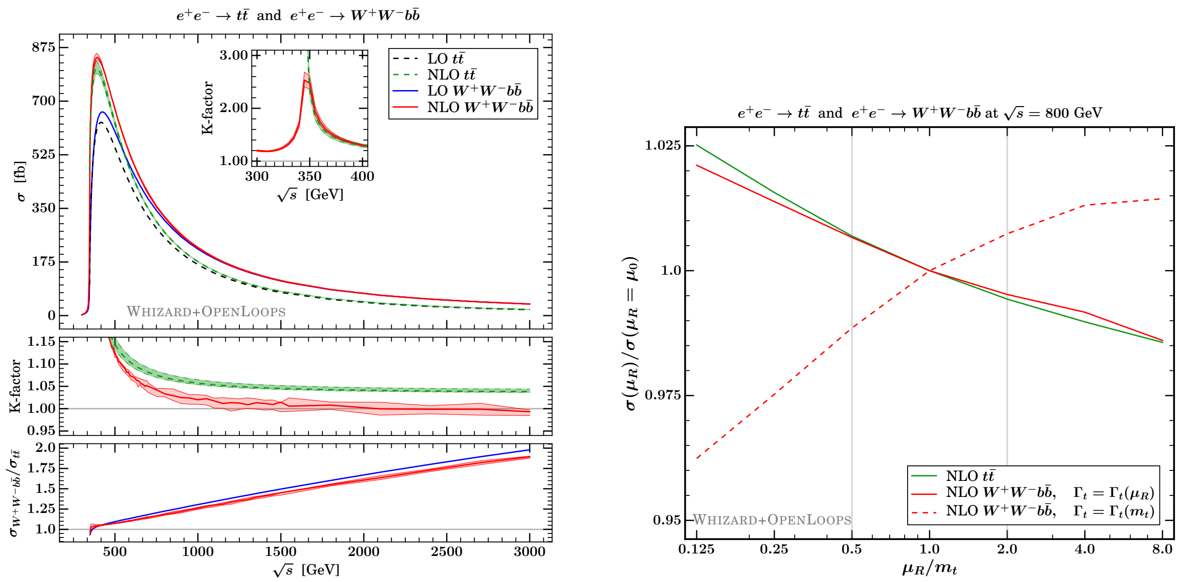

Figure 5.1 Total cross section for on-shell and off-shell $\mathrm{t\bar{t}}$ production as a function of $\sqrt{s}$ and μ_R. In the lower panels of the left plot, we show the K-factor for $\mathrm{t\bar{t}}$ and $\mathrm{W^+W^-b\bar{b}}$ in green and red, respectively, as well as the ratio of off-shell to on-shell results for LO and NLO in blue and red.

negative corrections to the background are of the same order of magnitude and partially cancel each other. This leads to very small NLO QCD corrections. However, at this level the currently unknown and possibly large NLO EW corrections to $\mathrm{e^+e^-} \to \mathrm{W^+W^-b\bar{b}}$ have to be included as well for reliable predictions. Comparing off-shell to on-shell cross sections, we see that they are roughly equal at threshold, but at $\sqrt{s} = 800\,\mathrm{GeV}$ the off-shell prediction is about 20% larger.

In the right panel of Fig. 5.1 we show the variation of the $\mathrm{e^+e^-} \to \mathrm{t\bar{t}}$ and $\mathrm{e^+e^-} \to \mathrm{W^+W^-b\bar{b}}$ NLO predictions with respect to the renormalization scale μ_R for $\sqrt{s} = 800\,\mathrm{GeV}$ in the interval $\mu_\mathrm{R} = [1/8, 8] \cdot m_\mathrm{t}$. Within the error band $[m_\mathrm{t}/2, 2m_\mathrm{t}]$ predictions for $\mathrm{t\bar{t}}$ and $\mathrm{W^+W^-b\bar{b}}$ with fixed top-quark width, $\Gamma_\mathrm{t} = \Gamma_\mathrm{t}(\mu_\mathrm{R} = m_\mathrm{t})$, vary at the level of a few per cent, however with an opposite slope. To understand this behavior, we show the scale variation of the off-shell process additionally with a scale-dependent width, $\Gamma_\mathrm{t}(\mu_\mathrm{R})$. With such a consistent setting of the width according to the input parameters, including μ_R, scale variations in the off-shell process are very similar to the on-shell one. We note that the scale dependence in the top width is in principle a higher-order effect, such that both approaches are viable to estimate missing higher order effects by means of scale variations. However, in order to properly recover the narrow width limit, the parameter settings for the width in the propagator and the decay part of the matrix element have to match, including the scale setting.

Inclusive cross sections for Higgs associated top-pair production are shown in the left panel of Fig. 5.2. The absolute maximum of the cross sections is located at around $\sqrt{s} = 800\,\mathrm{GeV}$, i.e. far above the production threshold at $2m_\mathrm{t} + m_\mathrm{H} \approx 471\,\mathrm{GeV}$, where $\sigma_\mathrm{incl.}(\sqrt{s} =$

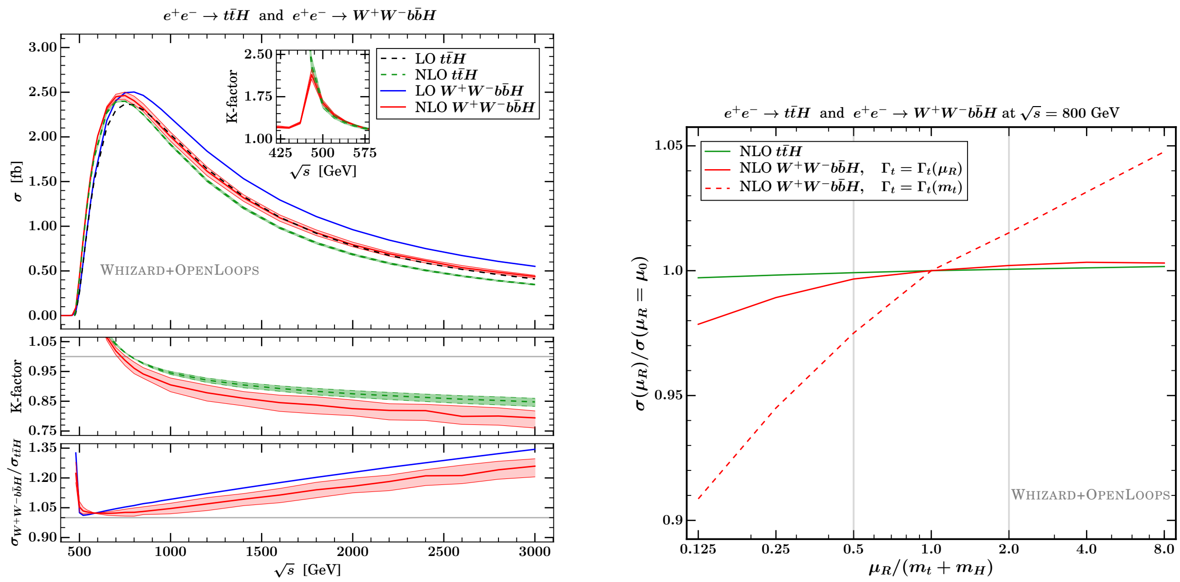

Figure 5.2 Total cross section of on-shell and off-shell $t\bar{t}H$ production subject to $\sqrt{s}$ and μ_R. Extra panels as in Fig. 5.1.

800 GeV) $\approx$ 2.4 fb. Again, NLO QCD corrections are sizable due to nonrelativistic Coulomb enhancements close to the production threshold. For the off-shell process $e^+e^- \to W^+W^-b\bar{b}H$ the corrections reach +100 % and remain large but finite below threshold, while for the on-shell process they diverge close to threshold. Around the maximum of the cross sections, NLO corrections vanish for both, the on-shell and the off-shell process. Above this maximum, the NLO corrections turn negative, yielding corrections at $\sqrt{s} = 3000$ GeV of up to −15 % for the on-shell process $e^+e^- \to t\bar{t}H$ and up to −20 % for the off-shell process $e^+e^- \to W^+W^-b\bar{b}H$. Again one should also consider how the off-shell cross sections behave relative to their on-shell counterparts. While at LO the $e^+e^- \to W^+W^-b\bar{b}H$ cross section decreases considerably slower with energy compared to the on-shell process $e^+e^- \to t\bar{t}H$, at NLO the corrections to the off-shell process are more sizable and negative with respect to the on-shell case, yielding comparable inclusive cross sections for the on-shell and off-shell process. Still, at 3000 GeV the off-shell inclusive cross section is about 20 % smaller than the on-shell one.

In the right panel of Fig. 5.2, we display renormalization scale variations at $\sqrt{s} = 800$ GeV for Higgs associated top-pair production. For this center-of-mass energy scale variation uncertainties in $e^+e^- \to t\bar{t}H$ are negligible (induced by vanishing NLO QCD corrections), while in $e^+e^- \to W^+W^-b\bar{b}H$ with the standard choice $\Gamma_t = \Gamma_t(\mu_R = m_t)$ they amount to several per cent in the considered variation band. Similar to the $t\bar{t}$ case, we also show scale variations taking consistently into account the scale dependence in the top-quark width. With this, the behavior of the off-shell process is very similar to the on-shell one.

Finally, we list inclusive cross sections for $t\bar{t}$ and $t\bar{t}H$ (both on- and off-shell) processes, respectively, for several representative center-of-mass energies in Tables 5.1 and 5.2. Listed uncertainties are results of scale variations with a factor of two, where we employ the fixed

Table 5.1 LO and NLO inclusive cross sections and K-factors for $\mathrm{e^+e^-} \to \mathrm{t\bar{t}}$ and $\mathrm{e^+e^-} \to \mathrm{W^+W^-b\bar{b}}$ for various center-of-mass energies. Uncertainties at NLO are due to scale variation.

	$\mathrm{e^+e^-} \to \mathrm{t\bar{t}}$			$\mathrm{e^+e^-} \to \mathrm{W^+W^-b\bar{b}}$		
$\sqrt{s}$[GeV]	σ^{LO}[fb]	σ^{NLO}[fb]	K-factor	σ^{LO}[fb]	σ^{NLO}[fb]	K-factor
500	548.4	$627.4^{+1.4\%}_{-0.9\%}$	1.14	600.7	$675.1^{+0.4\%}_{-0.8\%}$	1.12
800	253.1	$270.9^{+0.8\%}_{-0.4\%}$	1.07	310.2	$320.7^{+1.1\%}_{-0.7\%}$	1.03
1000	166.4	$175.9^{+0.7\%}_{-0.3\%}$	1.06	217.2	$221.6^{+1.1\%}_{-1.0\%}$	1.02
1400	86.62	$90.66^{+0.6\%}_{-0.2\%}$	1.05	126.4	$127.9^{+0.7\%}_{-1.5\%}$	1.01
3000	19.14	$19.87^{+0.5\%}_{-0.2\%}$	1.04	37.89	$37.63^{+0.4\%}_{-0.9\%}$	0.993

Table 5.2 LO and NLO inclusive cross sections and K-factors for $\mathrm{e^+e^-} \to \mathrm{t\bar{t}H}$ and $\mathrm{e^+e^-} \to \mathrm{W^+W^-b\bar{b}H}$ for various center-of-mass energies. Uncertainties at NLO are due to scale variation.

	$\mathrm{e^+e^-} \to \mathrm{t\bar{t}H}$			$\mathrm{e^+e^-} \to \mathrm{W^+W^-b\bar{b}H}$		
$\sqrt{s}$[GeV]	σ^{LO}[fb]	σ^{NLO}[fb]	K-factor	σ^{LO}[fb]	σ^{NLO}[fb]	K-factor
500	0.26	$0.42^{+3.6\%}_{-3.1\%}$	1.60	0.27	$0.44^{+2.6\%}_{-2.4\%}$	1.63
800	2.36	$2.34^{+0.1\%}_{-0.1\%}$	0.99	2.50	$2.40^{+2.1\%}_{-1.9\%}$	0.96
1000	2.02	$1.91^{+0.5\%}_{-0.5\%}$	0.95	2.21	$2.00^{+2.5\%}_{-2.5\%}$	0.90
1400	1.33	$1.21^{+0.9\%}_{-1.0\%}$	0.90	1.53	$1.32^{+2.6\%}_{-3.0\%}$	0.86
3000	0.41	$0.35^{+1.4\%}_{-1.8\%}$	0.84	0.55	$0.44^{+2.9\%}_{-4.3\%}$	0.79

top-width, $\Gamma_\mathrm{t} = \Gamma_\mathrm{t}(\mu_\mathrm{R} = m_\mathrm{t})$. In Section 5.2, we will continue our discussion of NLO corrections to top-pair and Higgs associated top-pair production at the differential level. There, we will focus on $\sqrt{s} = 800\,\mathrm{GeV}$, to maximize cross sections for $\mathrm{t\bar{t}H}$ production, which should offer the best condition for a precise determination of the top Yukawa coupling, as discussed in the following section. While we consider this as a viable running scenario for a precision measurement, one should keep in mind that for other energies the NLO QCD corrections will be larger in general, at least at the inclusive level.

5.1.2 Determination of the top Yukawa coupling

A precise measurement of Higgs associated top-pair production allows for the direct determination of the top-quark Yukawa coupling y_t at the per cent level [30, 31]. With this, many new physics models can be tested, as significant deviations from the Standard Model value $y_\mathrm{t}^\mathrm{SM} = \sqrt{2}m_\mathrm{t}/v$ are predicted, e.g. in generic two Higgs-doublet models, the MSSM or composite Higgs as well as Little Higgs models. A per cent level measurement of y_t is feasible at future high-energy lepton colliders, as the ttH and $\mathrm{W^+W^-b\bar{b}H}$ cross sections are very sensitive to y_t. The sensitivity of the $\mathrm{t\bar{t}H}$ processes (on- and off-shell) on y_t is commonly expressed in terms of [31, 223]

$$\frac{\Delta y_\mathrm{t}}{y_\mathrm{t}} = \kappa \frac{\Delta\sigma}{\sigma}. \tag{5.2}$$

In this way, the relative accuracy on the measured cross section can be directly translated to a relative accuracy on the top Yukawa coupling. Since the y_t-dependence of the cross section is approximately quadratic, κ is close to 0.5. More precisely, parameterizing deviations of the top-Yukawa coupling from its SM value as $y_\mathrm{t} = \xi_\mathrm{t} \cdot y_\mathrm{t}^\mathrm{SM}$, we can write the total cross section as $\sigma(\xi_\mathrm{t}) = \xi_\mathrm{t}^2 \cdot S + \xi_\mathrm{t} \cdot I + B$. Hereby, S and B denote $\mathrm{t\bar{t}H}$ signal[1] and background contributions, respectively, while I stands for interference terms. The y_t-sensitivity of $\mathrm{t\bar{t}H}$ cross sections can be determined with a linear fit of $\sigma(y_\mathrm{t})$, which corresponds to

$$\kappa = \lim_{\xi_\mathrm{t}\to 1} \sigma(\xi_\mathrm{t}) \left[\frac{\mathrm{d}\sigma(\xi_\mathrm{t})}{\mathrm{d}\xi_\mathrm{t}}\right]^{-1} = \frac{S+I+B}{2S+I} = \frac{1}{2} + \frac{I/2+B}{2S+I}. \tag{5.3}$$

Note that whereas B and S are strictly positive, we can make no statement about the sign of I. A reasonable assumption is that the signal is larger than half the interference, i.e. $|I| < 2\,|S|$. Thus, Eq. (5.3) shows that $\kappa < 0.5$ can only be realized via sufficiently large and negative interference contributions, $I < -2B$. From the above reasoning, we see that κ quantifies the contamination from the Higgsstrahlung subprocess in $\mathrm{e^+e^-} \to \mathrm{t\bar{t}H}$, and, for off-shell processes, of any additional background subprocess, including contributions

[1] More precisely, the S term corresponds to squared $e^+e^- \to \mathrm{t\bar{t}H}$ amplitudes, excluding Higgsstrahlung contributions.

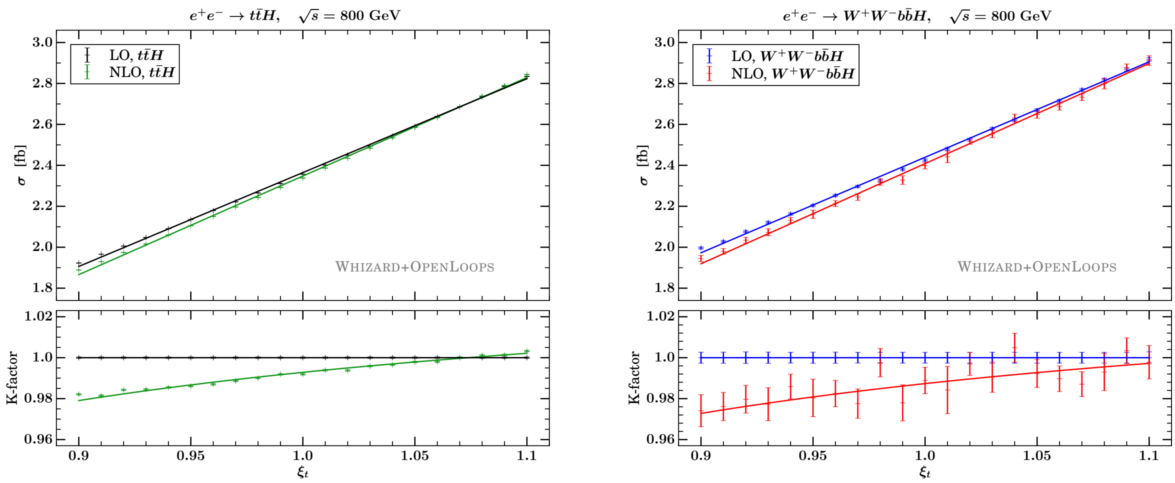

Figure 5.3 The $\mathrm{e^+e^-} \to \mathrm{t\bar{t}H}$ and $\mathrm{e^+e^-} \to \mathrm{W^+W^-b\bar{b}H}$ LO and NLO cross sections as a function of the top Yukawa coupling modifier $\xi_\mathrm{t} = y_\mathrm{t}/y_\mathrm{t}^\mathrm{SM}$, as well as a linear fit used to determine the coefficient κ as described in the text.

proportional to the HWW coupling.

In Tab. 5.3, we list the values of κ corresponding to the LO and NLO fits shown in Fig. 5.3. As expected, all listed κ-values are close to 0.5. For $\mathrm{e^+e^-} \to \mathrm{t\bar{t}H}$ at LO,

Table 5.3 The parameter κ as defined in Eq. (5.3) for $\mathrm{e^+e^-} \to \mathrm{t\bar{t}H}$ and $\mathrm{e^+e^-} \to \mathrm{W^+W^-b\bar{b}H}$ at LO and NLO for $\sqrt{s} = 800\,\mathrm{GeV}$.

$\mathrm{e^+e^-} \to$	κ^LO	κ^NLO	$\kappa^\mathrm{NLO}/\kappa^\mathrm{LO}$
$\mathrm{t\bar{t}H}$	0.514	0.485	0.943
$\mathrm{W^+W^-b\bar{b}H}$	0.520	0.497	0.956

the Higgsstrahlung contribution induces a value of $\kappa > 0.5$. For the off-shell process $\mathrm{e^+e^-} \to \mathrm{W^+W^-b\bar{b}H}$ we observe a slightly larger value compared to the on-shell process, originating from additional irreducible backgrounds. The NLO QCD corrections to κ turn out to be significant. They decrease κ by 5.7 % and 4.4 % compared to LO for the on- and off-shell case, respectively. This can be understood from a different behavior of the signal and background contributions with respect to QCD corrections. From Tab. 5.3 we can infer that at NLO interference terms are indeed negative for the on-shell $\mathrm{t\bar{t}H}$ process.

The sensitivity formula, Eq. (5.3), can be used to assess the impact of perturbative corrections on the extraction of y_t. This is roughly half as large as the corrections reported in Fig. 5.2. As already observed at the cross section level, the shifts in the extracted y_t value that result from the inclusion of NLO corrections and off-shell contributions have comparable size and opposite sign. The magnitude of the individual effects amounts to a few per cent at 800 GeV and grows up to about 10% at full CLIC energy. These results are now being used for the determination of the potential of the CLIC experiment to measure the top Yukawa coupling [224].

5.1.3 Polarization effects

Table 5.4 LO and NLO inclusive cross sections for $e^+e^- \to t\bar{t}$ with possible ILC beam polarization settings at $\sqrt{s} = 800$ GeV and 1500 GeV.

		$\sqrt{s} = 800$ GeV			$\sqrt{s} = 1500$ GeV		
$P(e^-)$	$P(e^+)$	σ^{LO}[fb]	σ^{NLO}[fb]	K-factor	σ^{LO}[fb]	σ^{NLO}[fb]	K-factor
0%	0%	253.7	272.8	1.075	75.8	79.4	1.049
−80%	0%	176.5	190.0	1.077	98.3	103.1	1.049
80%	0%	176.5	190.0	1.077	53.2	55.9	1.049
−80%	30%	420.8	452.2	1.074	124.9	131.0	1.048
−80%	60%	510.7	548.7	1.074	151.6	158.9	1.048
80%	−30%	208.4	224.5	1.077	63.0	66.1	1.049
80%	−60%	240.3	258.9	1.077	72.7	76.3	1.049

Table 5.5 LO and NLO inclusive cross sections for $e^+e^- \to t\bar{t}H$ with possible ILC beam polarization settings at $\sqrt{s} = 800$ GeV and 1500 GeV.

		$\sqrt{s} = 800$ GeV			$\sqrt{s} = 1500$ GeV		
$P(e^-)$	$P(e^+)$	σ^{LO}[fb]	σ^{NLO}[fb]	K-factor	σ^{LO}[fb]	σ^{NLO}[fb]	K-factor
0%	0%	2.358	2.337	0.991	1.210	1.064	0.879
−80%	0%	1.583	1.571	0.992	1.576	1.381	0.876
80%	0%	1.584	1.571	0.992	0.843	0.746	0.885
−80%	30%	3.988	3.950	0.990	2.003	1.757	0.877
−80%	60%	4.840	4.795	0.991	2.429	2.128	0.876
80%	−30%	1.860	1.846	0.992	0.996	0.879	0.883
80%	−60%	2.134	2.120	0.993	1.148	1.018	0.886

We complete our study of inclusive cross sections of top-pair and Higgs associated top-pair production with an investigation of possible beam polarization effects on these processes. Beam polarization is a powerful tool at linear colliders to disentangle contributing couplings and to reduce backgrounds [225, 226] or improve the measurement of the top Yukawa coupling [31]. In Tables 5.4 and 5.5, inclusive LO and NLO cross sections are listed with different polarization settings as suggested by the favored ILC running scenarios [227]. We show this for two different collider energies and both on-shell processes: $\mathrm{e^+e^-} \to \mathrm{t\bar{t}}$ and $\mathrm{e^+e^-} \to \mathrm{t\bar{t}H}$. While the cross sections vary strongly with the beam polarization, the K-factors are unaffected. These results confirm the expectation that NLO QCD corrections fully factorize with respect to the beam polarization due to the uncolored initial state. On the other hand, one can view the constant K-factors in Tables 5.4 and 5.5 as validation of the polarization dependent Whizard-OpenLoops-interface via BLHA extension. The factorization also holds when top-quark decays are considered and we refrain from showing polarized cross sections for off-shell processes.

5.2 Numerical predictions for differential distributions

Leptonic $\mathrm{t\bar{t}}$ and $\mathrm{t\bar{t}H}$ production and decay are fairly similar in various distributions. Therefore, a sound understanding of $\mathrm{t\bar{t}}$ production and decay in the continuum, where a large amount of data can easily be accumulated, is very useful for precision measurements of the top Yukawa coupling in the $\mathrm{e^+e^-} \to \mathrm{t\bar{t}H}$ process. In this section, we discuss differential predictions for $\mathrm{e^+e^-} \to \mathrm{t\bar{t}}$ and $\mathrm{e^+e^-} \to \mathrm{t\bar{t}H}$ at $\sqrt{s} = 800\,\mathrm{GeV}$ including NLO QCD corrections and off-shell effects in the decays. We also present predictions for the forward-backward asymmetry in $\mathrm{e^+e^-} \to \mathrm{t\bar{t}}$.

5.2.1 Off-shell top-pair production

We start our analysis of differential distributions for top-pair production and decay with the top-quark transverse momentum distribution in Fig. 5.4. We show it for the on-shell process $\mathrm{e^+e^-} \to \mathrm{t\bar{t}}$ and the corresponding off-shell process $\mathrm{e^+e^-} \to \mu^+\nu_\mu \mathrm{e}^-\bar{\nu}_\mathrm{e}\mathrm{b\bar{b}}$ including leptonic decays. For the latter, the top quark is reconstructed from its leptonic decay products at MC truth level, i.e. $p_{\mathrm{T},W^+\mathrm{j_b}} = p_{\mathrm{T},\ell^+\nu\mathrm{j_b}}$. Obviously, the two distributions are very differently normalized, as the on-shell process does not include the leptonic branching ratio. Apart from this, the LO and NLO shapes are very similar below the Jacobian peak located at around 350 GeV. The main effect, hereby, is a kinematic shift induced by real gluon radiation, which leads to an decrease of the peak and an increase for the lower p_T tail. Specifically, this yields corrections at the level of $-20\,\%$ at the peak and around $+20\,\%$ below the peak.

For the on-shell process, the phase-space above the Jacobian peak is kinematically not allowed at LO and gets only sparsely populated at NLO. In contrast, for the off-shell process this kinematic regime is allowed already at LO but at NLO the mentioned shift reduces the number of possible configurations. The observed sizable corrections in the

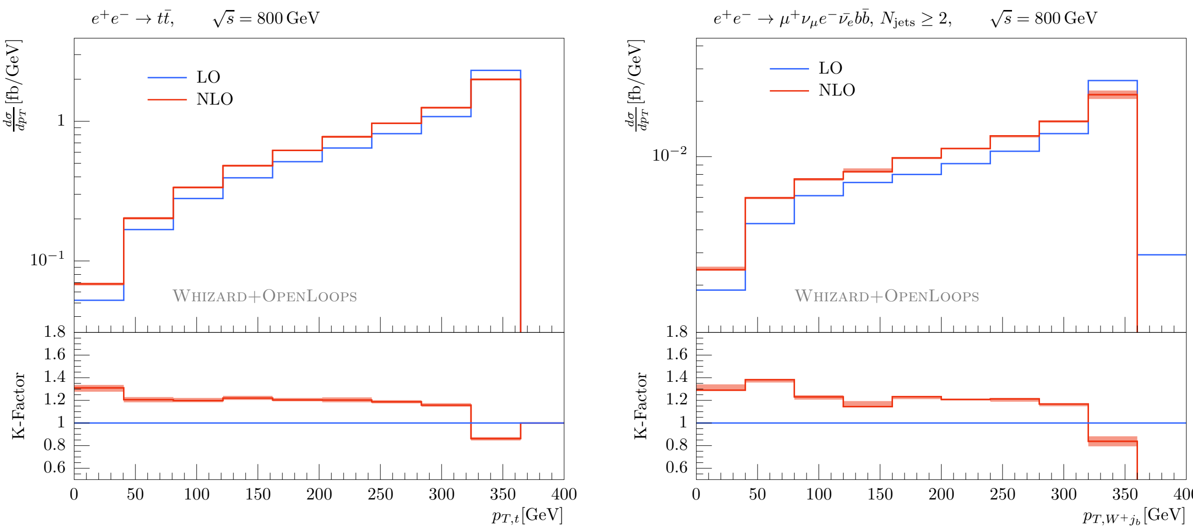

Figure 5.4 Differential distributions in the transverse momentum of the top quark in $\mathrm{e^+e^-} \to \mathrm{t\bar{t}}$ (left) and the reconstructed top quark in $\mathrm{e^+e^-} \to \mu^+\nu_\mu \mathrm{e}^-\bar{\nu}_\mathrm{e}\mathrm{b\bar{b}}$ (right). Shown are LO (blue) and NLO (red) predictions together with the corresponding K-factors and NLO scale uncertainties.

transverse momentum of the intermediate top quarks also translate into relevant corrections in the directly observable transverse momentum of the final state leptons, as shown in appendix C.1 (Fig. C.1). Namely, we find corrections of about $-30\,\%$ to $+15\,\%$ and $-20\,\%$ to $+10\,\%$ for the hardest and second hardest lepton, respectively, with an increase for low and a decrease for high p_T. In a realistic setup, where experimental selection cuts have to be applied on the leptons, such effects become also relevant for fiducial cross sections in precision top physics.

Experimentally, $p_{\mathrm{T},W^+\mathrm{j_b}}$ is not directly measurable in the considered leptonic decay mode: the top quark cannot be exactly reconstructed due to the two invisibly escaping neutrinos. As a proxy however, we can construct and measure the transverse momentum of the b-jet–lepton system, $p_{\mathrm{T},\ell^+\mathrm{j_b}}$. We show the corresponding predictions for $\mathrm{e^+e^-} \to \mu^+\nu_\mu \mathrm{e}^-\bar{\nu}_\mathrm{e}\mathrm{b\bar{b}}$ in Fig. 5.5 (left). Here, we also observe a tilt of the NLO shape with respect to the LO one, yielding corrections up to $20\,\%$ for small $p_{\mathrm{T},\ell^+\mathrm{j_b}}$ and up to $-40\,\%$ for large $p_{\mathrm{T},\ell^+\mathrm{j_b}}$. In contrast, the transverse momentum distribution of the $\mathrm{j_b}$–$\mathrm{j_{\bar{b}}}$ system, as shown on the right of Fig. 5.5, only receives mild QCD corrections at the level of $10\,\%$.

One of the observables of prime interest is the kinematic mass of the top resonance. In Fig. 5.6, we show on the left the reconstructed invariant top-quark mass, $m_{W^+\mathrm{j_b}} = m_{\ell^+\nu\mathrm{j_b}}$, where the $\ell^+\nu\mathrm{j_b}$ system is fully reconstructed. At LO and close to the peak, this distribution corresponds to the Breit-Wigner that arises due to the propagator. Off-shell effects and non-resonant contributions become visible a couple of GeV away from the pole and tend to increase the background. At NLO, we observe a drastic shape distortion compared to LO, in particular below the resonance peak. These NLO shape distortions are very sensitive to the parameters of the employed jet algorithm. They can be attributed to QCD radiation

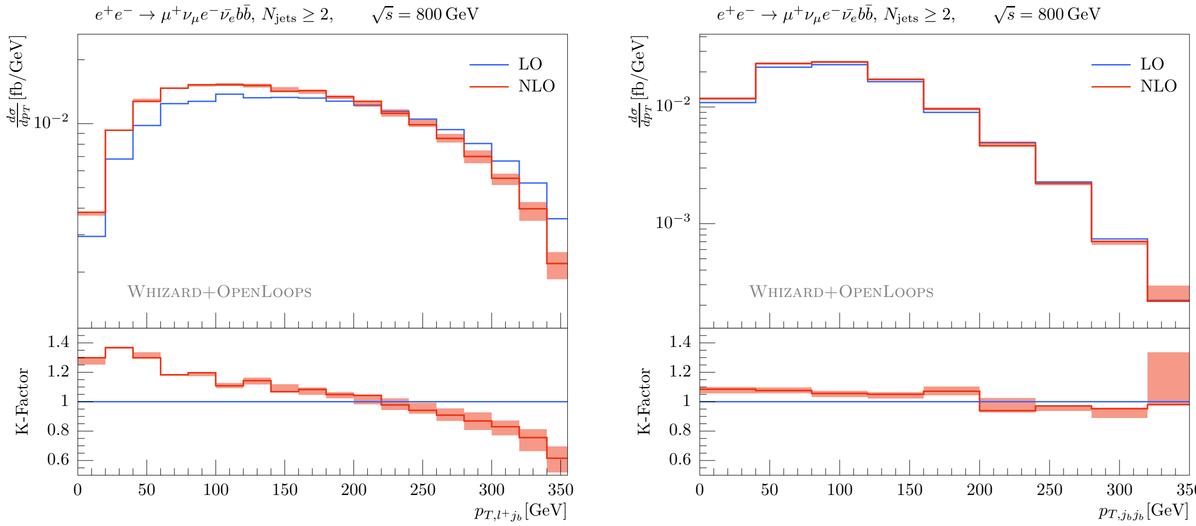

Figure 5.5 Transverse momentum distribution of the bottom-jet–lepton system (left), $p_{\mathrm{T},\ell^+\mathrm{j_b}}$, and of the $\mathrm{j_b}$–$\mathrm{j_{\bar{b}}}$ system (right), $p_{\mathrm{T,b\bar{b}}}$, in $\mathrm{e^+e^-} \to \mu^+\nu_\mu\mathrm{e}^-\bar{\nu}_\mathrm{e}\mathrm{b\bar{b}}$. Curves and bands as in Fig. 5.4.

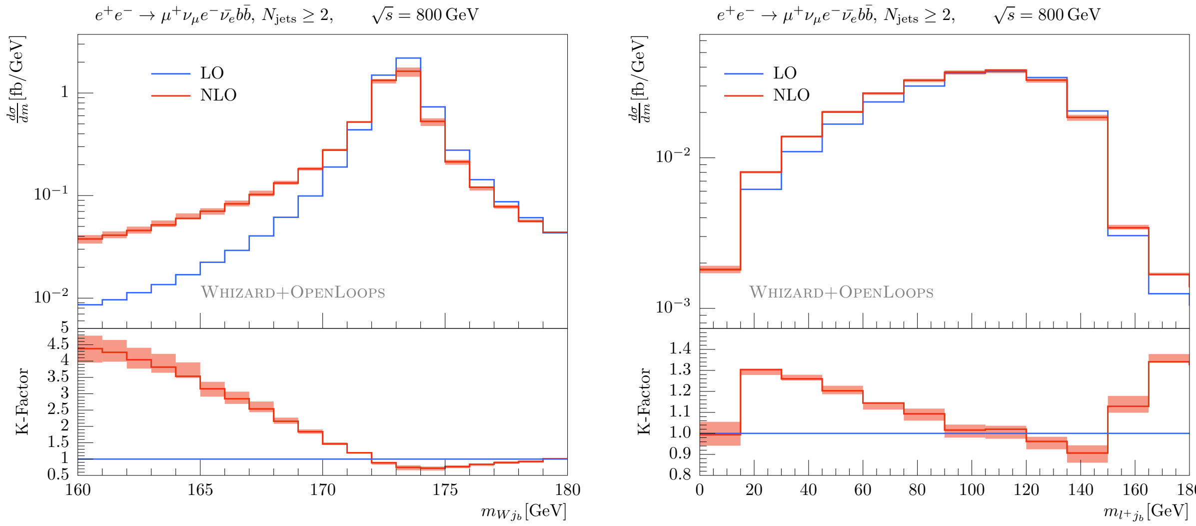

Figure 5.6 Reconstructed top invariant mass (left) and invariant mass of the b-jet–ℓ^+ system in $\mathrm{e^+e^-} \to \mu^+\nu_\mu\mathrm{e}^-\bar{\nu}_\mathrm{e}\mathrm{b\bar{b}}$. Curves and bands as in Fig. 5.4.

that escapes the b-jet. It thus forms either a separate light jet or is recombined with the other b-jet. The reconstructed invariant top-quark mass is thus significantly shifted towards lower values. Similar shape distortions have also been observed in Ref. [54] as well as at the LHC [228, 229].

Again, the perfectly reconstructed top-quark mass is not directly measurable due to the missing neutrinos. However, we can resort to the invariant mass of the b-jet and the associated charged lepton. In fact, this distribution can be used to measure the top-quark mass via [230–232]

$$m_{\mathrm{t}}^2 = m_{\mathrm{W}}^2 + \frac{2\langle m_{\ell \mathrm{j_b}}^2 \rangle}{1 - \langle \cos\theta_{\ell \mathrm{j_b}} \rangle}\,, \tag{5.4}$$

where $\langle m_{\ell \mathrm{j_b}}^2 \rangle$ and $\langle \cos\theta_{\ell \mathrm{j_b}} \rangle$ are the mean values of the corresponding invariant mass and angular distributions. Predictions for the $m_{\ell^+ \mathrm{j_b}}$ invariant mass distribution are shown on the right of Fig. 5.6. The position of the kinematic edge at around $m_{\ell^+ \mathrm{j_b}} \approx 150\,\mathrm{GeV}$ is unaffected by NLO QCD corrections. However, we observe significant shape effects below the edge with corrections varying between $-10\,\%$ and $+30\,\%$.

5.2.2 Forward-backward asymmetries

The top quark forward-backward asymmetry A_{FB} is defined as

$$A_{\mathrm{FB}} = \frac{\sigma(\cos\theta_{\mathrm{t}} > 0) - \sigma(\cos\theta_{\mathrm{t}} < 0)}{\sigma(\cos\theta_{\mathrm{t}} > 0) + \sigma(\cos\theta_{\mathrm{t}} < 0)}\,, \tag{5.5}$$

where θ_{t} is the angle between the positron beam axis and the outgoing top-quark. This asymmetry can be measured with a precision below 2% [225, 226]. The SM LO prediction for A_{FB} is non-zero due to interference contributions between s-channel Z- and γ^*-exchange in the dominant production process [233, 234]. Various new physics models can substantially alter the SM prediction (for an overview cf. [235]) and thus, a precise determination of A_{FB} serves as a stringent probe for new physics. [2]

In Fig. 5.7, we show the distribution of the angle of the (reconstructed) top quark with respect to the beam axis for on-shell top-pair production and the corresponding off-shell process $\mathrm{e}^+\mathrm{e}^- \to \mu^+\nu_\mu \mathrm{e}^-\bar{\nu}_{\mathrm{e}}\mathrm{b}\bar{\mathrm{b}}$. The prediction of a non-zero forward-backward asymmetry at lepton colliders is apparent in Fig. 5.7. The shape of this distribution is hardly affected by radiative corrections, which yield an almost constant K-factor of about 1.05. This is very promising for precision measurements of A_{FB} in the continuum. For $\cos\theta_{\mathrm{W}^+\mathrm{j_b}} \lesssim 0.75$, the angular distribution of the reconstructed top quark in $\mathrm{e}^+\mathrm{e}^- \to \mu^+\nu_\mu \mathrm{e}^-\bar{\nu}_{\mathrm{e}}\mathrm{b}\bar{\mathrm{b}}$ is very similar to the on-shell prediction. However, for $\cos\theta_{\mathrm{W}^+\mathrm{j_b}} \gtrsim 0.75$, there is an enhancement of events, which could stem from the single-top background. This has a significant effect

[2] As noted in Chapter 1, such an asymmetry can also be defined and measured at hadron colliders, where the dominant top-production channels are of QCD type, such that within the SM the LO forward-backward asymmetry is zero.

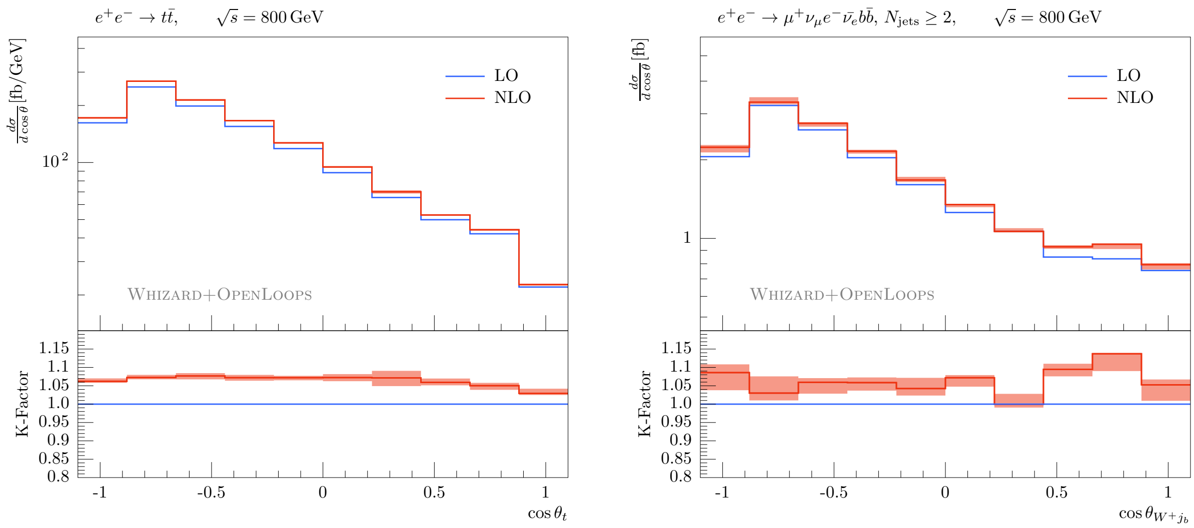

Figure 5.7 Differential distributions in the azimuthal angle of the top quark in $\mathrm{e}^+\mathrm{e}^- \to \mathrm{t}\bar{\mathrm{t}}$ (left) and $\mathrm{e}^+\mathrm{e}^- \to \mu^+\nu_\mu\mathrm{e}^-\bar{\nu}_\mathrm{e}\mathrm{b}\bar{\mathrm{b}}$ (right). Curves and bands as in Fig. 5.4.

Table 5.6 Forward-backward asymmetries of the top quark, A_{FB}, and the anti-top quark, $\bar{A}_{FB}$.

	$\mathrm{e}^+\mathrm{e}^- \to$	$A_{\mathrm{FB}}^{\mathrm{LO}}$	$A_{\mathrm{FB}}^{\mathrm{NLO}}$	$A_{\mathrm{FB}}^{\mathrm{NLO}}/A_{\mathrm{FB}}^{\mathrm{LO}}$
A_{FB}	$\mathrm{t}\bar{\mathrm{t}}$	-0.535	-0.539	1.013
	$\mathrm{W}^+\mathrm{W}^-\mathrm{b}\bar{\mathrm{b}}$	-0.428	-0.426	0.995
	$\mu^+e^-\nu_\mu\bar{\nu}_\mathrm{e}\mathrm{b}\bar{\mathrm{b}}$	-0.415	-0.409	0.986
	$\mu^+e^-\nu_\mu\bar{\nu}_\mathrm{e}\mathrm{b}\bar{\mathrm{b}}$, without neutrinos	-0.402	-0.387	0.964
$\bar{A}_{\mathrm{FB}}$	$\mathrm{t}\bar{\mathrm{t}}$	0.535	0.539	1.013
	$\mathrm{W}^+\mathrm{W}^-\mathrm{b}\bar{\mathrm{b}}$	0.428	0.426	0.995
	$\mu^+e^-\nu_\mu\bar{\nu}_\mathrm{e}\mathrm{b}\bar{\mathrm{b}}$	0.415	0.409	0.986
	$\mu^+e^-\nu_\mu\bar{\nu}_\mathrm{e}\mathrm{b}\bar{\mathrm{b}}$, without neutrinos	0.377	0.350	0.928

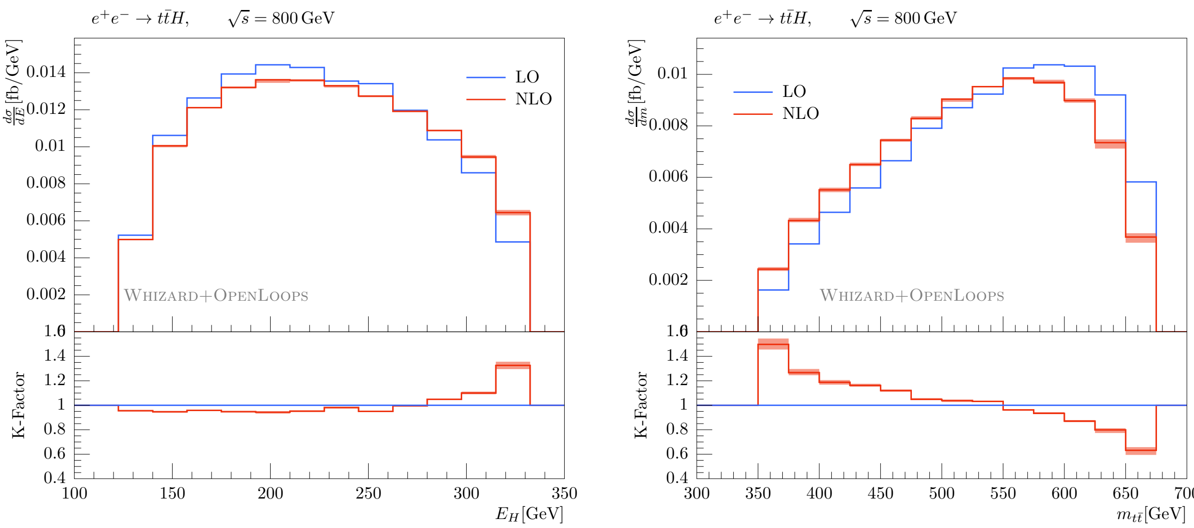

Figure 5.8 The energy of the Higgs boson, E_H, and the invariant mass of the top-quark pair, $m_{\mathrm{t}\bar{\mathrm{t}}}$, in $\mathrm{e}^+\mathrm{e}^- \to \mathrm{t}\bar{\mathrm{t}}\mathrm{H}$. Curves and bands as in Fig. 5.4.

on the reconstructed top forward-backward asymmetry, which is reduced by about 20 %, see the $\mathrm{e}^+\mathrm{e}^- \to \mu^+\nu_\mu\mathrm{e}^-\bar{\nu}_\mathrm{e}\mathrm{b}\bar{\mathrm{b}}$ and $\mathrm{e}^+\mathrm{e}^- \to \mathrm{W}^+\mathrm{W}^-\mathrm{b}\bar{\mathrm{b}}$ predictions in Tab. 5.6.

In Tab. 5.6, we list LO and NLO predictions for the forward-backward asymmetry A_FB (and the corresponding asymmetry for the anti-top quark), considering different treatments of the top-quark off-shellness. In $\mathrm{e}^+\mathrm{e}^- \to \mu^+\nu_\mu\mathrm{e}^-\bar{\nu}_\mathrm{e}\mathrm{b}\bar{\mathrm{b}}$, either the top-quark is reconstructed at MC truth level or the information of the neutrino momenta is dropped. NLO QCD corrections to A_FB are at a few per cent, which is small compared to the changes associated with increasing the final-state multiplicity and taking into account all off-shell and non-resonant effects. Note that if the neutrino momenta are omitted, the relation $A_\mathrm{FB} = -\bar{A}_{FB}$ is not fulfilled any more, both at LO and NLO. This can also observed directly in the angular distribution of ℓj_b-pairs, see Fig. C.2 in appendix C.1, where there is a slightly more pronounced dip at the lower edge of $\cos\theta_{\ell^- j_{\bar{\mathrm{b}}}}$ than at the one of $\cos\theta_{\ell^+ j_\mathrm{b}}$.

5.2.3 Off-shell Higgs associated top-pair production

We start our analysis of differential Higgs associated top-pair production by considering in Fig. 5.8 the energy of the Higgs boson, E_H, and the invariant mass of the $\mathrm{t}\bar{\mathrm{t}}$ system, $m_{\mathrm{t}\bar{\mathrm{t}}}$, in the on-shell process $\mathrm{e}^+\mathrm{e}^- \to \mathrm{t}\bar{\mathrm{t}}\mathrm{H}$. The energy of the Higgs boson is the key observable to identify $\mathrm{t}\bar{\mathrm{t}}$ threshold effects, and it is of great phenomenological relevance for realistic experimental analyses including Higgs boson decays. From the point of view of $\mathrm{t}\bar{\mathrm{t}}$ dynamics, the Higgs acts as a colorless recoiler, reducing the effective center-of-mass energy for the $\mathrm{t}\bar{\mathrm{t}}$ system.[3] For $m_{\mathrm{t}\bar{\mathrm{t}}} \to 2m_\mathrm{t} = 346.4\,\mathrm{GeV}$ the top-quark pairs are more and

[3]This is not strictly true for $\mathrm{b}\bar{\mathrm{b}}$ decays of the Higgs, where the colored final states can exchange gluons. However, these effects are strongly suppressed due to the extremely small Higgs width of 4.143 MeV.

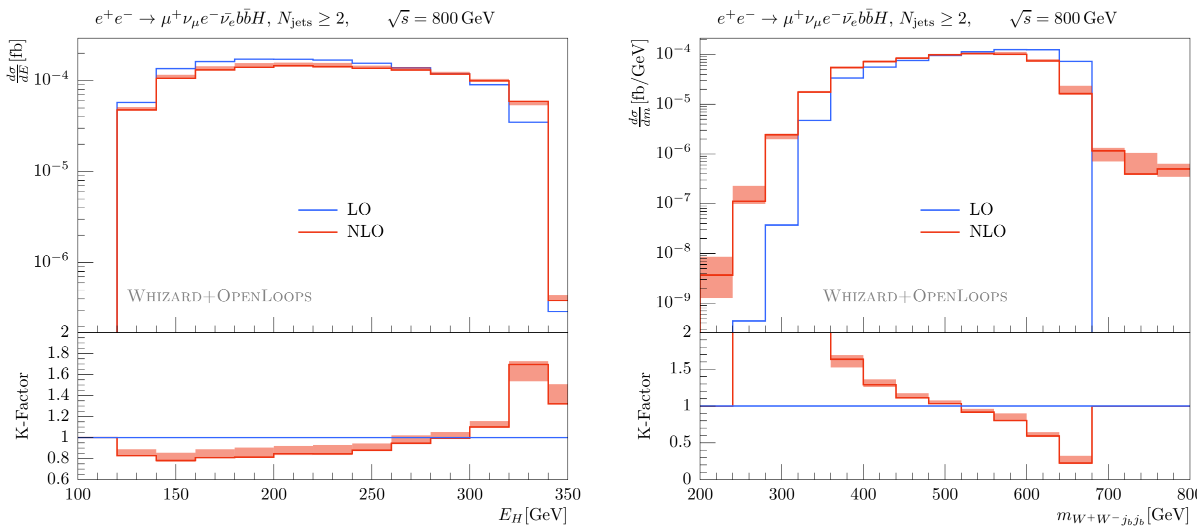

Figure 5.9 The energy of the Higgs boson, $E_{\rm H}$, and the invariant mass of the reconstructed top-quark pair, $m_{W^+W^-{\rm j_b j_{\bar{b}}}}$, in $\rm e^+e^- \to \mu^+\nu_\mu e^-\bar{\nu}_e b\bar{b}H$. Curves and bands as in Fig. 5.4.

more nonrelativistic, yielding large logarithmic enhancements in the loop matrix elements. The energy of the Higgs boson and the top-pair invariant mass are at LO directly related by

$$E_{\rm H} = \frac{1}{2\sqrt{s}}\left(s + m_{\rm H}^2 - m_{\rm t\bar{t}}^2\right) . \tag{5.6}$$

Thus, small $\rm t\bar{t}$ invariant masses correspond to large Higgs energies. And indeed, for large Higgs energies and small $m_{t\bar{t}}$, in Fig. 5.8 we observe sizable positive NLO QCD corrections up to +35% and +50% for the $E_{\rm H}$ and $m_{\rm t\bar{t}}$ distributions, respectively. Such large NLO QCD corrections should be resummed for a precise theoretical prediction.

For the on-shell process $\rm e^+e^- \to t\bar{t}H$, the lower kinematic bound of the $E_{\rm H}$ distribution is given by $E_{\rm H}^{\rm min} = m_{\rm H} = 125\,\text{GeV}$ and its upper bound by $E_{\rm H}^{\rm max} = 335\,\text{GeV}$, which follows from $m_{\rm t\bar{t}}^{\rm min} = 2m_{\rm t}$. Noteworthy, for small Higgs boson energies we observe an apparent mismatch of the NLO QCD corrections with respect to large top-pair masses. While for small Higgs boson energies the K-factor flattens out to an almost constant value of about 0.95, the K-factor for the top-pair invariant mass distribution monotonically decreases to a minimum value of about 0.60. This can be resolved by realizing that the Higgs boson energy distribution is a fully inclusive observable that is completely independent of the clustering applied to final state QCD radiation. On the other hand, the $m_{t\bar{t}}$ distribution does not include hard gluon radiation off the $\rm t\bar{t}$ system, while soft and collinear gluons are recombined with the top quarks. The resulting systematic shift in the $m_{t\bar{t}}$ distribution towards lower values results in the observed differences compared to the $E_{\rm H}$ distribution.

The corresponding distributions for the off-shell process $\rm e^+e^- \to \mu^+\nu_\mu e^-\bar{\nu}_e b\bar{b}H$ are shown in Fig. 5.9. Again, we observe a strong enhancement for large Higgs boson energies and small reconstructed top-pair masses, together with a strong suppression for large reconstructed top-pair masses. In contrast to the on-shell process, already at LO kinematic

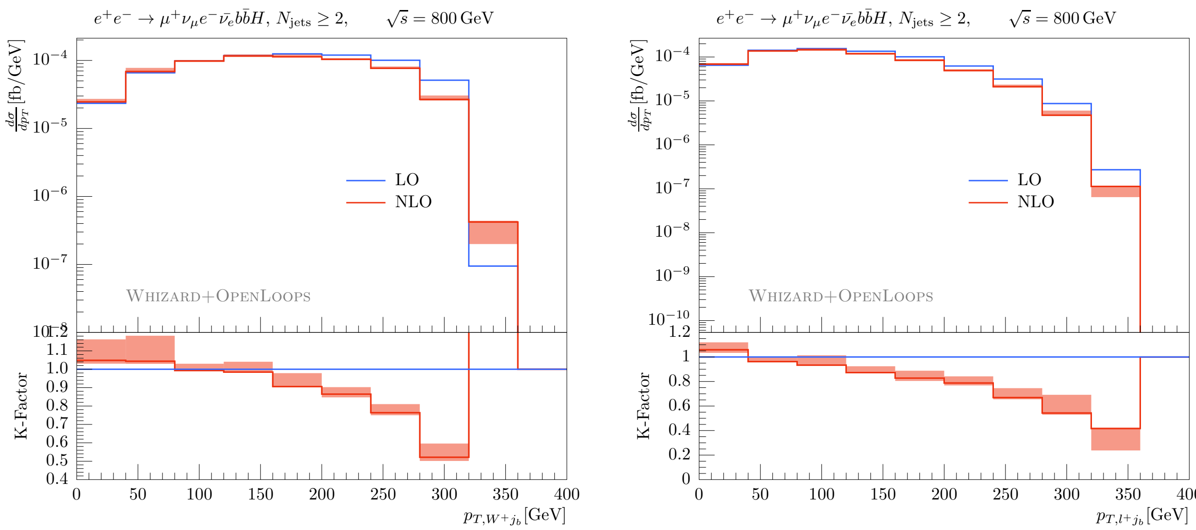

Figure 5.10 Transverse momentum distributions of the reconstructed top quark (left) and of the bottom-jet–lepton system (right), $p_{\mathrm{T},\ell^+\mathrm{j_b}}$, in $\mathrm{e^+e^-} \to \mu^+\nu_\mu\mathrm{e^-}\bar{\nu}_\mathrm{e}\mathrm{b\bar{b}H}$. Curves and bands as in Fig. 5.4.

boundaries are washed out due to off-shell and non-resonant contributions. In particular, the E_H distributions range to energies above 335 GeV, with sizable NLO corrections. The $m_{W^+W^-\mathrm{j_b j_{\bar{b}}}}$ distribution at LO falls off quickly below $m_{W^+W^-\mathrm{j_b j_{\bar{b}}}} = 2m_\mathrm{t}$, while at NLO it extends to very small values. As already discussed in the context of Fig. 5.6, this phase-space region is populated at NLO due to kinematic shifts of the reconstructed masses originating from the recombination of radiation from different stages of production and decay.

In Fig. 5.10, we show the transverse momentum distribution of the reconstructed top quark and the directly observable bottom-jet–lepton system in the off-shell process $\mathrm{e^+e^-} \to \mu^+\nu_\mu\mathrm{e^-}\bar{\nu}_\mathrm{e}\mathrm{b\bar{b}H}$. Comparing these distributions with the corresponding ones for top-pair production, shown in Fig. 5.4 and Fig. 5.5, we observe distinct shape differences. In this case, there is no Jacobian peak, which is related to $2 \to 2$-kinematics. Instead, we observe in the $p_{\mathrm{T},W^+\mathrm{j_b}}$ distribution a plateau between about 100 GeV and 250 GeV. At larger transverse momentum, the distribution drops sharply to its kinematical bound at around 325 GeV. NLO QCD corrections shift both the $p_{\mathrm{T},W^+\mathrm{j_b}}$ and the $p_{\mathrm{T},\ell^+\mathrm{j_b}}$ distribution towards smaller values inducing shape effects up to $-50\,\%$ at large $p_{\mathrm{T},W^+\mathrm{j_b}}$ and up to $-60\,\%$ at large $p_{\mathrm{T},\ell^+\mathrm{j_b}}$.

Finally, in Fig. 5.11 we turn to the reconstructed kinematic top mass, $m_{W^+\mathrm{j_b}}$, and its directly observable counterpart, $m_{\ell^+\mathrm{j_b}}$. We observe similar NLO shape distortions as already discussed in the case of top-pair production, shown in Fig. 5.6. For $m_{W^+\mathrm{j_b}} < m_\mathrm{t}$, i.e. below the top resonance, we observe a strong NLO enhancement that translates to $20\,\%$ shape corrections in the case of the $m_{\ell^+\mathrm{j_b}}$ distribution. As already noted before, the size of these corrections strongly depends on the details of the employed jet clustering. In

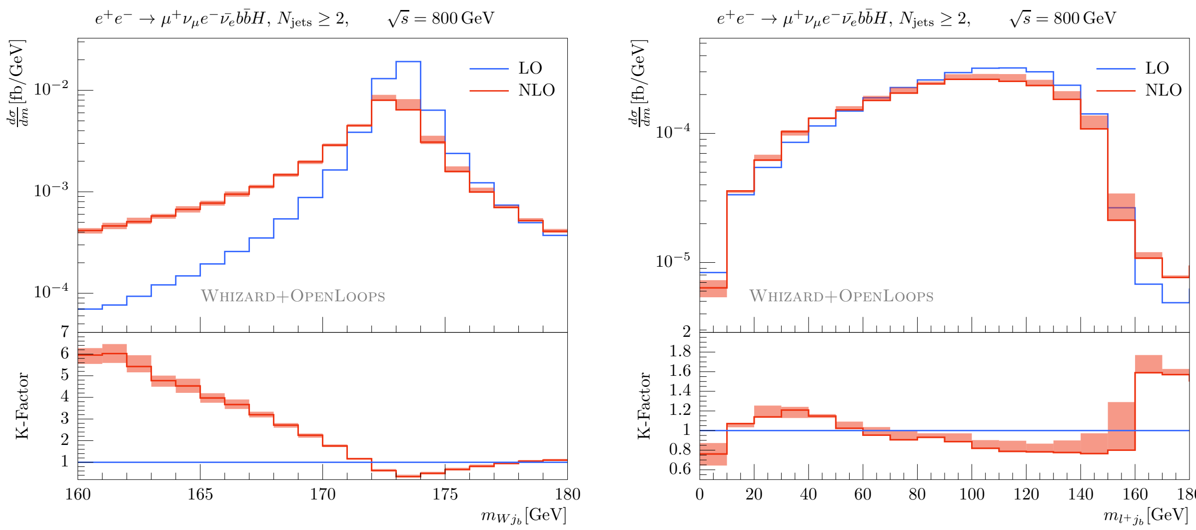

Figure 5.11 Reconstructed top invariant mass (left) and invariant mass distribution of the b-jet–ℓ^+ system (right) in $\mathrm{e^+e^-} \to \mu^+\nu_\mu \mathrm{e}^-\bar{\nu}_\mathrm{e}\mathrm{b\bar{b}H}$. Curves and bands as in Fig. 5.4.

Fig. C.3, we also show the distribution of the transverse momentum of the Higgs, $p_{\mathrm{T},H}$, which is, however, closely related to the energy, E_H, and shows the same physics.

5.3 Summary

In this part, we have presented the first major physics application of the Whizard NLO framework based on a process-independent interface between Whizard and the amplitude generator OpenLoops. We have performed a precision study for a future high-energy lepton collider considering for the first time at NLO QCD the processes $\mathrm{e^+e^-} \to \mu^+\nu_\mu\mathrm{e}^-\bar{\nu}_\mathrm{e}\mathrm{b\bar{b}}$ and $\mathrm{e^+e^-} \to \mu^+\nu_\mu\mathrm{e}^-\bar{\nu}_\mathrm{e}\mathrm{b\bar{b}H}$, i.e. off-shell top-pair and Higgs associated top-pair production. Finite-width effects for intermediate top quarks and W bosons, single-top and non-resonant contributions as well as their interferences together with spin correlations have been taken into account consistently at NLO.

We have presented a study of inclusive cross sections as a function of the center-of-mass energy considering different approximations for the top off-shellness and an in-depth study at the differential level for $\sqrt{s} = 800\,\mathrm{GeV}$. Off-shell effects play an important role even for the inclusive cross sections as the narrow-width approximation does not suffice to describe interference effects and background diagrams at energies far above threshold. NLO QCD corrections also influence the dependence of the cross section on the top Yukawa coupling for the $\mathrm{t\bar{t}H}$ processes, which has direct consequences for the achievable accuracy in measuring this coupling. In particular, we have shown that the NLO QCD corrections induce negative interference terms yielding a deviation from the quadratic Yukawa coupling dependence of the cross section ($\kappa^{\mathrm{NLO}} < 0.5$), both in the on-shell treatment of $\mathrm{t\bar{t}H}$ production and the corresponding off-shell process. In order to describe beam polarization, the BLHA for the interface between Whizard and OpenLoops was generalized. As expected, we found that beam polarization has no effect on the relative size of NLO QCD corrections. It is, however, important to incorporate polarization effects in the NLO framework of WHIZARD, as well as EW ISR and beamstrahlung, in order to allow for realistic MC simulations at a lepton collider.

In addition to these inclusive studies, NLO QCD effects on differential observables have been investigated. Our results show that NLO effects yield corrections at the $\mathcal{O}\,(20\,\%)$ level for most observables. Even larger corrections occur due to nonrelativistic top-threshold effects and below the top invariant mass peak. To obtain reliable predictions in the threshold region, a resummed calculation is required that is matched to the continuum computation. This will be the focus of the next part. Higgs observables are mostly unaffected by off-shell contributions and details of the pole mass, but can be influenced significantly by NLO QCD threshold corrections. Such observables can thus be used even at high-energies to perform precision measurements of short-distance top masses with the benefit of large data sets. Studying the top-quark forward-backward asymmetry, we found the effect of off-shell contributions dominating over NLO QCD corrections. This has to be stressed as the use of the on-shell NNLO computation for predicting A_{FB} and estimating the theory error thus systematically underestimates the physically more important off-shell effects, which have been presented in this part and which do not factorize with the QCD corrections.

Part III

Matching NLL threshold resummation to NLO QCD for off-shell $t\bar{t}$ production

Chapter 6

Motivation and setup of the computation

6.1 Introduction

As we have seen in the last chapter, QCD corrections can become large when heavy color-pairs are produced with little velocity. Reliable theory predictions in the threshold region crucially require the resummation of Coulomb singular $(\alpha_s/v)^n$ terms to all orders in perturbation theory. Here and throughout this part v denotes the nonrelativistic velocity of the top quarks. In the threshold region, we have $v \sim \alpha_s \sim 0.1$. Thus, each of the Coulomb terms $(\alpha_s/v)^n$ is of order one. This indicates that bound-state effects become important despite the fact that the top quarks decay before they can form a would-be toponium state. Note that this behavior is a result of the value of the top mass, m, and the top width, Γ. The resummation of the threshold enhanced terms is performed within the effective theory of nonrelativistic QCD (NRQCD) [236, 237], wherein hard gluon momenta of the hard scale m are integrated out. Then, a Schrödinger-type equation for the propagation of the top-antitop system has to be solved to obtain the corresponding Green's function. As we already mentioned in Chapter 1, the Coulomb resummation is so important that any fixed-order cross section at threshold has to include it for a reliable prediction, including additional corrections to the stated order.

The first predictions for top pair production at threshold given a large top width have already been computed in Ref. [238]. This has been followed by more detailed studies [239–241]. Inclusive NNLO calculations at threshold have been compared in Ref. [242]. The total production cross section is now known to NNNLO in the NRQCD expansion [57]. This has been achieved in a modified version of NRQCD, namely the potential NRQCD (pNRQCD) [243, 244], where one integrates out the soft modes of order mv. Besides the Coulomb singularities, large logarithms of the velocity $(\alpha_s \ln v)^n$ become sizable close to threshold. The systematic resummation of large logarithms is possible via (velocity) renormalization group (RG) equations in the velocity NRQCD (vNRQCD) [245–249] framework. Regarding RG improved predictions of $\mathrm{t\bar{t}}$ threshold production, the result of Ref. [250] is currently state of the art and is NNLL accurate for all practical purposes.

Schematically, we can write the normalized total cross section (R-Ratio) as

$$R = \frac{\sigma_{t\bar{t}}}{\sigma_{\mu^+\mu^-}} = v \sum_k \left(\frac{\alpha_s}{v}\right)^k \sum_i (\alpha_s \ln v)^i \times \\ \Big\{ 1\,(\mathrm{LL});\ \alpha_s, v\,(\mathrm{NLL});\ \alpha_s^2,\ \alpha_s v,\ v^2\,(\mathrm{NNLL});\ \ldots \Big\}. \quad (6.1)$$

The first factor of v emerges from the nonrelativistic phase space integration. In the respective fixed-order counting the sum over $(\alpha_s \ln v)^i$ is replaced by 1 as the logarithms in the velocity are not explicitely treated.

Above threshold, fixed-order full QCD corrections to the vector and axial-vector current contributions to (on-shell) $\mathrm{t\bar{t}}$ production have been computed inclusively to NNNLO [50, 251] and differentially to NNLO [51, 52], as discussed earlier. For the off-shell process (with $\mathrm{W^+W^-b\bar{b}}$ as final state) that is also defined below threshold, we have shown the NLO QCD results in the last part. As explained above, pure QCD fixed-order results without Coulomb resummation are, however, only reliable in the relativistic continuum sufficiently away from the $\mathrm{t\bar{t}}$ threshold. Thus, the current state of the art presents despite its sophistication some deficiencies. First of all, there is no quantitative analysis at which energy one is far enough away from threshold to justify using the pure fixed-order continuum result. Vice versa, it is not known how far one can trust a threshold computation moving away from the nonrelativistic limit. Thus, one has to first construct a matched computation for $\mathrm{e^+e^-} \to \mathrm{W^+W^-b\bar{b}}$ that combines the resummed with the fixed-order computation and is valid for all $\sqrt{s}$. This is especially important for the proposed 380 GeV stage of CLIC, where one could probe the threshold region due to radiation off the initial state. The convolution of theory threshold predictions with initial-state radiation and realistic beam spectra have been already studied in Ref. [25, 28]. Note, though, that these results are only reliable in case they are using the theory predictions solely in a small $\sim 10\,\mathrm{GeV}$ window around threshold, where the assumption that $v \sim \alpha_s$ holds. Given the spectrum of bremsstrahlung, it is questionable that this is possible without a matched prediction.

The next issue concerns the exclusiveness. While the $\mathrm{t\bar{t}}$ measurement can be fairly inclusive, the physical final states are still the leptonic, semi-leptonic and hadronic decay products. Therefore, any inclusive measurement will suffer from systematic uncertainties that result from the attempt to extrapolate the measured cross section in the fiducial phase space to the full phase space. These systematic uncertainties can only be reduced by providing improved theoretical predictions for the $\mathrm{W^+W^-b\bar{b}}$ final state. Off-shell effects at threshold have often been neglected or only computed approximately as they represent a subleading effect. Once electroweak corrections are included, the natural power counting near threshold is $v \sim \alpha_s \sim \sqrt{\alpha_{\mathrm{em}}}$. Non-resonant electroweak corrections to $\mathrm{W^+W^-b\bar{b}}$, i.e. where at least one of the top propagators is far off-shell or absent start to contribute at NLO [59, 60]. The $\mathcal{O}(\alpha_s)$ correction to this is thus a NNLO correction [61, 62, 252, 253]. We emphasize again that this counting is only sensible in the region of a couple of GeV around threshold where indeed $v \sim \alpha_s$. To improve the description of the top decay beyond the naive $E \to E + \mathrm{i}\Gamma_\mathrm{t}$ rule [238], one should take into account all aspects of the relativistic top decays, including the sizable QCD NLO corrections.

In this part, we address the issues mentioned above by providing a matched computation for $\mathrm{e}^+\mathrm{e}^- \to \mathrm{W}^+\mathrm{W}^-\mathrm{b}\bar{\mathrm{b}}$ correct to NLO in fixed-order QCD and NLL in vNRQCD. For this, we have to devise a master formula that *matches* the nonrelativistic computation in the threshold region with its relativistic counterpart in the continuum. Hereby, we maintain all irreducible backgrounds of $\mathrm{W}^+\mathrm{W}^-\mathrm{b}\bar{\mathrm{b}}$ also in the threshold region. We put additional emphasis on constructing a fully gauge-invariant result. To improve the description of the decay of the top pairs that are produced in vNRQCD, we apply an extended double-pole approximation that is also defined below the kinematical threshold. This allows us to compute the fixed-order QCD corrections to the decay as well. For a fully matched computation that is valid everywhere, we have to switch off unphysical terms in the resummed computation that result from the assumption that v is small. Usually, it suffices to only remove the double counting of fixed-order and resummed computation to achieve a reasonable matching, see e.g. Refs. [254, 255]. However, in the case of the top threshold at a lepton collider the nonrelativistic resummation is less of a refinement but more a completely different computation. For the threshold production of on-shell tops, the differential cross section in the top three momentum is available at NNLO [23]. This result is based on the numerical code Toppik. We also use this code in order to implement the Coulomb resummation in Whizard. First results of threshold resummation in Whizard have been presented in Ref. [58], which was, however, still based on a construction using signal diagrams.

The computation presented in this part obviously does not have the highest precision currently available for the fully inclusive $\mathrm{t}\bar{\mathrm{t}}$ result. For realistic final states and especially in the intermediate region between threshold and continuum, however, it represents the state of the art. In the nonrelativistic power counting, it contains various terms of NNLO and higher. Furthermore, it would be straightforward to augment our computation with a K-factor, $K^{\mathrm{NNLL}} = \sigma^{\mathrm{NNLL}}/\sigma^{\mathrm{NLL}}$, to increase the precision for inclusive observables.

We note that the authors of Ref. [256] have also embedded a numerical solution of the Bethe-Salpeter equation into a relativistic tree-level computation by weighting the cross section with a QCD correction factor while focusing on the CP properties in $\mathrm{t}\bar{\mathrm{t}}\mathrm{H}$. In Ref. [257], threshold effects have been incorporated in a MC simulation of kinematical distributions of top quarks at hadron colliders by multiplying signal diagrams with nonrelativistic Green functions. At hadron colliders, recently the on-shell process $\mathrm{t}\bar{\mathrm{t}}\mathrm{H}$ has been computed to NNLL, using soft-collinear effective theory (SCET) differentially [254] and with the direct QCD Mellin-space approach inclusively [255], and was matched to the NLO results similarly to our approach, i.e. the matched result is obtained by summing resummed and fixed-order results and subtracting the first order expansion of the resummed computation.

This part is structured as follows. In Section 6.2, we give an introduction into NRQCD as an effective field theory of QCD and summarize some basic results that are used in the following. The embedding of these results within the relativistic setting in WHIZARD is discussed in Section 6.3. In Section 7.1, we verify that this implementation works as expected by comparing to known results. Using this, we can discuss the necessary ingredients for the matching in Section 7.2 and study inclusive and differential results in Section 8.1 and Section 8.2, respectively.

6.2 Threshold resummation

6.2.1 vNRQCD

The effective Lagrangian of vNRQCD [245–249] contains heavy quark bilinear, soft, ultrasoft and potential terms. The leading bilinear terms in the quark field $\psi_{\boldsymbol{p}}$ are

$$\mathcal{L}(x) = \sum_{\boldsymbol{p}} \psi^\dagger_{\boldsymbol{p}}(x) \left(\mathrm{i}\partial^0 - \frac{\boldsymbol{p}^2}{2m} + \frac{\boldsymbol{p}^4}{8m^3} \right) \psi_{\boldsymbol{p}}(x) \;, \tag{6.2}$$

whereby a similar equation holds for the anti-quark field $\chi_{\boldsymbol{p}}$ and we abbreviate here and in the following

$$\boldsymbol{p} \equiv \boldsymbol{p}_t \;, \qquad p \equiv |\boldsymbol{p}| \;, \quad \text{and} \quad p_0 \equiv E_t - m \;. \tag{6.3}$$

The leading order potential includes the well-known Coulomb term

$$\mathcal{L}_{\text{pot}} = -\sum_{\boldsymbol{p},\boldsymbol{p}'} \frac{\mathcal{V}_c}{(\boldsymbol{p}-\boldsymbol{p}')^2} \psi^\dagger_{\boldsymbol{p}'} \psi_{\boldsymbol{p}} \chi^\dagger_{-\boldsymbol{p}'} \chi_{-\boldsymbol{p}} \quad \text{with} \quad \mathcal{V}_c = -4\pi C_F \alpha_s(m\nu) \;. \tag{6.4}$$

$\mathcal{V}_c$ is hereby the Coulomb Wilson coefficient for a color singlet heavy quark pair and ν is the vNRQCD velocity renormalization scale. The crucial feature of vNRQCD is that one is able to choose the $\overline{\text{MS}}$ subtraction scale for loop integrations over soft and potential momenta as μ_{S} separately from the integrations over ultrasoft momenta as μ_{U}. These two scales are inherently correlated through the quark equations of motion as they correspond to momentum (mv) and kinetic energy (mv^2), respectively. Eqs. (6.2) and (6.4) already yield the LL nonrelativistic top pair dynamics. The production and annihilation of top-antitop pairs is described by additional currents that connect to the electroweak production. The effect of the top decay can be incorporated in the effective Lagrangian by adding the bilinear operators [249]

$$\mathcal{L} = \sum_{\boldsymbol{p}} \psi^\dagger_{\boldsymbol{p}} \frac{\mathrm{i}}{2} \Gamma_{\mathrm{t}} \psi_{\boldsymbol{p}} + \sum_{\boldsymbol{p}} \chi^\dagger_{\boldsymbol{p}} \frac{\mathrm{i}}{2} \Gamma_{\mathrm{t}} \chi_{\boldsymbol{p}} \;, \tag{6.5}$$

which yields the shift of the energy by $\mathrm{i}\Gamma_t$. In this effective description, Γ_t is an input variable and can be set to the width computed in the SM with as many corrections as possible. In our computation, we describe the top decay fully differentially as discussed in Section 6.3, such that the width has to be set consistently with this description. We will use the same value of the top width in all parts of the computation.

6.2.2 Cross sections with the optical theorem

To validate the threshold resummation implemented in WHIZARD, we need inclusive results with the same accuracy. To this end, we use the computation that has been described in Ref. [59]. It relies on the use of the optical theorem, i.e. taking the imaginary part of the $\mathrm{e^+e^-} \to \mathrm{e^+e^-}$ forward scattering amplitude. This can be written as

$$\sigma_{\mathrm{tot}}(\mathrm{e^+e^-} \to \gamma^*/\mathrm{Z}^* \to \mathrm{t\bar{t}}) = \frac{4\pi\alpha^2}{3s}\left(f_v R_v + f_a R_a\right) \ , \tag{6.6}$$

where the f_v and f_a prefactors account for tree-level γ and Z exchange [249]. The vector and axial-vector R-ratios can be computed separately via

$$R^{v/a} = \frac{4\pi}{s}\mathrm{Im}\left[-\mathrm{i}\int \mathrm{d}^4x\, \mathrm{e}^{\mathrm{i}qx}\left\langle 0 \,\middle|\, \mathrm{T} j_\mu^{v/a}(x) j^{v/a\,\mu}(0) \,\middle|\, 0\right\rangle\right] \ , \tag{6.7}$$

with $q = (\sqrt{s}, \mathbf{0})$ and $j_\mu^{v/a}$ the vector/axial-vector current that produces a quark-antiquark pair. In the effective theory these currents are replaced by their nonrelativistic counterparts [249]

$$R^v = \frac{4\pi}{s}\mathrm{Im}\left[c_1^2\mathcal{A}_1 + 2c_1c_2\mathcal{A}_2\right] \quad \text{and} \quad R^a = \frac{4\pi}{s}\mathrm{Im}\left[c_3^2\mathcal{A}_3\right] \ . \tag{6.8}$$

The correlators $\mathcal{A}_1$, $\mathcal{A}_2$, and $\mathcal{A}_3$ can be determined by the zero-distance coordinate space Green functions $\tilde{G}$. They are solutions of the time-independent Schrödinger equation [23]

$$\left[\frac{\boldsymbol{k}^2}{m} - \frac{\boldsymbol{k}^4}{4m^3} - \left(\frac{p_0^2}{m} - \frac{p_0^4}{4m^3}\right)\right]\tilde{G}(\boldsymbol{k},\boldsymbol{k}';q^2) + \int \frac{\mathrm{d}^3\boldsymbol{p}'}{(2\pi)^3}\,\tilde{V}(\boldsymbol{k},\boldsymbol{p}')\tilde{G}(\boldsymbol{p}',\boldsymbol{k}';q^2) = (2\pi)^3\delta^{(3)}(\boldsymbol{k}-\boldsymbol{k}') \ . \tag{6.9}$$

$\tilde{V}$ contains hereby all contributing potential terms. TOPPIK [23] is a numerical code that solves this Schrödinger equation for the Coulomb potential and it has been interfaced to WHIZARD. As it is computationally quite expensive, we call it beforehand in a given range of center of mass energies $\sqrt{\hat{s}}$ and save the results in a grid that is furthermore differential in p and p_0.

6.2.3 Kinematics and masses

The effective velocity of the produced top quark is [249]

$$v = \sqrt{\frac{\sqrt{s} - 2m_t + \mathrm{i}\Gamma_\mathrm{t}}{m_t}} \tag{6.10}$$

with the pole mass m_t and the top width Γ_t as function of m_t. As noted above, including the top width Γ in Eq. (6.10) includes the leading order effect of the top decay in NRQCD [238]. The pole mass, though, is no reliable input parameter as we have motivated in Chapter 1. Thus, we implement in this work the 1S top quark mass definition [23], which is defined as half of the mass of the fictitious stable ${}^3S_1$ toponium ground state that is visible in the lineshape. The pole mass can then be computed as a function of the 1S top quark mass scheme. The relation can be written at (N)LL as [249]

$$m_t\left[M_t^{1S}\right] = M_t^{1S}\left(1 + \Delta M(\sqrt{s}, \alpha_s)\right) , \quad \text{where} \quad \Delta M_\mathrm{LL} = \frac{(C_F\alpha_\mathrm{S})^2}{8} \quad \text{and} \tag{6.11a}$$

$$\Delta M_\mathrm{NLL} = \Delta M_\mathrm{LL} + \frac{(C_F\alpha_\mathrm{S})^3}{8\pi C_F}\left\{\beta_0 \cdot \left(1 + \log\frac{hf\nu_*}{C_F\alpha_\mathrm{S}}\right) + \frac{A_1}{2}\right\} . \tag{6.11b}$$

Hereby, we have used [258, 259]

$$\beta_0 = \frac{11C_A - 2N_F}{3} , \qquad A_1 = \frac{31}{9}C_A - \frac{20}{9}T_R \cdot N_F , \tag{6.12}$$

with the usual constants $C_A = 3$, $N_F = 5$, and $T_R = 1/2$.

6.2.4 Scales and uncertainties

There are three scales that are relevant in vNRQCD: the hard scale μ_H, the soft scale μ_S, and the ultrasoft scale μ_U. In Ref. [250], a detailed study of uncertainties at (N)NLL has shown that they should be varied with only two parameters h and f. This correlates the three scales as

$$\mu_\mathrm{H} = hm , \quad \mu_\mathrm{S} = (hm)(f\nu_*) , \quad \text{and} \quad \mu_\mathrm{U} = (hm)(f\nu_*)^2 . \tag{6.13}$$

Hereby, $f\nu_* \equiv \nu$ is the subtraction velocity and ν_* corresponds to $|v|$ of Eq. (6.10), using M_t^{1S} as mass and adding a small constant,

$$\nu_*\left[\sqrt{s}\right] = 0.05 + \left|\sqrt{\frac{\sqrt{s} - 2M_t^{1S} + \mathrm{i}\Gamma_t(M_t^{1S})}{M_t^{1S}}}\right| . \tag{6.14}$$

To obtain the strong coupling at the soft scale, $\alpha_\mathrm{S} = \alpha_s\left[\mu_\mathrm{S} = hM_t^{1S} f\nu_*\right]$, we run from $\alpha_\mathrm{H} = \alpha_s\left[hM_t^{1S}\right]$ with a two- or one-loop running at NLL and LL, respectively. Finally, we obtain the coupling at the ultra-soft scale $\alpha_{\rm U} = \alpha_s\left[\mu_{\rm U} = hM_t^{1S}(f\nu_*)^2\right]$ by running from $\alpha_{\rm H}$ with a one-loop running to $\mu_{\rm U}$.

The resummation of logarithms of v is crucial to control large normalization uncertainties that arise from fixed-order nonrelativistic computations, only considering Coulomb potential insertions. The two-loop matching coefficients of NRQCD and QCD have been computed in Ref. [260]. For our computation, we only need the hard S/P-wave 1-loop matching coefficients. For the NLL running of quark currents, we use the Wilson coefficient c_1, cf. Eq. (62) in Ref. [261]. The current coefficient is then multiplied with the result from Toppik.

6.2.5 Basic analytic results

LL form factor

As noted before, the dominating terms at threshold are gluon ladders connecting the top pairs. This can be obtained in NRQCD on LL by iterating the Coulomb potential of Eq. (6.4) to obtain the LL S-wave form factor [59]

$$F_{\rm LL} = 1 + {\rm i}\, m\, v\, \rho\, \Gamma(\epsilon)\, \Gamma(1+\epsilon)\, \Gamma(1-\rho)\, \frac{z_2 - z_1}{p\, \Gamma(1+\epsilon-\rho)} \tag{6.15}$$

with

$$\rho = \frac{C_F\, \alpha_{\rm S}}{2\, v} \quad \text{and} \quad z_{1,2} = {}_2F_1\left(\epsilon, 1+\epsilon, 1+\epsilon-\rho; \frac{m\, v \mp {\rm i}\,(p \mp |p_0|)}{2\, mv}\right) ,$$

where ϵ is a small positive parameter, ${}_2F_1(a,b,c;z)$ the ordinary hypergeometric function and Γ the Euler gamma function. Note that the form factor is normalized such that $F = 1$ corresponds to the tree-level result when plugged in the appropriate production matrix element.

Expansion of the form factor

For the matching of the resummed with the fixed-order computation, we require the $\mathcal{O}(\alpha_s)$ expansion of the former. At LL, it is given by

$$F_{\rm LL}^{\rm exp}\left[\alpha_s\right] = 1 + \alpha_s \left(\frac{{\rm i} C_F m \log \frac{mv+p}{mv-p}}{2p}\right) . \tag{6.16}$$

Going to NLL, we obtain an additional hard correction factor

$$F_{\rm NLL}^{\rm exp}\left[\alpha_s\right] = F_{\rm LL}^{\rm exp}\left[\alpha_s\right] + \alpha_s \left(-\frac{2C_F}{\pi}\right) . \tag{6.17}$$

6.3 Implementation in Whizard

We implement and study different variants of embedding the form factor of the last section in the relativistic computation. Let us first remark that we can in principle modify the vector $t\gamma_\mu\bar{t}$ and axial-vector $t\gamma_\mu\gamma_5\bar{t}$ couplings to the A and Z fields directly in the tree-level matrix element. This is a straightforward modification and we refer to this as the *signal diagram* method. However, this modification breaks gauge invariance already on the Lagrangian level. The SM Lagrangian containing the covariant derivative $\bar{\psi}\mathrm{i}\not{D}\psi$, which generates the $t\gamma_\mu\bar{t}$ and $t\gamma_\mu\gamma_5\bar{t}$ interactions, is invariant under local gauge variations $\Psi_t \to e^{-\mathrm{i}Qg\theta(x)}\Psi_t$. This is no longer the case when we change the covariant derivative to take into account the form factor that we obtain from NRQCD for $t\gamma_\mu\bar{t}$ and $t\gamma_\mu\gamma_5\bar{t}$. Furthermore, it seems unrealistic to obtain NLO QCD corrections for this ansatz, as it would require attaching gluons to all colored particles of the amplitude. This especially includes final-final interactions necessitating the evaluation of loop integrals over the form factor. The form factor, however, depends on the momentum and is only available in a simple analytic form at LL.

It is thus preferable to multiply the form factor with a gauge invariant quantity using a factorized ansatz:

$$\mathcal{M} = \underbrace{\left\langle e^+e^- \,\middle|\, \mathcal{T}_{\mathrm{NRQCD}} \,\middle|\, t\bar{t} \right\rangle}_{\equiv \mathcal{M}_{\mathrm{prod}}} \left\langle t\bar{t} \,\middle|\, \mathcal{T} \,\middle|\, \mathrm{W}^+\mathrm{W}^-\mathrm{b}\bar{\mathrm{b}} \right\rangle \,, \tag{6.18}$$

where the form factor only enters the production matrix element $\mathcal{M}_{\mathrm{prod}}$ and NLO QCD corrections to the decay can be computed separately. We note that Ref. [256] uses a similar ansatz to study CP violation in top pair production in association with a Higgs boson at threshold. We discuss the exact form of Eq. (6.18) in Section 6.3.2, after a more general discussion of the possible violations of gauge invariance in the treatment of unstable particles in Section 6.3.1.

6.3.1 Possible violations of gauge invariance

Unstable particles like the top quark are notoriously problematic from a perturbative point of view. The Breit-Wigner distribution of the invariant mass is a result of resumming self-energy corrections to the propagator. Such a Dyson resummation mixes perturbative orders. As gauge invariance can only be guaranteed order by order, the associated Ward, Slavnov-Taylor and Nielsen identities can be violated. While these violations are associated with a higher order, they can be made arbitrarily large by applying an extreme gauge transformation [262]. This can be avoided by using the fact that the *complex* pole $p^2 = \mu^2$, where $\mu^2 = m^2 - im\Gamma$, of the propagator of an unstable particle is actually a gauge-invariant quantity [263, 264]. This fact is the basis of two approaches that we will use in this work: the *complex-mass scheme* and the *pole approximation (PA)*. For calculations that involve complete matrix elements, i.e. not the factorized parts, intermediate unstable particles are treated in the complex-mass scheme [181, 265]. The idea behind the complex-mass scheme is to add and subtract the width in the bare Lagrangian. While one of the terms is absorbed in the complex renormalized mass definition, the other one is part of the complex counterterm. Thus, no resummation is necessary to obtain the width. This leads to a gauge invariant treatment of finite width effects, as Ward or Slavnov-Taylor identities are exactly respected, while maintaining perturbative unitarity [218]. The PA will be discussed in Section 6.3.2.

Aside from problems associated with the width, one must also not treat signal diagrams differently than background diagrams, as they are in general no gauge-invariant objects separately. This is also noted in Ref. [257] but the authors still use this separation with an ad-hoc factor intended to cancel gauge-dependent effects. In fact, the smallest gauge-invariant subset that contains the signal diagrams in $\mathrm{W}^+\mathrm{W}^-\mathrm{b}\bar{\mathrm{b}}$ consists of *all* diagrams. In the language of Ref. [266], such a subset is called a *grove* and can be systematically constructed. Modifications of the signal diagrams like the attachment of a form factor will, therefore, spoil gauge invariance as we have already noted at the Lagrangian level at the start of this section.

6.3.2 Factorization in the DPA

Different approaches to treating unstable particles close to and above threshold have been compared in Ref. [267] for WW production. Above threshold, the differences between the approaches in unitary gauge have been found to be at the per cent level. Of these, we will refer in the following to the narrow-width approximation (NWA), the signal diagram (SD), and the PA. The NWA, see e.g. Ref. [268] and the references therein, performs the zero width limit of the signal diagram and results in the simple formula $\sigma = \sigma_{\mathrm{prod}} \cdot \mathrm{BR}$, where BR is the corresponding branching ratio. The approximation is gauge-invariant, allows for factorizable corrections but incorporates no off-shell behavior and defines no cross section below threshold. Hereby, the latter property is inherited from the production cross section σ_{prod}. The SD, on the other hand, can be evaluated off-shell and is finite below threshold. But it is neither gauge-invariant, as discussed in Section 6.3.1, nor is it suitable for radiative corrections. In fact, we have encountered negative cross sections when computing QCD corrections to the signal diagram far from threshold.

The *pole scheme* [262, 269] was one of the first schemes to enable gauge-invariant computations for kinematics where unstable particles can go on-shell. Hereby, a Laurent expansion of the full scattering amplitude is performed and then expanded order by order instead of only resumming one-loop truncated self-energy corrections. In the PA [270], one drops the nonresonant contributions to decrease the computational complexity. Thus, the denominator of the propagator of the SD, which contains the dominant off-shell effects, is kept but the gauge-dependent parts in the numerator are removed. This is achieved by ensuring that the momenta that enter the matrix elements are on-shell projected. The gauge-invariant property follows directly from the proof of the pole scheme as it is a

Laurent expansion about the point $p^2 = \mu^2$ and we need the residue at this point. In fully differential MCs, this requires on-shell projections, which cannot be uniquely defined and thus introduce an ambiguity in the results of $\mathcal{O}(\Gamma/m)$ [271]. In contrast, in an analytic calculation, one simply evaluates matrix elements with m^2 instead of p^2 but has no events available.

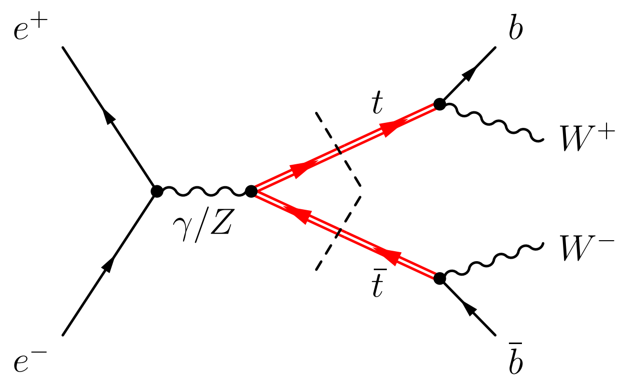

Figure 6.1 Factorized computation in the DPA. Double lines indicate t propagators and a dashed line through them a factorized computation with on-shell projection

In our case, we have to deal with two top-quark resonances and thus have to use a DPA [272, 273]. For illustration, we show the factorized computation diagrammatically in Fig. 6.1. The factorized matrix element in this approximation can be written as

$$\mathcal{M}_{\text{fact}} = \sum_{h_t,h_{\bar{t}}} \underbrace{\frac{1}{\left(p_t^2 - \mu_t^2\right)} \frac{1}{\left(p_{\bar{t}}^2 - \mu_t^2\right)}}_{\equiv \mathcal{P}_{t\bar{t}}} \mathcal{M}_{\text{prod}}^{h_t,h_{\bar{t}}}[\{\hat{p}\}] \mathcal{M}_{\text{dec},t}^{h_t}[\{\hat{p}\}] \mathcal{M}_{\text{dec},\bar{t}}^{h_{\bar{t}}}[\{\hat{p}\}] \;, \tag{6.19}$$

where h_t, $h_{\bar{t}}$ are the polarizations of the top quark resonances and $\mu_t^2 = m_t^2 - \mathrm{i} m_t \Gamma_\mathrm{t}$ is the complex top mass squared. $\{\hat{p}\}$ denotes a set of momenta that have been projected on-shell such that $\hat{p}_t^{\,2} = m_t^2$, while $\{p\}$ are the corresponding off-shell momenta with $p_t^2 \neq m^2$ in general. Besides the propagators of $\mathcal{M}_{\text{fact}}$, the off-shell momenta are used in the full matrix elements and event output. The details of the projection procedure are discussed in Section 6.3.2. We note that if p_t and $p_{\bar{t}}$ are already on-shell beforehand, one can use

$$\sum_{h_t} \left| u_{h_t}(p_t) \right\rangle \left\langle u_{h_t}(p_t) \right| = \not{p}_t + m_t \;, \qquad \sum_{h_{\bar{t}}} \left| v_{h_{\bar{t}}}(p_{\bar{t}}) \right\rangle \left\langle v_{h_{\bar{t}}}(p_{\bar{t}}) \right| = \not{p}_{\bar{t}} - m_t \tag{6.20}$$

and Eq. (6.19) becomes equal to the signal diagram. In fact, we have used this property to verify that the factorized computation has been correctly implemented. For each external helicity, we found perfect agreement up to the numerical precision for the complex amplitudes for an on-shell phase-space point. However, the relativistic 4-body phase space probes also all possible off-shell regions where Eq. (6.20) does not hold. Therefore, we expect a computation with signal diagrams to be at best approximately equal to $\mathcal{M}_{\text{fact}}$.

A nice aspect of the PA is that factorizable and nonfactorizable corrections are separately gauge-invariant. The factorizable corrections to the production and decay matrix elements are usually the dominant contributions and the only ones that we will address in this work. In Ref. [274], the nonfactorizable corrections have been given analytically for any number of unstable particles at the one-loop level for electroweak corrections.

Equation (6.19) is our preferred setup to describe $\mathrm{t\bar{t}}$ production within $\mathrm{W^+W^-b\bar{b}}$ and will also be referred to as *factorized, on-shell evaluated*. *Off-shell evaluated* would correspond to replacing $\{\hat{p}\}$ with $\{p\}$ and is only used as a test in Section 6.3.4. To include the nonrelativistic S- and P-wave form factor in this description, we only have to multiply it with the corresponding production matrix element. In the formalism of the DPA, it can be seen as a factorizable, gauge-invariant correction to the production. At the same time, we can also compute hard NLO QCD corrections to the decay, as described in Section 6.3.5.

Helicity correlations

Concerning helicity correlations, Eq. (6.19) can be considered as complete as possible. This implies that there are also quantum correlations in the density matrix that do not fit the classical picture of top production with a certain spin. In other words, when we square the matrix element, we have

$$|\mathcal{M}_{\mathrm{fact}}|^2 = \left(\sum_{h_t,h_{\bar{t}}} \mathcal{P}_{t\bar{t}} \mathcal{M}_{\mathrm{prod}}^{h_t,h_{\bar{t}}} \mathcal{M}_{\mathrm{dec},t}^{h_t} \mathcal{M}_{\mathrm{dec},\bar{t}}^{h_{\bar{t}}}\right) \left(\sum_{h'_t,h'_{\bar{t}}} \mathcal{P}_{t\bar{t}} \mathcal{M}_{\mathrm{prod}}^{h'_t,h'_{\bar{t}}} \mathcal{M}_{\mathrm{dec},t}^{h'_t} \mathcal{M}_{\mathrm{dec},\bar{t}}^{h'_{\bar{t}}}\right)^* , \tag{6.21}$$

where $h_t \neq h'_t$ in general. These off-diagonal correlations are expected to be strongly suppressed at threshold. Also on the practical level, we note that they are currently not available in OpenLoops, which we use to obtain the virtual corrections for the top decay. Thus, we define the following helicity approximation (HA), which still covers the important diagonal correlations ($h_t = h'_t$), also known as classical spin correlations, but neglects all off-diagonal entries ($h_t \neq h'_t$):

$$\begin{aligned} \left|\mathcal{M}_{\mathrm{fact}}^{\mathrm{HA}}\right|^2 &= \sum_{h_t,h_{\bar{t}}} |\mathcal{P}_{t\bar{t}}|^2 \left(\mathcal{M}_{\mathrm{prod}}^{h_t,h_{\bar{t}}} \mathcal{M}_{\mathrm{dec},t}^{h_t} \mathcal{M}_{\mathrm{dec},\bar{t}}^{h_{\bar{t}}}\right) \left(\mathcal{M}_{\mathrm{prod}}^{h_t,h_{\bar{t}}} \mathcal{M}_{\mathrm{dec},t}^{h_t} \mathcal{M}_{\mathrm{dec},\bar{t}}^{h_{\bar{t}}}\right)^* \\ &= \sum_{h_t,h_{\bar{t}}} |\mathcal{P}_{t\bar{t}}|^2 \left|\mathcal{M}_{\mathrm{prod}}^{h_t,h_{\bar{t}}}\right|^2 \left|\mathcal{M}_{\mathrm{dec},t}^{h_t}\right|^2 \left|\mathcal{M}_{\mathrm{dec},\bar{t}}^{h_{\bar{t}}}\right|^2 . \end{aligned} \tag{6.22}$$

We want to approximate even further for comparisons with analytic results, obtained with the optical theorem as described in Section 6.2.2. In the analytic approach, off-shell effects are only introduced through the spin-averaged width. To be able to compare with this, we apply an uncorrelated average to the decays and we call this the extra-helicity approximation (EHA):

$$\left|\mathcal{M}_{\text{fact}}^{\text{EHA}}\right|^2 = \sum_{h_t,h_{\bar{t}}} |\mathcal{P}_{t\bar{t}}|^2 \left|\mathcal{M}_{\text{prod}}^{h_t,h_{\bar{t}}}\right|^2 \left(\frac{1}{2}\sum_{h'_t}\left|\mathcal{M}_{\text{dec},t}^{h'_t}\right|^2\right)\left(\frac{1}{2}\sum_{h'_{\bar{t}}}\left|\mathcal{M}_{\text{dec},\bar{t}}^{h'_{\bar{t}}}\right|^2\right) \tag{6.23}$$

In all the above equations, we have of course implied that these are still to be summed over the external helicities of $\mathrm{e}^+\mathrm{e}^- \to \mathrm{W}^+\mathrm{W}^-\mathrm{b}\bar{\mathrm{b}}$.

On-shell projection

A generic algorithm and formulae to obtain on-shell projected momenta for any number of resonances can be found in Ref. [274]. In our case, the expressions simplify to

$$\hat{p}_t = \left(\frac{\sqrt{s}}{2}, \frac{\sqrt{s-4m_t^2}}{2}\boldsymbol{e_t}\right) \quad \text{and} \quad \hat{p}_{\bar{t}} = \left(\hat{p}_t^0, -\hat{\boldsymbol{p}}_t\right) , \tag{6.24}$$

where $\boldsymbol{e_t} = \boldsymbol{p_t}/\left|\boldsymbol{p_t}\right|$ is the unit vector of the top in the collision system. Again, we signify on-shell projected momenta with a hat and they fulfill by definition the on-shell condition $\hat{p}^2 = m^2$. Note that if we demand on-shell momenta

$$\hat{p}_t^2 = m_t^2 \tag{6.25a}$$
$$\hat{p}_{\bar{t}}^2 = m_t^2 \tag{6.25b}$$

as well as overall momentum conservation,

$$\hat{E}_t + \hat{E}_{\bar{t}} = \sqrt{s} , \qquad |\hat{\boldsymbol{p}}_t| = |\hat{\boldsymbol{p}}_{\bar{t}}| , \tag{6.26}$$

we obtain

$$\hat{E}_t^2 - \hat{\boldsymbol{p}}_t^2 = m_t^2 , \tag{6.27a}$$
$$(\sqrt{s} - \hat{E}_t)^2 - \hat{\boldsymbol{p}}_t^2 = m_t^2 . \tag{6.27b}$$

From Eq. (6.27) immediately follows that $\hat{E}_t = \sqrt{s}/2$ and thus $\left|\boldsymbol{p_t}\right| = \sqrt{s-4m_t^2}/2$. Thus, the only freedom in Eq. (6.24) is the direction of the three momentum as the rest is fixed by momentum conservation and the on-shell conditions. By using $\boldsymbol{e}_t$, we guarantee that we do not change the final state when they are already on-shell and maintain spatial correlations, which are important for the forward-backward asymmetry for example. Furthermore, it is important for interference terms of the factorized with the full amplitude to maintain all directions.

The projection, Eq. (6.24), is not applicable over the whole kinematical range at face value. Below threshold, $\sqrt{s} < 2m_t$, it will yield complex momenta. Thus, it is usually only defined for $\sqrt{s} > 2m_t$. The resummed computation, however, reaches its peak at

$\sqrt{s} = 2M_t^{1S} < 2m_t$. Therefore, we define the extended DPA as follows: For $\sqrt{s} > 2m_t$, the extended DPA is identical to the normal DPA. For $\sqrt{s} \leq 2m_t$, we project to a set of momenta that correspond to $\sqrt{s} = 2m_t + \epsilon$. ϵ is hereby a very small number that is only introduced to avoid numerical instabilities in the matrix elements, that occur for $\boldsymbol{v} = \boldsymbol{0}$. The direction $\boldsymbol{e}_t$ is maintained in the same way as above threshold. This extended DPA is an analytic continuation of the normal DPA, transitions smoothly into the normal DPA at threshold and, crucially, gives finite results below threshold in a gauge-invariant way by construction.

Having $\hat{p}_t$ and $\hat{p}_{\bar{t}}$ at hand, we also have to project the decay products. At the Born level, this is a simple $1 \to 2$ decay with the well-known solution [117, 274]

$$\begin{aligned} |\hat{\boldsymbol{p}}_W| = |\hat{\boldsymbol{p}}_b| &= \frac{\sqrt{\lambda(m_t^2, m_\mathrm{W}^2, m_\mathrm{b}^2)}}{2m_t} \,, \\ E_W &= \frac{m_t^2 + m_\mathrm{W}^2 - m_\mathrm{b}^2}{2m_t} \quad \text{and} \quad E_b = \frac{m_t^2 - m_\mathrm{W}^2 + m_\mathrm{b}^2}{2m_t} \,, \end{aligned} \tag{6.28}$$

in the frame where $\hat{p}_t = (m_t, \boldsymbol{0})$. Again we have the freedom concerning the angles and we choose analogously $\hat{\boldsymbol{p}}_W = \left|\hat{\boldsymbol{p}}_W\right| \boldsymbol{e}_W$, where $\boldsymbol{e}_W$ is the original direction of the W^+ in the top rest frame. Note that this also ensures that the flight direction of the b is conserved. These momenta can then be boosted back to the collision frame. The same procedure is applied to the anti-top decay products. The NLO case, involving the $1 \to 3$ decay, is discussed in Section 6.3.5.

6.3.3 Input parameters

The Z, W, Higgs, electron, muon as well as all quark but the top masses are as in Section 4.4.1. For the top quark, we use $M_t^{1S} = 172\,\mathrm{GeV}$ as input. Thus, the pole mass m_t depends on $\sqrt{s}$. With Eq. (6.11) and the other parameters in this section, we obtain at threshold ${m_t}^{\mathrm{LL}}\left[2M_t^{1S}\right] = 172.802\,\mathrm{GeV}$ and ${m_t}^{\mathrm{NLL}}\left[2M_t^{1S}\right] = 173.124\,\mathrm{GeV}$. The CKM matrix is still trivial and we stick to the G_μ-scheme for the electroweak coupling. For the strong coupling constant, we use $\alpha_s(m_\mathrm{Z}) = 0.118$ [275] and a three-loop running to the hard scale $\alpha_\mathrm{H} = \alpha_s\left[\mu_\mathrm{H} = M_t^{1S}\right]$ (including $n_f = 5$ active flavors). From this point, the running to the soft and ultra-soft scales proceeds as explained in Section 6.2.4.

With this setup, the top width is computed directly at LO and NLO. In the NLO computation, we use the same renormalization scale as in the full process, including scale variations. By evaluating matrix elements and the top-decay width at the same perturbative order, we guarantee that $\mathrm{t} \to \mathrm{Wb}$ branching ratios remain consistently equal to one at LO and NLO, as demonstrated in Part II. Note that the top width also depends on $\sqrt{s}$ as it is a function of m_t and is automatically recomputed by WHIZARD when $\sqrt{s}$ changes. At threshold, we obtain as numerical values $\Gamma_\mathrm{t}^{\mathrm{LO}}\left[2M_t^{1S}\right] = 1.4866\,\mathrm{GeV}$ and $\Gamma_\mathrm{t}^{\mathrm{NLO}}\left[2M_t^{1S}\right] = 1.3692\,\mathrm{GeV}$. The Higgs, W and Z width is set to $\Gamma_\mathrm{H} = 4.143\,\mathrm{MeV}$,

$\Gamma_{\mathrm{W}} = 2.049\,\mathrm{GeV}$, $\Gamma_{\mathrm{Z}} = 2.443\,\mathrm{GeV}$, respectively.

As noted in Section 6.3.1, we will use the complex-mass scheme for complete matrix elements. This necessitates complex-valued renormalized masses and weak mixing angles as in Section 4.4.1. We will, however, refrain from using the complex-valued objects to define α_{em} but use the real definition:

$$\alpha_{\mathrm{em}}\left[G_\mu\right] = \frac{\sqrt{2}}{\pi}\, m_{\mathrm{W}}^2\, \sin\theta_W^2\, G_\mu\,. \tag{6.29}$$

This allows us to use one consistent definition in all parts of the calculation. It is just a different convention that does not violate the gauge-invariant properties of the complex-mass scheme.

6.3.4 Validation of factorization approaches

All results shown in this subsection are obtained with a tree-level form factor of unity and a LO decay as well as $m_t = M_t^{1S}$, if not noted otherwise.

High-energy behavior

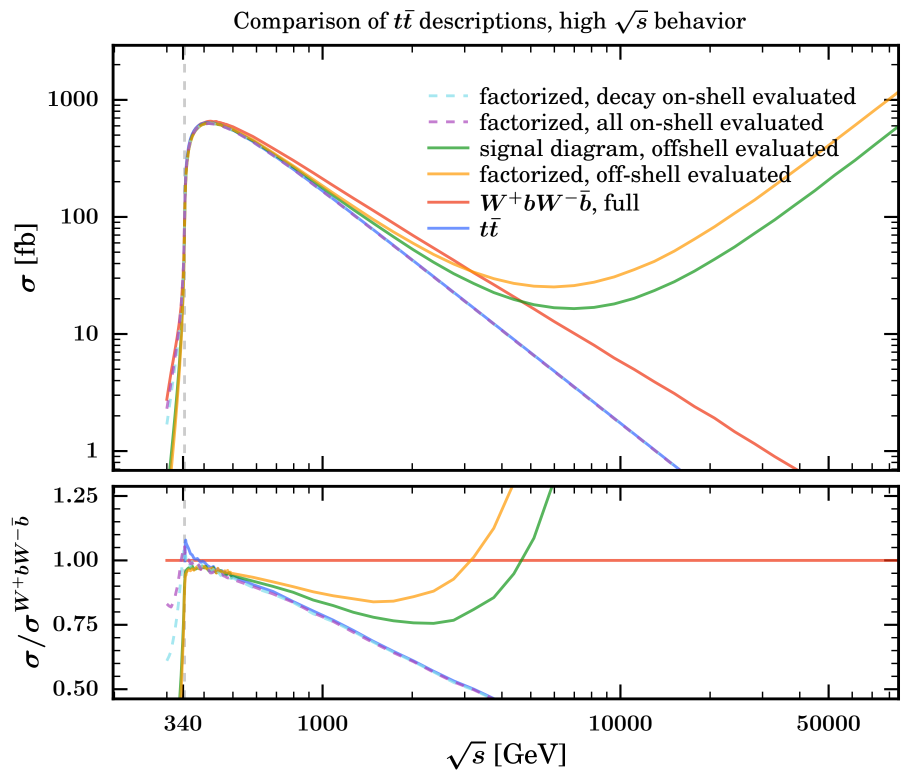

Figure 6.2 Behavior of different factorization approaches, described in more detail in the text, for high energies. The dashed gray line indicates $2M_t^{1S}$.

The high-energy behavior of cross sections can serve as a test for gauge-invariance. As known famously from WW production, the cross section only falls off with $\sqrt{s}$ in the high energy regime if it contains no gauge-dependent terms, which could affect perturbative unitarity. In Fig. 6.2, we show the different factorization approaches that have been implemented in WHIZARD. The full $\mathrm{W^+W^-b\bar{b}}$ LO cross section serves as reference in this case, as it is gauge-invariant and valid below threshold. One can see that while it agrees with the $\mathrm{t\bar{t}}$ cross section around threshold up to $\sim 10\,\%$, $\mathrm{t\bar{t}}$ falls off faster and constitutes only $50\,\%$ of the full cross section at $2\,\mathrm{TeV}$. At these energies, $\mathrm{t\bar{t}}$ is not describing the physical final state $\mathrm{W^+W^-b\bar{b}}$ anymore, which gets sizable contributions from single-top and nonresonant processes. We furthermore see that using the signal diagram (instead of the sum over all diagrams) leads to an unphysical rise of the cross section at high energies. The same holds for the factorized matrix element, Eq. (6.19), evaluated with off-shell momenta. The difference between the two descriptions is related to the fact that Eq. (6.20) only holds on-shell. The reason for the rise can only be the gauge dependence that is introduced in these descriptions as discussed in Section 6.3.1. Finally, we have two descriptions that closely follow $\mathrm{t\bar{t}}$ for high energies: the factorized computation with on-shell momenta in the decay and off-shell momenta in the production matrix element as well as the one with on-shell momenta in both. The similar results indicate that the gauge-breaking terms indeed arise from the off-shell evaluation of the decay.

While it is usually known that, in principle, signal diagrams are not gauge-invariant, it is often expected that the gauge dependence is small. E.g. signal diagrams have been used in Ref. [179] to estimate the energy dependence of the fraction of double-top contributions in $\mathrm{W^+W^-b\bar{b}}$ up to $3\,\mathrm{TeV}$. Considering that the signal diagram squared surpasses the full cross section at $5\,\mathrm{TeV}$ to start its arbitrary rise, one can expect that any conclusions drawn from signal diagrams at TeV energies are largely gauge-dependent and thus unphysical.

$t\bar{t}$ descriptions around threshold

The considerations in the last paragraph were instructive to understand which descriptions break unitarity but phenomenologically the behavior around threshold is more important. Therefore, we show in Fig. 6.3 the same results in a $100\,\mathrm{GeV}$ window around threshold. Obviously, $\mathrm{t\bar{t}}$ is only non-zero above $2m_t$. The other approaches all significantly deviate from $\mathrm{W^+W^-b\bar{b}}$ below threshold, while agreeing above threshold within $4\,\%$. This is partly expected, as $\mathrm{W^+W^-b\bar{b}}$ contains background diagrams that have nothing to do with top production, yielding a larger cross section below threshold. But again, we can see that the off-shell evaluation of the decay is the biggest effect. Whereas signal diagram and off-shell evaluated factorized matrix elements fall off quickly below $60\,\%$, the factorized descriptions with the on-shell decay are fairly under control. Below threshold, it also makes a difference if we project the production matrix element or not. This is easily understandable: as we defined the projection below threshold such that one projects back to momenta at threshold in Section 6.3.2, applying the projection below threshold increases the $\sqrt{s}$ that goes into the production matrix element. On the other hand, above threshold

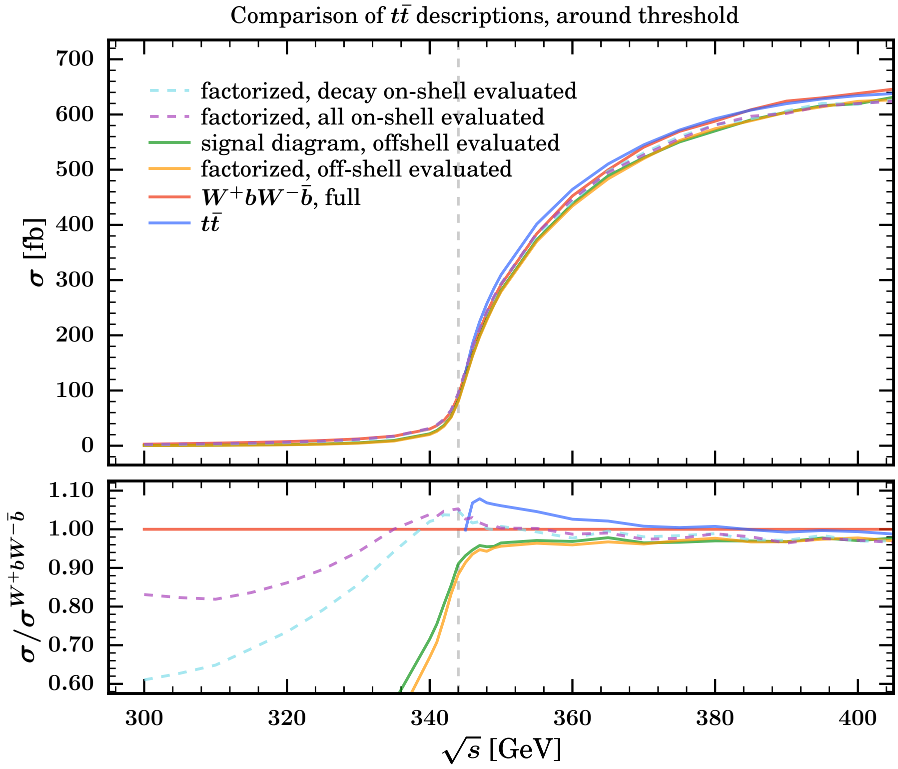

Figure 6.3 Behavior of different factorization approaches around threshold. Lines as in Fig. 6.2.

both approaches lead to the same $\sqrt{s}$ in the production matrix element. A strict DPA requires to project both production and decay matrix elements and as this also follows more closely the full cross section, we will use this as default.

Helicity correlations

In Fig. 6.4, we show the mutual effects of on-shell projection of the production, boost of momenta going into the decay and correlated (HA) or averaged (EHA) sum over top helicities. Using the projection for the production, leads for all other four options to minimal variations below 0.5 % in the relevant energy range. Not boosting the decay momenta to the center of mass energy, but using them in the rest frame, is only equivalent when the decay is spin-averaged. Otherwise, one connects helicities that have been defined in different reference frames. Therefore, we can expect the orange solid and blue dashed line to be equal and the green solid line to be different and wrong, which is confirmed by the results, although the differences are very small. For interference terms of the factorized with the full matrix element, this does not have to be the case as discussed in Section 6.3.4. Interestingly, not using the projection in the production leads to larger differences between the boosted correlated and the other approaches. In this case, it seems more important to maintain spin correlations in the correct way, even above threshold.

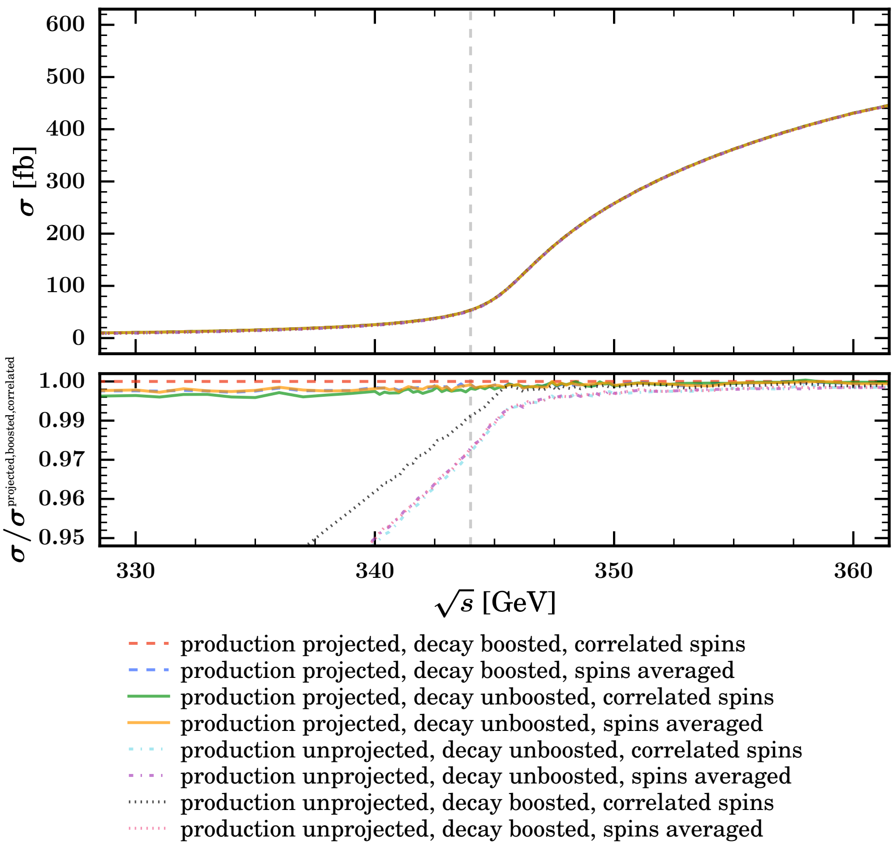

Figure 6.4 Mutual effects of on-shell projection of the production, boost of momenta going into the decay and correlated or averaged sum over top helicities. Production projected with (un-) boosted momenta is shown with (solid) dashed lines and unprojected with (dotted) dashdotted lines.

Interference terms

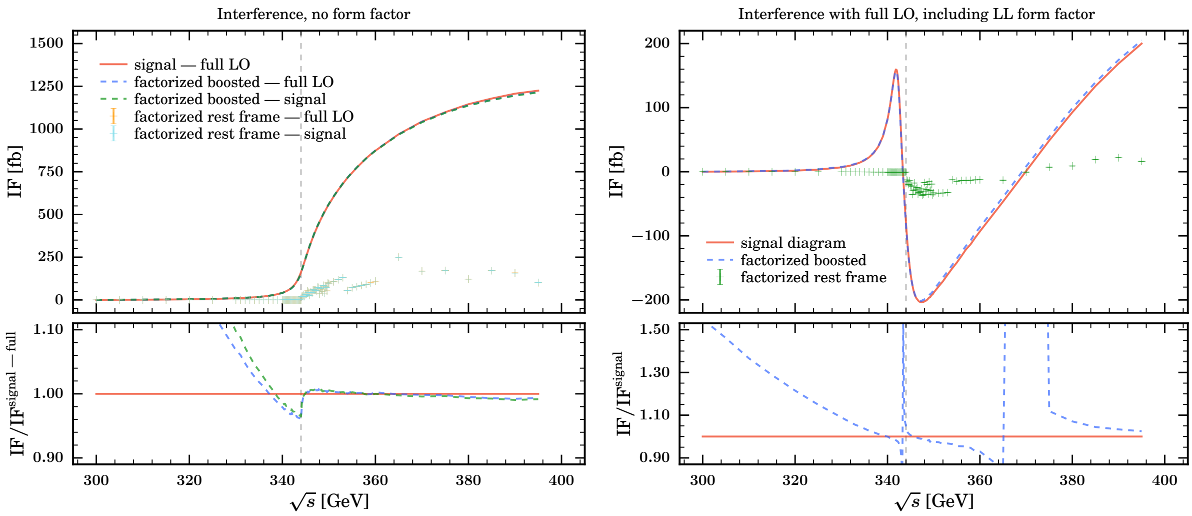

Figure 6.5 Integrated interference terms: signal diagram with full LO is indicated by a solid curve, factorized using boosted momenta by dashed and factorized using momenta in the decay rest frame with error bars and a + as indicator. Note that the errors are basically invisible and one can see only the indicator symbol. The ratio plot is ill-defined at the two zero crossings but is still shown to assess the quantitative difference, especially below threshold.

In the left plot of Fig. 6.5, we show different interference terms, IF $= 2\Re[\mathcal{M}_{\text{fact}} \cdot \mathcal{M}^*_{\text{full}}]$, with a form factor of $F = 1$ in the factorized computation. We will use terms like this to extend the factorized (N)LL computation with full LO information, where possible. Thus, it is crucial that the relative phase of the two amplitudes matches exactly. For comparison, we also show the interference term of the signal diagram with the full LO as a rough reference point. In this case, evaluating the decay with momenta in the rest frame fails completely. It seems to result in a $\sqrt{s}$-dependent nontrivial relative phase. To show that it is indeed not numeric noise, we show the vanishing error bars of the integrations for the factorized rest frame results. On the other hand, the boost of the decay momenta to the collision system yields comparable results to the signal-full LO integration. The differences are within similar bounds as observed in Fig. 6.3.

It is also instructive to see how this affects the matched results, i.e. when the factorized matrix element is evaluated with $F_{\text{LL}} - 1$ in the interference term. We show this in the right plot of Fig. 6.5. Again, the factorized rest frame fails to reproduce the correct results, while the factorized boosted and signal diagrams yield fairly similar results. The ratio is, of course, not reliable at the two zero-crossings. Below threshold, we observe that the signal diagram significantly undershoots the factorized computation. The overall shape of both curves is qualitatively the same as expected from the analytic properties of the real part of Eq. (6.15). In the following, we will always use the momenta boosted to the collision system to maintain the correct relative phase.

P and CP behavior

As the HA allows talking about spins as physical objects in the classical picture, we use this opportunity to discuss how the cross section is distributed across different helicities. This furthermore serves to validate our approximation. For further simplification, we disable at first the contribution of the Z and only use the photon diagram for top-pair production. The interference between Z and photon is well-known and the major cause of the forward-backward asymmetry in top-pair production at lepton colliders, cf. Section 5.2.2. Disabling the Z allows us to concentrate on other parity symmetry violations first.

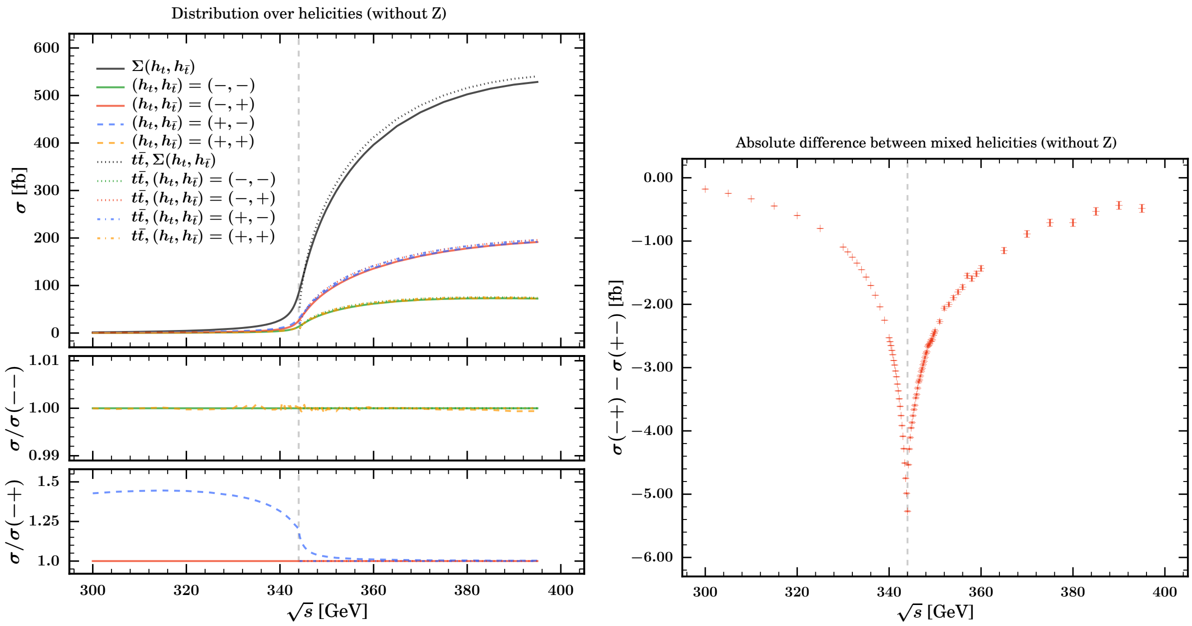

Figure 6.6 In the left plot, we show the distribution of the cross section over the different top helicity combinations (colored) as well as the sum (black) for $\mathrm{t\bar{t}}$ (dotted and dashdotted) and $\mathrm{W^+W^-b\bar{b}}$ (solid and dashed). The ratios have been formed separately for $\mathrm{t\bar{t}}$ and $\mathrm{W^+W^-b\bar{b}}$ by dividing by the respective cross section. As usual the dashed, vertical line shows $2M_t^{1S}$. In the right plot, the absolute difference of mixed top helicities are shown for $\mathrm{W^+W^-b\bar{b}}$. Note that the errors are asymmetric and growing above threshold in the absolute difference due to the constant relative error and the growing cross section.

In the left plot of Fig. 6.6, we show the distribution of the cross section over the different helicity configurations as well as the sum over all helicities for $\mathrm{W^+W^-b\bar{b}}$ and $\mathrm{t\bar{t}}$. Above 360 GeV, $\mathrm{W^+W^-b\bar{b}}$ and $\mathrm{t\bar{t}}$ cross sections are fairly similar. Especially the respective ratios of mixed top helicities $\sigma(+,-)/\sigma(-,+)$ and identical top helicities $\sigma(+,+)/\sigma(-,-)$ are practically identical. For $\mathrm{t\bar{t}}$, the ratios stay close to one for all energies. As the $\mathrm{t\bar{t}}$ cross section is given by the square of the production matrix $|\mathcal{M}_{\text{prod}}|^2$, we can identify that $|\mathcal{M}_{\text{prod}}|^2(-,-) = |\mathcal{M}_{\text{prod}}|^2(+,+)$ as well as $|\mathcal{M}_{\text{prod}}|^2(+,-) = |\mathcal{M}_{\text{prod}}|^2(-,+)$. This is, of course, to be expected as the electromagnetic production of fermion pairs conserve parity (P).

For the top decay, however, only the combination of charge conjugation and parity (CP) is a symmetry, due to the left-handed coupling. This implies for the DPA in HA that

$$\left|\mathcal{M}_{\text{fact}}^{\text{HA}}\right|^2(+,+) = |\mathcal{P}_{t\bar{t}}|^2 \left|\mathcal{M}_{\text{prod}}^{+,+}\right|^2 \left|\mathcal{M}_{\text{dec},t}^{+}\right|^2 \left|\mathcal{M}_{\text{dec},\bar{t}}^{+}\right|^2 \tag{6.30a}$$

$$\xrightarrow{CP} |\mathcal{P}_{t\bar{t}}|^2 \left|\mathcal{M}_{\text{prod}}^{-,-}\right|^2 \left|\mathcal{M}_{\text{dec},\bar{t}}^{-}\right|^2 \left|\mathcal{M}_{\text{dec},t}^{-}\right|^2 = \left|\mathcal{M}_{\text{fact}}^{\text{HA}}\right|^2(-,-) \tag{6.30b}$$

Note that t and $\bar{t}$ have been swapped due to the C conjugation in Eq. (6.30b), but due to the symmetric helicities this has no effect. For the mixed helicities, this is not the case. In fact,

$$\left|\mathcal{M}_{\text{fact}}^{\text{HA}}\right|^2(+,-) \xrightarrow{CP} \left|\mathcal{M}_{\text{fact}}^{\text{HA}}\right|^2(+,-) \neq \left|\mathcal{M}_{\text{fact}}^{\text{HA}}\right|^2(-,+)\,. \tag{6.31}$$

So from CP properties, we cannot infer the correct behavior of the ratio of mixed helicities for $\mathrm{W^+W^-b\bar{b}}$. It is thus interesting to see that for high energies the ratio still goes to unity and P becomes a good symmetry again. In the right plot of Fig. 6.6, we also show the absolute difference between the mixed helicities for $\mathrm{W^+W^-b\bar{b}}$, which is remarkably symmetric around threshold. One could work out the exact analytic behavior of the P violating terms in the cross section, but this is beyond the scope of this validation.

Finally, we also show the effect of including the Z in Fig. 6.7. As expected, identical helicities in $\mathrm{t\bar{t}}$ and $\mathrm{W^+W^-b\bar{b}}$ still give identical results, while the dominant contributions come from mixed helicities. For massless quark production, mixed helicities are the only contributing configurations due to the spin 1 intermediate gauge-bosons. Thus, identical contributions only occur due to the spin flip associated with the mass. We can also see that the ratios are the same as without the Z in the sense that for identical helicities they stay at unity and for mixed helicities the results for $\mathrm{W^+W^-b\bar{b}}$ approach $\mathrm{t\bar{t}}$ above 360 GeV and go to ~ 1.45 below threshold. The major difference is of course that already $\mathrm{t\bar{t}}$ shows a P violation in the mixed helicities that grows with energy. Overall, we see that the Z contributions enhance mostly the $(+,-)$ configuration while the others stay comparatively constant.

6.3.5 NLO QCD corrections with WHIZARD

Considered fixed-order corrections

As motivated in Section 6.3.2, we will include the form factor in the production matrix element of the DPA. The decay matrix elements, however, do not obtain nonrelativistic corrections, so we can compute the relativistic NLO corrections to them. This will allow us to use the NLO width in the corresponding parts of the matched computation and have NLO correctness in observables that are sensitive to the decay kinematics. Furthermore, we will need the full $\mathrm{W^+W^-b\bar{b}}$ fixed-order results at LO and NLO. We will now introduce a convenient notation for these computations that will be useful for the discussion of the matching in Section 7.2.

For $\mathrm{W^+W^-b\bar{b}}$ at LO, we just square the sum of the tree-level contributions, including

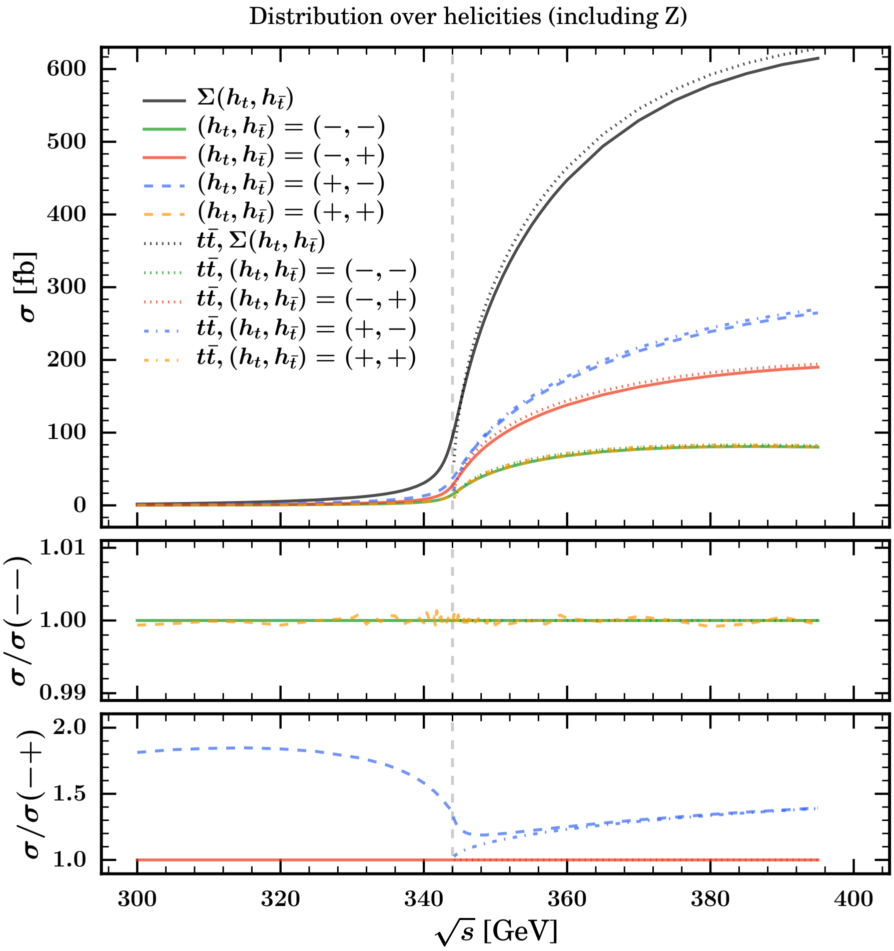

Figure 6.7 We show the distribution of the cross section over the different top helicity combinations (colored) as well as the sum (black) for $\mathrm{t\bar{t}}$ (dotted and dashdotted) and $\mathrm{W^+W^-b\bar{b}}$ (solid and dashed). The ratios have been formed separately for $\mathrm{t\bar{t}}$ and $\mathrm{W^+W^-b\bar{b}}$ by dividing by the respective cross section. As usual the dashed, vertical line shows $2M_t^{1S}$.

the interferences with all background processes,

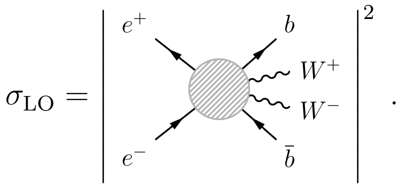

(6.32)

For the NLO contributions,  stands for all possible one-loop diagrams for this final state and order and $\left(a \int b\right) \equiv 2\Re\left[a \cdot b^*\right]$:[1]

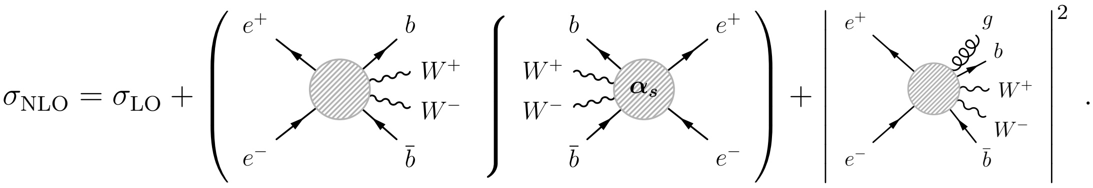

(6.33)

Hereby, all cancellations between real and virtual corrections are guaranteed by the KLN theorem and the cross section corresponds to a standard NLO calculation.

In the factorized case, we have at LO

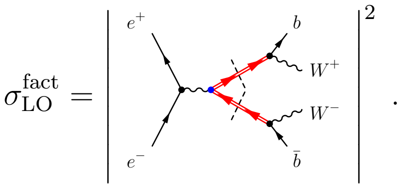

(6.34)

As before double lines indicate t propagators and a dashed line through them a factorized computation with on-shell projection. The NLO corrections to the decay can thus be written as

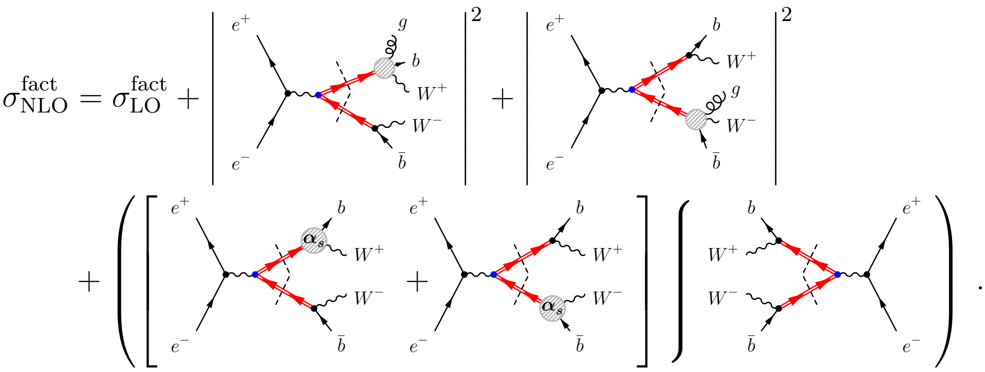

(6.35)

[1] Of course, σ_{NLO} does not directly contain σ_{LO} as we would use different parameters, especially for the width. But at this level we only care about the relevant diagrams.

Hereby, we have omitted final-state interferences between the legs in the real diagrams like

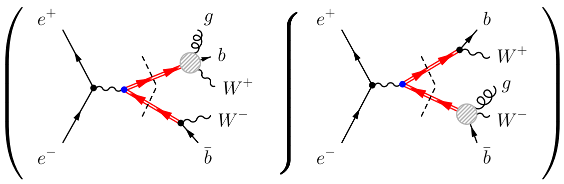

. (6.36)

The IR divergences of these diagrams only cancel when we would also consider virtual corrections that connect final-state bs. But these would require an integration over the form factor, which is unfeasible as described for the SD at the very beginning of this section, and are also not part of the factorizable corrections. Thus, we neglect these (basically NNLO) corrections.

Modifications to standard FKS for factorized NLO

In the following, we review the three main modifications to the FKS subtraction needed to cope with factorized NLO computations. We focus on top production but the statements also hold for general processes. We also emphasize that this approach, i.e. application of the DPA to Born, Real, and Virtual contributions, is particularly useful to compute NLO corrections to the decay only. In case, one is interested in simultaneous corrections to production and decay, one encounters further ambiguities in the real part. This is due to the different invariant mass of the resonance in case the radiation, carrying momentum, occurs in production or the decays. Thus, if one is only interested in fixed-order corrections, hybrid schemes have been devised, where the DPA is only applied to the virtual part [276]. In our situation, however, we have to embed the resummed form factor in the production, as described in Eq. (6.18), which already contains the Coulomb singularity. We can thus safely ignore issues related to real corrections to the production.

On-shell generation of the real phase-space Like the tree-level matrix element, the real matrix element has to be evaluated using on-shell momenta. To generate this phase-space, we use the same mappings as in resonance-aware FKS. As we described in Section 2.6, the real emission is generated in such a way that the invariant mass of the respective resonance is kept at its Born value, which removes mismatches between the real matrix element and its soft approximation. Thus, starting from an already on-shell projected Born momentum configuration, obtained as in Section 6.3.2, we apply this mapping to obtain an also on-shell projected real phase-space point. Note that, to ensure correct subtraction of soft divergences, also the real-emission FKS variables ξ and y need to be computed in the on-shell projected Born system. We stress that the on-shell momenta only enter the matrix elements and their subtraction terms but not the phase-space Jacobian. For the latter as well as event generation, the (physical) off-shell phase-space is used, which is generated alongside the on-shell case.

Decay subtraction The divergences in the factorized calculation all originate from the $t \to bWg$ matrix element. It consists of two Feynman diagrams. One in which the gluon is emitted from the top quark and another one in which it is emitted from the bottom. Divergences can only occur in emissions from particles with on-shell momenta and zero width. Therefore, in the full $\mathrm{W^+W^-b\bar{b}}$ matrix element, emissions from internal top quarks do not yield divergences, as they are regularized by the width. However, in the factorized approach, the gluon emission from the top quark is a singular contribution, which needs to be subtracted. We call this additional singular region a *pseudo-ISR* region. This way, each singular pair index (b, g) and $(\bar{b}, g)$ is associated with a pseudo-ISR tuple $(b, g)^*$ and $(\bar{b}, g)^*$, in which the gluon radiation occurs not from the bottom, but from the top quark. This means that in the corresponding singular region, the FKS phase-space contribution

$$d_{ij} = 2\left(p_i \cdot p_j\right) \frac{E_i E_j}{\left(E_i + E_j\right)^2}$$

is evaluated with $p_i \to p_{\mathrm{top}} = p_b + p_W$.

Omission of interference terms In the real matrix element, we omit interference terms between gluon emissions from different legs. In consequence, we must remove these interference contributions from the color-correlated Born matrix element. The same reasoning applies to the virtual part and its subtraction. The considered loop matrix elements do not include diagrams with gluon exchange between quarks on different legs since these contributions have already been resummed and are included in the form factor. Therefore, also in the soft part of the virtual subtraction terms, we leave out summands which correspond to gluon exchange between different legs. The absence of these interference terms allows to split up the FKS regions into two disjoint subsets of singular pairs, as depicted in Tab. 6.1.

Table 6.1 Singular regions in standard FKS for the full process $e^+e^- \to W^+W^-b\bar{b}$ and in modified FKS for the factorized process, split up into interference-free subsets and using pseudo-ISR regions.

α_r	emitter	singular pairs
1	5	$\{(5,7),(6,7)\}$
2	6	$\{(5,7),(6,7)\}$

α_r	emitter	pseudo-ISR	singular pairs
1	5	no	$\left\{(5,7),(5,7)^*\right\}$
2	5	yes	$\left\{(5,7),(5,7)^*\right\}$
3	6	no	$\left\{(6,7),(6,7)^*\right\}$
4	6	yes	$\left\{(6,7),(6,7)^*\right\}$

Chapter 7

Validation and Matching

7.1 Validation of the threshold resummation within Whizard

In order to validate the implementation in Whizard, we will compare the numeric MC integrations with analytic results obtained with the method described in Section 6.2.2. To remove nonphysical contributions from the analytic results, we should compare results for $\mathrm{W^+W^-b\bar{b}}$ with a Δ_{m_t} cut on the invariant mass of the reconstructed top momenta, i.e.

$$\left|\sqrt{(p_{W^+}+p_b)^2}-M_t^{1S}\right| \leq \Delta_{m_t} \quad \text{and} \quad \left|\sqrt{(p_{W^-}+p_{\bar{b}})^2}-M_t^{1S}\right| \leq \Delta_{m_t} \,. \tag{7.1}$$

We stress that although this cut depends on M_t^{1S}, the invariant mass distributions will be centered around m_t. While Eq. (7.1) is exact in Whizard, in the analytic calculation, cf. Ref. [250], we implement a cut on the *nonrelativistic invariant masses*,

$$t_{1,2} = 2m_t\Big(E_{1,2} - \frac{\boldsymbol{p}^2}{2m_t}\Big) \,, \tag{7.2}$$

by requiring that [59]

$$\left|t_{1,2}\right| \leq 2M_t^{1S}\Delta_{m_t} - \frac{3}{4}\Delta_{m_t}^2 + \mathcal{O}\left(v^2\right) \,. \tag{7.3}$$

The kinematic constraint $t_1 + t_2 < 2m_t(E_1 + E_2)$ is understood. Here, $E_{1,2}$ are the kinetic energies of top and anti-top quark, respectively, and $\boldsymbol{p}$ is the three momentum of the tops.

The different implementations of the cut is one source of disagreement between the Monte Carlo and the analytic results. In the threshold region, the difference should, however, be of higher order. To simplify the comparisons, we activate only S-wave contributions (the P-Wave only contributes beyond NLL to the inclusive cross section) and use the EHA in Whizard in the following.

7.1.1 Δ_{m_t} scans

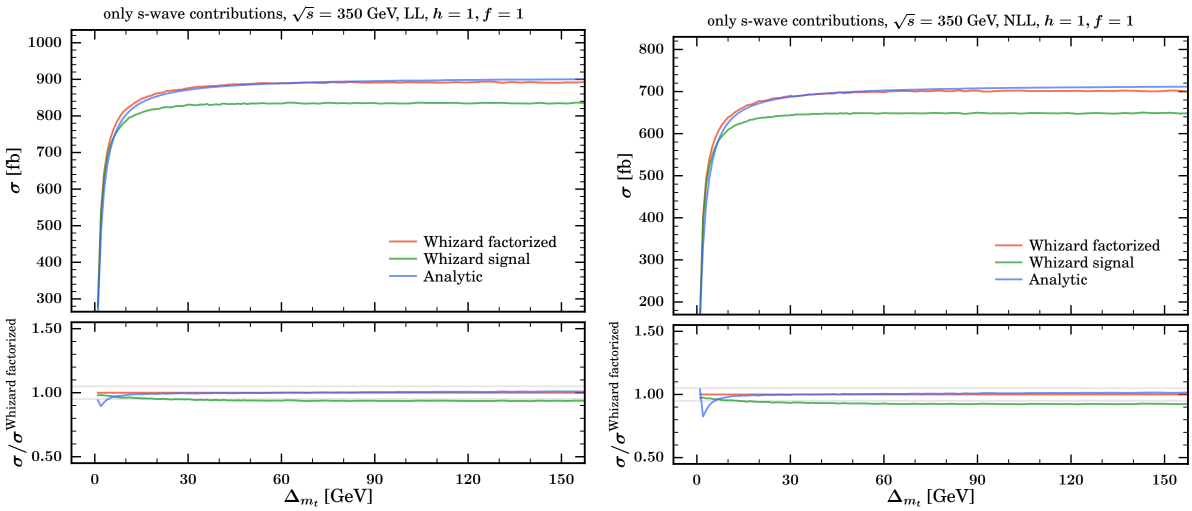

Figure 7.1 Comparison of analytic results with the implementation in WHIZARD with the factorized and the signal-diagram approach for $\sqrt{s} = 350\,\text{GeV}$ using a LL or NLL form factor. For better orientation, we indicate the $\pm 5\,\%$ range in the ratio with horizontal gray lines.

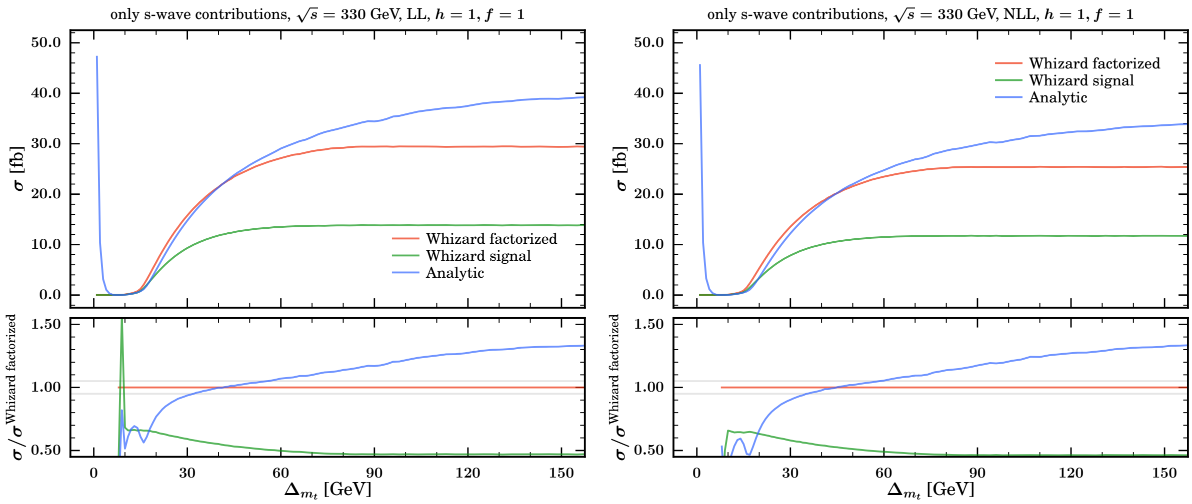

Figure 7.2 Comparison of analytic results with the implementation in WHIZARD with the factorized and the signal-diagram approach for $\sqrt{s} = 330\,\text{GeV}$ using a LL or NLL form factor.

In Fig. 7.1, we show Δ_{m_t} scans for a fixed energy above threshold of $\sqrt{s} = 350\,\text{GeV}$ using a LL and NLL form factor. As expected, the ratio of WHIZARD and the analytic results are nearly independent of the used form factor. At this energy, all approaches yield nearly the same results for all values of Δ_{m_t}. Only the signal diagram is a bit too low but is, anyhow, only shown for comparison. We note further that already here the analytic results fall off stronger for very small Δ_{m_t}. As they have been obtained by using an expansion in $(mv^2)/\Delta_{m_t}$, deviations for small Δ_{m_t}, comparable with mv^2, are expected. In Fig. 7.2, we go significantly below threshold, where the imaginary part of v grows further. At this energy, the analytic computation is unstable already at $\sim 15\,\text{GeV}$ and even rises for lower values of Δ_{m_t}. Also the MC integration of WHIZARD has problems to find double-resonant configurations within a $5\,\text{GeV}$ window at this energy. At high values of Δ_{m_t}, we encounter another problem of the analytic results, i.e. that they do not stabilize as soon as the physical phase-space has been covered. This is related to the second expansion in Δ_{m_t}/m_t that is performed. WHIZARD on the other hand, becomes stable around $80\,\text{GeV}$ as the physical phase-space does not allow for larger invariant masses at this energy. The signal-diagram is, as expected from Section 6.3.4, completely unreliable at this energy. Again, the ratios are independent of the used form factor.

7.1.2 $\sqrt{s}$ scans

In Fig. 7.3, we show $\sqrt{s}$ scans for a fixed value of Δ_{m_t}. According to the findings of the last section, we choose a *moderate*, $\Delta_{m_t} = 30\,\text{GeV}$, and a *loose* cut, $\Delta_{m_t} = 100\,\text{GeV}$, for this. An example of a *tight* cut, $\Delta_{m_t} = 15\,\text{GeV}$, is shown in Appendix D.2. As explained above, the analytic computation is only reliable for moderate cuts. To also check the implemented scale variations, we have produced bands according to a scale variation of

$$\begin{aligned} \Big(h, f\Big) &= \Big(2, 1\Big)\,, & \Big(h, f\Big) &= \Big(2, \frac{1}{2}\Big)\,, \\ \Big(h, f\Big) &= \Big(\frac{1}{2}, 2\Big)\,, & \Big(h, f\Big) &= \Big(\frac{1}{2}, 1\Big)\,. \end{aligned} \tag{7.4}$$

These capture approximately the possible area of scale uncertainties shown in Fig. 2 of Ref. [250]. Additionally to the LL and NLL, we also show the α_s expanded form factor, defined in Eq. (6.17), evaluated with α_{H}. Yet again, the shown ratios depend on the used form factor only very mildly. Some differences are, in principle, possible, as the form factor has a phase-space dependence on $\boldsymbol{p}$ and p_0. For $\Delta_{m_t} = 30\,\text{GeV}$, we observe perfect agreement between the analytic computation and WHIZARD with the factorized approach within a window around threshold of at least $10\,\text{GeV}$. For $\Delta_{m_t} = 100\,\text{GeV}$, this range is reduced due to nonphysical additional contributions below threshold in the analytic results. Notably, the behavior above threshold is not strongly affected but the ratio of analytic over WHIZARD falls off with approximately the same slope for both cut values. This is likely due to uncontrolled large v contributions that are not contained in the analytic results but occur in the full relativistic computation. This is not too concerning as neither of these results are to be trusted for these large values of $\sqrt{s}$ but have to be treated within the matched approach, which is introduced in Section 7.2. In addition to the shown validation plots, we have confirmed for fixed phase-space points that the independent implementations of the expanded, LL and NLL form factor agree up to numerical precision.

Overall, we can confirm that the NLL form factor is correctly and consistently embedded

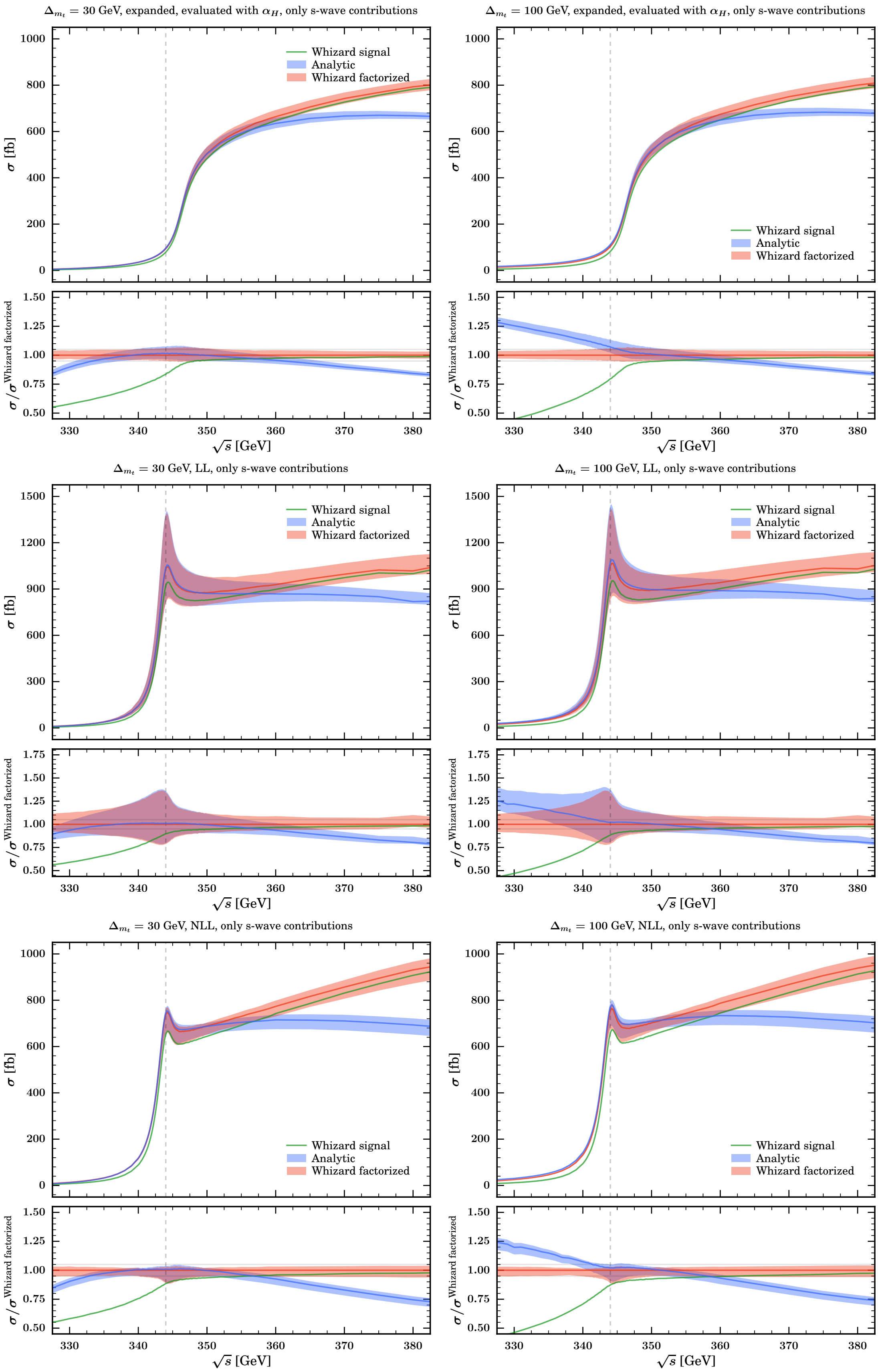

Figure 7.3 Comparison of analytic results with the implementation in WHIZARD with the factorized and the signal-diagram approach for $\Delta_{m_t} = 30\,\text{GeV}$ and $\Delta_{m_t} = 100\,\text{GeV}$ using an expanded, LL or NLL form factor. The bands correspond to the envelope of the scale variations mentioned in the text.

in WHIZARD. The differences to the analytic calculation are understood and we can rely on the implementation in WHIZARD with the factorized approach as it is more stable for small and large Δ_{m_t} values and yields fully differential results.

7.2 Matching

In this section, we combine the (N)LL cross sections σ_{NRQCD} with a (N)LO decay with the full, fixed-order (N)LO results σ_{FO} for $\mathrm{W^+W^-b\bar{b}}$ including all irreducible background processes and interferences. We maintain hereby as many interference terms as possible and keep terms of higher order in the nonrelativistic power counting.

Before we get into the details of the calculation, let us first remind that the resummed form factor is computed based on the assumption that $v \sim \alpha_s$. In a matched computation, which is valid to arbitrarily high $\sqrt{s}$, this assumption is, of course, no longer valid. Therefore, we need to introduce a switch-off function, which vanishes where we do not trust the resummed computation anymore and goes to one in the threshold region. The implementation that we are using is discussed in Section 7.2.2. We multiply this switch-off function with the couplings that enter the resummed computation.

Furthermore, we have to subtract the α_s expansion of the form factor to avoid double counting of the first order. The explicit form of the expanded form factor is shown in Section 6.2.5. With these ingredients, we can write down schematically a master formula

$$\begin{aligned}\sigma_{\mathrm{matched}} = \sigma_{\mathrm{FO}}\left[\alpha_{\mathrm{F}}\right] + \sigma^{\mathrm{full}}_{\mathrm{NRQCD}}\left[f_s\,\alpha_{\mathrm{H}},\ f_s\,\alpha_{\mathrm{S}},\ f_s\,\alpha_{\mathrm{U}}\right] \\ - \sigma^{\mathrm{expanded}}_{\mathrm{NRQCD}}\left[f_s\,\alpha_{\mathrm{F}}\right]\ ,\end{aligned} \tag{7.5}$$

with α_s evaluated at the hard (μ_{H}), firm (μ_{F}), soft (μ_{S}) and ultra-soft scales (μ_{U})

$$\begin{aligned}\alpha_{\mathrm{H}} &= \alpha_s\left[\mu_{\mathrm{H}} = hM_t^{1S}\right]\ , & \alpha_{\mathrm{F}} &= \alpha_s\left[\mu_{\mathrm{F}} = hM_t^{1S}\sqrt{\nu_*}\right]\ , \\ \alpha_{\mathrm{S}} &= \alpha_s\left[\mu_{\mathrm{S}} = hM_t^{1S} f\nu_*\right]\ , & \alpha_{\mathrm{U}} &= \alpha_s\left[\mu_{\mathrm{U}} = hM_t^{1S}(f\nu_*)^2\right]\ .\end{aligned} \tag{7.6}$$

We subtract hereby the leading α_s correction, which contains the dominating Coulomb singularity, with the firm scale α_{F} that is also used in σ_{FO}. We are introducing the firm scale here for the first time. It is the geometric mean between the soft and the hard scale and is constructed as an effective scale to reduce the difference between $\sigma^{\mathrm{full}}_{\mathrm{NRQCD}}$ and σ_{FO}. From the fixed-order point of view, α_{F} is a reasonable choice with a safe IR behavior.[1] We discuss the phenomenological impact on choosing α_{F} over α_{H} in Section 8.1.1. Returning to the matching, we choose to remove the first order at the firm scale, to maintain the scales in $\sigma^{\mathrm{full}}_{\mathrm{NRQCD}}$ at threshold. The switch-off function f_s guarantees that we obtain only σ_{FO} in the continuum. The exact contributions in σ_{FO}, $\sigma^{\mathrm{full}}_{\mathrm{NRQCD}}$ and $\sigma^{\mathrm{expanded}}_{\mathrm{NRQCD}}$ depend on

[1] There are known to exist IR-unsafe scales that evaluate significantly differently for Born and Real kinematics yielding ill-defined results.

the order and are discussed in detail in the next subsection.

7.2.1 Contributions in the matched cross section

It is not directly obvious which terms and interferences we have to take into account. Of course, we have to set it up in such a way that the cancellation of IR divergences between real and virtual QCD corrections works. Furthermore, we aim to include the dominating interference terms. We discuss all contributions in a diagrammatic way, omitting phase-space factors and ignoring parameters as it was introduced in Section 6.3.5. All shown contributions consist of gauge-invariant contributions only, cf. Section 6.3.1.

Although phenomenologically irrelevant, it is instructive to discuss how we would perform a matching of LO and LL. As already mentioned in Section 6.3.2, the LL cross section is obtained by multiplying the production matrix elements in Eq. (6.19) with the nonrelativistic form factor F. To extend this approach, we define $\tilde{F} \equiv F - 1$. Thus, $\tilde{F}$ contains everything of the form factor but the tree-level contribution, i.e. all terms of $\tilde{F}$ are $\mathcal{O}(\alpha_s)$ and higher. With this, we can expand the absolute square

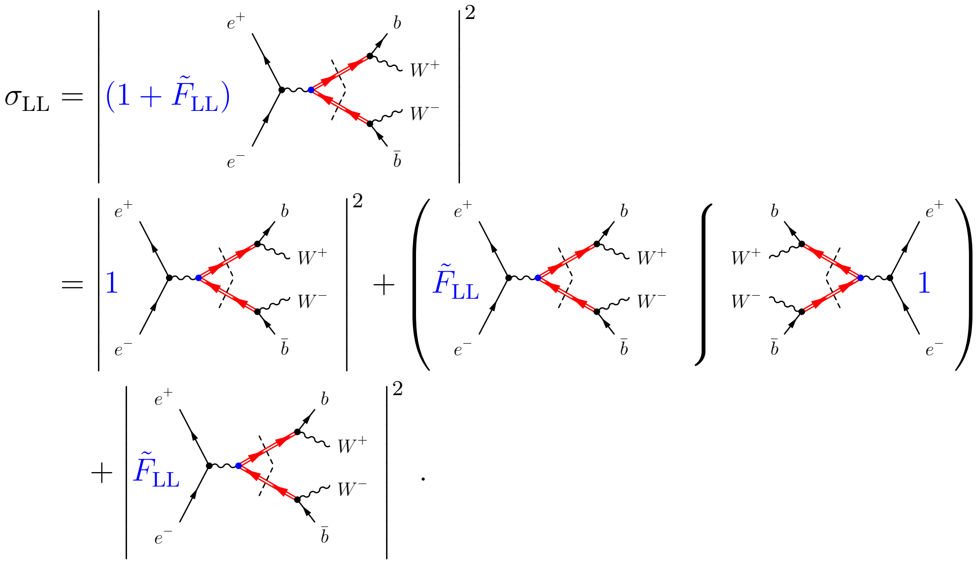

(7.7)

Again, the 1 corresponds to tree-level $\mathrm{t\bar{t}}$ production. So, we can straightforwardly include the full LO by replacing the 1 term by $\sigma_{\rm LO}$. As $\sigma_{\rm LO}$ does not contain α_s terms, no double-counting occurs and the expansion that we subtract, $\sigma_{\rm NRQCD}^{\rm expanded}$ of Eq. (7.5), is just the 1 term and is realized in the interference term of Eq. (7.7). Now considering the interference term, we want to improve the matched cross section by also including the interferences between the resummed and the full matrix element. We expect this to be the most important electroweak correction at threshold because it multiplies the large form factor on one side with all double-top, single-top and background diagrams on the other. As the DPA guarantees that the factorization works on the level of the complex amplitude, this is actually possible. Therefore, the full matched LO+LL reads

$\sigma_{\mathrm{LO+LL}}^{\mathrm{LOdecay}} = \sigma_{\mathrm{LO}} + \Bigg(\tilde{F}_{\mathrm{LL}}$ 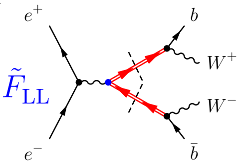

$\Bigg]$ 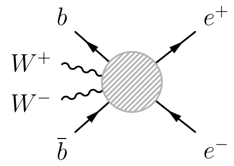

$\Bigg)$

$+ \Bigg| \tilde{F}_{\mathrm{LL}}$ 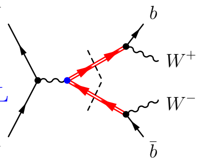

$\Bigg|^2 .$ (7.8)

It is understood that the scales and switch-off functions are applied as noted in Eq. (7.5). As all top decays are at the LO level, we obviously use the LO width for $\sigma_{\mathrm{LO+LL}}$.

As an intermediate step, we will now consider to include the full NLO cross section, σ_{NLO}, while still using a factorized LO decay. To simplify the discussion, we also use from now on a NLL form factor everywhere, although it would be possible to merely use a LL one at some points. As σ_{NLO} contains terms of $\mathcal{O}(\alpha_s)$, $\sigma_{\mathrm{NRQCD}}^{\mathrm{expanded}}$ now has to use the α_s expansion of the form factor, given in Eq. (6.17). Note that the tilde still only denotes the subtraction of the 1, $\tilde{F}_{\mathrm{NLL}} \equiv F_{\mathrm{NLL}} - 1$. Thus, $F_{\mathrm{NLL}} - F_{\mathrm{NLL}}^{\mathrm{exp}} \neq \tilde{F}_{\mathrm{NLL}}$ and we obtain

$\sigma_{\mathrm{NLO+NLL}}^{\mathrm{LOdecay}} = \sigma_{\mathrm{NLO}} + \Bigg((F_{\mathrm{NLL}} - F_{\mathrm{NLL}}^{\mathrm{exp}})$ 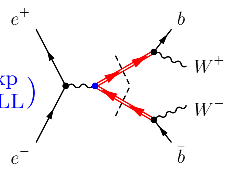

$\Bigg]$ 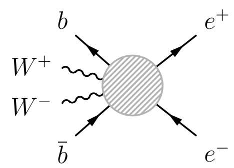

$\Bigg)$

$+ \Bigg| \tilde{F}_{\mathrm{NLL}}$ 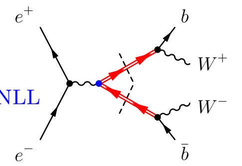

$\Bigg|^2 .$ (7.9)

Diagrammatically, Eq. (7.9) is very clear and the only difference to Eq. (7.8) is the α_s correction. Concerning the top width, however, we are now in a dilemma. From the point of view of the factorized computation, we are still using a LO decay, so a LO width is appropriate for both the $|\tilde{F}|^2$ term as well as the interference term. On the other hand, when we consider $F_{\mathrm{NLL}}^{\mathrm{exp}}$ as the dominating term in σ_{NLO}, due to the large Coulomb singularity, we would require a NLO width to match the term in the virtual part of σ_{NLO}. This problem is an artifact of trying to match two computations that treat the top decay differently. We can solve it by incorporating the factorized NLO decay, introduced in Section 6.3.5.

The interference term can by construction not receive real and virtual corrections. When we try to add gluons to the left and the right hand side of the interference term, we see that the IR structure of those diagrams is quite different. Thus, we only have to compute corrections to $|\tilde{F}|^2$ to arrive at our final matching formula

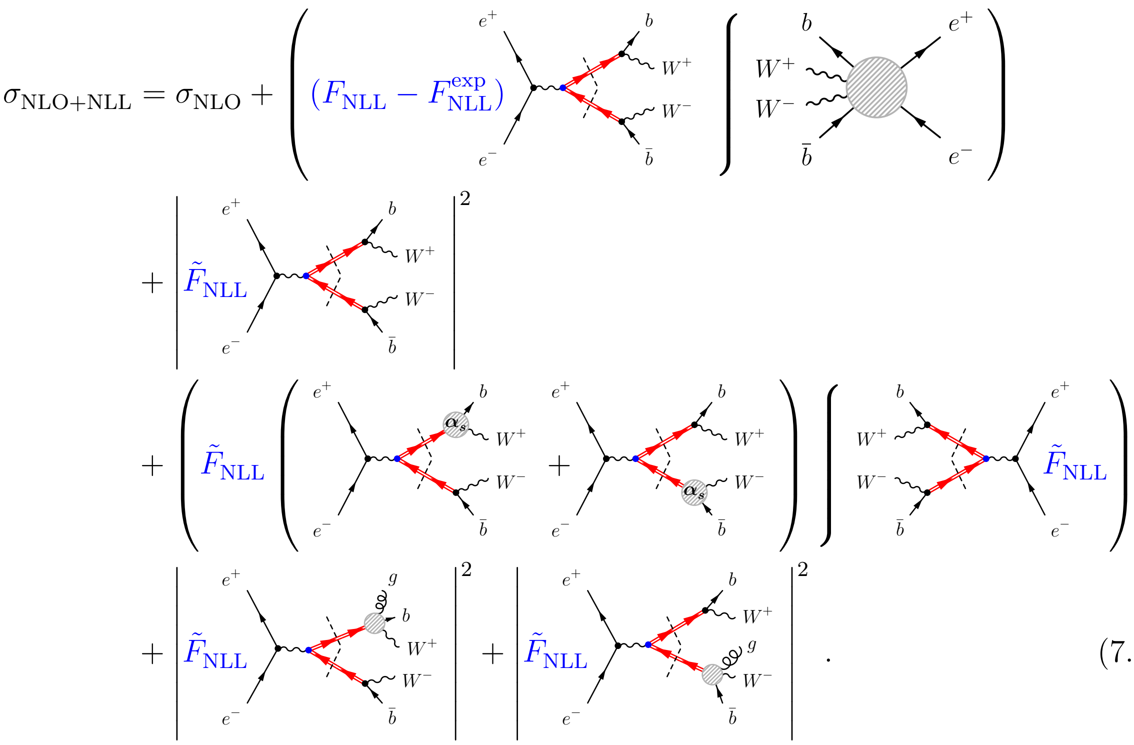

(7.10)

Hereby, the last two lines can be seen as part of the NNLO corrections to $\mathrm{W^+W^-b\bar{b}}$ at threshold.

7.2.2 Switch-off function

As noted before, we need a well-defined way to switch off the resummation where we do not trust the results anymore and use the full fixed-order NLO instead. The minimal requirements for the switch-off function $f_s(v_{1S})$ are

$$f_s\left(v_{1S}\left(\sqrt{s} = 2M_t^{1S}\right)\right) = 1 \quad \text{and} \quad f_s(1) = 0\,, \tag{7.11}$$

where the 1S-velocity, $v_{1\mathrm{S}}$, is obtained by replacing m_t in Eq. (6.10) by $M_t^{1S}$and $\Gamma_\mathrm{t}\left[m_t\right]$ by $\Gamma_\mathrm{t}\left[M_t^{1S}\right]$

$$v_{1\mathrm{S}} = \sqrt{\frac{\sqrt{s} - 2M_t^{1S} + \mathrm{i}\Gamma_\mathrm{t}\left[M_t^{1S}\right]}{M_t^{1S}}} \tag{7.12}$$

This is motivated by the fact that we want to ensure that the 1S peak is not affected by f_s. Thus, we center the switch-off around the 1S mass and not around the pole mass. To simplify the notation, we will in the following refer to v_{1S} as v when it is clear that it is in the context of f_s. As v is complex by definition but the power counting that motivates Eq. (7.11) is only meaningful for a real parameter, we can use the imaginary part, real part or absolute value of v. All of these are shown in Fig. 7.4. We see that real and imaginary

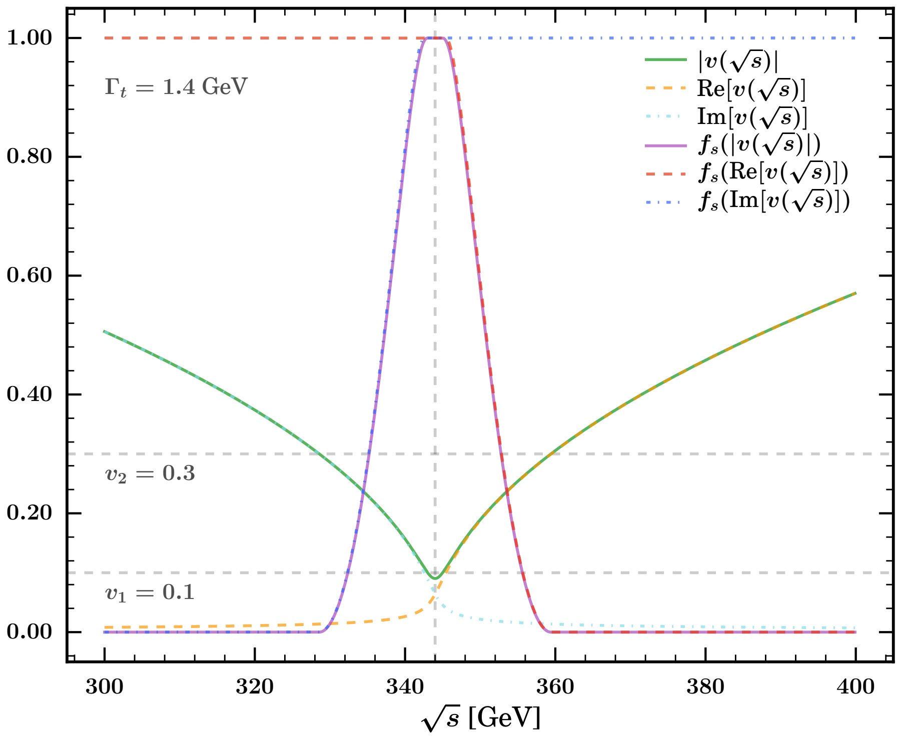

Figure 7.4 Absolute value as well as real and imaginary part of the velocity v. The switch-off function, f_s, is shown as a function of each of these. In addition to the vertical line at $2M_t^{1S}$, we signify the two used matching parameters v_1 and v_2 with horizontal lines.

part of v are roughly mirrored at $2M_t^{1S}$ with a slight asymmetry due to the $+\mathrm{i}\Gamma_\mathrm{t}$ in the radicand of Eq. (7.12). To switch off the resummation for large values of $\sqrt{s}$, it would be sufficient to only use the real part of v. However, also a couple of GeV below threshold, the resummed calculation contains unphysical contributions [250] and we prefer to use fixed-order results there. This is mostly important in terms of relative deviations as the cross section is very small below threshold. Thus, we take $|v|$ as measure of how close we are to threshold. Note that due to the width that enters the definition of the velocity, $|v| = \sqrt{\Gamma_\mathrm{t}/M_t^{1S}} \sim 0.1$ at $2M_t^{1S}$ is the minimal value and v never vanishes. This, of course, enables the reliable perturbative computation in the first place as the width acts as an effective IR cutoff.

The explicit form of f_s is not too important as it is only a tool to remove unphysical contributions. There are, however, two properties one should avoid when devising f_s. Firstly, it should be not only continuous but also continuously differentiable like any physical cross section. This property disqualifies the most simple solution of a linear switch-off between start v_1 and end v_2:

$$f_s(v) = \begin{cases} 1 & v < v_1 \\ 1 - \frac{v-v_1}{v_2-v_1} & v_1 \leq v \leq v_2 \\ 0 & v > v_2 \end{cases} . \tag{7.13}$$

Secondly, when using polynomials of high order that at first switch off slowly but transition quickly, one risks to introduce an unphysical wiggle in the cross section. After experimenting with different types of switch-off functions, cf. Appendix D.1, we decided to use a simple polynom of the lowest order that satisfies continuity and continuous differentiability at both v_1 and v_2:

$$f_s(v) = \begin{cases} 1 & v < v_1 \\ 1 - 3\left(\frac{v-v_1}{v_2-v_1}\right)^2 - 2\left(\frac{v-v_1}{v_2-v_1}\right)^3 & v_1 \leq v \leq v_2 \\ 0 & v > v_2 \end{cases} . \tag{7.14}$$

Equation (7.14) is a cubic Hermite interpolation that is in the context of interpolation also known as *smoothstep*. For illustration, we show in Fig. 7.4 the switch-off function as a function of the absolute value as well as real and imaginary part. The used matching parameters, $v_1 = 0.1$ and $v_2 = 0.3$, are included as horizontal lines and their intersection with v identify start and end point of the matching. Judging from Fig. 7.4, $v_1 = 0.1$ in fact seems to be an advisable lower limit for v_1 as going lower would in turn not guarantee that $f = 1$ at $2M_t^{1S}$ and thus artificially reduce the threshold peak. On the other hand, it is harder to devise a strict rule for an upper limit of v_2. We think that one could go further than the shown $v_2 = 0.3$, which leads to a fairly quick switch-off, up to 0.4. Going further seems questionable, though, as this is already more than two times $\alpha_s\left[m_Z\right]$.

Let us finally remark that it would in principle also be possible to multiply the switch-off function with the cross sections instead of the couplings. For the first order, both approaches would be equivalent. For the subsequent higher orders, contained in the form factor, this is no longer the case. Here, multiplying the couplings should lead to a smoother, more sensible switch-off compared to the more ad hoc solution of turning off the cross section.

7.2.3 Theoretical uncertainties

For scale variations, we will vary over the hard scale with the multiplier h as well as over the soft and ultra-soft scales with the multiplier f as discussed in Section 6.2.4. In particular, we sample the corners of the space of scale variations, as discussed already in

Section 7.1.2, defining the set

$$\begin{aligned} \mathrm{HF} = \Big\{ \Big(h,f\Big) = \Big(2,1\Big)\,, \qquad\qquad & \Big(h,f\Big) = \Big(2,\frac{1}{2}\Big)\,, \\ \Big(h,f\Big) = \Big(\frac{1}{2},2\Big)\,, \qquad\qquad & \Big(h,f\Big) = \Big(\frac{1}{2},1\Big) \Big\}\,. \end{aligned} \tag{7.15}$$

Furthermore, we have to vary over the matching scales. As noted above, we will vary v_1 and v_2 within [0.1, 0.4] and also vary the difference between v_1 and v_2 therein. Considering the reliability on the obtained variation bands, we have to consider that it has been shown in Ref. [250] that the traditional NLL scale variation band does not envelop the NNLL prediction. While we include additional electroweak and relativistic corrections, we have to assume that this also applies to our computation. A possible more conservative estimate of the theoretical uncertainties would be to symmetrize the NLL scale uncertainties, which are highly asymmetric with respect to the central value, cf. Fig. 7.3. This can be realized by computing

$$\sigma_{\max} = \max\left[\max_{i\in\mathrm{HF}} \sigma_i\ ,\ \sigma_0 + (\sigma_0 - \min_{i\in\mathrm{HF}} \sigma_i)\right] \tag{7.16a}$$

$$\sigma_{\min} = \min\left[\min_{i\in\mathrm{HF}} \sigma_i\ ,\ \sigma_0 - (\max_{i\in\mathrm{HF}} \sigma_i - \sigma_0)\right] \tag{7.16b}$$

for each $\sqrt{s}$ point where $\sigma_0 \equiv \sigma(h=1, f=1)$ is the cross section at central value. The obtained bands are then symmetric in the sense that $\sigma_{\max} - \sigma_0 = \sigma_0 - \sigma_{\min}$ for all $\sqrt{s}$, as follows directly from Eq. (7.16). Note that we perform this procedure for each of the matching parameters. To obtain a final uncertainty band of matched NLO+NLL, we take the envelope of all of these bands. This will be shown in the next chapter.

Chapter 8

Numerical predictions

8.1 Inclusive results

8.1.1 Fixed-order results

In Fig. 8.1, we show NLO predictions for $\mathrm{W^+W^-b\bar{b}}$ and $\mathrm{t\bar{t}}$ as a function of $\sqrt{s}$ and the renormalization scale μ_R. For the off-shell production, we show the effect of replacing the

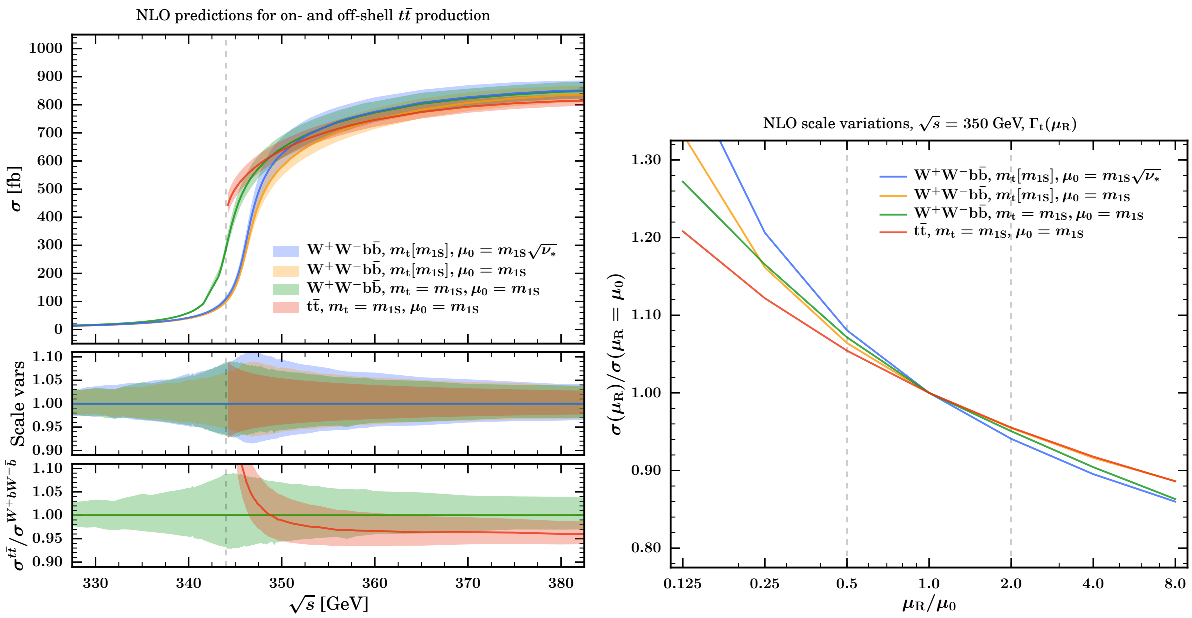

Figure 8.1 Total cross sections for on-shell and off-shell $\mathrm{t\bar{t}}$ production as a function of $\sqrt{s}$ and μ_R. In the lower panels of the $\sqrt{s}$ scan around the threshold region, we show the scale variations of each computation as well as the ratio of $\mathrm{t\bar{t}}$ over $\mathrm{W^+W^-b\bar{b}}$. For $\mathrm{W^+W^-b\bar{b}}$, we show the impact of replacing the pole mass by the 1S mass ($m_t = M_t^{1S}$) and using M_t^{1S} or $M_t^{1S}\sqrt{\nu_*}$ as renormalization scale. The details of the scale variations are explained in the text.

pole mass m_t by the 1S mass M_t^{1S} and of different scales. As expected, computing the pole mass with Eq. (6.11) leads to a shift of the full NLO cross section. The form of the scale variations, however, does not change significantly. This is especially noteworthy, as we have varied both h and f (which modifies ΔM as shown in Eq. (6.11)), according to

Eq. (7.15), to obtain the $m_t[M_t^{1S}]$ band. Hereby, h modifies the renormalization scale that enters fixed-order matrix elements as well. For the other bands, only the h variation is performed and f is ignored. The f variation is only a minor effect for the full NLO, as one can see in the similarity of the scale variations in Fig. 8.1.

We have already discussed in Section 7.2 that we prefer to match the fixed-order result with the firm scale, which is more sensitive to the threshold dynamics. Thus, we also show results for $\mu_0 = \mu_\mathrm{F} \equiv M_t^{1S}\sqrt{\nu_*}$. The corresponding results are very similar to the ones with the hard scale but yield a slightly bigger scale variation band that is more sensitive to the threshold. The central value is also mildly increased. To assess the impact of the off-shell description at the inclusive level at NLO, we also show predictions for $\mathrm{t\bar{t}}$. We find that it systematically lies 3 % to 4 % below $\mathrm{W^+W^-b\bar{b}}$, starting from $\sim 355\,\mathrm{GeV}$. Concerning the high-energy behavior, we refer to Part II, where the deviations are even larger. Below 350 GeV, i.e. approaching the threshold, where off-shell effects play a major role, $\mathrm{t\bar{t}}$ deviates strongly from $\mathrm{W^+W^-b\bar{b}}$. In the right plot of Fig. 8.1, we show the scale variations in a wider range for fixed $\sqrt{s} = 350\,\mathrm{GeV}$. In this case, we omitted the f variations and just vary μ_R via h. The qualitative scale behavior is the same for all descriptions. Note that for this it is important that the width is computed with the same renormalization scale as it is used in the full computation, as also described in Part II. Overall, the variations are slightly asymmetric with stronger deviations for lower μ_R.

8.1.2 Matched results

In Fig. 8.2, we show matched results employing the NLL form factor in combination with a NLO decay and full NLO contributions to $\mathrm{W^+W^-b\bar{b}}$ as described in Eq. (7.10). We study four different matching parameter choices by varying $v_1 \in \{0.1, 0.15\}$ and $v_2 \in \{0.3, 0.4\}$. The difference between the different matching parameters is nonnegligible, especially in the cross-over region of $\sim 348\,\mathrm{GeV}$ and below the peak, where the scale variations of each of the matched descriptions is small. This makes it very clear that it is not enough to pick only one suitable set of matching parameters as the scale variations do not suffice to cover other equally viable matching choices in the transition region. We observe, however, that the matching fulfills quantitatively what we demanded qualitatively a priori: In the threshold region (the $\sim 5\,\mathrm{GeV}$ around $\sqrt{s} = 2M_t^{1S}$) and in the continuum region ($\gtrsim 375\,\mathrm{GeV}$ and $\lesssim 330\,\mathrm{GeV}$) we recover the resummed and the fixed-order result, respectively. Note that our best prediction in the threshold region is not the NLL one, which is only shown for comparison, but the enhanced version of Eq. (7.10) without a switch-off function, which includes single-top as well as background contributions in terms both with and without the form factor. Phenomenologically, we observe that in the threshold region the matched descriptions are slightly larger than the NLL prediction, which is a correction that coincides in size and direction roughly with the NNLL results [250]. The asymmetric NLL scale variations, cf. Fig. 7.3, are also present in the matched results. This can be seen in more detail in Fig. 8.3: In the left plot, we show the individual behavior of the

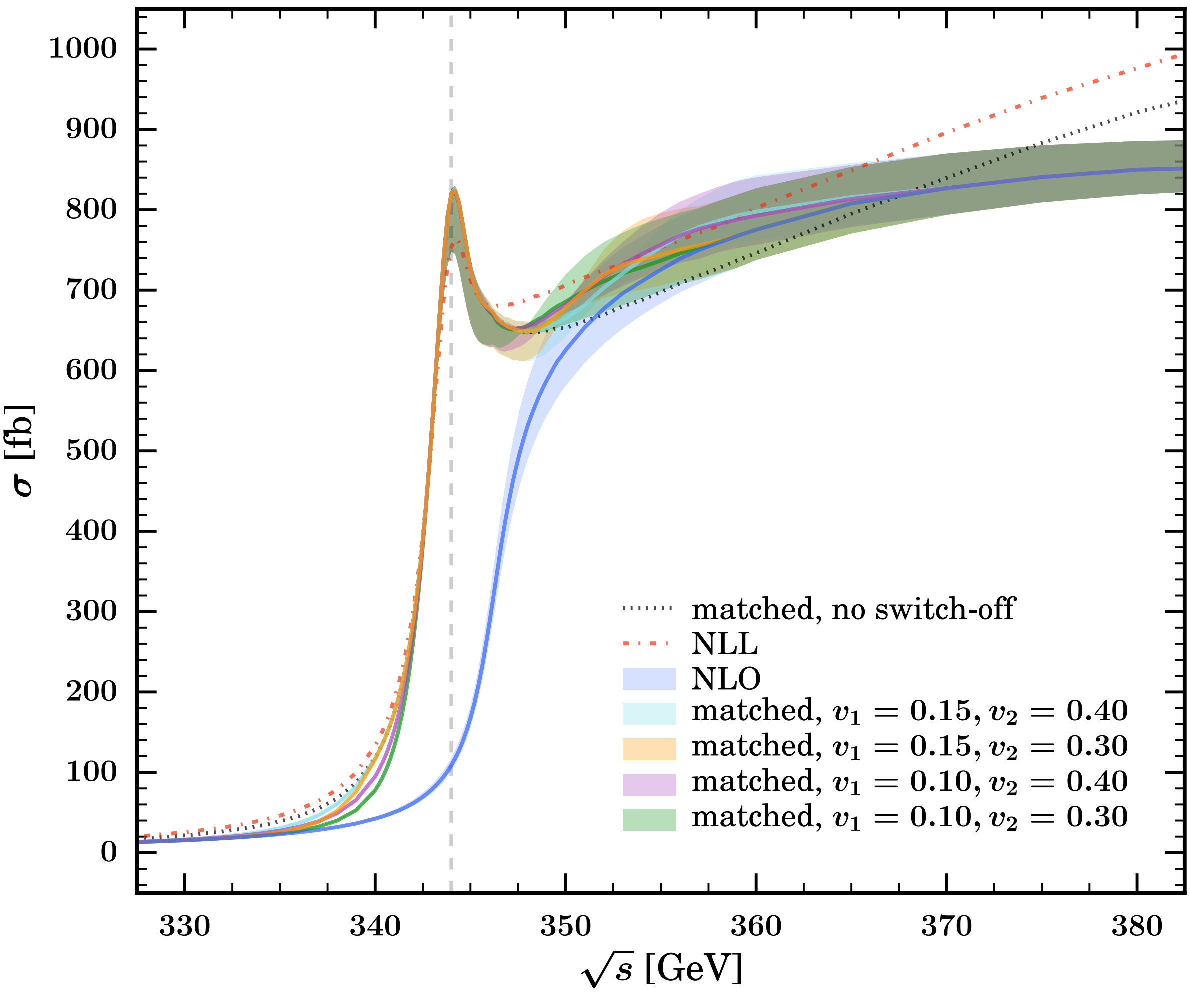

Figure 8.2 Inclusive cross section according to the matching description employing the NLL form factor in combination with a NLO decay and full NLO contributions to $\mathrm{W}^+\mathrm{W}^-\mathrm{b}\bar{\mathrm{b}}$ as described in Eq. (7.10). We show four different matching parameters with the cyan, orange, purple and green bands, the matched cross section without switch-off function as black dotted line, the NLL as red dashdotted line as well as the pure fixed-order NLO result for $\mathrm{W}^+\mathrm{W}^-\mathrm{b}\bar{\mathrm{b}}$ as blue band. The bands correspond to h and f variations as described in Section 7.2.3.

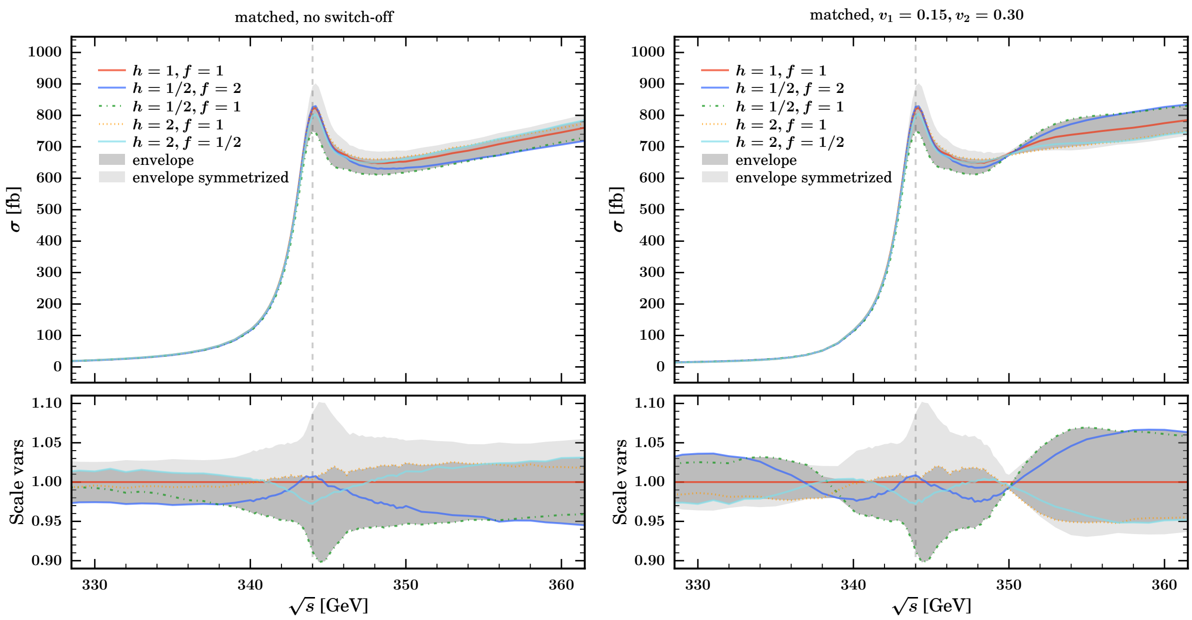

Figure 8.3 Inclusive cross section according to different scale choices for either no switch-off function (left) and $v_1 = 0.15$, $v_2 = 0.30$ (right). In addition to the lines that can be identified with the legend, we show an envelope in dark gray as well as the symmetrized envelope in light gray, which was introduced in Section 7.2.3.

different h, f scale choices without an active switch-off. Note the nontrivial interplay going from continuum to threshold to continuum again. The largest σ_i is given for different $\sqrt{s}$ by either $(h, f) = (2, 1/2)$, $(h, f) = (2, 1)$ or even $(h, f) = (1/2, 2)$. For other energies, $(h, f) = (1/2, 2)$ can also be the smallest σ_i although the characteristic dip at threshold is given by $(h, f) = (1/2, 1)$. For a more conservative theory error estimate, we also show the symmetrized envelope that has been computed with the procedure outlined in Section 7.2.3 in light gray. In the right plot of Fig. 8.3, we can study the already mentioned cross-over effect when the switch-off function is active. It is a result of the opposite scale behavior of the NLL in the threshold region and the more simple NLO in the continuum. The NLO scale variations are as one would naively expect and as we have already shown in Fig. 8.1. For smaller renormalization scales (controlled by h), α_s increases and thus the cross section increases. The opposite is true for larger scales. The f variation is only a minor modification on top of this as it only indirectly changes the result by changing m_t. The NLL, however, has a more or less opposite behavior and this creates a very small scale variation in the cross-over region. Note that the symmetrization of the envelope barely affects the continuum region and also does not remove the cross-over. The cross-over becomes, however, irrelevant as soon as one includes a variation over multiple switch-off parameters. This is shown in Fig. 8.4. The full combination of scale variations and matching variations is our best and most conservative prediction for $\mathrm{W^+W^-b\bar{b}}$ production at threshold and continuum. It shows no more cross-over regions as they occur at different $\sqrt{s}$ for different matching parameters. By also performing the symmetrization, we believe to have a reliable estimate of the theory uncertainty in the sense that the next order result

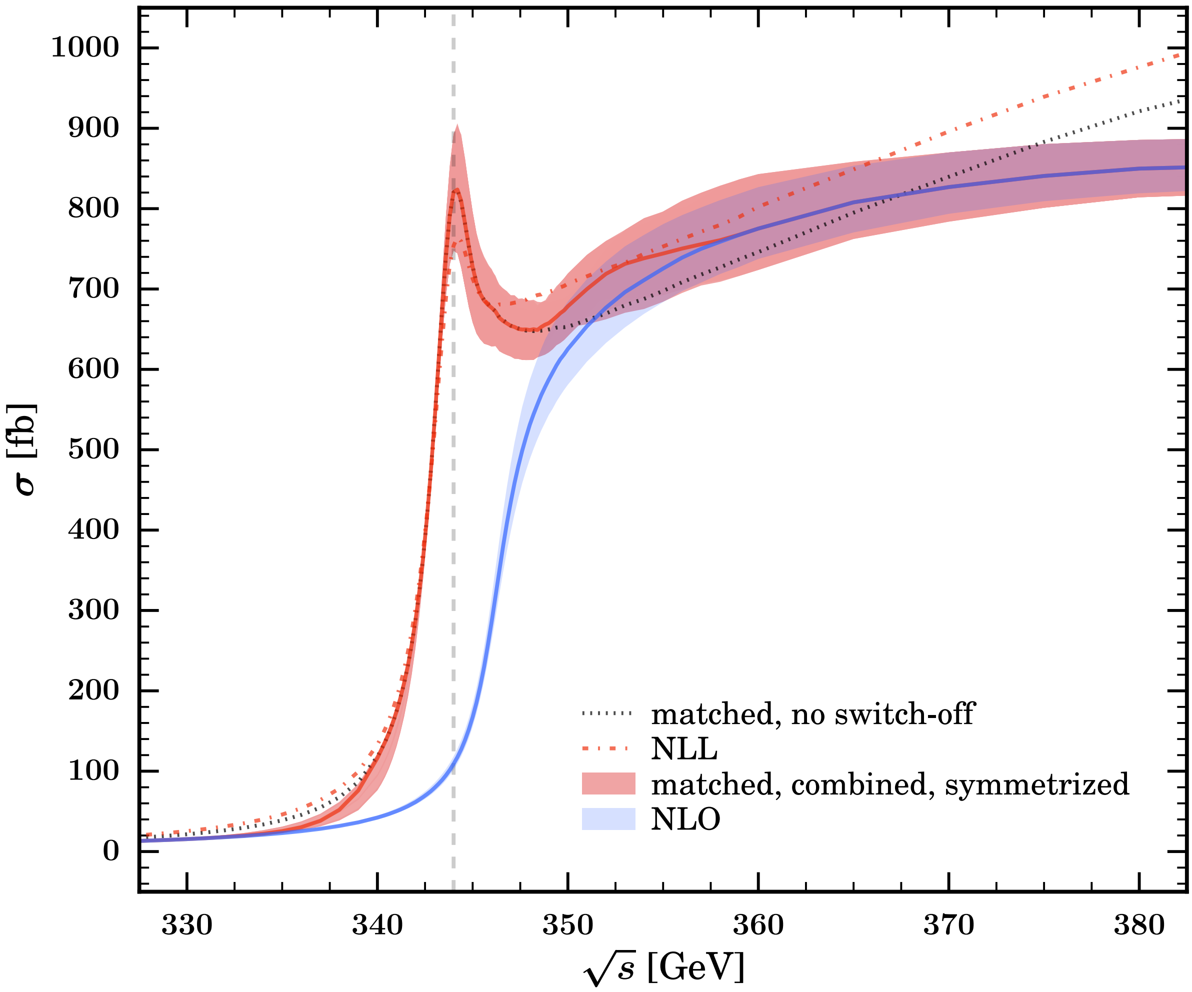

Figure 8.4 Inclusive cross section according to the matching description by combining the symmetrized scale variation envelopes of different variation parameters. Other lines and band as in Fig. 8.2.

is likely included in our bands. Of course, this does not include the fixed-order NLO EW corrections, which have to be considered on top of this.

8.2 Differential results

For the analysis of the generated events, we use a custom Rivet [116] analysis. Partons are clustered with the generalized k_T algorithm (`ee_genkt` in FastJet) [175, 219] with $R = 0.4$ and $p = -1$. A minimal jet energy of 1 GeV is required. We assume a perfect b-tagging efficiency including the charge. Thus a b-jet ($\overline{\mathrm{b}}$-jet), $\mathrm{j_b}$ ($\mathrm{j_{\bar{b}}}$), is a jet containing a b ($\overline{\mathrm{b}}$) quark. We always require at least two jets during the analysis. For distributions of observables that are identical for $\mathrm{t} \leftrightarrow \overline{\mathrm{t}}$, $\mathrm{b} \leftrightarrow \overline{\mathrm{b}}$ and $\mathrm{W}^+ \leftrightarrow \mathrm{W}^-$, we only show t, b and W^+, respectively. If not stated otherwise, the results are obtained at $\sqrt{s} = 2M_t^{1S} = 344\,\mathrm{GeV}$. Keep in mind that this is slightly below the kinematical threshold $\sqrt{s} = 2m_t$, thus the preferred kinematical situation is one with one on-shell and one off-shell top propagator.

8.2.1 Top observables

We start the discussion of differential distributions with the classic top observables, which can already be defined for the on-shell $\mathrm{e}^+\mathrm{e}^- \to \mathrm{t}\overline{\mathrm{t}}$ process. In Fig. 8.5, we show the top and anti-top polar angle as well as the top energy, invariant mass, three-momentum and transverse momentum. The polar angle distribution is fairly flat already at NLO. This is expected, as the forward-backward asymmetry for top-pair production at lepton colliders is minimal at threshold [233]. Note that $\sigma_\mathrm{matched}/\sigma_\mathrm{NLO}$ shows a slight slope opposite to the polar angle distribution and thus flattens the distribution even further. The energy of the reconstructed top quark peaks strongly around m_t, corresponding to on-shell tops with no velocity. The matched description enhances this peak by a factor of ~ 14, while contributing very little to the off-shell configurations. The invariant top mass shows a very similar behavior. As we are including all irreducible backgrounds to $\mathrm{W}^+\mathrm{W}^-\mathrm{b}\overline{\mathrm{b}}$ to NLO in QCD, there are still contributions for $\Delta M > 30\,\mathrm{GeV}$ at the per cent level from σ_NLO in σ_matched. At this point, we remind the reader that the $\sigma_\mathrm{matched} - \sigma_\mathrm{NLO}$ part is, apart from interference terms, only containing double-top propagators according to Eq. (7.10). Thus, it corresponds approximately to a pure Breit-Wigner distribution, which falls off quicker than σ_NLO, especially for larger $m^{\mathrm{W}^+\mathrm{j_b}}$ as seen in Fig. 8.5. Finally, the three-momentum, $|\mathbf{p}|^{\mathrm{W}^+\mathrm{j_b}}$, distribution is a key figure in understanding the dynamics at threshold. As expected, low three-momenta are preferred both at NLO and in the matched descriptions. We observe a strong enhancement of low momenta due to the threshold resummation, leading to an enhancement of over ~ 17 below 20 GeV that flattens to below 2 above 70 GeV. The projection to the transverse plane results in a very similar distribution in $p_\mathrm{T}^{\mathrm{W}^+\mathrm{j_b}}$. As noted earlier, we omit the histograms for E, m, $|\mathbf{p}|$ and p_T for $\mathrm{W}^-\mathrm{j_{\bar{b}}}$, as they are nearly identical to their top counterparts.

In Fig. 8.6, we show a more finely binned distribution of the top invariant mass. Unsurprisingly, it peaks in the bins 172 GeV to 174 GeV, which correspond to the pole mass $m_t = 173.124\,\mathrm{GeV}$. It is interesting to see, though, that $\sigma_\mathrm{matched}/\sigma_\mathrm{NLO}$ is maximal slightly below the peak in the 170 GeV to 171 GeV bin. This is related to the dominant

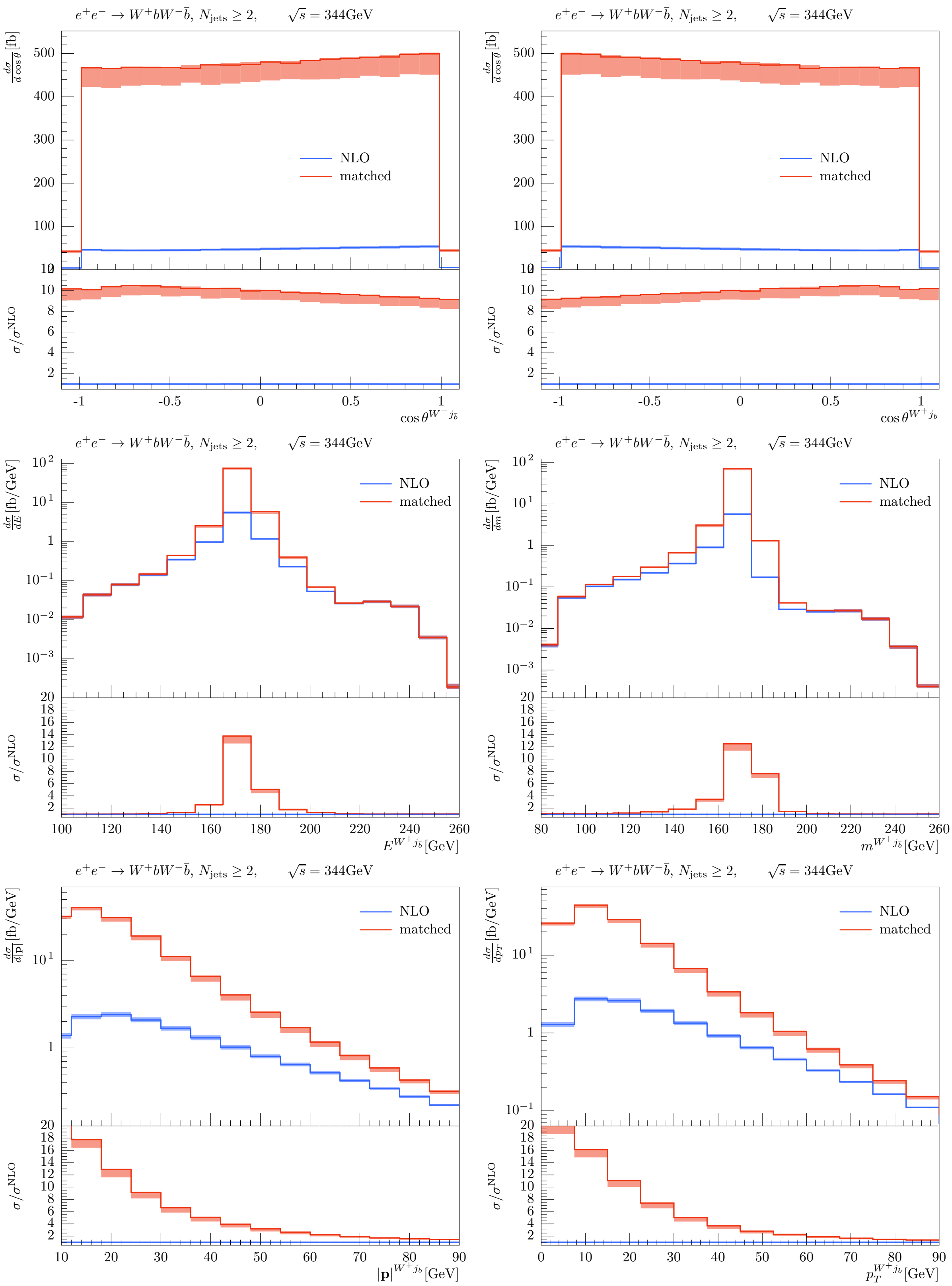

Figure 8.5 Top and anti-top polar angle as well as the top energy, invariant mass, three-momentum and transverse momentum distributions. The blue line describes the fixed-order σ_{NLO} cross section, while the red line contains all contributions of σ_{matched} according to Eq. (7.10). The bands correspond to the scale variations, described in Eq. (7.15), i.e. they have not been symmetrized as proposed in Section 7.2.3. In the lower panel, we show the ratio of $\sigma_{\text{matched}}/\sigma_{\text{NLO}}$.

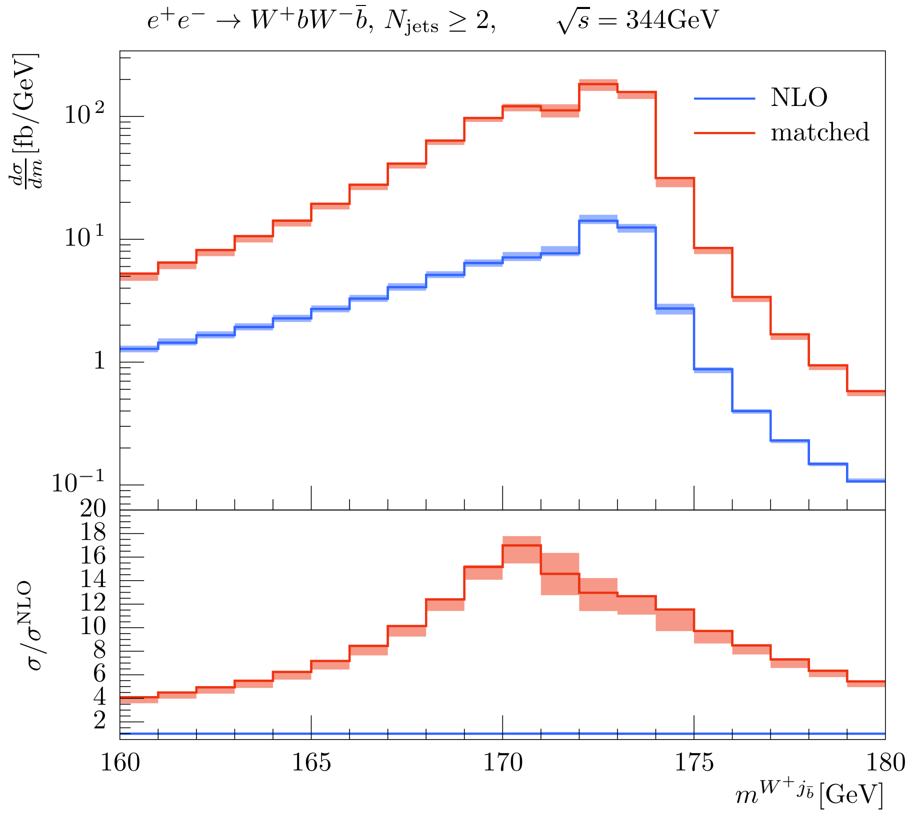

Figure 8.6 Invariant mass distribution of reconstructed top quarks close to the mass peak. Lines, bands and panels as in Fig. 8.5.

kinematic configuration that is realized with two top-quark propagators slightly below threshold, i.e. one is on-shell and the other one is slightly off-shell due to the insufficient energy.

8.2.2 Top decay products

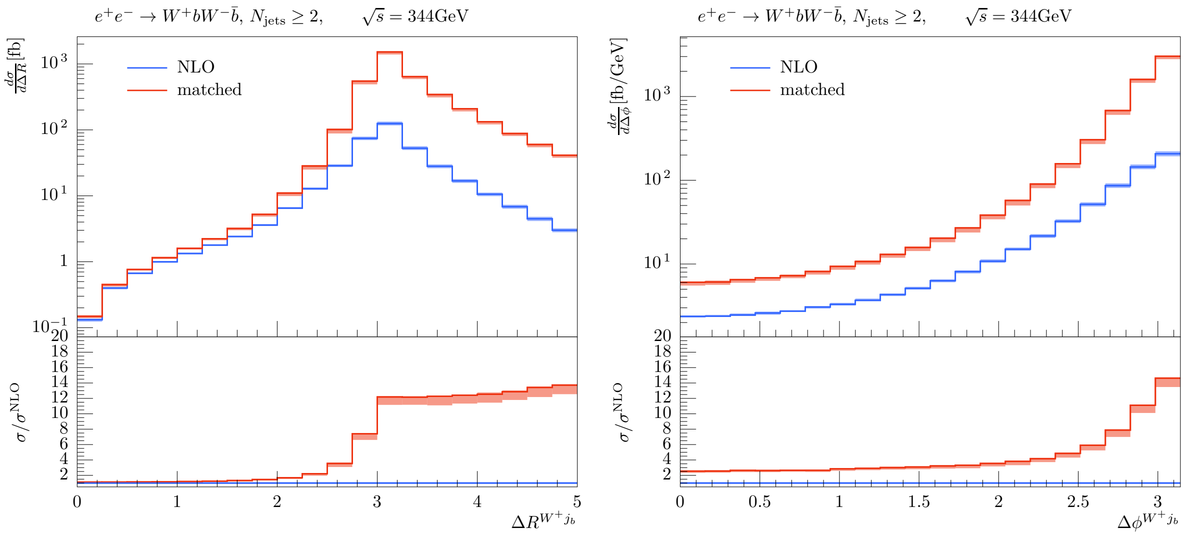

Figure 8.7 Distributions of rapidity and azimuthal angle differences between b-jets and W^+ bosons. Lines, bands and panels as in Fig. 8.5.

In Fig. 8.7, we show the rapidity and azimuthal angle differences between b-jets and W^+ bosons. These tell us a lot about the kinematics of the top decay and the underlying background. In the rapidity difference, we observe already in the NLO results a peak around $\Delta R^{\mathrm{W}^+\mathrm{j_b}} = 3$. This is quite different from the situation at high energies, like 800 GeV, where a rather low R separation of ~ 1 is favored. Obviously, this is related to the boost of the top decay products. At threshold, the tops have preferably low three momenta $\left|\mathbf{p}\right|^{\mathrm{W}^+\mathrm{j_b}}$, cf. the bottom left plot in Fig. 8.5. Thus, the back-to-back decay is nearly unboosted and W^+ and $\mathrm{j_b}$ move in opposite directions in the lab frame. On the other hand, at high energies W^+ and $\mathrm{j_b}$ will be boosted in the same direction and thus move preferably in a cone around the original top momentum, leading to a smaller average ΔR. Going to the matched results, we see that they lead to an almost constant enhancement of the $\Delta R \geq 3$ regime, while barely enhancing the NLO results for $\Delta R \leq 2$. Thus, we can expect the events for $\Delta R \leq 2$ to be dominantly irreducible backgrounds of $\mathrm{W^+W^-b\bar{b}}$. Finally, we note that in the azimuthal angle difference the same physics is reflected. Here, we can see a preferred angle separation of $\Delta\Phi = \pi$, as expected at threshold. For comparison, at 800 GeV a value of $\sim \pi/4$ is favored. Also in this case, the matched results enhance the pure top-decay topology. Compared to the R separation, there is no jump in $\sigma_{\text{matched}}/\sigma_{\text{NLO}}$, though, but a continuous increase going to larger angles.

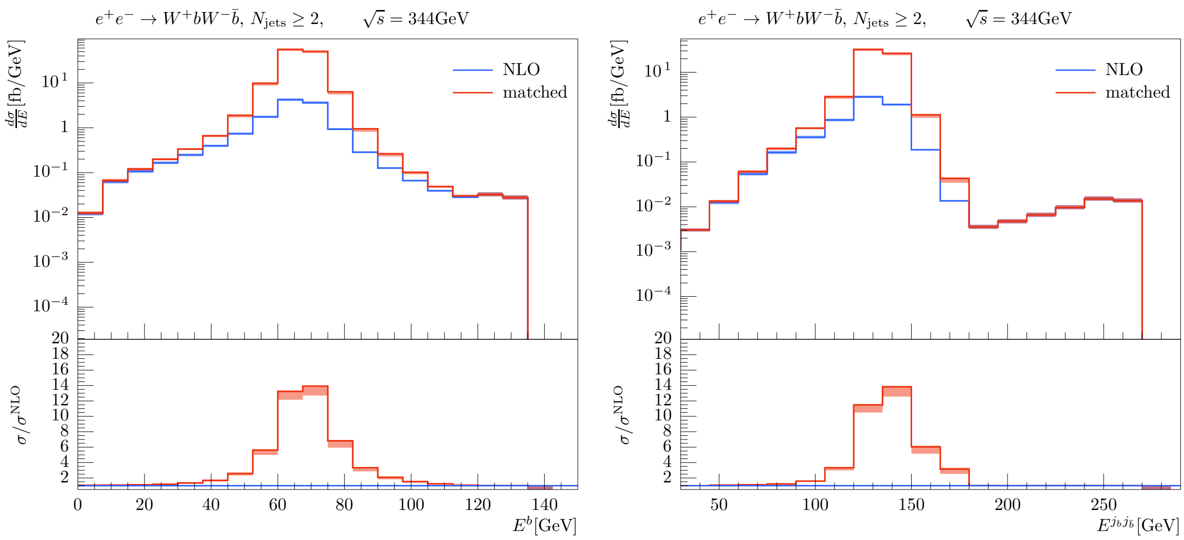

Figure 8.8 Energy distributions of b-jets and (b-jet,$\overline{\text{b}}$-jet) pairs. Lines, bands and panels as in Fig. 8.5.

While it is fairly obvious that rapidity and azimuthal angle difference between W^+ and b-jet will carry information about the top decay, it is interesting to see whether even single final state distributions of b-jet or W^+ carry similar information. In Fig. 8.8, we can clearly confirm this in the b-jet energy distribution. It peaks around 70 GeV with a major threshold enhancement of ~ 14. In fact, the peak position of b-jets has been proposed as a possibility to measure m_t [277–279], which has been realized by CMS using 8 TeV data [280]. We note that the peak position is consistent with the rest frame energy

$$E_{\text{b}}^* = \frac{m_t^2 - m_{\text{W}}^2}{2m_t} = 67.900\,\text{GeV} \tag{8.1}$$

as it has been shown for unpolarized top decays, massless b-quarks and arbitrary boosts in Ref. [277]. In our case, this is of course especially expected as nearly no boost of the top decay is present. The intriguing aspect of this analysis is that no correct reconstruction of b-jets with W^+ have to be performed and even the charge of the b-jets is irrelevant. Going to pairs of b and $\overline{\text{b}}$-jets in the right plot of Fig. 8.8, we observe that the peak in E_{b}^{j} around 70 GeV is translated to a peak in $E^{\text{j}_\text{b}\text{j}_\text{b}}$ around 140 GeV. We stress that these results have to be interpreted with caution as we have neglected final-final state interferences between b and $\overline{\text{b}}$, which could affect precisely this observable.

In Fig. 8.9, we show the transverse momentum of b-jets and W^+ bosons. As we know that the b-jet energy peaks around 70 GeV, we can expect $p_{\text{T}}^{\text{j}_\text{b}}$ to have its maximum slightly below this value due to small bottom mass $m_{\text{b}} = 4.2\,\text{GeV}$. As a result of momentum conservation, $p_{\text{T}}^{\text{W}^+}$ has to follow a similar distribution. This is exactly what we observe in Fig. 8.9. Compared to the b-jet energy, the peak is not as pronounced and more smeared to smaller values, which can still correspond to the peak jet energy due to the projection

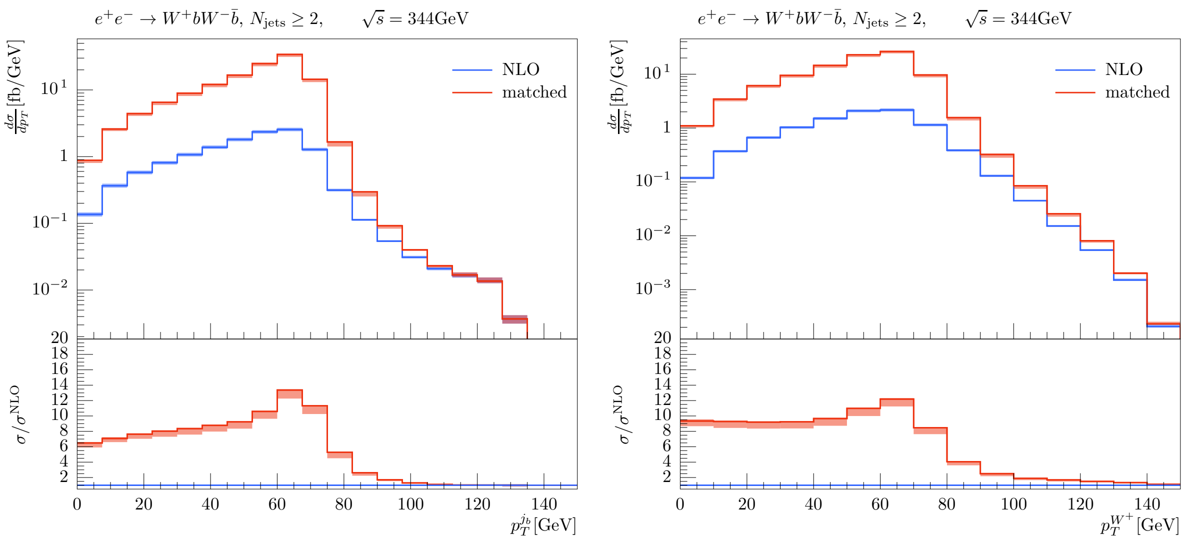

Figure 8.9 Transverse momentum distributions of b-jets and W^+ bosons. Lines, bands and panels as in Fig. 8.5.

to the transverse plane. Accordingly, $\sigma_{\rm matched}/\sigma_{\rm NLO}$ is large, a factor of 6–13, from 0 GeV to 70 GeV and quickly goes to 1 above 90 GeV, where the contributions largely stem from the $W^+W^-b\bar{b}$ background.

Finally, we show in Fig. 8.10 the energy of W^+ bosons. Also in this distribution, we can identify the footprint of the top decay in the peak and large threshold enhancement in the 100 GeV to 106 GeV bin. Compared to Fig. 8.8 though, we observe even for large W^+ boson energies still sizable threshold enhancements of a factor of ~ 2. Thus, the top quark contributions are not as localized as in the E^{j_b} case.

In summary, we have seen in this chapter that the matched NLO+NLL works excellently thanks to our comprehensive ansatz. The devised method for conservative theory uncertainties with symmetrized bands at threshold is easily implemented and very likely to envelope the next orders. The obtained differential results at threshold look promising to guide semi-inclusive future measurements as we could identify regions of phase space that are fully dominated by backgrounds. In the publication, which is in preparation, we will give further focus on the physics applications by studying M_t^{1S} variations. Furthermore, we will include ISR and beamstrahlung effects and discuss how this changes the classification of what can be considered pure continuum or threshold. This is especially important for the planned 380 GeV stage of CLIC.

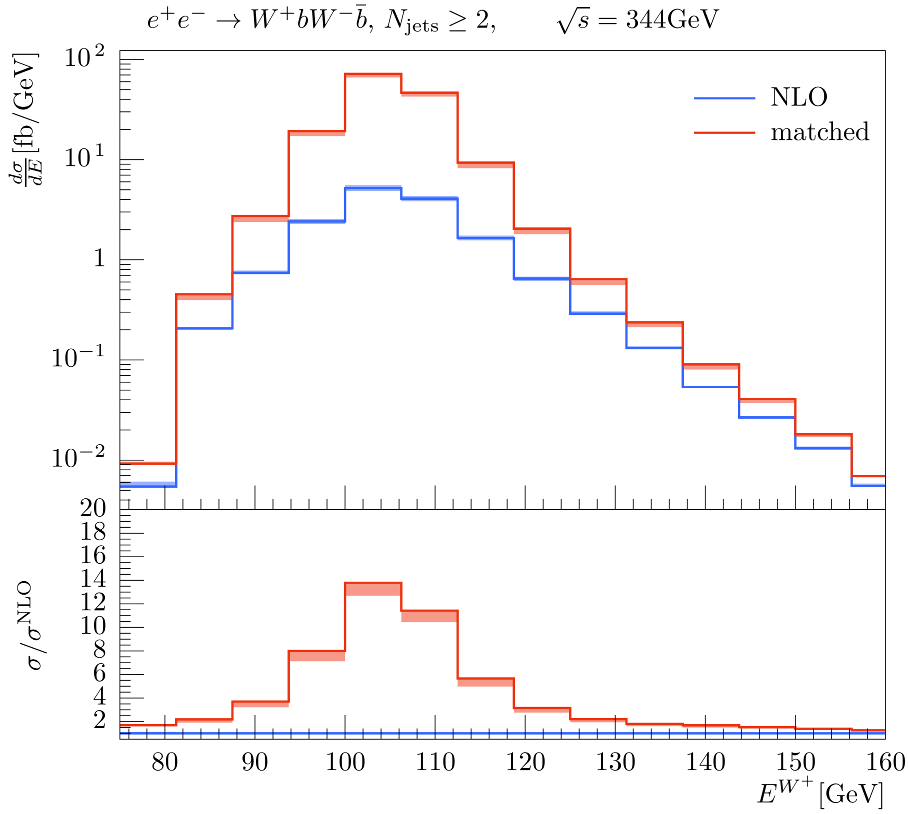

Figure 8.10 Energy distribution of W^+ bosons. Lines, bands and panels as in Fig. 8.5.

Chapter 9

Conclusions and outlook

In this work, we have studied the two most interesting processes for top physics in lepton collisions: top-pair production in association with and without a Higgs boson. These allow for a precise determination of top-quark properties, which in turn is a powerful opportunity to find possible hints of new physics and has far reaching consequences for our understanding of the universe. To study these processes, we have introduced the multi-purpose event generator WHIZARD for NLO computations in Part I. Hereby, we have focused on the specific aspects that are not seen in most NLO MC generators such as the generic implementation of the resonance-aware FKS subtraction, the possiblity to generate unweighted events at NLO or the separation of finite and singular contributions. Especially the resonance-aware FKS subtraction was key, hereby, to obtain reliable predictions for off-shell top-pair production at a lepton collider due to the irreducible background of $\mathrm{H} \to \mathrm{b\bar{b}}$ contributions, which is not present at hadron colliders at LO EW. To account for the resummation of soft and collinear emissions, we have presented an independent implementation of the POWHEG matching scheme that builds on the automation of QCD NLO corrections in WHIZARD. The key feature of the POWHEG matching, namely the suppression of the fixed-order differential cross section for small relative p_{T}, has been reproduced. We have discussed, in particular, how the distributions can be smoothly interpolated between an almost NLO and a pure POWHEG prediction, when the separation scale of soft and finite real contributions is varied appropriately. As both results are within the NLO+LL approximation, we have to consider this an additional uncertainty that should be varied for physics predictions. Furthermore, we have shown for the first time the impact of the POWHEG matching on distributions for $\mathrm{e^+e^-} \to \mathrm{t\bar{t}H}$.

In Part II, we have advanced the state of the art for off-shell $\mathrm{t\bar{t}}$ and $\mathrm{t\bar{t}H}$ production by including all off-shell effects for the leptonic decay mode ($\mu^+\nu_\mu \mathrm{e}^-\bar{\nu}_\mathrm{e}\mathrm{b\bar{b}}$ and $\mu^+\nu_\mu \mathrm{e}^-\bar{\nu}_\mathrm{e}\mathrm{b\bar{b}H}$) at NLO QCD. Especially for the precision measurement of the top Yukawa coupling, we have shown that off-shell effects and NLO corrections have to be considered simultaneously to fully capture the negative interference effects as well as the positive background contributions. One can see that these effects do not factorize if one tries to estimate the dependency of the cross section on the Yukawa coupling by multiplying the on-shell K-factor with the LO $\mathrm{W^+W^-b\bar{b}H}$ cross section. This leads to a shift of 1.3 % compared to the irreducible result while the correction itself is only 1.2 %. Similar findings show that also the forward-backward asymmetry can only be reliably described if off-shell effects and QCD corrections are taken into account simultaneously. In this case, off-shell effects even dominate over QCD corrections, rendering the $\mathrm{W^+W^-b\bar{b}}$ at NLO computation more relevant for the measurement than $\mathrm{t\bar{t}}$ at NNLO. Thus, it is indispensable to use off-shell predictions for precision predictions. A more detailed summary of Part II can be found in Section 5.3. In addition to its phenomenological relevance, the presented calculations demonstrate the flexibility of WHIZARD for NLO QCD computations at lepton colliders and the smooth interplay with one-loop providers. All distributions can be reproduced easily with these publicly available tools and finely adjusted to the experimental requirements.

In Part III, we have shown that one can systematically combine results obtained at threshold in NRQCD and in the continuum at fixed order in QCD. The core ingredients are the removal of double counting with an appropriate master formula, the switch-off of unphysical threshold contributions in the continuum and the embedding of the NRQCD results in a gauge-invariant, relativistic factorization formula. To the best of our knowledge, this is the first time such a computation has been performed as usually a simple master formula is sufficient for matching fixed-order with resummed results. We have put particular emphasis on a completely gauge-invariant construction and have shown the sizable difference to approaches that rely on signal diagrams, which has been used in the literature for similar processes. The obtained matched results are valid for all energies and allow to study at which fixed $\sqrt{s}$ one can rely exclusively on either the threshold or continuum computation. Furthermore, we have composed reliable theory uncertainties, even in the intermediate regions, by symmetrizing the asymmetric NLL scale uncertainties and creating an envelope over all matching variations.

Based on our results in Section 8.1, we can establish that the proposed 380 GeV stage of CLIC is sufficiently away from threshold to justify using a pure continuum computation. Of course, this requires an event selection with $\sqrt{\hat{s}} \approx \sqrt{s}$. In case this results in a measurement that is limited by statistics, one can use our matched computation, which is valid for all $\sqrt{\hat{s}}$. In fact, this measurement should be performed either way as the contributions for lower $\sqrt{\hat{s}}$ will be enhanced similar to the radiative return to the Z peak. A detailed study of the expected cross sections considering ISR and beamstrahlung will follow in the publication that corresponds to Part III. Furthermore, we will study therein the potential for top measurements using our NLO+NLL computation by considering the impact of variations of M_t^{1S} on the predictions.

Furthermore, we emphasize that the matched computation has shown intriguing differential results. The NRQCD contributions embedded in the double-pole approximation strongly enhance top-pair production kinematics, while backgrounds are fully described by $\mathrm{W^+W^-b\bar{b}}$ at NLO QCD. This can be also seen in the top decay products, where the phase-space in some variables can be neatly separated into signal and background. The very clean $\mathrm{t\bar{t}}$ signature will be the optimal environment to completely understand the most fundamental MC vs short-distance mass issues. Given enough progress in this aspect, certain differential distributions could be used to perform competitive mass measurements.

We conclude this work by identifying the core areas for future improvements of our studies and further directions. While we have shown the off-shell NLO QCD effects for leptonic decays, also semileptonic and hadronic decays should be studied in more detail. This will be computationally more challenging due to the increase of combinatorial possibilities in e.g. $\mathrm{c\bar{b}b\bar{c}b\bar{b}H}$ and of singular regions for the FKS subtractions. Hypothetically, one could even consider to treat the finite Higgs-width contributions (the 8 fermion final state). However, as the Higgs width is orders of magnitude smaller, the corrections will likely be negligible, i.e. far below the per cent level. For a more realistic event simulation, one should apply for all decay channels the POWHEG matching, as presented in Section 3.3, and add the parton shower and hadronization stages. This will allow also to increase the precision for differential observables to the NLO+LL level. While this is straightforward for the fixed-order prediction, it still has to be shown that this can be also applied to the matched computation of Section 7.2. From the fixed-order perspective, there are no obvious obstacles as both the threshold and the POWHEG matching avoid double counting. The simultaneous correctness to NLL at threshold and LL in p_T should be discussed in more detail, though. Furthermore, also NLO EW corrections and their interplay with the QCD corrections have to be considered in the future as they are well known to play an important role for the considered on-shell processes and are likely to be even more relevant for the full off-shell processes. Note that EW corrections do not factorize with the polarizations in contrast to the QCD corrections.

Concerning the next order in QCD, we are mildly optimistic that WHIZARD could be extended to handle NNLO computations. From the technical point of view, this is not very different from the current setup, especially if an FKS scheme like STRIPPER [281] is used, where the double-real phase-space is described by the Born phase-space times radiation functions. On top of the Born, real and virtual components, one would allocate additional double-virtual, double-real and real-virtual components. All matrix elements but the double-virtual ones can already be obtained from the interfaced OLPs. This would be one of the major missing pieces to realize a full NNLL+NNLO matching for $\mathrm{W^+W^-b\bar{b}}$. It will require, though, substantial improvements in the automation of two-loop computations to handle the massive number of diagrams. Likely, this is only acchievable if a mapping to a tree structure, which can be handled recursively, is found, similar to the one-loop idea [194]. These problems might be tackled in time given that there is still considerable time until first lepton-beam collisions, even in best case scenarios. In case the theory community advances quickly or the next high-energy lepton collider is delayed even further, this might be accomplished in time.

Finally, we would like to highlight an interesting follow-up project to our work that would combine Parts II and III even further: $\mathrm{t\bar{t}H}$ with threshold resummation. As we have seen in Section 5.2, there are *always* $\mathrm{t\bar{t}}$ threshold contributions in $\mathrm{t\bar{t}H}$ for large Higgs energies. In Refs. [282, 283], it has been shown how to use TOPPIK for the threshold resummation of on-shell $\mathrm{t\bar{t}H}$ up to NLL, which would form the basic ingredient. Technically, the threshold resummation for $W^+W^-b\bar{b}H$ can be setup the same way as for $W^+W^-b\bar{b}$, treating the H as a colorless recoiler, resulting in a lower effective $\sqrt{\hat{s}}$ for the top-pair system. Next to adding the technical infrastructure for this computation, one should study hereby how the $t\bar{t}$ threshold can be accessed in $t\bar{t}H$ at 500 GeV. This would be very interesting as the 500 GeV run is at the same time useful to measure both $t\bar{t}H$ itself, because it is close enough to threshold, as well as to conduct Higgs physics and search for BSM signatures. Thus, it is planned [227] to collect most of the integrated luminosity at 500 GeV in any of the possible running scenarios of the intial phase of the ILC. Note that in a very clean decay channel like $\gamma\gamma$, the energy distribution of the Higgs could be used for a measurement of a short-distance mass as it would be an almost inclusive measurement of the $t\bar{t}$ system. This might allow for a measurement of a short-distance mass at 500 GeV that is competitive to the threshold scan and thus to improve our understanding of the EW vacuum.

Appendix A

Conventions and Notation

We use natural units where $\hbar = c = 1$. Furthermore, we use the metric corresponding to flat space time with the one true signature $g^{\mu\nu} = \mathrm{diag}(+1, -1, -1, -1)$, such that $p^\mu = (E(\boldsymbol{p}), \boldsymbol{p})$, $p^2 = m^2$ and $E(\boldsymbol{p}) = \sqrt{m^2 + \boldsymbol{p}^2}$. Three-vector valued objects are either notated bold-faced, like $\boldsymbol{a}$, or indexed by Latin indices, a^i. The indices of four vectors in Minkowskian space-time are denoted by Greek indices or simply omitted, $p^\mu \to p$. The indices of a four vector go from 0 to 3 with the time as first component and the space components ordered as (a_x, a_y, a_z). This especially implies that four vectors with negative norm are called space-like, zero norm light-like and positive norm time-like. The Feynman slash is defined by $\not{p} = p_\mu \gamma^\mu$, whereby here and everywhere else a sum over repeated indices is implied. The sum is, however, made explicit where it improves clarity.

Appendix B

Supplements to Part I

B.1 Algorithm for MLM merging

There is no formal proof for the correctness of the MLM merging. We summarize in Fig. B.1 the algorithm as it is usually implemented. The maximal (Q_{max}), merging scale (Q_{MS}) and cut-off (Q_{cut}) scales can be in principle defined for any hardness measure like virtuality or by the clustering algorithm like k_{T}.

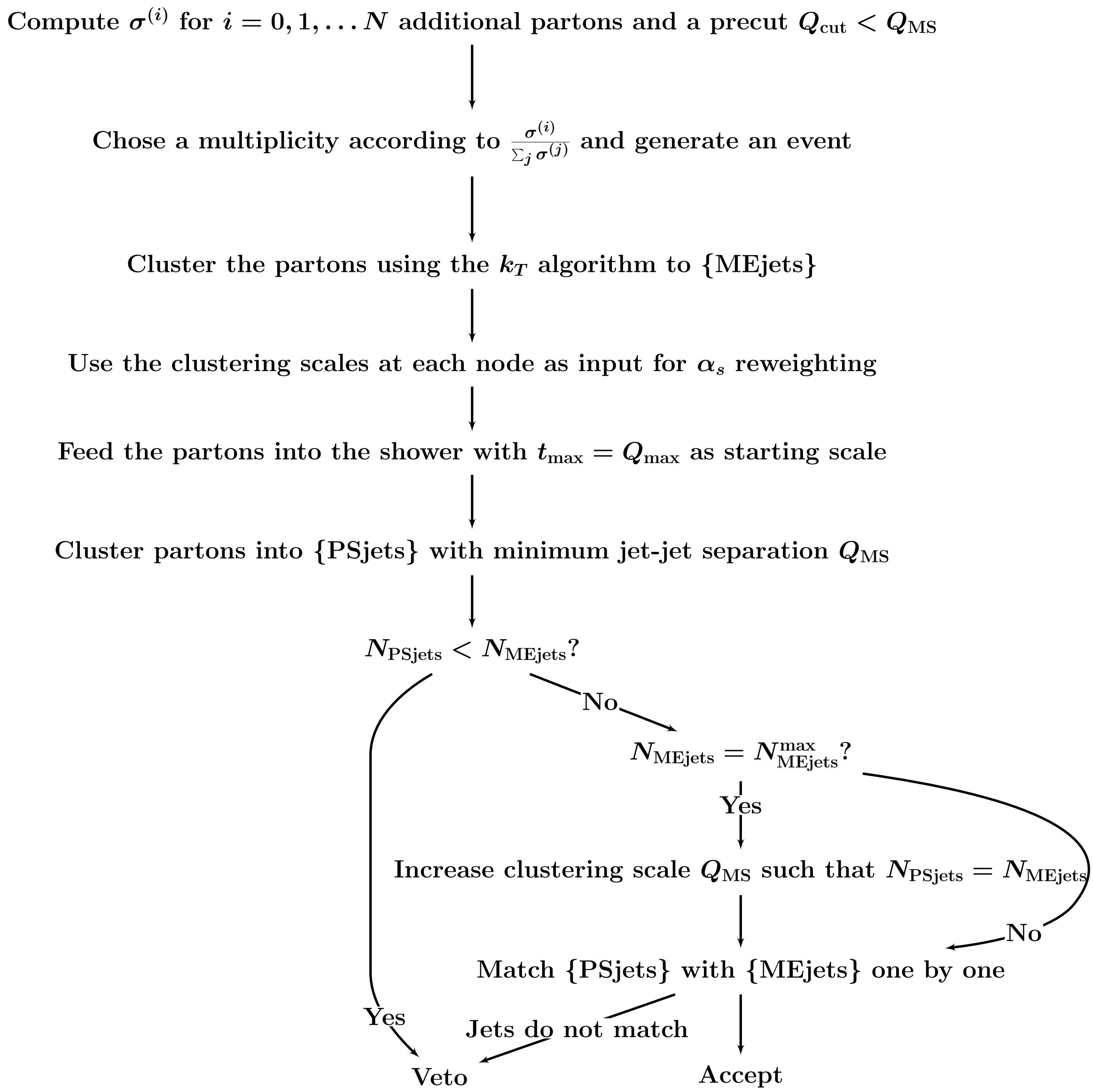

Figure B.1 Schematic representation of the MLM merging scheme.

B.2 Details on Sudakov veto algorithm in Powheg

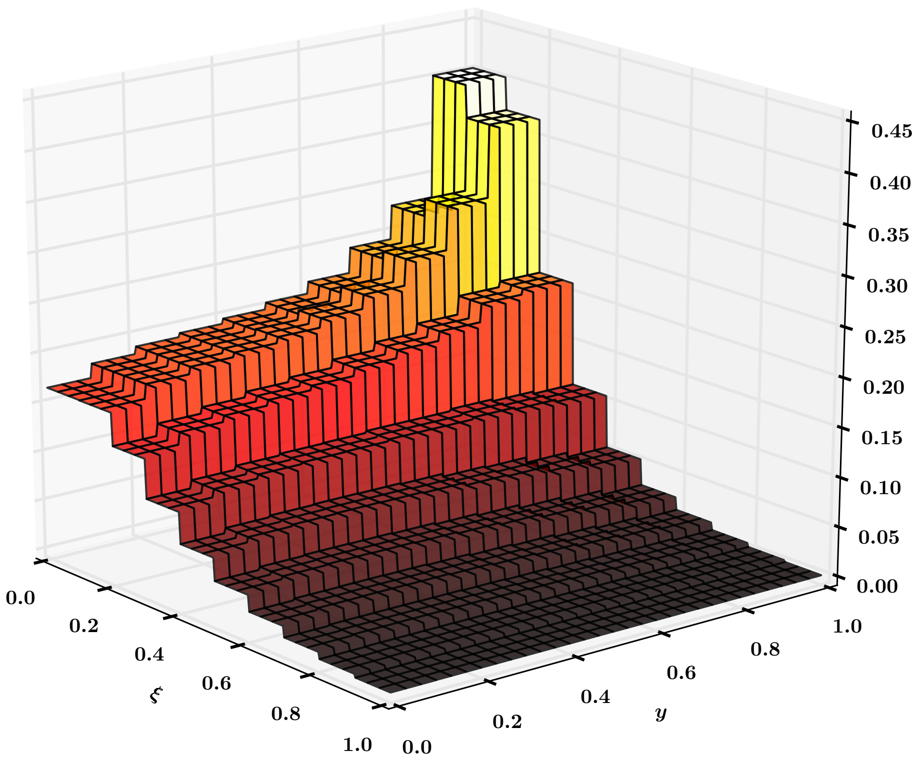

Figure B.2 $N(\xi, y)$ for $\alpha_r = 1$ in $t\bar{t}$ production at a lepton collider. Note that N is finite for all ξ, y as the leading divergence is captured by $U(\xi, y)$. $N(\xi, y)$ describes the non-universal behavior of the process.

We rely heavily on the Sudakov veto algorithm, introduced in Section 3.1.3, to shape the differential splitting probabilities. Specifically, we use as overestimator

$$U(\xi, y, \alpha_s^{\mathrm{rad}})\, N_{\max}\ , \tag{B.1}$$

whereby ξ and y are related to the FKS variables for energy and angular separation of the emitted parton (to the emitter) normalized to the $[0, 1]$ interval. The form of the upper bounding function $U(\xi, y, \alpha_s)$ depends on the type of emitter but for massless final-state radiation it is simply

$$U(\xi, y, \alpha_s) = \frac{\alpha_s(k_{\mathrm{T}}^2(\xi, y))}{\xi(1-y)}\ . \tag{B.2}$$

All implemented upper bounding functions and their integrals can be found in Ref. [79]. α_s^{rad} is the simplest expression for α_s, which overestimates or equals the α_s^{true} that is set by the user,

$$\alpha_s^{\mathrm{rad}}(p_{\mathrm{T}}^2) = \frac{1}{b_0 \log \frac{p_{\mathrm{T}}^2}{\Lambda_{\mathrm{gen}}^2}}\ , \tag{B.3}$$

with Λ_{gen} being computed before event generation by setting $\alpha_s^{\text{rad}} = \alpha_s^{\text{true}}\big|_{p_{\text{T}}=p_{\text{T,min}}}$. As mentioned in Section 3.3.1, we use a normalization grid $N(\xi, y)$, which is also sampled in a warmup stage with

$$N(\xi, y) = N(\{\tilde{\xi}, \tilde{y}\}) \quad \text{for} \quad \xi, y \in \{\tilde{\xi}, \tilde{y}\} \quad \text{and} \quad N(\{\tilde{\xi}, \tilde{y}\}) = \max_{\forall \xi, y \in \{\tilde{\xi}, \tilde{y}\}} \frac{R(\xi, y)\mathcal{J}(\xi, y)}{BU(\xi, y, \alpha_s^{\text{true}})} \tag{B.4}$$

whereby J is the Jacobian from the radiation phase space to the dimensionless FKS variables ξ and y and the binning of the ξ, y unit square into $\{\tilde{\xi}, \tilde{y}\}$ elements can be adjusted to the process complexity. We show an example of $N(\xi, y)$ in Fig. B.2. To transform Eq. (B.1) into

$$\frac{R(\xi, y)\mathcal{J}(\xi, y)}{B}\,, \tag{B.5}$$

we apply the following veto procedure. At each step, we generate a random number x_i and check if it less than a veto probability $\mathcal{P}_i$. This multiplies $\mathcal{P}_i$ with the generated distribution and by virtue of the Sudakov veto algorithm, cf. Section 3.1.3, even exponentiates and thus modifies the differential splitting probabilities directly. The veto probabilities and the transformation of Eq. (B.1) are as follows

$$\mathcal{P}_1 = \frac{\alpha_s^{\text{true}}}{\alpha_s^{\text{rad}}} \quad \text{Eq. (B.1)} \Rightarrow U(\xi, y, \alpha_s^{\text{true}})\, N_{\max} \tag{B.6a}$$

$$\mathcal{P}_2 = \frac{N(\xi, y)}{N_{\max}} \quad \Rightarrow U(\xi, y, \alpha_s^{\text{true}})\, N(\xi, y) \tag{B.6b}$$

$$\mathcal{P}_3 = \frac{R(\xi, y)\mathcal{J}(\xi, y)}{BU(\xi, y, \alpha_s^{\text{true}})N(\xi, y)} \quad \Rightarrow \text{Eq. (B.5)}\,. \tag{B.6c}$$

Hereby, Eq. (B.6b) is not strictly necessary but reduces the number of evaluations of the real matrix element, as shown in Tab. B.1. In this example, the number of matrix-element evaluations is greatly lowered by about 76 %.

Table B.1 Summary of POWHEG veto procedure for $\alpha_r = 1$ in $\mathrm{e}^+\mathrm{e}^- \to \mathrm{t}\bar{\mathrm{t}}$ for 10 000 events. We note that in this run 549 excess events occured in the last step, corresponding to 0.7 %. The $\xi_{\max}$ veto is an additional special step for massive upper bounding functions that ensures that the kinematic bound $\xi \leq \xi_{\max}$ is fulfilled.

	N_{calls}	N_{vetoed}	$N_{\text{vetoed}}/N_{\text{calls}}$
α_s	386 215	13 066	3 %
$\xi_{\max}$	373 149	44 589	12 %
$N(\xi, y)$	328 560	250 579	76 %
$R(\xi, y)/B$	77 981	70 563	90 %

Appendix C

Supplements to Part II

C.1 Further predictions for $e^+e^- \to \mu^+\nu_\mu e^-\bar{\nu}_e b\bar{b}$

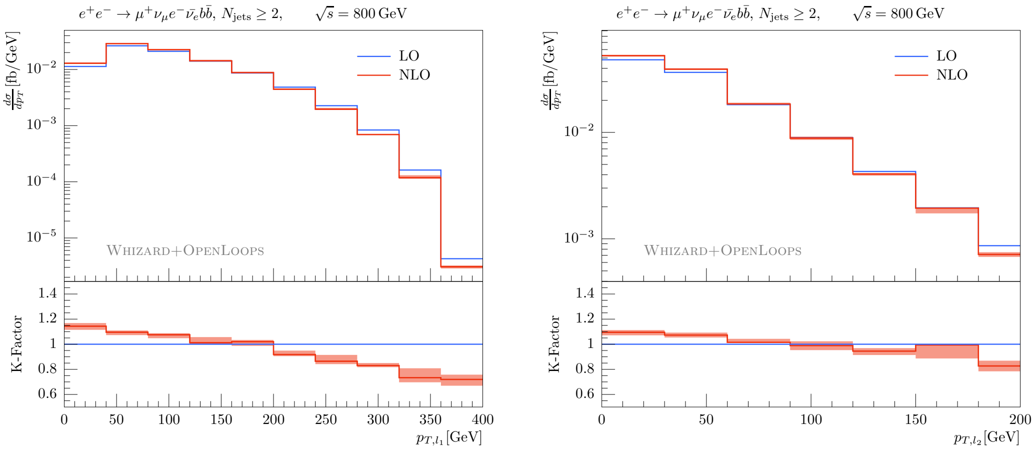

Figure C.1 Transverse momentum distributions of the hardest and second hardest lepton in $e^+e^- \to \mu^+\nu_\mu e^-\bar{\nu}_e b\bar{b}$. Curves and bands as in Fig. 5.4.

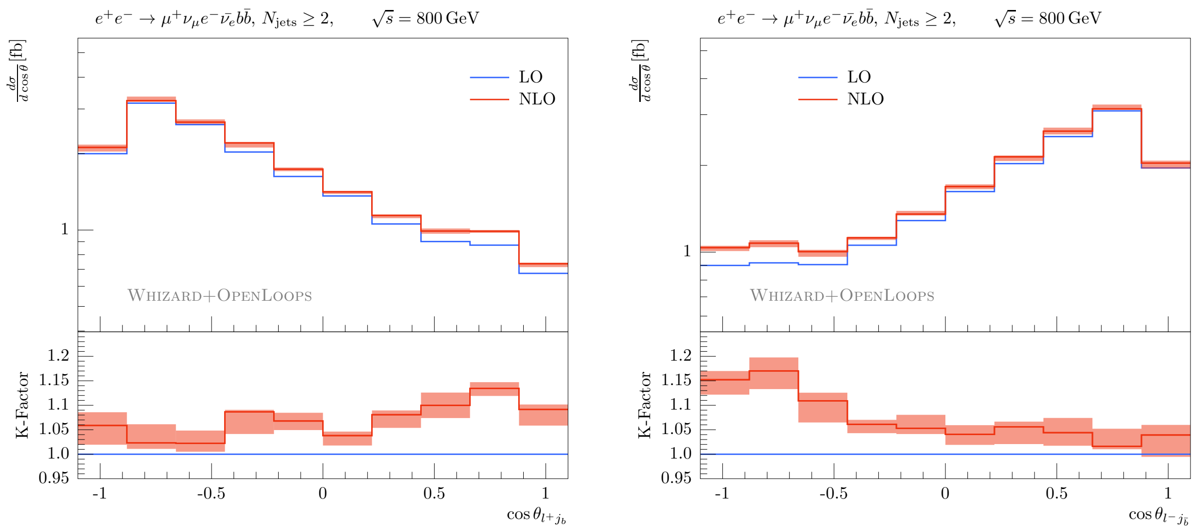

Figure C.2 Differential distributions of the azimuthal angle of $\ell^+ \mathrm{j_b}$ (left) and $\ell^- \mathrm{j_{\bar{b}}}$ (right) for $\mathrm{e^+e^-} \to \mu^+\nu_\mu \mathrm{e}^-\bar{\nu}_\mathrm{e}\mathrm{b\bar{b}}$. Curves and bands as in Fig. 5.4.

C.2 Further predictions for $\mathrm{e^+e^-} \to \mu^+\nu_\mu \mathrm{e}^-\bar{\nu}_\mathrm{e}\mathrm{b\bar{b}H}$

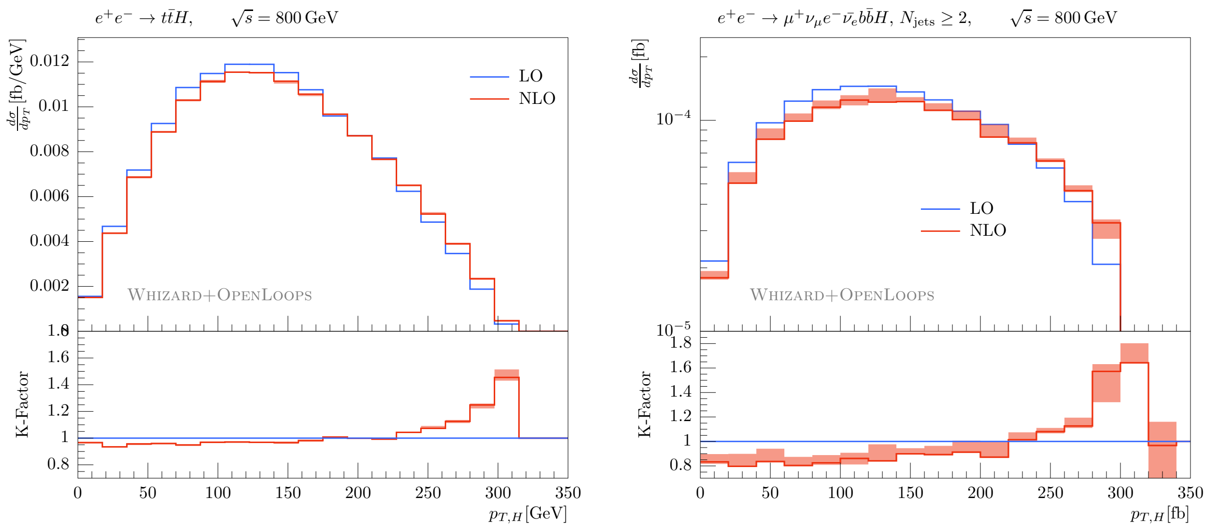

Figure C.3 Transverse momentum distributions of the Higgs boson in $\mathrm{e^+e^-} \to \mathrm{t\bar{t}H}$ (left) and in $\mathrm{e^+e^-} \to \mu^+\nu_\mu \mathrm{e}^-\bar{\nu}_\mathrm{e}\mathrm{b\bar{b}H}$ (right). Curves and bands as in Fig. 5.4.

Appendix D

Supplements to Part III

D.1 Alternative switch-off functions

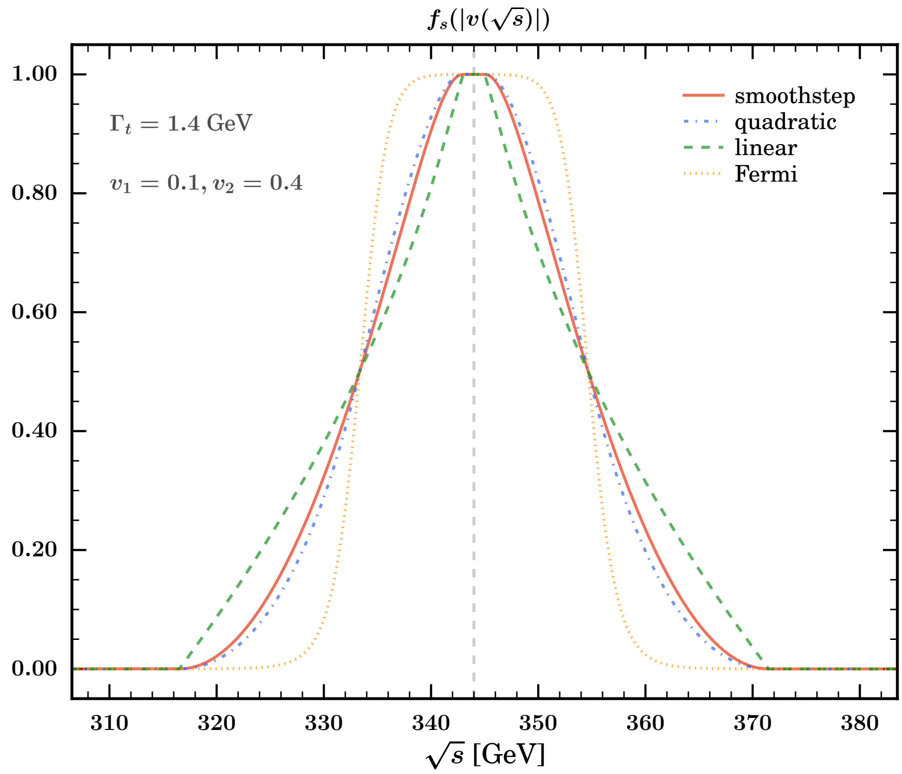

Figure D.1 Various switch-off functions as explained in the text in a wide switch-off window between $v_1 = 0.1$ and $v_2 = 0.4$.

For reference, we show alternatives to the smoothstep switch-off function that is used in Part III. Specifically, we depict in Fig. D.1 a smoothstep, quadratic, linear and a Fermi function. Overall, we have observed that higher curvature functions lead to artificial bumps or wiggles in the matched cross section. This is suppressed best with the linear switch-off but this is not a smoothly differentially function and hence would produce unphysical edges at v_1 and v_2. The quadratic switch-off function is actually not a simple function between v_1 and v_2 but consists of two quadratic functions:

$$f_s(v) = \begin{cases} 1 & v < v_1 \\ 1 - 2\frac{(v-v_1)^2}{(v_2-v_1)^2} & v_1 < v < \frac{v_1+v_2}{2} \\ 2\frac{(v-v_2)^2}{(v_2-v_1)^2} & \frac{v_1+v_2}{2} < v < v_2 \\ 0 & v > v_2 \end{cases} . \tag{D.1}$$

This quadratic function follows smoothstep fairly closely but is always further away from the linear behavior. The Fermi-Dirac distribution has been generated with a mean of $(v_1 + v_2)/2$ and a width of $(v_2 - v_1)/20$. Note that while one can get a behavior closer to the linear function around the mean with a larger width, this leads to f_s not being approximately 1 and 0 at v_1 and v_2, respectively. Thus, the smoothstep function appears as the best alternative, while most other parametrizations give results within the matching variation.

D.2 Additional validation results

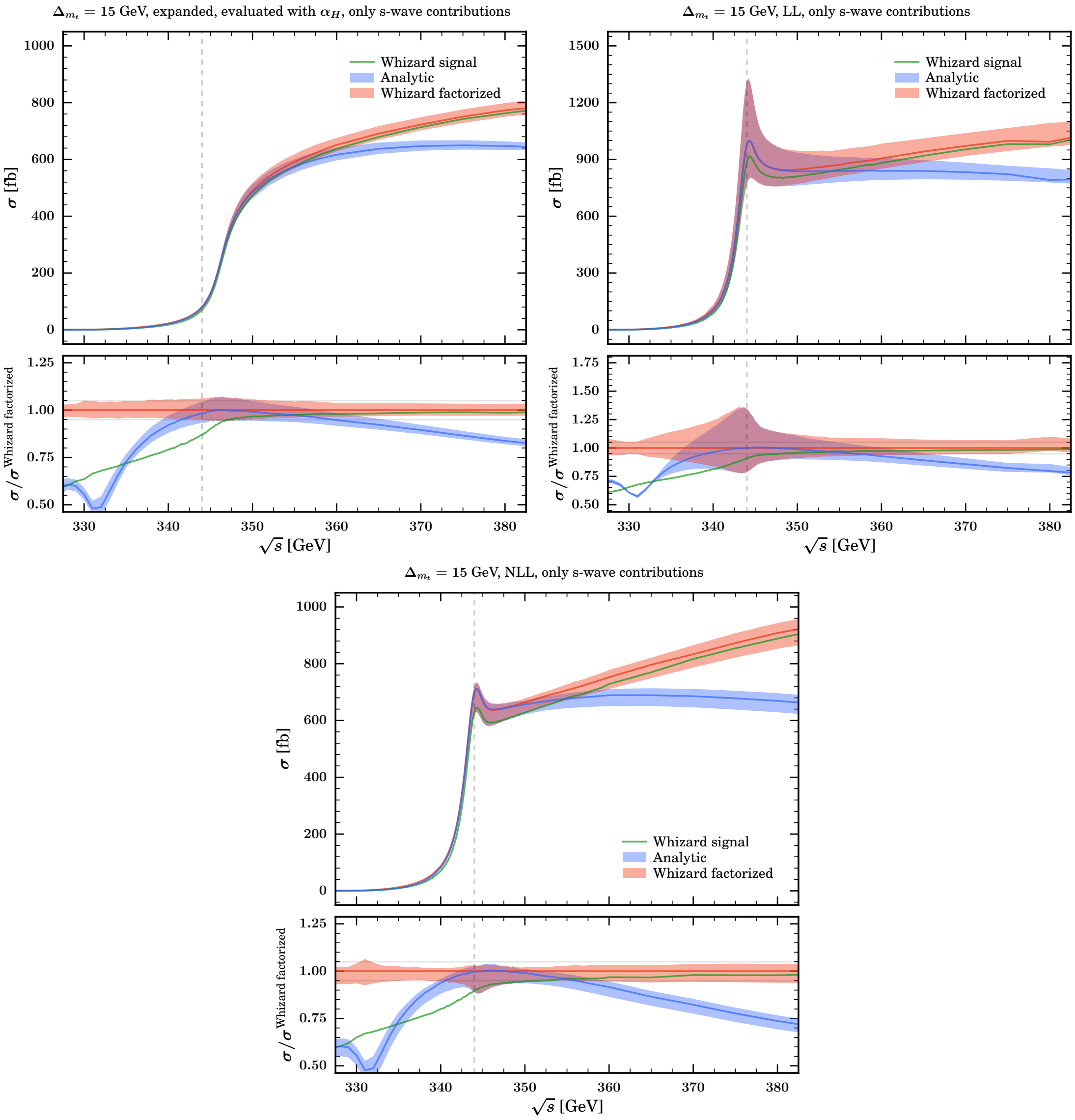

Figure D.2 Comparison of analytic results with the implementation in WHIZARD with the factorized and the signal-diagram approach for $\Delta_{m_t} = 15\,\text{GeV}$ using an expanded, LL or NLL form factor. The bands and lines as in Fig. 7.3.

Bibliography

[1] CMS Collaboration. Observation of a new boson at a mass of 125 GeV with the CMS experiment at the LHC. In *Phys. Lett.*, **B716**: (2012), pp. 30–61. arXiv: 1207.7235 [hep-ex].

[2] ATLAS Collaboration. Observation of a new particle in the search for the Standard Model Higgs boson with the ATLAS detector at the LHC. In *Phys. Lett.*, **B716**: (2012), pp. 1–29. arXiv: 1207.7214 [hep-ex].

[3] P. W. Graham, D. E. Kaplan, and S. Rajendran. Cosmological Relaxation of the Electroweak Scale. In *Phys. Rev. Lett.*, **115**:22 (2015), p. 221801. arXiv: 1504.07551 [hep-ph].

[4] J. Elias-Miro, J. R. Espinosa, G. F. Giudice, G. Isidori, et al. Higgs mass implications on the stability of the electroweak vacuum. In *Phys. Lett.*, **B709**: (2012), pp. 222–228. arXiv: 1112.3022 [hep-ph].

[5] J. Ellis, J. R. Espinosa, G. F. Giudice, A. Hoecker, and A. Riotto. The Probable Fate of the Standard Model. In *Phys. Lett.*, **B679**: (2009), pp. 369–375. arXiv: 0906.0954 [hep-ph].

[6] S. Alekhin, A. Djouadi, and S.-O. Moch. The top quark and Higgs boson masses and the stability of the electroweak vacuum. In *Phys. Lett.*, **B716**: (2012), pp. 214–219. arXiv: 1207.0980 [hep-ph].

[7] G. Degrassi, S. Di Vita, J. Elias-Miro, J. R. Espinosa, et al. Higgs mass and vacuum stability in the Standard Model at NNLO. In *JHEP*, **08**: (2012), p. 098. arXiv: 1205.6497 [hep-ph].

[8] D. Buttazzo, G. Degrassi, P. P. Giardino, G. F. Giudice, et al. Investigating the near-criticality of the Higgs boson. In *JHEP*, **12**: (2013), p. 089. arXiv: 1307.3536 [hep-ph].

[9] A. V. Bednyakov, B. A. Kniehl, A. F. Pikelner, and O. L. Veretin. Stability of the Electroweak Vacuum: Gauge Independence and Advanced Precision. In *Phys. Rev. Lett.*, **115**:20 (2015), p. 201802. arXiv: 1507.08833 [hep-ph].

[10] M. Baak, J. Cúth, J. Haller, A. Hoecker, et al., Gfitter Group. The global electroweak fit at NNLO and prospects for the LHC and ILC. In *Eur. Phys. J.*, **C74**: (2014), p. 3046. arXiv: 1407.3792 [hep-ph].

[11] ATLAS, CDF, CMS, D0. First combination of Tevatron and LHC measurements of the top-quark mass. In (2014). arXiv: 1403.4427 [hep-ex].

[12] P. Z. Skands and D. Wicke. Non-perturbative QCD effects and the top mass at the Tevatron. In *Eur. Phys. J.*, **C52**: (2007), pp. 133–140. arXiv: hep-ph/0703081 [HEP-PH].

[13] M. Butenschoen, B. Dehnadi, A. H. Hoang, V. Mateu, et al. Top Quark Mass Calibration for Monte Carlo Event Generators. In *Phys. Rev. Lett.*, **117**:23 (2016), p. 232001. arXiv: 1608.01318 [hep-ph].

[14] T. Sjöstrand, S. Ask, J. R. Christiansen, R. Corke, et al. An Introduction to PYTHIA 8.2. In *Comput. Phys. Commun.*, **191**: (2015), pp. 159–177. arXiv: 1410.3012 [hep-ph].

[15] J. Kieseler, K. Lipka, and S.-O. Moch. Calibration of the Top-Quark Monte-Carlo Mass. In *Phys. Rev. Lett.*, **116**:16 (2016), p. 162001. arXiv: 1511.00841 [hep-ph].

[16] M. Beneke. Renormalons. In *Phys. Rept.*, **317**: (1999), pp. 1–142. arXiv: hep-ph/9807443 [hep-ph].

[17] M. Czakon, P. Fiedler, and A. Mitov. Total Top-Quark Pair-Production Cross Section at Hadron Colliders Through $O(\alpha_S^4)$. In *Phys. Rev. Lett.*, **110**: (2013), p. 252004. arXiv: 1303.6254 [hep-ph].

[18] ATLAS Collaboration. Measurement of the $t\bar{t}$ production cross-section using $e\mu$ events with b-tagged jets in pp collisions at $\sqrt{s} = 7$ and 8 TeV with the ATLAS detector. In *Eur. Phys. J.*, **C74**:10 (2014). [Addendum: Eur. Phys. J.C76,no.11,642(2016)], p. 3109. arXiv: 1406.5375 [hep-ex].

[19] S. Alekhin, S.-O. Moch, and S. Thier. Determination of the top-quark mass from hadro-production of single top-quarks. In *Phys. Lett.*, **B763**: (2016), pp. 341–346. arXiv: 1608.05212 [hep-ph].

[20] H. Baer, T. Barklow, K. Fujii, Y. Gao, et al. The International Linear Collider Technical Design Report - Volume 2: Physics. In (2013). arXiv: 1306.6352 [hep-ph].

[21] H. Abramowicz et al. The International Linear Collider Technical Design Report - Volume 4: Detectors. In (2013). Ed. by T. Behnke, J. E. Brau, P. N. Burrows, J. Fuster, et al. arXiv: 1306.6329 [physics.ins-det].

[22] L. Linssen, A. Miyamoto, M. Stanitzki, and H. Weerts. Physics and Detectors at CLIC: CLIC Conceptual Design Report. In (2012). arXiv: 1202.5940 [physics.ins-det].

[23] A. H. Hoang and T. Teubner. Top quark pair production close to threshold: Top mass, width and momentum distribution. In *Phys. Rev.*, **D60**: (1999), p. 114027. arXiv: hep-ph/9904468 [hep-ph].

[24] M. Beneke. A quark mass definition adequate for threshold problems. In *Phys. Lett.*, **B434**: (1998), pp. 115–125. arXiv: hep-ph/9804241 [hep-ph].

[25] K. Seidel, F. Simon, M. Tesar, and S. Poss. Top quark mass measurements at and above threshold at CLIC. In *Eur. Phys. J.*, **C73**:8 (2013), p. 2530. arXiv: 1303.3758 [hep-ex].

[26] T. Horiguchi, A. Ishikawa, T. Suehara, K. Fujii, et al. Study of top quark pair production near threshold at the ILC. In (2013). arXiv: 1310.0563 [hep-ex].

[27] M. Beneke, A. Maier, J. Piclum, and T. Rauh. Higgs effects in top anti-top production near threshold in e^+e^- annihilation. In *Nucl. Phys.*, **B899**: (2015), pp. 180–193. arXiv: 1506.06865 [hep-ph].

[28] F. Simon. "A First Look at the Impact of NNNLO Theory Uncertainties on Top Mass Measurements at the ILC". In *Proceedings, International Workshop on Future Linear Colliders (LCWS15): Whistler, B.C., Canada, November 02-06, 2015.* 2016. arXiv: 1603.04764 [hep-ex].

[29] K. Fujii et al. The Potential of the ILC for Discovering New Particles. In (2017). arXiv: 1702.05333 [hep-ph].

[30] K. Agashe et al., Top Quark Working Group. "Working Group Report: Top Quark". In *Proceedings, Community Summer Study 2013: Snowmass on the Mississippi (CSS2013): Minneapolis, MN, USA, July 29-August 6, 2013.* 2013. arXiv: 1311.2028 [hep-ph].

[31] T. Price, P. Roloff, J. Strube, and T. Tanabe. Full simulation study of the top Yukawa coupling at the ILC at $\sqrt{s} = 1$ TeV. In *Eur. Phys. J.*, **C75**:7 (2015), p. 309. arXiv: 1409.7157 [hep-ex].

[32] A. Arbey et al. Physics at the e^+e^- Linear Collider. In *Eur. Phys. J.*, **C75**:8 (2015). Ed. by G. Moortgat-Pick, H. Baer, M. Battaglia, G. Belanger, et al., p. 371. arXiv: 1504.01726 [hep-ph].

[33] G. Cullen et al. GoSam-2.0: a tool for automated one-loop calculations within the Standard Model and beyond. In *Eur. Phys. J.*, **C74**:8 (2014), p. 3001. arXiv: 1404.7096 [hep-ph].

[34] F. Cascioli, P. Maierhöfer, and S. Pozzorini. Scattering Amplitudes with Open Loops. In *Phys. Rev. Lett.*, **108**: (2012), p. 111601. arXiv: 1111.5206 [hep-ph].

[35] S. Actis, A. Denner, L. Hofer, A. Scharf, and S. Uccirati. Recursive generation of one-loop amplitudes in the Standard Model. In *JHEP*, **04**: (2013), p. 037. arXiv: 1211.6316 [hep-ph].

[36] S. Actis, A. Denner, L. Hofer, J.-N. Lang, et al. RECOLA: REcursive Computation of One-Loop Amplitudes. In *Comput. Phys. Commun.*, **214**: (2017), pp. 140–173. arXiv: 1605.01090 [hep-ph].

[37] T. Gleisberg, S. Höche, F. Krauss, M. Schönherr, et al. Event generation with SHERPA 1.1. In *JHEP*, **02**: (2009), p. 007. arXiv: 0811.4622 [hep-ph].

[38] J. Alwall, R. Frederix, S. Frixione, V. Hirschi, et al. The automated computation of tree-level and next-to-leading order differential cross sections, and their matching to parton shower simulations. In *JHEP*, **07**: (2014), p. 079. arXiv: 1405.0301 [hep-ph].

[39] J. Bellm et al. Herwig 7.0/Herwig++ 3.0 release note. In *Eur. Phys. J.*, **C76**:4 (2016), p. 196. arXiv: 1512.01178 [hep-ph].

[40] C. Weiss, B. Chokoufe Nejad, W. Kilian, and J. Reuter. Automated NLO QCD Corrections with WHIZARD. In *PoS*, **EPS-HEP2015**: (2015), p. 466. arXiv: 1510.02666 [hep-ph].

[41] F. Cascioli, T. Gehrmann, M. Grazzini, S. Kallweit, et al. ZZ production at hadron colliders in NNLO QCD. In *Phys. Lett.*, **B735**: (2014), pp. 311–313. arXiv: 1405.2219 [hep-ph].

[42] M. Grazzini, S. Kallweit, and D. Rathlev. ZZ production at the LHC: fiducial cross sections and distributions in NNLO QCD. In *Phys. Lett.*, **B750**: (2015), pp. 407–410. arXiv: 1507.06257 [hep-ph].

[43] T. Gehrmann, M. Grazzini, S. Kallweit, P. Maierhöfer, et al. W^+W^- Production at Hadron Colliders in Next to Next to Leading Order QCD. In *Phys. Rev. Lett.*, **113**:21 (2014), p. 212001. arXiv: 1408.5243 [hep-ph].

[44] M. Grazzini, S. Kallweit, and D. Rathlev. $W\gamma$ and $Z\gamma$ production at the LHC in NNLO QCD. In *JHEP*, **07**: (2015), p. 085. arXiv: 1504.01330 [hep-ph].

[45] J. M. Campbell, R. K. Ellis, Y. Li, and C. Williams. Predictions for diphoton production at the LHC through NNLO in QCD. In *JHEP*, **07**: (2016), p. 148. arXiv: 1603.02663 [hep-ph].

[46] C. Anastasiou, C. Duhr, F. Dulat, F. Herzog, and B. Mistlberger. Higgs Boson Gluon-Fusion Production in QCD at Three Loops. In *Phys. Rev. Lett.*, **114**: (2015), p. 212001. arXiv: 1503.06056 [hep-ph].

[47] V. M. Abazov et al., D0. Measurement of the forward-backward asymmetry in the distribution of leptons in $t\bar{t}$ events in the lepton+jets channel. In *Phys. Rev.*, **D90**: (2014), p. 072001. arXiv: 1403.1294 [hep-ex].

[48] T. A. Aaltonen et al., CDF. Measurement of the inclusive leptonic asymmetry in top-quark pairs that decay to two charged leptons at CDF. In *Phys. Rev. Lett.*, **113**: (2014). [Erratum: Phys. Rev. Lett.117,no.19,199901(2016)], p. 042001. arXiv: 1404.3698 [hep-ex].

[49] M. Czakon, P. Fiedler, and A. Mitov. Resolving the Tevatron Top Quark Forward-Backward Asymmetry Puzzle: Fully Differential Next-to-Next-to-Leading-Order Calculation. In *Phys. Rev. Lett.*, **115**:5 (2015), p. 052001. arXiv: 1411.3007 [hep-ph].

[50] Y. Kiyo, A. Maier, P. Maierhöfer, and P. Marquard. Reconstruction of heavy quark current correlators at $O(\alpha_s^3)$. In *Nucl. Phys.*, **B823**: (2009), pp. 269–287. arXiv: 0907.2120 [hep-ph].

[51] J. Gao and H. X. Zhu. Top Quark Forward-Backward Asymmetry in e^+e^- Annihilation at Next-to-Next-to-Leading Order in QCD. In *Phys. Rev. Lett.*, **113**:26 (2014), p. 262001. arXiv: 1410.3165 [hep-ph].

[52] L. Chen, O. Dekkers, D. Heisler, W. Bernreuther, and Z.-G. Si. Top-quark pair production at next-to-next-to-leading order QCD in electron positron collisions. In *JHEP*, **12**: (2016), p. 098. arXiv: 1610.07897 [hep-ph].

[53] L. Guo, W.-G. Ma, R.-Y. Zhang, and S.-M. Wang. One-loop QCD corrections to the $e^+e^- \to W^+W^-b\bar{b}$ process at the ILC. In *Phys. Lett.*, **B662**: (2008), pp. 150–157. arXiv: 0802.4124 [hep-ph].

[54] S. Liebler, G. Moortgat-Pick, and A. S. Papanastasiou. Probing the top-quark width through ratios of resonance contributions of $e^+e^- \to W^+W^-b\bar{b}$. In *JHEP*, **03**: (2016), p. 099. arXiv: 1511.02350 [hep-ph].

[55] S. Dittmaier, M. Kramer, Y. Liao, M. Spira, and P. M. Zerwas. Higgs radiation off top quarks in e^+e^- collisions. In *Phys. Lett.*, **B441**: (1998), pp. 383–388. arXiv: 9808433 [hep-ph].

[56] G. Bélanger, F. Boudjema, J. Fujimoto, T. Ishikawa, et al. Full $\mathcal{O}(\alpha)$ electroweak and $\mathcal{O}(\alpha_s)$ corrections to $e^+e^- \to t\bar{t}H$. In *Phys. Lett.*, **B571**: (2003), pp. 163–172. arXiv: 0307029 [hep-ph].

[57] M. Beneke, Y. Kiyo, P. Marquard, A. Penin, et al. Next-to-Next-to-Next-to-Leading Order QCD Prediction for the Top Antitop S-Wave Pair Production Cross Section Near Threshold in e^+e^- Annihilation. In *Phys. Rev. Lett.*, **115**:19 (2015), p. 192001. arXiv: 1506.06864 [hep-ph].

[58] F. Bach and M. Stahlhofen. Top pair threshold production at a linear collider with WHIZARD. In (2014). arXiv: 1411.7318 [hep-ph].

[59] A. H. Hoang, C. J. Reisser, and P. Ruiz Femenía. Phase Space Matching and Finite Lifetime Effects for Top-Pair Production Close to Threshold. In *Phys. Rev.*, **D82**: (2010), p. 014005. arXiv: 1002.3223 [hep-ph].

[60] M. Beneke, B. Jantzen, and P. Ruiz Femenía. Electroweak non-resonant NLO corrections to $e^+e^- \to W^+W^-b\bar{b}$ in the $t\bar{t}$ resonance region. In *Nucl. Phys.*, **B840**: (2010), pp. 186–213. arXiv: 1004.2188 [hep-ph].

[61] P. Ruiz Femenía. First estimate of the NNLO nonresonant corrections to top-antitop threshold production at lepton colliders. In *Phys. Rev.*, **D89**:9 (2014), p. 097501. arXiv: 1402.1123 [hep-ph].

[62] M. Beneke, A. Maier, J. Piclum, and T. Rauh. Non-QCD contributions to top-pair production near threshold. In *PoS*, **EPS-HEP2015**: (2015), p. 315. arXiv: 1511.00801 [hep-ph].

[63] T. J. G. Rauh. *Precise top and bottom quark masses from pair production near threshold in e^+e^- collisions*. PhD thesis. Munich, Tech. U., 2016-08-09.

[64] M. Beneke. Unstable-particle effective field theory. In *Nucl. Part. Phys. Proc.*, **261-262**: (2015), pp. 218–231. arXiv: 1501.07370 [hep-ph].

[65] M. Böhm, A. Denner, and H. Joos. *Gauge theories of the strong and electroweak interaction*. 2001.

[66] T. Kinoshita. Mass singularities of Feynman amplitudes. In *J. Math. Phys.*, **3**: (1962), pp. 650–677.

[67] T. D. Lee and M. Nauenberg. Degenerate Systems and Mass Singularities. In *Phys. Rev.*, **133**: (1964), B1549–B1562.

[68] F. Bloch and A. Nordsieck. Note on the Radiation Field of the electron. In *Phys. Rev.*, **52**: (1937), pp. 54–59.

[69] S. Catani and M. H. Seymour. A General algorithm for calculating jet cross-sections in NLO QCD. In *Nucl. Phys.*, **B485**: (1997). [Erratum: Nucl. Phys.B510,503(1998)], pp. 291–419. arXiv: hep-ph/9605323 [hep-ph].

[70] S. Catani, S. Dittmaier, M. H. Seymour, and Z. Trócsányi. The dipole formalism for next-to-leading order QCD calculations with massive partons. In *Nucl. Phys.*, **B627**: (2002), pp. 189–265. arXiv: 0201036 [hep-ph].

[71] T. Gleisberg and F. Krauss. Automating dipole subtraction for QCD NLO calculations. In *Eur. Phys. J.*, **C53**: (2008), pp. 501–523. arXiv: 0709.2881 [hep-ph].

[72] S. Frixione, Z. Kunszt, and A. Signer. Three jet cross-sections to next-to-leading order. In *Nucl. Phys.*, **B467**: (1996), pp. 399–442. arXiv: hep-ph/9512328 [hep-ph].

[73] S. Frixione. A General approach to jet cross-sections in QCD. In *Nucl. Phys.*, **B507**: (1997), pp. 295–314. arXiv: hep-ph/9706545 [hep-ph].

[74] R. Frederix, S. Frixione, F. Maltoni, and T. Stelzer. Automation of next-to-leading order computations in QCD: The FKS subtraction. In *JHEP*, **10**: (2009), p. 003. arXiv: 0908.4272 [hep-ph].

[75] C. H. Chung, M. Kramer, and T. Robens. An alternative subtraction scheme for next-to-leading order QCD calculations. In *JHEP*, **06**: (2011), p. 144. arXiv: 1012.4948 [hep-ph].

[76] J. M. Campbell, M. A. Cullen, and E. W. N. Glover. Four jet event shapes in electron - positron annihilation. In *Eur. Phys. J.*, **C9**: (1999), pp. 245–265. arXiv: hep-ph/9809429 [hep-ph].

[77] J. Reuter, F. Bach, B. Chokoufe Nejad, W. Kilian, et al. Modern Particle Physics Event Generation with WHIZARD. In *J. Phys. Conf. Ser.*, **608**:1 (2015), p. 012063. arXiv: 1410.4505 [hep-ph].

[78] J. Reuter, F. Bach, B. Chokoufe Nejad, A. H. Hoang, et al. "Top Physics in WHIZARD". In *Proceedings, International Workshop on Future Linear Colliders (LCWS15): Whistler, B.C., Canada, November 02-06, 2015.* 2016. arXiv: 1602.08035 [hep-ph].

[79] C. Weiss. *Top-quark Physics as a Prime Application of Automated Higher-order Corrections.* PhD thesis. Hamburg University, 2017.

[80] M. Moretti, T. Ohl, and J. Reuter. O'Mega: An Optimizing matrix element generator. In (2001), pp. 1981–2009. arXiv: hep-ph/0102195 [hep-ph].

[81] W. Kilian, T. Ohl, and J. Reuter. WHIZARD: Simulating Multi-Particle Processes at LHC and ILC. In *Eur. Phys. J.*, **C71**: (2011), p. 1742. arXiv: 0708.4233 [hep-ph].

[82] W. Kilian, D. Rainwater, and J. Reuter. Pseudo-axions in little Higgs models. In *Phys. Rev.*, **D71**: (2005), p. 015008. arXiv: hep-ph/0411213 [hep-ph].

[83] K. Hagiwara, W. Kilian, F. Krauss, T. Ohl, et al. Supersymmetry simulations with off-shell effects for CERN LHC and ILC. In *Phys. Rev.*, **D73**: (2006), p. 055005. arXiv: hep-ph/0512260 [hep-ph].

[84] M. Beyer, W. Kilian, P. Krstonošić, K. Monig, et al. Determination of New Electroweak Parameters at the ILC - Sensitivity to New Physics. In *Eur. Phys. J.*, **C48**: (2006), pp. 353–388. arXiv: hep-ph/0604048 [hep-ph].

[85] A. Alboteanu, W. Kilian, and J. Reuter. Resonances and Unitarity in Weak Boson Scattering at the LHC. In *JHEP*, **11**: (2008), p. 010. arXiv: 0806.4145 [hep-ph].

[86] J. Kalinowski, W. Kilian, J. Reuter, T. Robens, and K. Rolbiecki. Pinning down the Invisible Sneutrino. In *JHEP*, **10**: (2008), p. 090. arXiv: 0809.3997 [hep-ph].

[87] W. Kilian, T. Ohl, J. Reuter, and M. Sekulla. High-Energy Vector Boson Scattering after the Higgs Discovery. In *Phys. Rev.*, **D91**: (2015), p. 096007. arXiv: 1408.6207 [hep-ph].

[88] N. D. Christensen and C. Duhr. FeynRules - Feynman rules made easy. In *Comput. Phys. Commun.*, **180**: (2009), pp. 1614–1641. arXiv: 0806.4194 [hep-ph].

[89] F. Staub. Exploring new models in all detail with SARAH. In *Adv. High Energy Phys.*, **2015**: (2015), p. 840780. arXiv: 1503.04200 [hep-ph].

[90] N. D. Christensen, C. Duhr, B. Fuks, J. Reuter, and C. Speckner. Introducing an interface between WHIZARD and FeynRules. In *Eur. Phys. J.*, **C72**: (2012), p. 1990. arXiv: 1010.3251 [hep-ph].

[91] F. Staub, T. Ohl, W. Porod, and C. Speckner. A Tool Box for Implementing Supersymmetric Models. In *Comput. Phys. Commun.*, **183**: (2012), pp. 2165–2206. arXiv: 1109.5147 [hep-ph].

[92] C. Degrande, C. Duhr, B. Fuks, D. Grellscheid, et al. UFO - The Universal FeynRules Output. In *Comput. Phys. Commun.*, **183**: (2012), pp. 1201–1214. arXiv: 1108.2040 [hep-ph].

[93] W. Kilian, J. Reuter, and T. Robens. NLO Event Generation for Chargino Production at the ILC. In *Eur. Phys. J.*, **C48**: (2006), pp. 389–400. arXiv: hep-ph/0607127 [hep-ph].

[94] T. Robens, J. Kalinowski, K. Rolbiecki, W. Kilian, and J. Reuter. (N)LO Simulation of Chargino Production and Decay. In *Acta Phys. Polon.*, **B39**: (2008), pp. 1705–1714. arXiv: 0803.4161 [hep-ph].

[95] T. Binoth, N. Greiner, A. Guffanti, J. Reuter, et al. Next-to-leading order QCD corrections to $pp \to b\bar{b}b\bar{b} + X$ at the LHC: the quark induced case. In *Phys. Lett.*, **B685**: (2010), pp. 293–296. arXiv: 0910.4379 [hep-ph].

[96] N. Greiner, A. Guffanti, T. Reiter, and J. Reuter. NLO QCD corrections to the production of two bottom-antibottom pairs at the LHC. In *Phys. Rev. Lett.*, **107**: (2011), p. 102002. arXiv: 1105.3624 [hep-ph].

[97] A. van Hameren, C. G. Papadopoulos, and R. Pittau. Automated one-loop calculations: A Proof of concept. In *JHEP*, **09**: (2009), p. 106. arXiv: 0903.4665 [hep-ph].

[98] G. Bevilacqua, M. Czakon, M. V. Garzelli, A. van Hameren, et al. HELAC-NLO. In *Comput. Phys. Commun.*, **184**: (2013), pp. 986–997. arXiv: 1110.1499 [hep-ph].

[99] V. Hirschi, R. Frederix, S. Frixione, M. V. Garzelli, et al. Automation of one-loop QCD corrections. In *JHEP*, **05**: (2011), p. 044. arXiv: 1103.0621 [hep-ph].

[100] S. Kallweit, J. M. Lindert, P. Maierhöfer, S. Pozzorini, and M. Schönherr. NLO electroweak automation and precise predictions for W+multijet production at the LHC. In *JHEP*, **04**: (2015), p. 012. arXiv: 1412.5157 [hep-ph].

[101] S. Kallweit, J. M. Lindert, P. Maierhöfer, S. Pozzorini, and M. Schönherr. NLO QCD+EW predictions for V + jets including off-shell vector-boson decays and multijet merging. In *JHEP*, **04**: (2016), p. 021. arXiv: 1511.08692 [hep-ph].

[102] S. Frixione, V. Hirschi, D. Pagani, H. S. Shao, and M. Zaro. Electroweak and QCD corrections to top-pair hadroproduction in association with heavy bosons. In *JHEP*, **06**: (2015), p. 184. arXiv: 1504.03446 [hep-ph].

[103] R. Frederix, S. Frixione, V. Hirschi, D. Pagani, et al. The complete NLO corrections to dijet hadroproduction. In (2016). arXiv: 1612.06548 [hep-ph].

[104] B. Biedermann, S. Bräuer, A. Denner, M. Pellen, et al. Automation of NLO QCD and EW corrections with Sherpa and Recola. In (2017). arXiv: 1704.05783 [hep-ph].

[105] T. Ohl. Vegas revisited: Adaptive Monte Carlo integration beyond factorization. In *Comput. Phys. Commun.*, **120**: (1999), pp. 13–19. arXiv: hep-ph/9806432 [hep-ph].

[106] T. Ohl. CIRCE version 1.0: Beam spectra for simulating linear collider physics. In *Comput. Phys. Commun.*, **101**: (1997), pp. 269–288. arXiv: hep-ph/9607454 [hep-ph].

[107] W. Kilian, T. Ohl, J. Reuter, and C. Speckner. QCD in the Color-Flow Representation. In *JHEP*, **10**: (2012), p. 022. arXiv: 1206.3700 [hep-ph].

[108] R. Kleiss and R. Pittau. Weight optimization in multichannel Monte Carlo. In *Comput. Phys. Commun.*, **83**: (1994), pp. 141–146. arXiv: hep-ph/9405257 [hep-ph].

[109] G. P. Lepage. A New Algorithm for Adaptive Multidimensional Integration. In *J. Comput. Phys.*, **27**: (1978), p. 192.

[110] C. Rimbault, P. Bambade, O. Dadoun, G. Le Meur, et al. GuineaPig++: An Upgraded Version of the Linear Collider Beam Beam Interaction Simulation Code GuineaPig. In *Conf. Proc.*, **C070625**: (2007), p. 2728.

[111] D. Schulte. Beam-beam simulations with GuineaPig. In (1999).

[112] W. Kilian, J. Reuter, S. Schmidt, and D. Wiesler. An Analytic Initial-State Parton Shower. In *JHEP*, **04**: (2012), p. 013. arXiv: 1112.1039 [hep-ph].

[113] M. Dobbs and J. B. Hansen. The HepMC C++ Monte Carlo event record for High Energy Physics. In *Comput. Phys. Commun.*, **134**: (2001), pp. 41–46.

[114] S. Aplin, J. Engels, F. Gaede, N. A. Graf, et al. "LCIO: A Persistency Framework and Event Data Model for HEP". In *Proceedings, 2012 IEEE Nuclear Science Symposium and Medical Imaging Conference (NSS/MIC 2012): Anaheim, California, USA, October 29-November 3, 2012.* 2012, pp. 2075–2079.

[115] F. Gaede, T. Behnke, N. Graf, and T. Johnson. LCIO: A Persistency framework for linear collider simulation studies. In *eConf*, **C0303241**: (2003), TUKT001. arXiv: physics/0306114 [physics].

[116] A. Buckley, J. Butterworth, L. Lönnblad, D. Grellscheid, et al. Rivet user manual. In *Comput. Phys. Commun.*, **184**: (2013), pp. 2803–2819. arXiv: 1003.0694 [hep-ph].

[117] E. Byckling and K. Kajantie. *Particle Kinematics*. Jyväskylä, Finland: John Wiley & Sons, 1973.

[118] B. Chokoufe Nejad, T. Ohl, and J. Reuter. Simple, parallel virtual machines for extreme computations. In *Comput. Phys. Commun.*, **196**: (2015), pp. 58–69. arXiv: 1411.3834 [physics.comp-ph].

[119] J. Reuter, B. Chokoufe Nejad, and T. Ohl. Making extreme computations possible with virtual machines. In *J. Phys. Conf. Ser.*, **762**:1 (2016), p. 012071. arXiv: 1602.07242 [physics.comp-ph].

[120] S. Alioli, P. Nason, C. Oleari, and E. Re. NLO vector-boson production matched with shower in POWHEG. In *JHEP*, **07**: (2008), p. 060. arXiv: 0805.4802 [hep-ph].

[121] S. Alioli, P. Nason, C. Oleari, and E. Re. NLO Higgs boson production via gluon fusion matched with shower in POWHEG. In *JHEP*, **04**: (2009), p. 002. arXiv: 0812.0578 [hep-ph].

[122] K. Kondo. Dynamical Likelihood Method for Reconstruction of Events With Missing Momentum. 1: Method and Toy Models. In *J. Phys. Soc. Jap.*, **57**: (1988), pp. 4126–4140.

[123] K. Kondo. Dynamical likelihood method for reconstruction of events with missing momentum. 2: Mass spectra for $2 \to 2$ processes. In *J. Phys. Soc. Jap.*, **60**: (1991), pp. 836–844.

[124] V. M. Abazov et al., D0. In *Nature*, **429**: (2004), pp. 638–642. arXiv: hep-ex/0406031 [hep-ex].

[125] A. Abulencia et al., CDF. Top quark mass measurement from dilepton events at CDF II with the matrix-element method. In *Phys. Rev.*, **D74**: (2006), p. 032009. arXiv: hep-ex/0605118 [hep-ex].

[126] J. Alwall, A. Freitas, and O. Mattelaer. The Matrix Element Method and QCD Radiation. In *Phys. Rev.*, **D83**: (2011), p. 074010. arXiv: 1010.2263 [hep-ph].

[127] J. M. Campbell, W. T. Giele, and C. Williams. The Matrix Element Method at Next-to-Leading Order. In *JHEP*, **11**: (2012), p. 043. arXiv: 1204.4424 [hep-ph].

[128] J. M. Campbell, W. T. Giele, and C. Williams. "Extending the Matrix Element Method to Next-to-Leading Order". In *Proceedings, 47th Rencontres de Moriond on QCD and High Energy Interactions: La Thuile, France, March 10-17, 2012*. 2012, pp. 319–322. arXiv: 1205.3434 [hep-ph].

[129] J. M. Campbell, R. K. Ellis, W. T. Giele, and C. Williams. Finding the Higgs boson in decays to $Z\gamma$ using the matrix element method at Next-to-Leading Order. In *Phys. Rev.*, **D87**:7 (2013), p. 073005. arXiv: 1301.7086 [hep-ph].

[130] T. Martini and P. Uwer. Extending the Matrix Element Method beyond the Born approximation: Calculating event weights at next-to-leading order accuracy. In *JHEP*, **09**: (2015), p. 083. arXiv: 1506.08798 [hep-ph].

[131] T. Martini and P. Uwer. The Matrix Element Method at Next-to-Leading Order Accuracy. In *Acta Phys. Polon.*, **B46**:11 (2015), p. 2143. arXiv: 1511.07150 [hep-ph].

[132] W. T. Giele, G. C. Stavenga, and J.-C. Winter. A Forward Branching Phase-Space Generator. In (2011). arXiv: 1106.5045 [hep-ph].

[133] T. Ježo and P. Nason. On the Treatment of Resonances in Next-to-Leading Order Calculations Matched to a Parton Shower. In *JHEP*, **12**: (2015), p. 065. arXiv: 1509.09071 [hep-ph].

[134] T. Ježo, J. M. Lindert, P. Nason, C. Oleari, and S. Pozzorini. An NLO+PS generator for $t\bar{t}$ and Wt production and decay including non-resonant and interference effects. In *Eur. Phys. J.*, **C76**:12 (2016), p. 691. arXiv: 1607.04538 [hep-ph].

[135] R. K. Ellis, W. J. Stirling, and B. R. Webber. QCD and collider physics. In *Camb. Monogr. Part. Phys. Nucl. Phys. Cosmol.*, **8**: (1996), pp. 1–435.

[136] A. Buckley et al. General-purpose event generators for LHC physics. In *Phys. Rept.*, **504**: (2011), pp. 145–233. arXiv: 1101.2599 [hep-ph].

[137] Particle Data Group. Review of Particle Physics. In *Chin. Phys.*, **C40**:10 (2016), p. 100001.

[138] L. Lönnblad. Fooling Around with the Sudakov Veto Algorithm. In *Eur. Phys. J.*, **C73**:3 (2013), p. 2350. arXiv: 1211.7204 [hep-ph].

[139] H. Contopanagos, E. Laenen, and G. F. Sterman. Sudakov factorization and resummation. In *Nucl. Phys.*, **B484**: (1997), pp. 303–330. arXiv: hep-ph/9604313 [hep-ph].

[140] V. V. Sudakov. Vertex parts at very high-energies in quantum electrodynamics. In *Sov. Phys. JETP*, **3**: (1956). [Zh. Eksp. Teor. Fiz.30,87(1956)], pp. 65–71.

[141] Y. L. Dokshitzer. Calculation of the Structure Functions for Deep Inelastic Scattering and e^+e^- Annihilation by Perturbation Theory in Quantum Chromodynamics. In *Sov. Phys. JETP*, **46**: (1977). [Zh. Eksp. Teor. Fiz.73,1216(1977)], pp. 641–653.

[142] V. N. Gribov and L. N. Lipatov. Deep inelastic e p scattering in perturbation theory. In *Sov. J. Nucl. Phys.*, **15**: (1972). [Yad. Fiz.15,781(1972)], pp. 438–450.

[143] G. Altarelli and G. Parisi. Asymptotic Freedom in Parton Language. In *Nucl. Phys.*, **B126**: (1977), pp. 298–318.

[144] T. Sjöstrand, S. Mrenna, and P. Z. Skands. PYTHIA 6.4 Physics and Manual. In *JHEP*, **05**: (2006), p. 026. arXiv: hep-ph/0603175 [hep-ph].

[145] S. Frixione, P. Nason, and C. Oleari. Matching NLO QCD computations with Parton Shower simulations: the POWHEG method. In *JHEP*, **11**: (2007), p. 070. arXiv: 0709.2092 [hep-ph].

[146] W. T. Giele, D. A. Kosower, and P. Z. Skands. Higher-Order Corrections to Timelike Jets. In *Phys. Rev.*, **D84**: (2011), p. 054003. arXiv: 1102.2126 [hep-ph].

[147] M. Bengtsson and T. Sjöstrand. Coherent Parton Showers Versus Matrix Elements: Implications of PETRA - PEP Data. In *Phys. Lett.*, **B185**: (1987), p. 435.

[148] T. Sjöstrand and M. Bengtsson. The Lund Monte Carlo for Jet Fragmentation and e^+e^- Physics. Jetset Version 6.3: An Update. In *Comput. Phys. Commun.*, **43**: (1987), p. 367.

[149] M. L. Mangano, M. Moretti, F. Piccinini, and M. Treccani. Matching matrix elements and shower evolution for top-quark production in hadronic collisions. In *JHEP*, **01**: (2007), p. 013. arXiv: hep-ph/0611129 [hep-ph].

[150] S. Catani, F. Krauss, R. Kuhn, and B. R. Webber. QCD matrix elements + parton showers. In *JHEP*, **11**: (2001), p. 063. arXiv: hep-ph/0109231 [hep-ph].

[151] S. Höche and S. Prestel. Triple collinear emissions in parton showers. In (2017). arXiv: 1705.00742 [hep-ph].

[152] N. Lavesson and L. Lönnblad. Merging parton showers and matrix elements: Back to basics. In *JHEP*, **04**: (2008), p. 085. arXiv: 0712.2966 [hep-ph].

[153] CMS Collaboration. Measurement of the double differential Drell-Yan cross section at low and high masses of the di-muon system at sqrts = 7 TeV. In (2014). eprint: CMS-PAS-FSQ-13-003.

[154] L. Lönnblad. Correcting the color dipole cascade model with fixed order matrix elements. In *JHEP*, **05**: (2002), p. 046. arXiv: hep-ph/0112284 [hep-ph].

[155] L. Lönnblad and S. Prestel. Unitarising Matrix Element + Parton Shower merging. In *JHEP*, **02**: (2013), p. 094. arXiv: 1211.4827 [hep-ph].

[156] S. Plätzer. Controlling inclusive cross sections in parton shower + matrix element merging. In *JHEP*, **08**: (2013), p. 114. arXiv: 1211.5467 [hep-ph].

[157] J. Bellm. *Higher Order Corrections to Multi Jet Final States at Colliders*. PhD thesis. KIT, Karlsruhe, IKP, 2015.

[158] L. Hartgring, E. Laenen, and P. Skands. Antenna Showers with One-Loop Matrix Elements. In *JHEP*, **10**: (2013), p. 127. arXiv: 1303.4974 [hep-ph].

[159] T. Gehrmann, S. Höche, F. Krauss, M. Schönherr, and F. Siegert. NLO QCD matrix elements + parton showers in $e^+e^- \to$ hadrons. In *JHEP*, **01**: (2013), p. 144. arXiv: 1207.5031 [hep-ph].

[160] L. Lönnblad and S. Prestel. Merging Multi-leg NLO Matrix Elements with Parton Showers. In *JHEP*, **03**: (2013), p. 166. arXiv: 1211.7278 [hep-ph].

[161] S. Frixione and B. R. Webber. Matching NLO QCD computations and parton shower simulations. In *JHEP*, **06**: (2002), p. 029. arXiv: hep-ph/0204244 [hep-ph].

[162] P. Nason. A New method for combining NLO QCD with shower Monte Carlo algorithms. In *JHEP*, **11**: (2004), p. 040. arXiv: hep-ph/0409146 [hep-ph].

[163] P. Nason and G. Ridolfi. A Positive-weight next-to-leading-order Monte Carlo for Z pair hadroproduction. In *JHEP*, **08**: (2006), p. 077. arXiv: hep-ph/0606275 [hep-ph].

[164] S. Alioli, P. Nason, C. Oleari, and E. Re. A general framework for implementing NLO calculations in shower Monte Carlo programs: the POWHEG BOX. In *JHEP*, **06**: (2010), p. 043. arXiv: 1002.2581 [hep-ph].

[165] S. Höche, F. Krauss, M. Schönherr, and F. Siegert. Automating the POWHEG method in Sherpa. In *JHEP*, **04**: (2011), p. 024. arXiv: 1008.5399 [hep-ph].

[166] S. Plätzer and S. Gieseke. Dipole Showers and Automated NLO Matching in Herwig++. In *Eur. Phys. J.*, **C72**: (2012), p. 2187. arXiv: 1109.6256 [hep-ph].

[167] W. T. Giele, D. A. Kosower, and P. Z. Skands. A simple shower and matching algorithm. In *Phys. Rev.*, **D78**: (2008), p. 014026. arXiv: 0707.3652 [hep-ph].

[168] N. Fischer, S. Prestel, M. Ritzmann, and P. Skands. Vincia for Hadron Colliders. In *Eur. Phys. J.*, **C76**:11 (2016), p. 589. arXiv: 1605.06142 [hep-ph].

[169] A. Mück. Parton-shower matching for electroweak corrections. In *Nucl. Part. Phys. Proc.*, **261-262**: (2015), pp. 308–310.

[170] S. Plätzer. ExSample: A Library for Sampling Sudakov-Type Distributions. In *Eur. Phys. J.*, **C72**: (2012), p. 1929. arXiv: 1108.6182 [hep-ph].

[171] O. Latunde-Dada, S. Gieseke, and B. Webber. A Positive-Weight Next-to-Leading-Order Monte Carlo for e^+e^- Annihilation to Hadrons. In *JHEP*, **02**: (2007), p. 051. arXiv: hep-ph/0612281 [hep-ph].

[172] O. Latunde-Dada. "The POWHEG method applied to top pair production and decays at the ILC". In *Linear colliders. Proceedings, International Linear Collider Workshop, LCWS08, and International Linear Collider Meeting, ILC08, Chicago, USA, November 16-20, 2008.* 2008. arXiv: 0812.3297 [hep-ph].

[173] B. Chokoufe Nejad, W. Kilian, J. Reuter, and C. Weiss. Matching NLO QCD Corrections in WHIZARD with the POWHEG scheme. In *PoS*, **EPS-HEP2015**: (2015), p. 317. arXiv: 1510.02739 [hep-ph].

[174] J. Reuter, B. Chokoufe Nejad, A. H. Hoang, W. Kilian, et al. Automation of NLO processes and decays and POWHEG matching in WHIZARD. In *J. Phys. Conf. Ser.*, **762**:1 (2016), p. 012059. arXiv: 1602.06270 [hep-ph].

[175] M. Cacciari, G. P. Salam, and G. Soyez. FastJet User Manual. In *Eur. Phys. J.*, **C72**: (2012), p. 1896. arXiv: 1111.6097 [hep-ph].

[176] M. Vos et al. Top physics at high-energy lepton colliders. In (2016). arXiv: 1604.08122 [hep-ex].

[177] J. Fleischer, A. Leike, T. Riemann, and A. Werthenbach. Electroweak one loop corrections for e^+e^- annihilation into t anti-top including hard bremsstrahlung. In *Eur. Phys. J.*, **C31**: (2003), pp. 37–56. arXiv: hep-ph/0302259 [hep-ph].

[178] A. Denner, S. Dittmaier, M. Roth, and M. M. Weber. Radiative corrections to Higgs boson production in association with top quark pairs at e^+e^- colliders. In *Nucl. Phys.*, **B680**: (2004), pp. 85–116. arXiv: hep-ph/0309274 [hep-ph].

[179] J. Fuster, I. García, P. Gomis, M. Perelló, et al. Study of single top production at high energy electron positron colliders. In *Eur. Phys. J.*, **C75**: (2015), p. 223. arXiv: 1411.2355 [hep-ex].

[180] C. R. Schmidt. Top quark production and decay at next-to-leading order in e^+e^- annihilation. In *Phys. Rev.*, **D54**: (1996), pp. 3250–3265. arXiv: hep-ph/9504434 [hep-ph].

[181] A. Denner, S. Dittmaier, M. Roth, and L. H. Wieders. Electroweak corrections to charged-current $e^+e^- \to 4$ fermion processes: Technical details and further results. In *Nucl. Phys.*, **B724**: (2005). [Erratum: Nucl. Phys.B854,504(2012)], pp. 247–294. arXiv: hep-ph/0505042 [hep-ph].

[182] G. Bevilacqua, M. Czakon, A. van Hameren, C. G. Papadopoulos, and M. Worek. Complete off-shell effects in top quark pair hadroproduction with leptonic decay at next-to-leading order. In *JHEP*, **02**: (2011), p. 083. arXiv: 1012.4230 [hep-ph].

[183] A. Denner, S. Dittmaier, S. Kallweit, and S. Pozzorini. NLO QCD corrections to WWbb production at hadron colliders. In *Phys. Rev. Lett.*, **106**: (2011), p. 052001. arXiv: 1012.3975 [hep-ph].

[184] A. Denner, S. Dittmaier, S. Kallweit, and S. Pozzorini. NLO QCD corrections to off-shell top-antitop production with leptonic decays at hadron colliders. In *JHEP*, **10**: (2012), p. 110. arXiv: 1207.5018 [hep-ph].

[185] G. Heinrich, A. Maier, R. Nisius, J. Schlenk, and J. Winter. NLO QCD corrections to $W^+W^-b\bar{b}$ production with leptonic decays in the light of top quark mass and asymmetry measurements. In *JHEP*, **06**: (2014), p. 158. arXiv: 1312.6659 [hep-ph].

[186] R. Frederix. Top Quark Induced Backgrounds to Higgs Production in the $WW^{(*)} \to ll\nu\nu$ Decay Channel at Next-to-Leading-Order in QCD. In *Phys. Rev. Lett.*, **112**:8 (2014), p. 082002. arXiv: 1311.4893 [hep-ph].

[187] F. Cascioli, S. Kallweit, P. Maierhöfer, and S. Pozzorini. A unified NLO description of top-pair and associated Wt production. In *Eur. Phys. J.*, **C74**:3 (2014), p. 2783. arXiv: 1312.0546 [hep-ph].

[188] A. Denner and M. Pellen. NLO electroweak corrections to off-shell top-antitop production with leptonic decays at the LHC. In *JHEP*, **08**: (2016), p. 155. arXiv: 1607.05571 [hep-ph].

[189] A. Denner and R. Feger. NLO QCD corrections to off-shell top-antitop production with leptonic decays in association with a Higgs boson at the LHC. In *JHEP*, **11**: (2015), p. 209. arXiv: 1506.07448 [hep-ph].

[190] G. Bevilacqua, H. B. Hartanto, M. Kraus, and M. Worek. Top Quark Pair Production in Association with a Jet with Next-to-Leading-Order QCD Off-Shell Effects at the Large Hadron Collider. In *Phys. Rev. Lett.*, **116**:5 (2016), p. 052003. arXiv: 1509.09242 [hep-ph].

[191] G. Bevilacqua, H. B. Hartanto, M. Kraus, and M. Worek. Off-shell Top Quarks with One Jet at the LHC: A comprehensive analysis at NLO QCD. In (2016). arXiv: 1609.01659 [hep-ph].

[192] B. Chokoufe Nejad, W. Kilian, J. M. Lindert, S. Pozzorini, et al. NLO QCD Predictions for off-shell $t\bar{t}$ and $t\bar{t}H$ Production and Decay at a Linear Collider. In *JHEP*, **12**: (2016), p. 075. arXiv: 1609.03390 [hep-ph].

[193] The OpenLoops one-loop generator by F. Cascioli, J. Lindert, P. Maierhöfer and S. Pozzorini is publicly available at http://openloops.hepforge.org.

[194] A. van Hameren. Multi-gluon one-loop amplitudes using tensor integrals. In *JHEP*, **07**: (2009), p. 088. arXiv: 0905.1005 [hep-ph].

[195] F. A. Berends and W. T. Giele. Recursive Calculations for Processes with n Gluons. In *Nucl. Phys.*, **B306**: (1988), pp. 759–808.

[196] A. Kanaki and C. G. Papadopoulos. HELAC: A Package to compute electroweak helicity amplitudes. In *Comput. Phys. Commun.*, **132**: (2000), pp. 306–315. arXiv: hep-ph/0002082 [hep-ph].

[197] F. Caravaglios and M. Moretti. An algorithm to compute Born scattering amplitudes without Feynman graphs. In *Phys. Lett.*, **B358**: (1995), pp. 332–338. arXiv: hep-ph/9507237 [hep-ph].

[198] G. Ossola, C. G. Papadopoulos, and R. Pittau. CutTools: A Program implementing the OPP reduction method to compute one-loop amplitudes. In *JHEP*, **0803**: (2008), p. 042. arXiv: 0711.3596 [hep-ph].

[199] G. Ossola, C. G. Papadopoulos, and R. Pittau. Reducing full one-loop amplitudes to scalar integrals at the integrand level. In *Nucl.Phys.*, **B763**: (2007), pp. 147–169. arXiv: 0609007 [hep-ph].

[200] A. van Hameren. OneLOop: For the evaluation of one-loop scalar functions. In *Comput.Phys.Commun.*, **182**: (2011), pp. 2427–2438. arXiv: 1007.4716 [hep-ph].

[201] A. Denner, S. Dittmaier, and L. Hofer. Collier: a fortran-based Complex One-Loop LIbrary in Extended Regularizations. In (2016). arXiv: 1604.06792 [hep-ph].

[202] A. Denner and S. Dittmaier. Reduction of one loop tensor five point integrals. In *Nucl. Phys.*, **B658**: (2003), pp. 175–202. arXiv: 0212259 [hep-ph].

[203] A. Denner and S. Dittmaier. Reduction schemes for one-loop tensor integrals. In *Nucl. Phys.*, **B734**: (2006), pp. 62–115. arXiv: 0509141 [hep-ph].

[204] A. Denner and S. Dittmaier. Scalar one-loop 4-point integrals. In *Nucl. Phys.*, **B844**: (2011), pp. 199–242. arXiv: 1005.2076 [hep-ph].

[205] G. Ossola, C. G. Papadopoulos, and R. Pittau. On the Rational Terms of the one-loop amplitudes. In *JHEP*, **0805**: (2008), p. 004. arXiv: 0802.1876 [hep-ph].

[206] T. Binoth, J. P. Guillet, and G. Heinrich. Algebraic evaluation of rational polynomials in one-loop amplitudes. In *JHEP*, **0702**: (2007), p. 013. arXiv: 0609054 [hep-ph].

[207] A. Bredenstein, A. Denner, S. Dittmaier, and S. Pozzorini. NLO QCD corrections to t anti-t b anti-b production at the LHC: 1. Quark-antiquark annihilation. In *JHEP*, **0808**: (2008), p. 108. arXiv: 0807.1248 [hep-ph].

[208] P. Draggiotis, M. Garzelli, C. Papadopoulos, and R. Pittau. Feynman Rules for the Rational Part of the QCD 1-loop amplitudes. In *JHEP*, **0904**: (2009), p. 072. arXiv: 0903.0356 [hep-ph].

[209] M. Garzelli, I. Malamos, and R. Pittau. Feynman rules for the rational part of the Electroweak 1-loop amplitudes. In *JHEP*, **1001**: (2010), p. 040. arXiv: 0910.3130 [hep-ph].

[210] M. Garzelli, I. Malamos, and R. Pittau. Feynman rules for the rational part of the Electroweak 1-loop amplitudes in the R_ξ gauge and in the Unitary gauge. In *JHEP*, **1101**: (2011), p. 029. arXiv: 1009.4302 [hep-ph].

[211] M. Garzelli and I. Malamos. R2SM: A Package for the analytic computation of the R_2 Rational terms in the Standard Model of the Electroweak interactions. In *Eur.Phys.J.*, **C71**: (2011), p. 1605. arXiv: 1010.1248 [hep-ph].

[212] H.-S. Shao, Y.-J. Zhang, and K.-T. Chao. Feynman Rules for the Rational Part of the Standard Model One-loop Amplitudes in the 't Hooft-Veltman γ_5 Scheme. In *JHEP*, **1109**: (2011), p. 048. arXiv: 1106.5030 [hep-ph].

[213] S. Alioli et al. Update of the Binoth Les Houches Accord for a standard interface between Monte Carlo tools and one-loop programs. In *Comput. Phys. Commun.*, **185**: (2014), pp. 560–571. arXiv: 1308.3462 [hep-ph].

[214] T. Binoth et al. A Proposal for a standard interface between Monte Carlo tools and one-loop programs. In *Comput. Phys. Commun.*, **181**: (2010). [,1(2010)], pp. 1612–1622. arXiv: 1001.1307 [hep-ph].

[215] Particle Data Group. Review of Particle Physics. In *Chin. Phys.*, **C38**: (2014), p. 090001.

[216] A. Denner and T. Sack. The Top width. In *Nucl. Phys.*, **B358**: (1991), pp. 46–58.

[217] A. H. Hoang and C. J. Reisser. On electroweak matching conditions for top pair production at threshold. In *Phys. Rev.*, **D74**: (2006), p. 034002. arXiv: hep-ph/0604104 [hep-ph].

[218] A. Denner and J.-N. Lang. The Complex-Mass Scheme and Unitarity in perturbative Quantum Field Theory. In *Eur. Phys. J.*, **C75**:8 (2015), p. 377. arXiv: 1406.6280 [hep-ph].

[219] M. Cacciari, G. P. Salam, and G. Soyez. The Anti-k(t) jet clustering algorithm. In *JHEP*, **04**: (2008), p. 063. arXiv: 0802.1189 [hep-ph].

[220] M. Jezabek and J. H. Kühn. Semileptonic Decays of Top Quarks. In *Phys. Lett.*, **B207**: (1988), pp. 91–96.

[221] M. Jezabek and J. H. Kühn. Lepton Spectra from Heavy Quark Decay. In *Nucl. Phys.*, **B320**: (1989), pp. 20–44.

[222] M. Jezabek and J. H. Kühn. QCD Corrections to Semileptonic Decays of Heavy Quarks. In *Nucl. Phys.*, **B314**: (1989), pp. 1–6.

[223] P. Roloff and J. Strube. Measurement of the top Yukawa Coupling at a 1 TeV International Linear Collider using the SiD detector. In (2013). arXiv: 1307.7644 [hep-ex].

[224] P. Roloff. private communication.

[225] M. S. Amjad, M. Boronat, T. Frisson, I. Garcia, et al. A precise determination of top quark electro-weak couplings at the ILC operating at $\sqrt{s} = 500$ GeV. In (2013). arXiv: 1307.8102 [hep-ex].

[226] M. S. Amjad et al. A precise characterisation of the top quark electro-weak vertices at the ILC. In *Eur. Phys. J.*, **C75**:10 (2015), p. 512. arXiv: 1505.06020 [hep-ex].

[227] T. Barklow, J. Brau, K. Fujii, J. Gao, et al. ILC Operating Scenarios. In (2015). arXiv: 1506.07830 [hep-ex].

[228] R. Frederix, S. Frixione, A. S. Papanastasiou, S. Prestel, and P. Torrielli. Off-shell single-top production at NLO matched to parton showers. In *JHEP*, **06**: (2016), p. 027. arXiv: 1603.01178 [hep-ph].

[229] M. Kraus. "NLO QCD off-shell effects for top pair production with a jet in the dilepton channel". In *4th Large Hadron Collider Physics Conference (LHCP 2016) Lund, Sweden, June 13-18, 2016*. 2016. arXiv: 1608.05296 [hep-ph].

[230] A. Kharchilava. Top mass determination in leptonic final states with J/ψ. In *Phys. Lett.*, **B476**: (2000), pp. 73–78. arXiv: 9912320 [hep-ph].

[231] M. Beneke et al. "Top quark physics". In *1999 CERN Workshop on standard model physics (and more) at the LHC, CERN, Geneva, Switzerland, 25-26 May: Proceedings*. 2000. arXiv: 0003033 [hep-ph].

[232] S. Biswas, K. Melnikov, and M. Schulze. Next-to-leading order QCD effects and the top quark mass measurements at the LHC. In *JHEP*, **08**: (2010), p. 048. arXiv: 1006.0910 [hep-ph].

[233] J. Jersák, E. Laermann, and P. M. Zerwas. QCD Corrected Forward Backward Asymmetry of Quark Jets in e^+e^- Annihilation. In *Phys. Lett.*, **B98**: (1981), pp. 363–366.

[234] W. Bernreuther, R. Bonciani, T. Gehrmann, R. Heinesch, et al. Two-Parton Contribution to the Heavy-Quark Forward-Backward Asymmetry in NNLO QCD. In *Nucl. Phys.*, **B750**: (2006), pp. 83–107. arXiv: 0604031 [hep-ph].

[235] F. Richard. Present and future constraints on top EW couplings. In (2014). arXiv: 1403.2893 [hep-ph].

[236] W. E. Caswell and G. P. Lepage. Effective Lagrangians for Bound State Problems in QED, QCD, and Other Field Theories. In *Phys. Lett.*, **B167**: (1986), pp. 437–442.

[237] G. T. Bodwin, E. Braaten, and G. P. Lepage. Rigorous QCD analysis of inclusive annihilation and production of heavy quarkonium. In *Phys. Rev.*, **D51**: (1995). [Erratum: Phys. Rev.D55,5853(1997)], pp. 1125–1171. arXiv: hep-ph/9407339 [hep-ph].

[238] V. S. Fadin and V. A. Khoze. Threshold Behavior of Heavy Top Production in e^+e^- Collisions. In *JETP Lett.*, **46**: (1987). [Pisma Zh. Eksp. Teor. Fiz.46,417(1987)], pp. 525–529.

[239] M. J. Strassler and M. E. Peskin. The Heavy top quark threshold: QCD and the Higgs. In *Phys. Rev.*, **D43**: (1991), pp. 1500–1514.

[240] M. Jezabek, J. H. Kühn, and T. Teubner. Momentum distributions in t anti-t production and decay near threshold. In *Z. Phys.*, **C56**: (1992), pp. 653–660.

[241] Y. Sumino, K. Fujii, K. Hagiwara, H. Murayama, and C. K. Ng. Top quark pair production near threshold. In *Phys. Rev.*, **D47**: (1993), pp. 56–81.

[242] A. H. Hoang et al. Top - anti-top pair production close to threshold: Synopsis of recent NNLO results. In *Eur. Phys. J.direct*, **C3**: (2000), pp. 1–22. arXiv: 0001286 [hep-ph].

[243] A. Pineda and J. Soto. Effective field theory for ultrasoft momenta in NRQCD and NRQED. In *Nucl. Phys. Proc. Suppl.*, **64**: (1998), pp. 428–432. arXiv: hep-ph/9707481 [hep-ph].

[244] N. Brambilla, A. Pineda, J. Soto, and A. Vairo. Potential NRQCD: An Effective theory for heavy quarkonium. In *Nucl. Phys.*, **B566**: (2000), p. 275. arXiv: hep-ph/9907240 [hep-ph].

[245] M. E. Luke, A. V. Manohar, and I. Z. Rothstein. Renormalization group scaling in nonrelativistic QCD. In *Phys. Rev.*, **D61**: (2000), p. 074025. arXiv: hep-ph/9910209 [hep-ph].

[246] A. V. Manohar and I. W. Stewart. Renormalization group analysis of the QCD quark potential to order v^2. In *Phys. Rev.*, **D62**: (2000), p. 014033. arXiv: hep-ph/9912226 [hep-ph].

[247] A. V. Manohar and I. W. Stewart. The QCD heavy quark potential to order v^2: One loop matching conditions. In *Phys. Rev.*, **D62**: (2000), p. 074015. arXiv: hep-ph/0003032 [hep-ph].

[248] A. V. Manohar and I. W. Stewart. Running of the heavy quark production current and 1 / v potential in QCD. In *Phys. Rev.*, **D63**: (2001), p. 054004. arXiv: hep-ph/0003107 [hep-ph].

[249] A. H. Hoang, A. V. Manohar, I. W. Stewart, and T. Teubner. The Threshold t-tbar cross-section at NNLL order. In *Phys. Rev.*, **D65**: (2002), p. 014014. arXiv: hep-ph/0107144 [hep-ph].

[250] A. H. Hoang and M. Stahlhofen. The Top-Antitop Threshold at the ILC: NNLL QCD Uncertainties. In *JHEP*, **05**: (2014), p. 121. arXiv: 1309.6323 [hep-ph].

[251] A. H. Hoang, V. Mateu, and S. Mohammad Zebarjad. Heavy Quark Vacuum Polarization Function at $O(\alpha_s^2)$ and $O(\alpha_s^3)$. In *Nucl. Phys.*, **B813**: (2009), pp. 349–369. arXiv: 0807.4173 [hep-ph].

[252] A. A. Penin and J. H. Piclum. Threshold production of unstable top. In *JHEP*, **01**: (2012), p. 034. arXiv: 1110.1970 [hep-ph].

[253] B. Jantzen and P. Ruiz-Femenía. Next-to-next-to-leading order nonresonant corrections to threshold top-pair production from e^+e^- collisions: Endpoint-singular terms. In *Phys. Rev.*, **D88**:5 (2013), p. 054011. arXiv: 1307.4337 [hep-ph].

[254] A. Broggio, A. Ferroglia, B. D. Pecjak, and L. L. Yang. NNLL resummation for the associated production of a top pair and a Higgs boson at the LHC. In *JHEP*, **02**: (2017), p. 126. arXiv: 1611.00049 [hep-ph].

[255] A. Kulesza, L. Motyka, T. Stebel, and V. Theeuwes. Associated $t\bar{t}H$ production at the LHC. In (2017). arXiv: 1704.03363 [hep-ph].

[256] K. Hagiwara, K. Ma, and H. Yokoya. Probing CP violation in e^+e^- production of the Higgs boson and toponia. In *JHEP*, **06**: (2016), p. 048. arXiv: 1602.00684 [hep-ph].

[257] Y. Sumino and H. Yokoya. Bound-state effects on kinematical distributions of top quarks at hadron colliders. In *JHEP*, **09**: (2010). [Erratum: JHEP06,037(2016)], p. 034. arXiv: 1007.0075 [hep-ph].

[258] M. Peter. The Static quark - anti-quark potential in QCD to three loops. In *Phys. Rev. Lett.*, **78**: (1997), pp. 602–605. arXiv: hep-ph/9610209 [hep-ph].

[259] Y. Schröder. The Static potential in QCD to two loops. In *Phys. Lett.*, **B447**: (1999), pp. 321–326. arXiv: hep-ph/9812205 [hep-ph].

[260] B. A. Kniehl, A. Onishchenko, J. H. Piclum, and M. Steinhauser. Two-loop matching coefficients for heavy quark currents. In *Phys. Lett.*, **B638**: (2006), pp. 209–213. arXiv: hep-ph/0604072 [hep-ph].

[261] A. H. Hoang and P. Ruiz Femenía. Heavy pair production currents with general quantum numbers in dimensionally regularized NRQCD. In *Phys. Rev.*, **D74**: (2006), p. 114016. arXiv: hep-ph/0609151 [hep-ph].

[262] R. G. Stuart. Gauge invariance, analyticity and physical observables at the Z^0 resonance. In *Phys. Lett.*, **B262**: (1991), pp. 113–119.

[263] P. A. Grassi, B. A. Kniehl, and A. Sirlin. Width and partial widths of unstable particles. In *Phys. Rev. Lett.*, **86**: (2001), pp. 389–392. arXiv: hep-th/0005149 [hep-th].

[264] P. Gambino and P. A. Grassi. The Nielsen identities of the SM and the definition of mass. In *Phys. Rev.*, **D62**: (2000), p. 076002. arXiv: hep-ph/9907254 [hep-ph].

[265] A. Denner and S. Dittmaier. The Complex-mass scheme for perturbative calculations with unstable particles. In *Nucl. Phys. Proc. Suppl.*, **160**: (2006), pp. 22–26. arXiv: hep-ph/0605312 [hep-ph].

[266] E. Boos and T. Ohl. Minimal gauge invariant classes of tree diagrams in gauge theories. In *Phys. Rev. Lett.*, **83**: (1999), pp. 480–483. arXiv: hep-ph/9903357 [hep-ph].

[267] A. Aeppli, F. Cuypers, and G. J. van Oldenborgh. O(Λ) corrections to W pair production in e^+e^- and $\gamma\gamma$ collisions. In *Phys. Lett.*, **B314**: (1993), pp. 413–420. arXiv: hep-ph/9303236 [hep-ph].

[268] E. Fuchs, S. Thewes, and G. Weiglein. Interference effects in BSM processes with a generalised narrow-width approximation. In *Eur. Phys. J.*, **C75**: (2015), p. 254. arXiv: 1411.4652 [hep-ph].

[269] M. J. G. Veltman. Unitarity and causality in a renormalizable field theory with unstable particles. In *Physica*, **29**: (1963), pp. 186–207.

[270] A. Aeppli, G. J. van Oldenborgh, and D. Wyler. Unstable particles in one loop calculations. In *Nucl. Phys.*, **B428**: (1994), pp. 126–146. arXiv: hep-ph/9312212 [hep-ph].

[271] A. Denner, S. Dittmaier, M. Roth, and D. Wackeroth. Electroweak radiative corrections to $e^+e^- \to WW \to 4$ fermions in double pole approximation: The RACOONWW approach. In *Nucl. Phys.*, **B587**: (2000), pp. 67–117. arXiv: hep-ph/0006307 [hep-ph].

[272] A. Denner, S. Dittmaier, M. Roth, and D. Wackeroth. $O(\alpha)$ corrections to $e^+e^- \to WW \to 4$ fermions (+ gamma): First numerical results from RACOON W W. In *Phys. Lett.*, **B475**: (2000), pp. 127–134. arXiv: hep-ph/9912261 [hep-ph].

[273] W. Beenakker, F. A. Berends, and A. P. Chapovsky. Radiative corrections to pair production of unstable particles: results for $e^+e^- \to$ four fermions. In *Nucl. Phys.*, **B548**: (1999), pp. 3–59. arXiv: hep-ph/9811481 [hep-ph].

[274] S. Dittmaier and C. Schwan. Non-factorizable photonic corrections to resonant production and decay of many unstable particles. In *Eur. Phys. J.*, **C76**:3 (2016), p. 144. arXiv: 1511.01698 [hep-ph].

[275] S. Bethke, G. Dissertori, and G. P. Salam. World Summary of α_s (2015). In *EPJ Web Conf.*, **120**: (2016), p. 07005.

[276] M. W. Grünewald et al. Reports of the Working Groups on Precision Calculations for LEP2 Physics: Proceedings. Four fermion production in electron positron collisions. In (2000). arXiv: hep-ph/0005309 [hep-ph].

[277] K. Agashe, R. Franceschini, and D. Kim. Simple "invariance" of two-body decay kinematics. In *Phys. Rev.*, **D88**:5 (2013), p. 057701. arXiv: 1209.0772 [hep-ph].

[278] K. Agashe, R. Franceschini, S. Hong, and D. Kim. Energy spectra of massive two-body decay products and mass measurement. In *JHEP*, **04**: (2016), p. 151. arXiv: 1512.02265 [hep-ph].

[279] K. Agashe, R. Franceschini, D. Kim, and M. Schulze. Top quark mass determination from the energy peaks of b-jets and B-hadrons at NLO QCD. In *Eur. Phys. J.*, **C76**:11 (2016), p. 636. arXiv: 1603.03445 [hep-ph].

[280] CMS Collaboration. Measurement of the top-quark mass from the b jet energy spectrum. In (2015).

[281] M. Czakon. A novel subtraction scheme for double-real radiation at NNLO. In *Phys. Lett.*, **B693**: (2010), pp. 259–268. arXiv: 1005.0274 [hep-ph].

[282] C. Farrell and A. H. Hoang. The Large Higgs energy region in Higgs associated top pair production at the linear collider. In *Phys. Rev.*, **D72**: (2005), p. 014007. arXiv: hep-ph/0504220 [hep-ph].

[283] C. Farrell and A. H. Hoang. Next-to-leading-logarithmic QCD corrections to the cross section $\sigma(e^+e^- \to t\bar{t}H)$ at 500 GeV. In *Phys. Rev.*, **D74**: (2006), p. 014008. arXiv: hep-ph/0604166 [hep-ph].

[284] F. Bach, B. Chokoufe Nejad, A. H. Hoang, W. Kilian, J. Reuter, M. Stahlhofen, T. Teubner, C. Weiss. "Matching NLL threshold resummation with fixed-order QCD for differential top-pair production". In prep.

[285] J. Reuter, B. Chokoufe Nejad, and C. Weiss. "NLO QCD Corrections to Off-shell $t\,\bar{t}$ and $t\,\bar{t}\,H$ at the ILC". In *International Workshop on Future Linear Colliders 2016 (LCWS2016) Morioka, Iwate, Japan, December 5-9, 2016*. 2017. arXiv: 1703.05791 [hep-ph].

[286] J. Reuter, F. Bach, B. Chokoufe Nejad, W. Kilian, et al. QCD NLO with Powheg matching and top threshold matching in WHIZARD. In *PoS*, **RADCOR2015**: (2015), p. 088. arXiv: 1601.02459 [hep-ph].

List of acronyms

BLHA Binoth Les Houches Accord

BSM beyond the SM

CKKW Catani, Krauss, Kuhn, Webber

CLIC Compact Linear Collider

CS Catani-Seymour

DPA double-pole approximation

EW electroweak

EHA extra-helicity approximation

GKS Giele, Kosower, Skands

FKS Frixione, Kunszt, Signer

HA helicity approximation

ILC International Linear Collider

ISR initial-state radiation

IR infrared

KLN Kinoshita, Lee, Nauenberg

LO leading order

LL leading logarithm

LHC Large Hadron Collider

MC Monte Carlo

MEM matrix-element method

MLM M. L. Mangano

MPI message passing interface

NLL next-to-leading log

NLO next-to-leading order

NRQCD nonrelativistic QCD

NWA narrow-width approximation

OLP One-Loop Provider

OVM OMEGA virtual machine

PA pole approximation

PDF parton distribution function

PS parton shower

QCD quantum chromodynamics

RG renormalization group

SCET soft-collinear effective theory

SD signal diagram

SM Standard Model

UFO universal FeynRules output

UV ultraviolet

vNRQCD velocity NRQCD

List of publications

Publications and proceedings on the results presented in this thesis:

In prep. F. Bach, B. Chokoufe Nejad, A. H. Hoang, W. Kilian, J. Reuter, M. Stahlhofen, T. Teubner, C. Weiss. Matching NLL threshold resummation with fixed-order QCD for differential top-pair production. [284]

Mar 2017 B. Chokoufe Nejad, J. Reuter, C. Weiss. NLO QCD Corrections to Off-shell $t\,\bar{t}$ and $t\,\bar{t}\,H$ at the ILC. Journal of High Energy Physics. [285].

Sep 2016 B. Chokoufe Nejad, W. Kilian, J. Lindert, S. Pozzorini, J. Reuter, C. Weiss. NLO QCD predictions for off-shell $t\bar{t}$ and $t\bar{t}H$ production and decay at a linear collider. Journal of High Energy Physics. [192].

Feb 2016 J. Reuter, F. Bach, B. Chokoufe Nejad, A. Hoang, W. Kilian, M. Stahlhofen, T. Teubner, C. Weiss. Top Physics in WHIZARD. Proceedings, International Workshop on Future Linear Colliders (LCWS15). [78].

Feb 2016 J. Reuter, B. Chokoufe Nejad, A. Hoang, W. Kilian, M. Stahlhofen, T. Teubner, C. Weiss. Automation of NLO processes and decays and Powheg matching in WHIZARD. Journal of Physics: Conference Series, ACAT2016. [174].

Jan 2016 J. Reuter, F. Bach, B. Chokoufe Nejad, W. Kilian, M. Stahlhofen, C. Weiss. QCD NLO with Powheg matching and top threshold matching in WHIZARD. Proceedings, 12th International Symposium on Radiative Corrections. [286].

Oct 2015 B. Chokoufe, W. Kilian, J. Reuter, C. Weiss. Matching NLO QCD corrections in WHIZARD with the POWHEG scheme. Proceedings of Science, EPS-HEP2015. [173].

Oct 2015 C. Weiss, B. Chokoufe, W. Kilian, J. Reuter. Automated NLO QCD Corrections with WHIZARD. Proceedings of Science, EPS-HEP2015. [40].

Further publications and proceedings during my Ph.D.:

Jan 2016 J. Reuter, B. Chokoufe Nejad, T. Ohl. Making extreme computations possible with virtual machines. Journal of Physics: Conference Series, ACAT2016. [119].

Nov 2015 B. Chokoufe Nejad, J. Reuter, T. Ohl. Simple, parallel virtual machines for extreme computations. Computer Physics Communications. [118].

Oct 2014 J. Reuter, F. Bach, B. Chokoufe Nejad, W. Kilian, T. Ohl, M. Sekulla, C. Weiss. Modern Particle Physics Event Generation with WHIZARD. Journal of physics: Conference Series, ACAT2014. [77].

Conferences, where I presented various topics of this thesis:

Dec 2016 From Continuum to Threshold: Off-shell top pair production at a lepton collider. 12th VCES on Particle Physics and Quantum Field Theory, Vienna, Austria. Poster presentation.

Jul 2016 Whizard for $t\bar{t}$ production – from threshold to continuum. Workshop on Top physics at the LC 2016, Top@LC2016, KEK, Tsukuba, Japan. Invited talk.

Jun 2016 Matching the NLL threshold resummation with fixed-order QCD corrections in top-pair production. ECFA - Linear Collider Workshop, Santander, Spain. Talk in parallel session.

May 2016 Top physics at lepton colliders. ECFA - Linear Collider Workshop, Santander, Spain. Invited summary Talk.

Nov 2015 Matching the NLL threshold resummation with fixed-order QCD corrections in top-pair production. 9th Annual Meeting of the Helmholtz Alliance "Physics at the Terascale", Hamburg, Germany. Talk in parallel session.

Jul 2015 Matching NLO QCD Corrections in WHIZARD with the POWHEG scheme. European Physical Society Conference on High Energy Physics 2015, Vienna, Austria. Talk in parallel session.

Mar 2015 Analytic Parton Shower & Unitary Matching+Merging in WHIZARD. 2nd International WHIZARD Forum, University of Würzburg. Talk.

Acknowledgements

While the creation of a dissertation is by design a single-handed endeavor, every step that leads to it is filled with collaborative work and discussions between scientists. Thus, I want to use this opportunity to thank all the persons that either directly or indirectly influenced the successful completion of this work:

Jürgen Reuter for giving me the opportunity to perform my PhD under his supervision. It has been a chance for me to grow and experience not only the life as a scientist but also the ups and downs of open-source software development. Furthermore, I am grateful for his proofreading and comments.

Andre Hoang for the countless discussions that were the foundation for the third part of this thesis and the corresponding publications.

Sven Moch for guiding me in administrative questions concerning the University as my second supervisor as well as examining this thesis.

Gudrid Moortgat-Pick, Dieter Horns and Andreas Meyer for joining my thesis committee.

Christian Weiss for the very close and productive collaboration. We have formed a formidable team that certainly was more than the sum of its parts.

Jonas Lindert and Maximilian Stahlhofen for collaborating on and validating sections of the second and third part, respectively.

Other members of the Whizard development team for mostly productive collaboration meetings with entertaining evenings.

DESY for financial support not only in terms of salary but also enabling me to visit various summer schools and international conferences.

Julia Herrmann and Cristina Guerrero for helping with all the administrative duties and formalities.

My other office mates: Elina Fuchs, Matthias Schlaffer, Julian Schweizer, Marco Scalisi and Jonas Wittbrodt for encouraging and distracting me.

Tomáš Ježo for visiting us at DESY to allow a fruitful exchange about the resonance-aware FKS method.

Nico Greiner for enlightening discussions on NLO event generation and GoSam.

Emanuele Bagnaschi for interesting discourse on Powheg matching and Italian food.

Christian Schwinn for stimulating discussions on nonrelativistic computations, double-pole approximations and thresholds.

Thomas Rauh and Christopher Schwan for helpful correspondence and discussions about the work presented in this thesis.

Michael Peskin for an insightful idea for presentation of the threshold computation.

Many more (partially former) members of the DESY and University theory group for the overall amazing environment and conversations on physics and beyond: So Young Shim, Anne Ernst, Thomas Lübbert, Jan Peter Carstensen, Markus Dierigl, Severin Lüst, Markus Ebert, Stefan Liebler, Clemens Wiek, Laura Sagunski, Janis Kummer, Sebastian Passehr, Wolfgang Hollik, Peter Drechsel, Gauthier Durieux, Felix Kahlhöfer, Shruti Patel, Lorena Rothen, Stefano Di Vita, Piotr Pietrulewicz, Maarten Buffing and everyone I have forgotten.

Ina Geier for all the support, encouragement and love throughout the years as well as for bravely reading the whole thesis.

My family for always supporting me in my decisions and nagging me to visit more often.

Eidesstattliche Erklärung

Hiermit erkläre ich an Eides statt, dass ich die vorliegende Dissertationsschrift selbst verfasst und keine anderen als die angegebenen Quellen und Hilfsmittel benutzt habe.

Hamburg, den 17. Juli 2017 Unterschrift